UNIVERSITY OF NOTTINGHAM, UK

School of the built environment

An investigation of a jet-pump thermal (ice) storage system powered by low-grade heat

By

Mark Worall

Thesis submitted to the University of Nottingham for the Doctor of Philosophy

May 2001

Abstract

This thesis investigates a novel combination of a jet-pump refrigeration cycle and a thermal (ice) storage (TIS) system that could substantially reduce the electrical energy requirements attributable to comfort cooling. Two methods of TIS were identified; spray ice TIS would use evaporative freezing to store ice on a vertical surface, and encapsulated ice TIS would freeze a bed of encapsulated elements by sublimation freezing. The study also investigates jet-pump refrigeration at part-load and a convergent-divergent design manufactured from a thermoset plastic to make recommendations for performance enhancement for a system that has a low COP. An experimental rig was built to investigate the novel concepts in the laboratory.

Encapsulated ice TIS was superior to spray ice TIS because, for the same nominal secondary flow, sublimation freezing causes an increase in coolth storage rate of about 10 % compared to evaporative freezing. Encapsulated ice stores experience difficulties in fully discharging their coolth (approximately 6 % in this case), but spray ice TIS can be used to produce an ice/brine slurry enabling all of the ice to be used, and so may be more suitable if the unmelted ice represents a large proportion of the cooling capacity.

Approximately 85 % to 90 % of the ice formed on the vertical surface during spray ice TIS testing was formed by evaporative freezing from a falling film. At high saturation conditions, heat is transferred mainly by conduction across the falling film

Both the growth of an ice layer on a vertical surface and freezing of encapsulated elements were found to be successful, but a large data spread was observed during spray ice TIS testing. It was thought that a variation in the steady-state saturation conditions in the evaporator/ice store was caused by variability of droplet size

distribution from the spray nozzle flow, which may make a full-scale system unreliable.

The COP of the spray ice TIS system was approximately 0.15 compared to a COP of approximately 0.25 found during encapsulated ice TIS testing. The difference was because of the use of an over-expanded primary nozzle, which restricted secondary flow and increased momentum losses. A primary nozzle that expands close to the design evaporator saturation conditions should be used to maximise entrainment ratio. The COP of a jet-pump TIS is low, but a system designed to operate at off-peak periods could increase the COP to about 0.8 by taking advantage of the lower ambient conditions.

The measurement of entrainment ratio was used successfully to determine ice storage rate and COP. This was valid because of the assumption that the saturation conditions in the evaporator/ice store approached steady-state. However, over longer periods that would be found in large-scale systems, the ice storage rate and entrainment ratio may fall substantially. The steady-state assumption could still be used to observe the change in evaporator conditions by sampling over short time intervals (30 minutes).

At part-load, increases in evaporator saturation temperature could increase entrainment ratio substantially (50 % increase) for only a small reduction in critical pressure lift ratio N_s^* (15 % reduction). A variation in chilled water temperature could be used to boost entrainment ratio at the peak demand. The variation in N_s^* is too small to use this strategy to control the jet-pump with respect to condenser operating conditions.

The entrainment ratio is approximately proportional to the diffuser to primary nozzle area ratio. A doubling of entrainment ratio was attained for only a 15 % reduction in N_s^*.

The change in geometry from a constant area throat to a convergent-divergent design caused the flow through the jet-pump to vary with outlet conditions indicating that secondary flow was not choked. Higher entrainment ratios and pressure lift ratios were observed, but the entrainment ratio varied with outlet conditions in the form of peaks and troughs, making its operation unpredictable. This was thought to be caused by the restriction in secondary flow area due to the interaction of the primary jet and the curved wall.

The convergent-divergent design manufactured from a thermoset plastic was successfully tested, showing that a plastic material can be used as a material of construction. In principle, a large number of jet-pump units could be manufactured from a single mould, reducing the first cost.

The investigation proved the concept of jet-pump TIS. Waste-heat could be utilised over 24 hours and year round, increasing the efficiency of the process. The use of a convergent-divergent throat design, multiple geometry jet-pumps and operation at off-peak periods can maximise the performance over a cooling season, and be competitive with other TIS and chiller systems. The mass production of jet-pumps using injection moulding techniques could reduce substantially the capital cost of a system. All of these factors should encourage the development of such systems, so that the harmful emissions caused by the use of air conditioning systems can be minimised.

Acknowledgements

I would like to thank my supervisors Dr Ian Eames and Professor Saffa Riffat for their help, encouragement, support and patience in guiding me through the ups and downs of the research and writing process. The original test rig was designed and built by Dr Shenyi Wu, and so I would like to thank him for providing an excellent test facility, and for offering advice. I would not have been able to follow the research programme if it were not for the financial support of Sanken Setsubi Kogyo, Japan who sponsored the project. In particular I would like to thank Dr Ken Hongo who visited the research project a couple of times and offered kindness, and guidance, and Miss Hiromi, who also visited us and supplied data for comparison with the results presented in this thesis. I could not have carried out the encapsulated ice TIS tests without the help and assistance of David Oliver who manufactured the vast majority of the encapsulated gel sachets. I am also indepted to him for the technical support that he has offered. I would also like to thank the department technicians, Jonathan Moss, Dave Taylor and Bob Clarke for their technical assistance. Finally I could not have completed the study without the support of my brother Phillip Worall, who has been very patient and understanding.

Table of contents

List of tables

List of Figures

Nomenclature

A	area	m^2
A_d	ratio of jet-pump throat to primary nozzle throat	
A_t	primary throat cross-sectional area	m^2
A_x	primary nozzle exit cross-sectional area	m^2
A_2	jet-pump throat cross-sectional	m^2
B	bias	
C_{cu}	specific heat capacity of copper	$J.kg^{-1}.K^{-1}$
C_f	specific heat capacity of food	$J.kg^{-1}.K^{-1}$
C_{gl}	specific heat capacity of glass	$J.kg^{-1}.K^{-1}$
C_i	specific heat capacity of ice	$J.kg^{-1}.K^{-1}$
C_{pv}	specific heat capacity of water vapour	$J.kg^{-1}.K^{-1}$
C_{pw}	specific heat capacity of liquid water	$J.kg^{-1}.K^{-1}$
C_{ss}	specific heat capacity of stainless steel	$J.kg^{-1}.K^{-1}$
C_{wall}	specific heat capacity of vessel wall	$J.kg^{-1}K^{-1}$
COP	coefficient of performance	
COP_{eje}	coefficient of performance of ejector sub-cycle	
COP_{comp}	coefficient of performance of vapour-compression sub-cycle	
COP_{actual}	coefficient of performance of actual jet-pump cycle	
COP_{mech}	coefficient of performance of jet-pump cycle neglecting generator heat input	
CR	condensation rate	$kg.s^{-1}$
c	local speed of sound	$m.s^{-1}$
d	diameter	m
d_2	diameter of diffuser throat	m
d_{cap}	capsule diameter	m
d_t	diameter of primary nozzle throat	m
d_x	outlet diameter of primary nozzle at plane x-x	m
D_v	evaporator vessel diameter	m
ER	evaporation rate	$kg.s^{-1}$
F_c	condensate vessel calibration factor	$g.mm^{-1}$
F_p	generator vessel calibration factor	$g.mm^{-1}$
f_1	proportional factor for evaporation rate	$kg.s^{-1}.Pa^{-1}$
f_2	proportional factor for condensation rate	$kg.s^{-1}.Pa^{-1}$
g	acceleration due to gravity	$m.s^{-2}$
H	height	m
h	specific enthalpy	$J.kg^{-1}$
$h_{f,Tc}$	enthalpy of saturated liquid at condenser saturation temperature	$J.kg^{-1}$
h_{fg}	latent heat of vaporisation	$J.kg^{-1}$
$h_{g,Tg}$	enthalpy of saturated vapour at generator saturation state	$J.kg^{-1}$
h_{if}	latent heat of ice fusion	$J.kg^{-1}$
h_{ix}	specific enthalpy of the primary flow at nozzle exit plane	$J.kg^{-1}$
h_o	specific enthalpy from evaporator stagnation state	$J.kg^{-1}$

h_{ox}	specific enthalpy of the primary flow at nozzle exit plane	$J.kg^{-1}$
h_{sub}	latent heat of sublimation	$J.kg^{-1}$
k	index of compression/expansion	
M	Mach number	
M_{px}	Mach number of the primary flow at x-x	
M_s	secondary flow Mach number	
M_{sx}	Mach number of the secondary flow at x-x	
M*	critical Mach number	
m	mass	kg
m_{cu}	mass of copper capsules	kg
m_{cap}	mass of water in an individual capsule	kg
m_{dry}	mass of dry capsules (polymer granules, copper capsules sachet material)	kg
Δm_e	mass evaporated during sensible cooling	kg
m_F	mass of liquid water contained in the evaporator/ice store when nucleation begins	kg
m_f	mass of food	kg
m_{gl}	mass of the glass vessel	kg
m_i	mass of ice at the end of the charge test	kg
m_{isub}	mass of ice formed during sublimation	kg
Σm_i	total mass of ice formed due to supercooling and sublimation	kg
m_{iF}	mass of ice formed during the supercooling regime	kg
m_L	mass of liquid water at the start of sublimation freezing	kg
Δm_{sub}	mass sublimated after solidification of the bed of capsules	kg
m_{sub}	mass sublimated	kg
m_{ss}	mass of stainless steel plates	kg
m_w	mass of water	kg
m_{wall}	mass of vessel wall	kg
m_{wet}	mass of capsules after the absorption of water	kg
m_0	initial mass of water contained in the bed of capsules	kg
$m_v C_v$	the sum of heat capacities of glass vessel, stainless steel plates copper capsules	$J.K^{-1}$
$\dot{m}$	mass flow	$kg.s^{-1}$
$\dot{m}_c$	condensate mass flow	$kg.s^{-1}$
$\dot{m}_{ch}$	chiller side pump mass flow (gear pump)	$kg.s^{-1}$
$\dot{m}_e$	evaporation rate	$kg.s^{-1}$
$\dot{m}_{espray}$	evaporation rate from spray nozzle flow	$kg.s^{-1}$
$\dot{m}_i$	ice storage rate	$kg.s^{-1}$
$\dot{m}_{ispray}$	ice storage rate from spray nozzle flow	$kg.s^{-1}$
$\dot{m}_p$	primary mass flow	$kg.s^{-1}$

$\dot{m}_s$	secondary mass flow	kg.s^{-1}
$\dot{m}_{sub}$	rate of sublimation	kg.s^{-1}
$\dot{m}_{spray}$	mass flow through spray nozzle	kg.s^{-1}
$\dot{m}_w$	mass flow of water after evaporation	kg.s^{-1}
n	number of rings of spheres	
n	number of samples	
N	number of capsules packed into a single layer	
N_{is}	ratio of outlet to primary stagnation pressure	
N_{sp}	ratio of evaporator to generator stagnation pressure	
N_n	ratio of primary to secondary stagnation pressure	
N_p	ratio of primary stagnation to critical condenser pressure	
N_R	number of layers of spheres in the evaporator vessel	
N_s	ratio of condenser to evaporator pressure (pressure lift ratio)	
N_s*	ratio of critical condenser to evaporator pressure (critical pressure lift ratio)	
N_T	total number of spheres	
N_z	ratio of wall static to generator stagnation pressure	
PF	packing factor	
P	pressure	Pa
ΔP	pressure difference	Pa
P_a	absorbent vapour pressure	Pa
P_i	generator stagnation pressure	Pa
P_L	liquid pressure	Pa
P_o	evaporator stagnation pressure	Pa
P_v	evaporator vapour pressure	Pa
P_0	stagnation pressure	Pa
P_{sat}	saturation pressure	Pa
P_x	static pressure at the nozzle exit plane x-x	Pa
P_3*	critical condenser pressure	Pa
Q	heat transfer	J
Q_{dis}	heat transfer from ice store during discharge	J
Q_e	evaporator cooling load	J
Q_g	generator heat input	J
Q_i	coolth stored as ice	J
Q_{int}	heat transfer in intercooler	J
Q_s	solar heat input	J
Q_{sub}	heat released by sublimation	J
$\dot{Q}$	rate of heat transfer	W
$\dot{Q}_e$	evaporator cooling load	W
$\dot{Q}_g$	generator heat input	W
$\dot{Q}_i$	coolth storage rate	W

$\dot{Q}_{sub}$	heat transferred by sublimation	W
R	characteristic gas constant	$J.kg^{1}.K^{-1}$
R	result of a sample	
$\bar{R}$	mean of random sample	
r	radius	m
r_i	inside radius of sphere	m
S	standard error of n independent sample means	
S	thickness of ice in a solidifying shell	
S	standard deviation of a sample	
SA	surface area	m^2
T	temperature	°C
T_F	equilibrium freezing temperature	°C
T_i	stagnation temperature in the generator	°C
T_L	liquid water temperature	°C
T_o	stagnation temperature in the evaporator	°C
T_{sat}	saturation temperature	°C
T_v	vapour temperature	°C
T_W	coolant temperature	°C
ΔT	temperature difference	K
ΔT_F	degree of supercooling	K
$T(x,t)$	temperature of liquid as functions of position and time	°C
$T(0,t)$	temperature of vapour as a function of time	°C
T_0	stagnation temperature	°C
T_3	stagnation temperature at outlet from the jet-pump	°C
t	t-distribution factor	
t	time	s
t^*	dimensionless time	
Δt	time interval	s
U	velocity	$m.s^{-1}$
U_{px}	velocity of the primary flow at nozzle exit plane x-x	$m.s^{-1}$
U_{sx}	velocity of secondary stream at nozzle exit plane x-x	$m.s^{-1}$
U_1	velocity of combined stream at section 1	$m.s^{-1}$
U^*	velocity when local Mach number is 1	$m.s^{-1}$
V	volume	m^3
v	specific volume	$m^3.kg^{-1}$
W	work input	J
$\dot{W}$	rate of work input	W
$X(t)$	thickness of semi-infinite ice layer	m
$X_1(t)$	distance from initial solid/vapour interface to solid/liquid interface	m
y	axial location of secondary flow minimum area	m
z	axial coordinate in direction of jet-pump flow	m

Subscripts

c	condenser
e	evaporator
g	generator
i	ice
i	generator inlet state
o	evaporator inlet state
t	conditions at jet-pump throat
x	condition at the exit from the primary nozzle
1	condition of mixed stream before normal shock
2	condition of mixed stream after normal shock
3	condition of mixed stream on exit from the diffuser
x,y,z	refer to errors in arithmetic operations

Greek symbols

Δ	change in variable	
α	true value of a sample	
ε	error	
ε_p	percentage relative error	
ε_R	relative error	
ε_S	systematic error or bias	
ε_T	total error or accuracy	
η	efficiency	
η_c	solar collector efficiency	
η_d	diffuser isentropic efficiency	
η_p	primary nozzle isentropic efficiency	
η_s	overall system efficiency	
λ	wavelength of a jet	m
ϕ_m	mixing section loss coefficient	
ω	entrainment ratio	
π	pi	
ρ	density	$kg.m^{-3}$
ρ_L	density of liquid	$kg.m^{-3}$
σ	surface tension	$N.m^{-1}$
τ	ratio of evaporator to generator stagnation temperatures	

Chapter 1. Introduction

This thesis describes and evaluates the results of an experimental investigation of a novel jet-pump thermal (ice) storage (referred to as TIS in the remainder of the thesis) system. A jet-pump, driven by low-grade heat, could utilise waste heat from CHP and co-generation plant or renewable sources of energy such as solar thermal or geothermal systems. This chapter describes the reasons for undertaking the investigation and briefly outlines the operation of conventional jet-pump and TIS. The coupling of a jet-pump with TIS is then discussed and two methods identified. Improvements in jet-pump performance by the use of multiple jet-pumps and a novel convergent-divergent design are then proposed.

1.1. Rational

TIS has become increasingly popular since the early nineteen-eighties for managing peak electrical energy consumption, as described in the literature survey in Chapter 2. The use of TIS can reduce the pollution emissions attributable to a building's cooling system because the most efficient and least polluting power plant are used, and chillers are operated close to their full load condition. However, the main reasons for its use are to enable utility supply companies to manage their energy supply, and to allow the occupiers of buildings to reduce their running costs by taking advantage of off peak tariffs. If TIS were to be driven by a low-grade heat source such as waste heat from a CHP plant then the efficiency of the plant is increased because of higher availability and the electrical energy consumption required for cooling is reduced. The environmental benefits of using the most efficient and least polluting plant and operating the chiller close to full load are then complimentary to the reduction in harmful emissions by employing heat driven TIS. If the low-grade heat is from a renewable source then the emissions caused by TIS are zero.

1.2. Jet-pump refrigeration

A jet-pump is employed to compress low-pressure vapour from an evaporator, causing evaporative cooling. A full description of the jet-pump cycle can be found in Chapter 4. Normally, jet-pump operation is limited by the freezing point of water, however it was found in a review of vacuum freezing methods described in Chapter 2, that jet-pumps could be successfully employed to produce ice in desalination systems. Evaporative freezing techniques could be used in a novel application to couple TIS and a jet-pump refrigeration system driven by a low-grade heat source.

1.3. Thermal (ice) storage TIS

TIS systems fall into two general categories because of their different characteristics. Dynamic TIS produces ice continually on refrigerated plates or drums, whilst static TIS charges and discharges a fixed capacity ice store in separate phases. Jet-pump TIS systems were devised to simulate both dynamic and static TIS. In steam jet-pump refrigeration, return water from the cooling system of a building is cooled to the saturation temperature in the evaporator by flash evaporation. This process was identified as a possible method of dynamic TIS because if the flash evaporator were at a pressure and temperature below the freezing point of water, then a proportion of the water would freeze. Spray ice TIS would use a novel ice production technique where crystallisation took place on the vertical surface of a vessel, as described in Chapter 5. The novel jet-pump TIS system, therefore, requires testing to establish the performance of the jet-pump with respect to the TIS system and to analyse the evaporative freezing and nucleation process.

In static TIS systems, a large quantity of water is required in the evaporator to maximise cooling capacity, and it was concluded that encapsulated ice TIS would provide the most appropriate coupling of jet-pump refrigeration and static TIS.

Chapter 6 describes the assumed freezing process, which is mainly by sublimation. Spherical capsules have a high surface area to volume ratio and therefore present a large surface area for sublimation. Sanken Setsubi Kogyo Ltd of Japan has developed a polymer gel system that absorbs water, and can be retained in absorbent heat sealed sachets. A large number of small diameter capsules were manufactured to contain the water/gel system in the form of spherical elements to maximise the TIS bed surface area. The use of a polymer gel in maximising surface area and a jet-pump to freeze the elements are novel techniques and require testing and analysis.

1.4. Jet-pump operation

The jet-pump is known as a "constant capacity" device because the mass flow of vapour pumped from the evaporator is approximately constant for variations in outlet conditions up to a critical limit, beyond which the flow becomes unstable and rapidly decreases to zero. The "constant capacity" characteristic means that the jet-pump operating at constant inlet conditions cannot respond to changes in outlet conditions, and so cannot be optimised. One method of varying the jet-pump performance with respect to outlet conditions is to use different geometries in response to changes in outlet conditions. Three jet-pumps were manufactured to analyse the changes in performance with geometry. The design procedure and results are described in Chapter 4.

1.5. Convergent-divergent throat jet-pump

A conventional jet-pump consists on a convergent mixing section, a constant area throat, and a divergent diffuser. A jet-pump design that replaced the constant area throat with a convergent-divergent profile was proposed in an attempt to eliminate a shock process that occurs in the conventional jet-pump. The elimination of the shock process would allow the jet-pump to operate at higher outlet conditions, and

analysis of its operation would compliment the conclusions from jet-pump TIS testing. The modified design and results are described in Chapter 7.

1.6. Objectives of study

The objectives of this investigation were to experimentally test the jet-pump TIS concept in the laboratory. Initially, the jet-pump designed for TIS was calibrated to analyse differences between theoretical and actual performance. Further analysis was carried out under part-load conditions, together with variations in the geometry of the jet-pump and the primary nozzle, in order to make recommendations for the optimisation of performance with respect to evaporative freezing conditions. The performance characteristics of the spray ice TIS system were then determined at the design point and at part-load, and the novel evaporative freezing and nucleation processes examined for their practicability. The performance characteristics of the novel encapsulated ice TIS system were determined, and compared with spray ice TIS, so that the advantages and disadvantages of each system could be identified, and recommendations for improvement made. The performance of a convergent-divergent throat jet-pump was analysed to determine if the shock process could be eliminated, thus enhancing jet-pump performance.

1.7. Conclusions

This chapter has briefly described the problems that comfort cooling of buildings present in managing and reducing the use of electrical energy, namely, the emission of greenhouse gases from fossil fuel burning power stations. The only method of providing comfort cooling and cutting substantially emissions would be to utilise waste heat or renewable sources of energy. Two novel methods of TIS were described in order to utilise low-grade heat in comfort cooling applications. Spray ice TIS would manufacture ice by flash evaporative freezing and encapsulated ice TIS would provide coolth by sublimation freezing of a novel

polymer gel system. The performances of both systems would be analysed and compared in order to examine their relative merits. Optimum performance using multiple jet-pumps would be investigated using three different geometries and a novel design to reduce losses using a convergent-divergent throat. Each experimental programme is important in its own right, but together the results provide a comprehensive study of the jet-pump TIS system.

Chapter 2. Literature review

2.1. Introduction

The philosophy underlying this thesis is that low-grade heat can be used to create ice either in phase with the cooling requirements of a building, or in separate charge and discharge cycles. The coolth stored as ice is then used to reduce the electrical energy requirements and potential greenhouse gas emissions attributable to cooling systems. If the heat source is from a power plant and it would otherwise be wasted then it operates more efficiently and has a year round capability. If the heat source is renewable, such as solar thermal or geothermal systems, then cooling is achieved with zero pollution emissions and negligible energy costs.

Ice storage has grown and developed in recent years because of its ability to shift peak cooling loads to off-peak periods. Ice produced by vacuum has found its place in desalination, mine cooling and fruit cooling processes. Jet-pumps have recently undergone a revival of interest because of the need to eliminate CFC/HCFC based refrigerants and to harness low-grade heat for comfort cooling applications.

The review will describe and evaluate the development of the different aspects of the ice storage/vacuum freezing/jet-pump processes up to the present, and evaluate their application to jet-pump TIS.

2.2. Ice storage

Ice has been used for the preservation of foods and the cooling of residences for thousands of years, long before the development of artificial means of ice making and refrigeration. In places where snowfall was a seasonal effect natural snow and ice would be collected and stored in insulated buildings and then used in the hot

seasons for cooling and food preservation. Both Greeks and Romans are known to have stored compressed snow and ice in snow cellars. Storage was mainly restricted to areas with easy access to ice and snow, with only small scale transportation occurring. Ice transportation had developed by the mid 1800s when it was extracted in large volumes from rivers in New England and transported to places such as the Southern United States, the West Indies, South America and the Asian sub-continent, according to Jordan and Priester [1].

Woolrich [2] described some early methods of artificial ice making. It is recorded that in the fifth century B.C. Egyptians were artificially cooling water and producing ice in porous clay pitchers by exposing the water surface to the night sky and sprinkling the outer surface with water. Radiant cooling from the water to the sky and evaporative cooling through the porous pitcher produced cooling and ice crystallisation. In 1748 William Cullen described the artificial production of cold by the evaporation of fluids. Ether was evaporated in a partial vacuum to produce a reduction in temperature. Gorrie invented the first commercial ice making machine for refrigeration and air conditioning, receiving a patent in 1851. The ice maker was a compressed air refrigerator and was used to cool rooms for the treatment of fever patients in Apalachicola in the Southern United States. Ferdinand Carré patented an ammonia/water absorption refrigeration system in the United States in 1860. It was the first system to use a heat driven absorption cycle. In 1873 Giffard invented an open cycle air-compression refrigeration system for mine cooling. The air was cooled by the refrigeration cycle and delivered directly to the mine air.

2.3. TIS

TIS has been used since the early 1900s for cooling buildings such as theatres, churches and dairies, where cooling loads were infrequent and short in duration, according to Rule [3]. The cooling load was spread over an extended period by storing coolth as ice, then discharged to meet the demand. By spreading the

cooling load over a longer period the size of cooling plant was reduced, decreasing capital cost. More efficient chillers and low energy costs led to the decline in TIS systems.

Escalating energy demand has led energy utility companies to introduce tariff systems in an attempt to manage peak energy usage. This together with concern about the depletion of fossil fuel reserves and the increase in carbon dioxide emissions due to inefficient power plant and part-load performance of cooling systems has led to a rapid increase in TIS systems since the early 1980s. Potter *et al* [4] surveyed the operational experience of TIS systems. It was estimated that by 1993 there were between 1300 and 1733 ice storage systems operational in the United States with the average storage capacity of about 10,000 kWh and a peak cooling load of about 1000 kW. Seeley [5] showed that district cooling using chilled water or ice storage had increased from 59 plants in 1980 to over 100 by 1996 in the United States.

Figure 2.1 shows a typical daily energy consumption curve for a commercial office building taken from a design guide to TIS by CIBSE [6]. The diagram also shows the contribution ice storage can make to the reduction in cooling capacity and peak cooling load of conventional electrically driven chiller systems. Conventional chiller systems without TIS are normally designed to meet the peak cooling load, at about 4 p.m. in this case.

Potter *et al* [4] suggested that this had two detrimental consequences on system performance. First, the chiller is operating at part-load for most of the time, causing a marked reduction in coefficient of performance. Second, the base cooling load is met by the most efficient and least polluting generation plant such as nuclear, gas and high efficiency coal burning units, but when the demand rises, generators such as low efficiency coal and oil burning units may be brought on line, increasing harmful emissions. The second reason would depend on the specific stand-by plant and so may not be detrimental, as suggested.

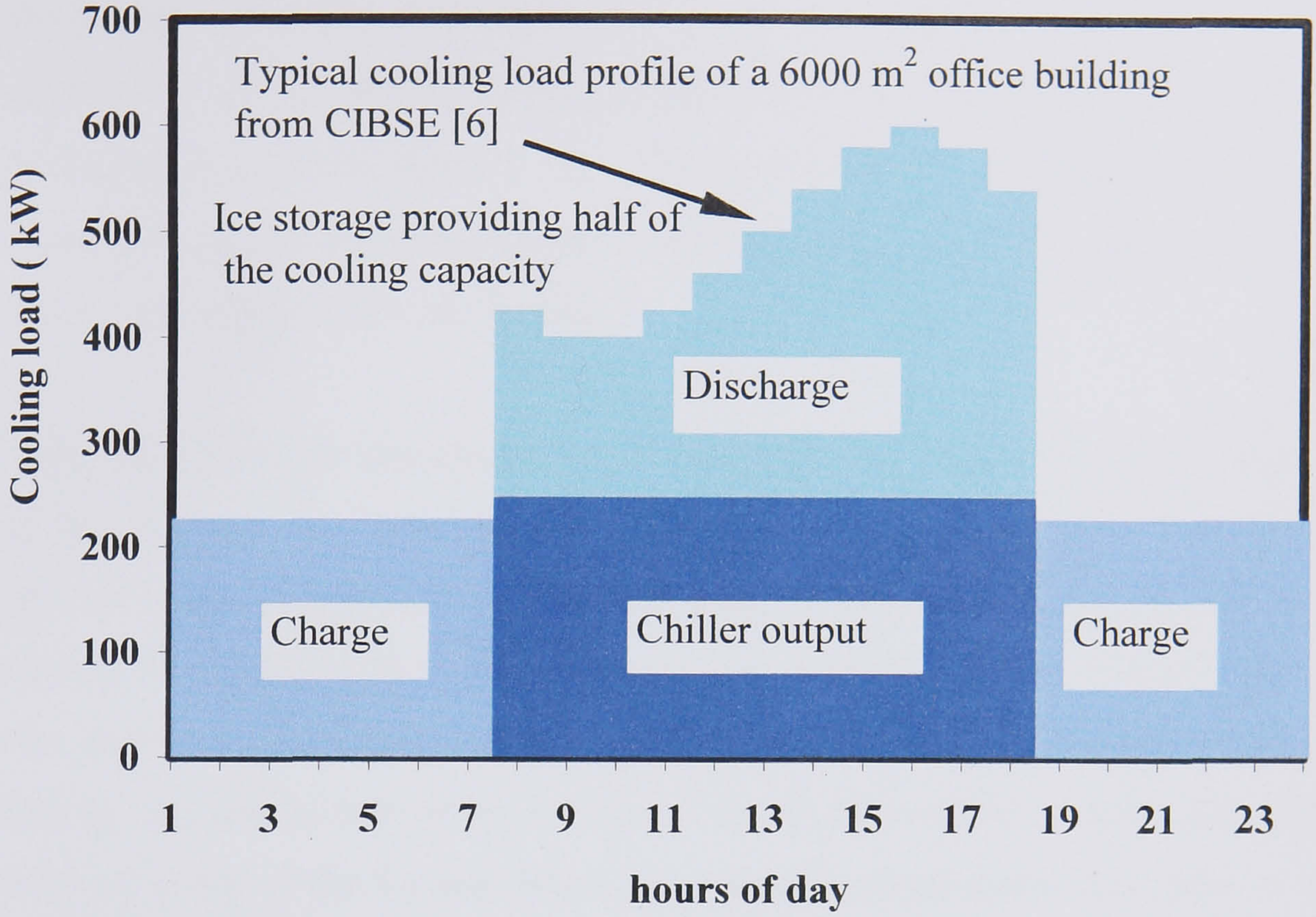

Figure 2.1. A typical charge and discharge cycle over 24-hours and cooling load profile, CIBSE [6].

A survey by Beyene *et al* [7] showed that most conventional chillers were considerably oversized because of having to match the peak summer load. Chillers operated on average at about 50 % part load. They showed that the ratio of electrical input to the cooling energy required increased substantially under part load conditions, especially plants operating at less than 30 % of full load. It was concluded that TIS used to shave peak loads would reduce conventional chiller capacity and enable chillers to operate closer to their design capacity (70 % to 80 % of peak), thus maximising their efficiency.

Brady [8] compared a conventional heating ventilation and air conditioning (HVAC) system with a TIS system using a 45,000 m^2 building complex with a combined cooling load at peak demand of about 5,000 MW. The HVAC system consisted of three centrifugal chillers and cooling towers. The TIS system consisted of three rotary screw compressors, an ice-on-coil storage tank and three

evaporative condensers. It was shown that cooling supplied by the TIS system could reduce electrical consumption by nearly 28 % because the chilled water was supplied to the air-moving system at about 2 °C instead of an average HVAC chiller temperature of about 7 °C. Brady highlighted the advantages of using lower air distribution temperatures by reducing fan power requirements and duct size because of the lower air density.

Hittle and Smith [9] showed how important the use of heat recovery could be to the performance of a conventional TIS system. A system was analysed in which ice was produced and stored during off-peak periods, then melted when building cooling was required to provide cooling in conjunction with a chiller. Heat was also recovered from the condenser and stored for use in hot water and space heating. Simulation tests were carried out for an office using weather data from a range of cities in the United States. The results demonstrated that without heat recovery, the annual energy consumption for both heating and cooling was about the same for both conventional chiller and ice storage systems. With both heat recovery and storage, the overall energy consumption could be reduced, especially with the replacement of resistive heating systems. It was predicted that an office block in Dallas, using heat recovery and storage, could reduce its annual heating energy requirements by up to 90% whilst increasing the chiller requirements by about 15 % using an intelligent control strategy. It was also found that chiller energy consumption increased because the system COP was lower when making ice. However fan power could be substantially reduced by utilising the lower air distribution temperatures possible with ice storage systems, but heating energy increased because of air re-heating at the delivery zone. On balance it was predicted that the overall energy consumption of the building including heating, cooling and fan power, was reduced. It was interesting to note that cold air distribution was shown to decrease the peak power demand by about half that achieved by ice storage alone because of the reduction in fan power.

The papers presented by Beyene *et al* [7], Brady [8], and Hittle and Smith [9] are not directly relevant to jet-pump TIS, but a low-grade heat driven TIS system would replace a conventional TIS system. The advantages of operating of air-conditioning systems at full load and utilising heat recovery and low air-distribution in order to maximise the efficiency of the TIS system would be is applicable to jet-pump TIS.

An absorption TIS system using exhaust heat from a gas engine was described by Hisaki *et al* [10], which is comparable with the proposed jet-pump TIS system. This consisted of two silica absorbers operating in an alternate heating and cooling mode, a water/ice storage tank, containing multiple trays filled with water, and a condenser. When water vapour was being absorbed in the cooling mode, water was evaporated in the water/ice tank, producing cooling and freezing when the pressure in the water/ice tank reached the triple point of water. A 35 kW prototype operated at a hot water inlet temperature of 85 °C and a cooling water inlet temperature of 25 °C. The ice store charge and discharge periods were 12 and 11 hours, respectively. The system COP was 0.31 but a COP of 0.6 was expected for a larger capacity system. The jet-pump TIS system was assumed to operate at a COP of between 0.2 and 0.3, and so the experimental absorption TIS system operated in that range, but the proposed system would be less complex, and may be used to boost the COP of the vapour-absorption system, making it competitive, in terms of performance.

Spray ice TIS would be most applicable with respect to ice slurry delivery, because ice could be continually manufactured and used in synchronization with the cooling requirements of a district. Paul [11] surveyed district cooling systems using water as the refrigerant. It was shown to be advantageous to pump slurry ice over long pipe runs as this maintained constant temperature whilst melting. A greater enthalpy difference between inlet and return from slurry ice compared to chilled water reduced the required pipe size (approximately 40 % smaller). It was thought important to choose the most cost effective and efficient combination of

different refrigeration systems available because the systems had different temperature limits and operational characteristics.

2.4. Encapsulated TIS

Tao [12] presented a numerical model of the freezing of a single spherical capsule. The model predicted the time-wise position of the interface between the ice and water phases and the temperature profile during freezing. Riley *et al* [13] and Hill and Kucera [14] developed analytical solutions of a liquid sphere solidifying inwards surrounded by a coolant, as shown in Figure 2.3. Where r is the radial coordinate, S is the radial distance between the outer surface at r_i and the solidification front, T_F is the fusion temperature and T_W is the coolant temperature. The papers presented by Tao [12], Riley *et al* [13] and Kucera [14] only analyse the solidification of a single sphere due to conduction across the solid shell, and does not consider solidification of a sphere due to sublimation from the shell surface, as would be the case in jet-pump TIS.

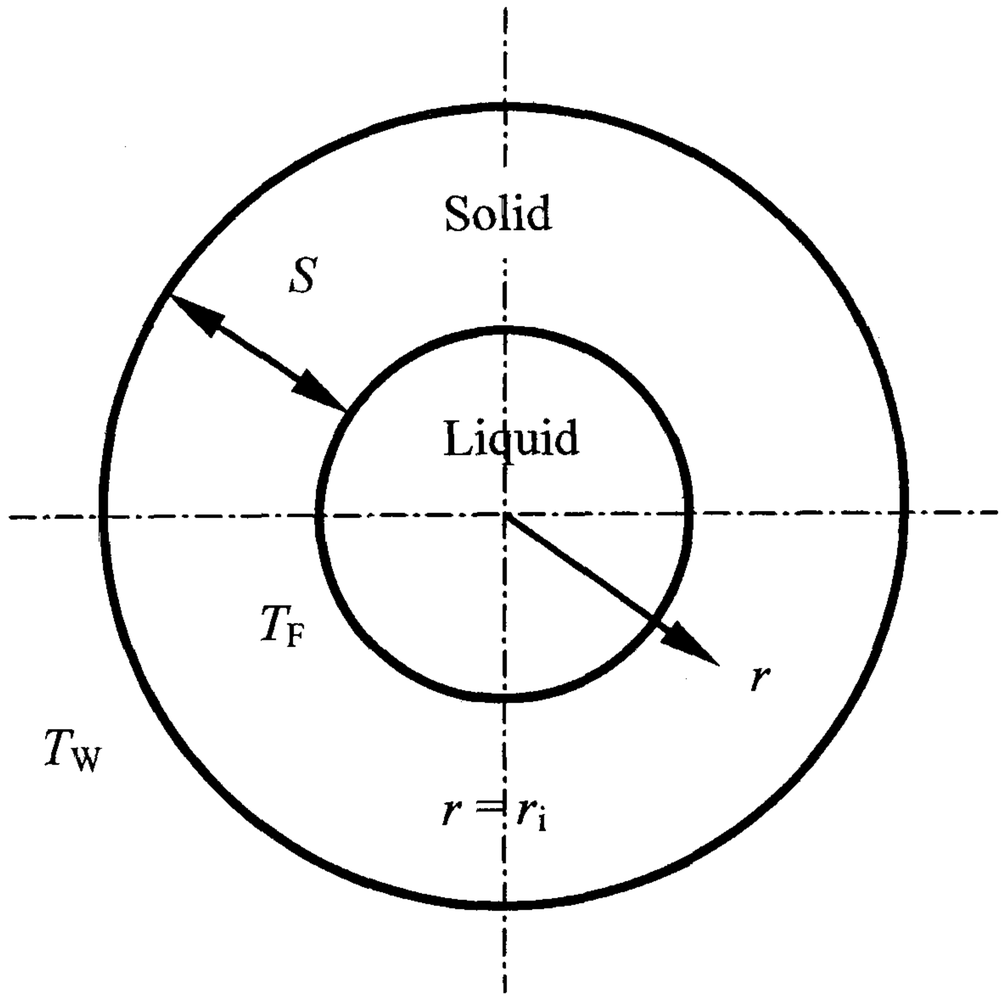

Figure 2.3. The cylindrical configuration for an inward-travelling solidification front.

Arnold [15] presented a mathematical model of the charge and discharge of an encapsulated TIS system. Eames and Adref [16, 17] described a mathematical model for the charge phases of an encapsulated ice store and compared them with experimental results. The solution used energy balances during the charge phase. These models referred to conventional encapsulated ice TIS systems in which a refrigerated water/glycol solution froze a bed of capsules, but the models are not directly applicable to jet-pump TIS because freezing is caused by sublimation from the encapsulated elements in the case of encapsulated ice TIS.

Siatoh [18] described a numerical method to model the melting of a spherical ice capsule. It was shown that as the ice sphere melted, two types of heat transfer would occur. Heat would be transferred directly to the secondary fluid in contact with the upper surface, and natural convection currents would transfer heat from the secondary fluid to the underside of the ice. Results were compared with other numerical solutions and the melting front in contact with the convection currents, which predicted about 15 % faster melting rates.

2.5. Vacuum freezing

Desalination plants have used vacuum freezing techniques for many years to separate salt from fresh water. In such systems, sea water is cooled below its triple point temperature by a reduction in its vapour pressure, causing ice crystals to grow, which separates the salt from the water. In 1971 Koretchko and Hajela [19] described a vacuum freezing jet-pump absorption process. Figure 2.4 shows a simplified schematic diagram of the process. A dilute solution of sodium hydroxide/water enters the concentrator/generator where steam is evolved, increasing the concentration of the solution. Steam from the concentrator/generator drives the jet-pump, which entrains water vapour from the freezer so reducing its vapour pressure and cooling the saline solution in the freezer. The jet-pump mixes and compresses the two streams, which are then condensed. Heat of condensation is used to melt the ice, which leaves the melter at 0 °C. Some water vapour from

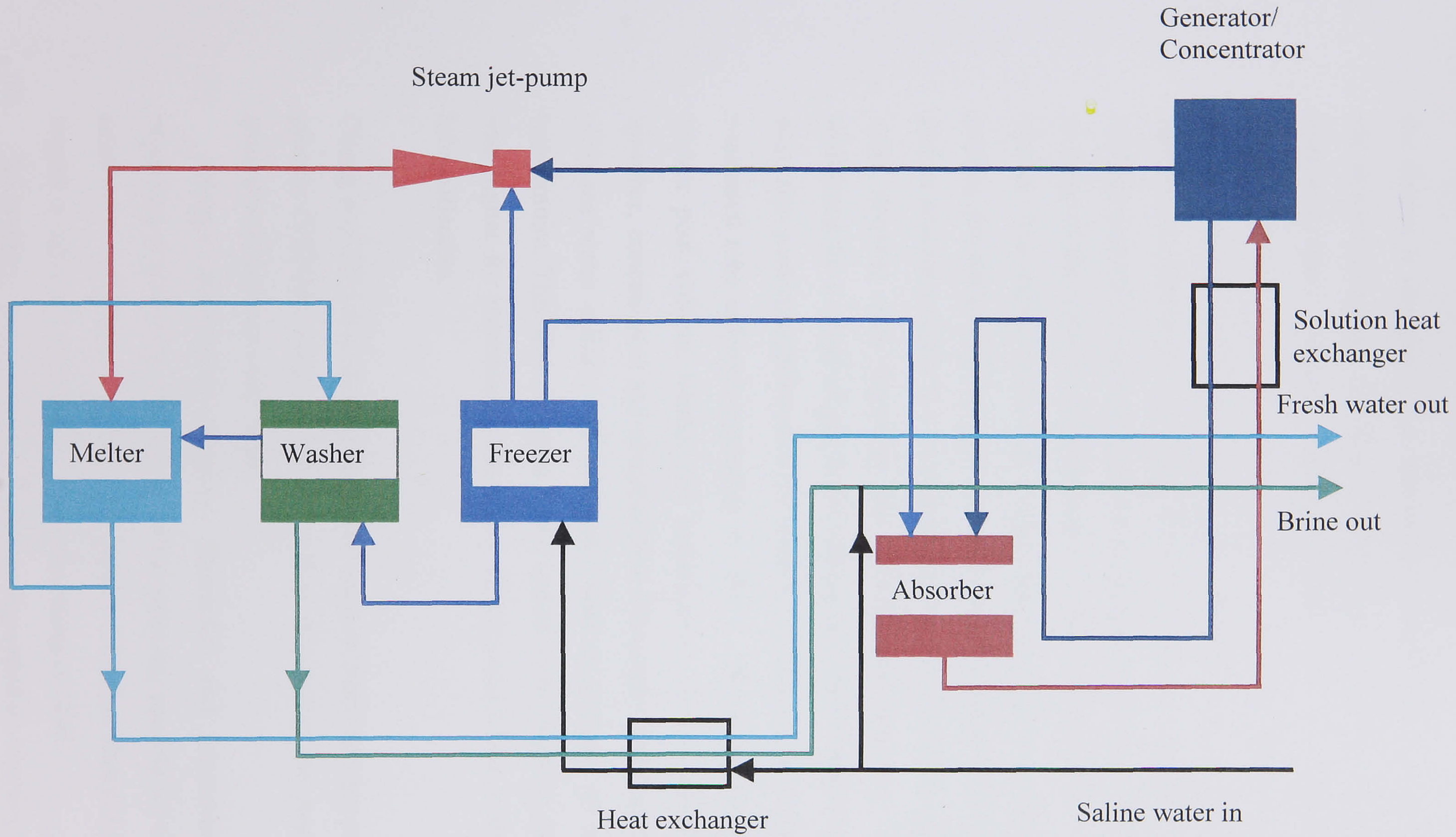

Figure 2.4. Vacuum freezing jet-pump absorption process, Koretchko and Hajela [19].

the freezer is absorbed by a concentrated solution of sodium hydroxide/water in the absorber, causing additional evaporative cooling in the freezer. The sodium hydroxide/water solution becomes dilute and is delivered back to the concentrator/generator via a solution heat exchanger. The heat exchanger reduces the heat transfer requirements for the absorber and the generator. Below the equilibrium freezing temperature, ice crystal growth will occur. The ice crystals exclude impurities, but some impurities are trapped between the individual crystals so some of the water leaving the melter is used to separate the brine and ice in the washer. The treated water and a brine-sea water mix pass through the absorber, cooling the sodium hydroxide/water solution. El-Nashar [20] described the design and an economic analysis of a vacuum freezing jet-pump absorption process using solar thermal heat input to the concentrator/generator. Calculations were performed for a range of sea water salinity and water temperatures. Comparisons were also performed between a flat plate solar collector operating at 90 °C, and an evacuated tube collector operating at 120 °C. The simulation assumed constant freezer pool volume, washer and melter areas. It was found that the required absorber, concentrator and absorber heat exchanger heat transfer areas increased with sea water salinity and decreased with an increase in collector operating temperature. This was reflected in the capital cost, showing that the capital cost was higher for increases in sea water salinity, and lower when using evacuated tube collectors.

Cheng *et al* [21] described an improved vacuum freezing high-pressure ice melting process (VFPIM). Figure 2.5 shows a flow diagram of the process, which can be generalised into four main steps;

(1) Primary evaporative freezing: Deaerated and precooled water is flash vaporised to below the triple point of the solution, causing ice crystallisation. The solution is transformed into a low-pressure ice-brine slurry. Low-pressure water vapour is fed to the outside of a heat conducting conduit.

(2) Ice washing: Ice crystals and brine are separated by washing with fresh water.

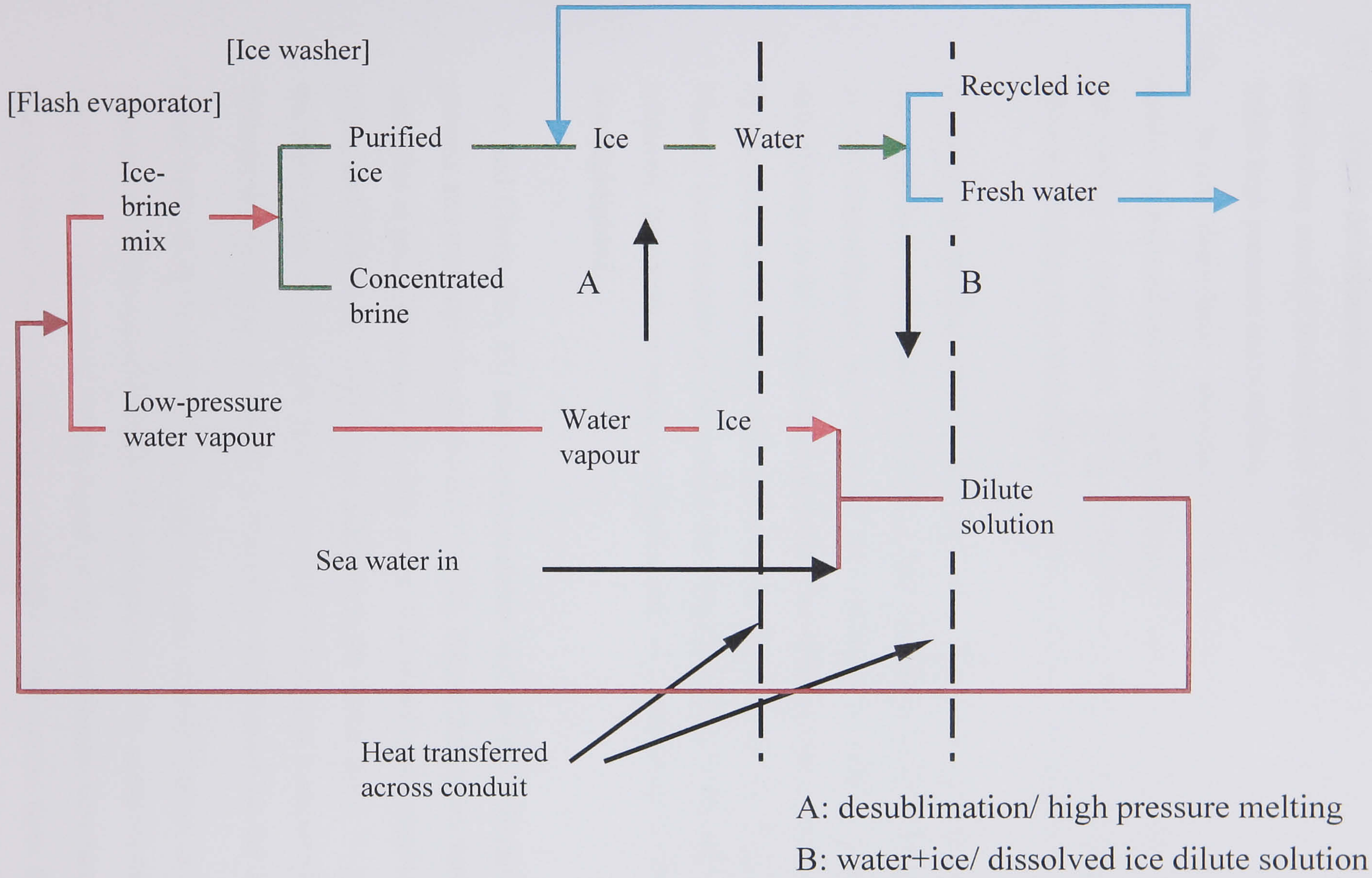

Figure 2.5. Process flow sheet of VFPIM process, Cheng *et al* [21].

(3) Vapor desublimation and high-pressure ice-melting: On the outside of a heat conducting conduit low-pressure vapour desublimates directly to ice, and on the inside high pressure ice is melted.

(4) In-situ desublimate dissolution: The pressure inside the heat conducting conduit is reduced and sea-water is brought into contact with the desublimate on the outside of the conduit. Heat is transferred across the conduit from inside to outside, resulting in a water-ice mix on the inside and diluted brine on the outside.

A compartmentalised, rotating tray is used to bring the vapour into contact with the conduits. Desublimate builds up on the outside as ice on the inside melts. One of the compartments then exposes the conduits to saline water, melting the desublimate on the surface and removing the ice-brine solution. It was shown that by pumping an ice slurry with ice contents of between 20 % and 50 % during Phase 3 heat transfer coefficients in the range of 850 to 1100 $W.m^{-2}.K^{-1}$ could be achieved. Increases in water production rate and reductions in work input were also highlighted.

Yeh and Cheng [22, 23] described equations used for the analysis of the VFPIM process and extended the application to TIS. Figure 2.6 shows how a water layer solidifies at pressures below its triple point. The water is assumed to be at its triple point, and there is no temperature gradient in the water layer. At pressures below the triple point an ice layer grows, the heat of fusion is transferred by conduction through the ice layer and vapour is formed by sublimation on the ice surface. The latent heat of sublimation is h_{sub} and the rate of sublimation is m_{sub}, which is assumed to be constant. $T(0,t)$ is the temperature at the solid/vapour interface and $T(x,t)$ is the temperature of the liquid at the solid/liquid interface. The distance from the initial position $X_1(t)$ at $t = 0$ increases, but the ice layer thickness $X(t)$ is less than that because of sublimation from the surface, but moves in the same direction. The model described by Yeh and Cheng [23, 24] was the only analysis found that related ice storage and sublimation freezing driven by a reduction in

vapour pressure, but the semi-infinite layer is not a practical model with respect to operational ice storage systems such as encapsulated ice TIS.

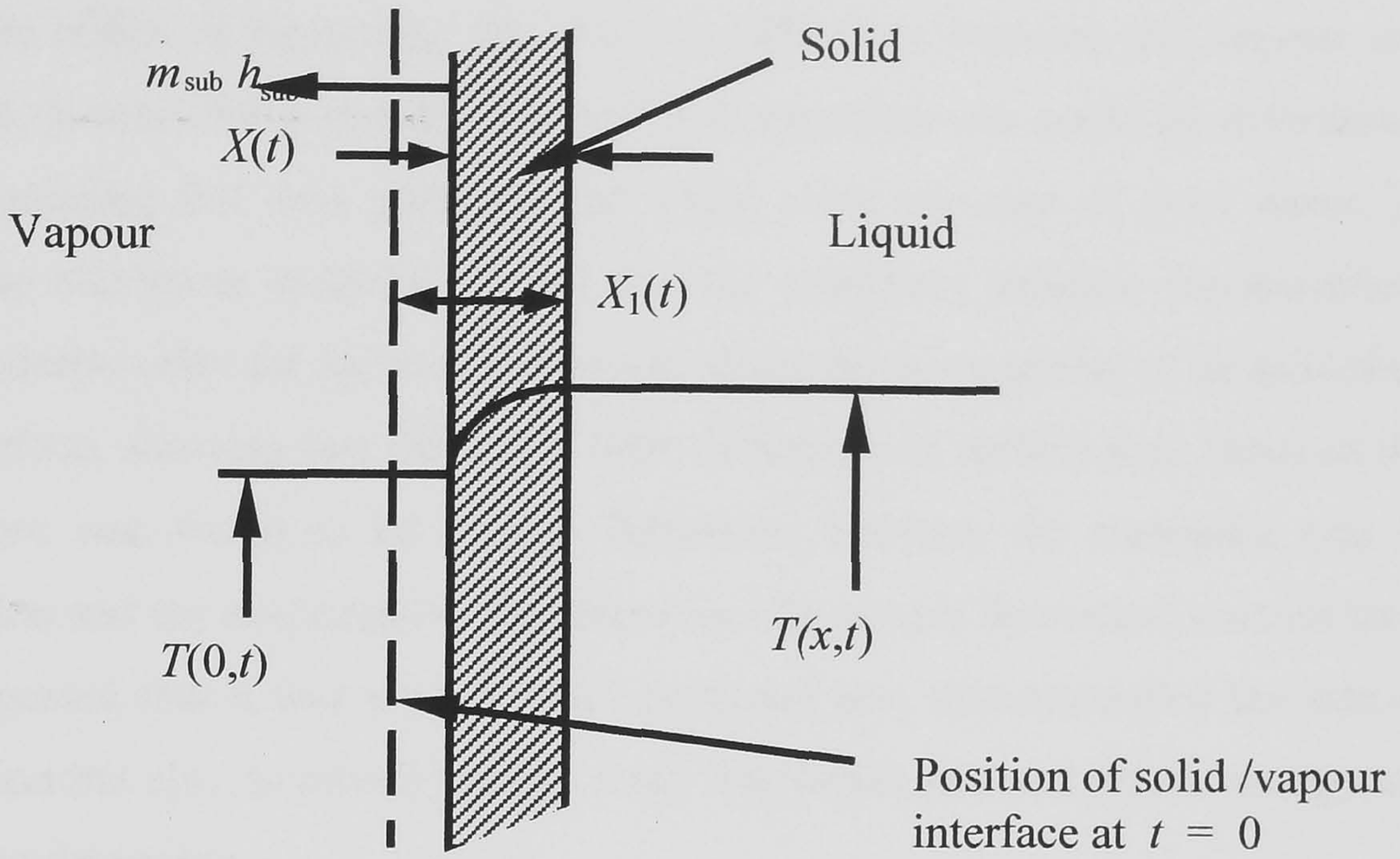

Figure 2.6. Freezing semi-infinite water with constant rate of sublimation at the ice surface, Yeh and Cheng [22, 23].

The evaporation of water in an absorption vacuum freezing process was investigated by Dickey [24]. It was shown that the evaporation rate was dependent upon the difference between the liquid pressure P_L and the measured vapour pressure P_v.

$$ER = f_1(P_L - P_v) \tag{2.2}$$

Where f_1 is a constant. The condensate rate was shown to depend upon the difference between the vapour pressure and the absorbent vapour pressure P_a.

$$CR = f_2(P_v - P_a) \tag{2.3}$$

Where f_2 is a constant. Balancing the evaporation of water in the evaporator to the absorption of water in the absorber,

$$ER \cong CR \tag{2.4}$$

The vapour pressure could be determined for a given set of operating conditions, and the plant size found for other operating conditions. At concentrated freezer

solutions the vapour pressure would approach the absorber pressure, but at low freezer concentrations, or undersized absorption plant, the vapour pressure would approach the freezer solution pressure. The condensation capacity was reduced to record the effect of increasing the pressure difference between the vapour and absorbent. It was shown that the maximum evaporation rate could be determined by extrapolating test data points to the triple point pressure of pure water, so giving the maximum evaporation rate and the absorbent solution concentration. The evaporation rate for agitated slurry was about the same as that of an unbroken slurry surface, showing that there was little difference in surface area between the two. There was found to be a large difference between the measured rate of evaporation and the evaporation rate determined by simple theoretical calculations. This suggested that it was not only the interfacial area that controlled the rate of evaporation but also its kinetic energy. Both interfacial area and kinetic energy are difficult to determine.

A mathematical model of evaporative cooling was presented by Houška *et al* [25]. The model was proposed to analyse the process of the cooling of food by means of a reduction in pressure in a vessel containing the food. The rate of evaporation was determined from Equation 2.5.

$$\frac{dm}{dt} = h_m SA(P_v - P) \tag{2.5}$$

Where m is the mass of food, t is time, h_m is the mass transfer coefficient, SA is the surface area available for mass transfer, P_v is the saturated vapour pressure of the product at the bottom of the vessel and P is the total pressure. It was assumed that the heat absorbed by evaporation caused sensible cooling described by Equation 2.6.

$$\frac{dQ}{dt} = h_{fg}\frac{dm}{dt} = \frac{dT}{dt}(m_f C_f + m_{wall} C_{wall}) \tag{2.6}$$

Where Q is the heat transferred, h_{fg} is the latent heat of vaporisation, T is the food temperature, m_f is the mass and C_f is the specific heat capacity of the food, and m_{wall} and C_{wall} are the mass and specific heat capacity of the vessel wall. The

Equations described above were used together with equations of state and vacuum pump characteristics to predict changes in pressure, temperature and condensate removed from the vessel. The procedure predicted changes in pressure and temperature within 19 kPa and 7 °C, respectively. A modified version of Equation 2.6 was used in Chapter 6 to estimate the mass evaporated from a bed of encapsulated elements during sensible cooling.

Shone [26] presented a review of slurry ice research, and related it to mine cooling and desalination of mine water. For mine cooling purposes slurry ice is advantageous over conventional machines because the ice crystals form within the body of the solution and not on a refrigerated surface, which reduces the resistance to heat transfer by an ice layer build up. Ice slurry has a higher heat transfer coefficient than a secondary refrigerant, so cooling capacity can be increased or plant size reduced for a given capacity. Disadvantages of ice slurry are that the requirement of a saline solution depresses the freezing point temperature, so increasing the energy requirements, and as water is only a proportion of the mixture the potential of utilising the latent heat of fusion is reduced. For mine desalination, ice and brine must be separated efficiently to reduce cost of washing. Large uniformly sized ice crystals are easier to wash than small closely packed ones. A freezing process was described in which ice crystals were initially nucleated in a primary crystalliser and then developed in a growth vessel. The primary crystalliser could use a jet-pump to produce the freezing in the evaporator as was proposed in this thesis. The crystal growth vessel was an insulated chamber in which the ice-brine mix would be agitated and kept at the solution freezing point. Large uniform ice crystals could be formed because the mixing of the solution caused larger crystals to grow at the expense of smaller ones.

Andersen and Fleming [27] described a vacuum freezing system for mine cooling using a water vapour-compression refrigeration cycle. Figure 2.7 is a simplified schematic diagram of the system. Mine service water is pumped, via filters and a heat exchanger into the freezer. Ice crystallisation by evaporative freezing occurs

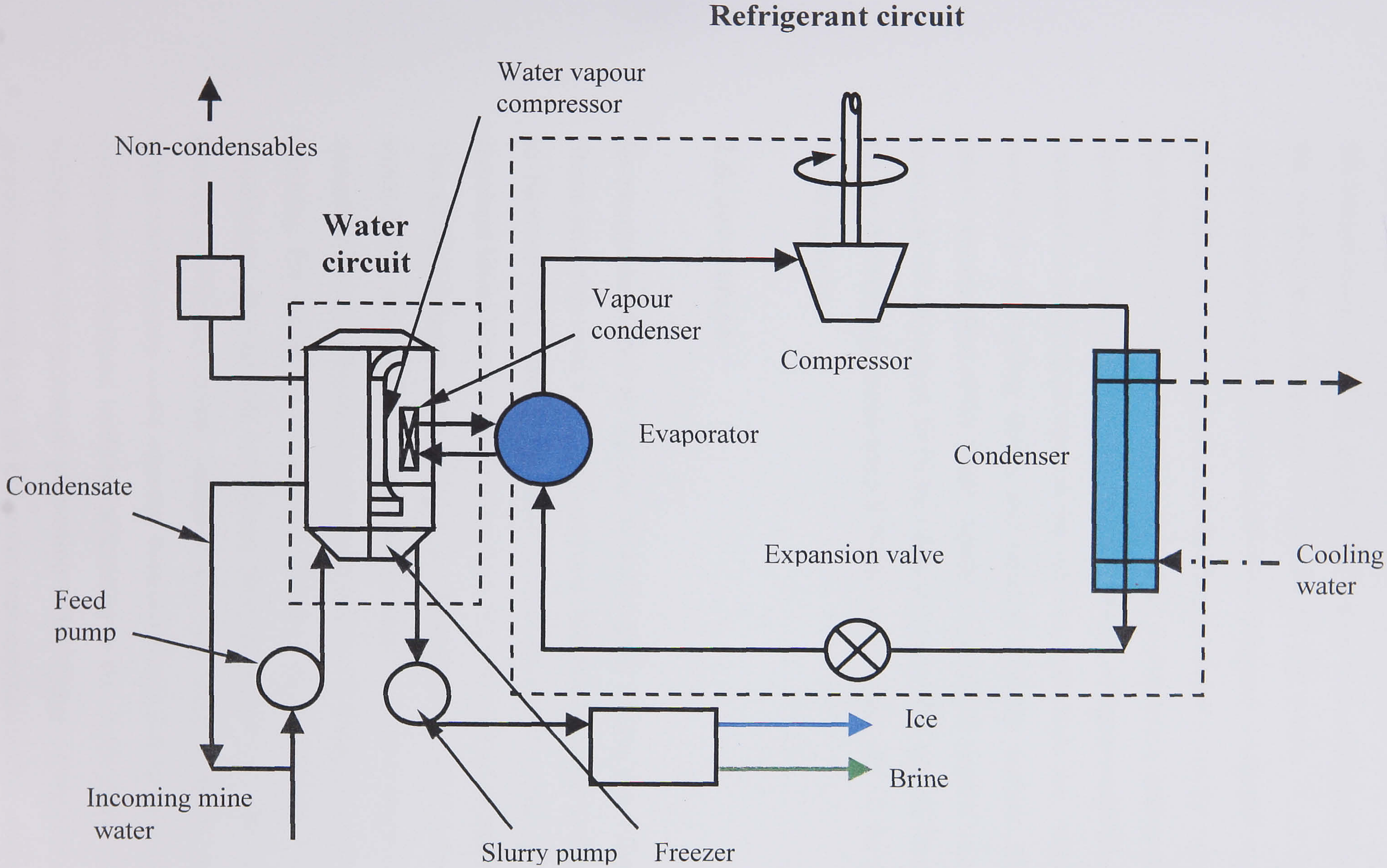

Figure2.7. Schematic of vapour-compression vacuum freezing system, Andersen and Fleming [27].

as described earlier. A radial flow type water vapour-compressor situated inside the freezer compresses the vapour. The vapour is then condensed on the outside of the condenser as refrigerant evaporates on the inside. A conventional vapour-compression refrigeration cycle maintains the water condenser at about -1 °C. Ice-brine slurry is then pumped from the freezer where it can be separated. Andersen and Fleming [27] compared a water vapour compression system with two forms of dynamic TIS. Plate ice, where ice is formed on refrigerated plates and occasionally loosened by melting a layer at the surface, and scale ice, where ice is formed continually on rotating drums and scraped from the surface. It was shown that power consumption of the water vapour-compression system was about 30 % less than plate ice and about 50 % less than scale ice. The typical freezer temperatures for the different machines were 0 °C for vacuum ice, -15 °C for plate ice and -28 °C for scale ice.

2.6. Jet-pumps

Jet-pumps developed as the use of steam grew during the industrial revolution. Steam jets were used to provide artificial drafts in locomotives by 1829 according to Siemens [28]. The design and application of jet-pumps for exhausting air remained limited because of relative high steam consumption and low pressure lift. The Giffard injector was invented in 1858 to force water into a high-pressure steam boiler using a jet of steam of the same or a lower pressure. Siemens [28] described how the design of a steam jet-pump delivering air could be improved by reducing the losses in the mixing chamber and increasing pressure recovery. Experiments showed that the volume flow depended upon the surface of contact between the air and steam, irrespective of the steam pressure, up to the limit to which the jet-pump could operate. Siemens found that the maximum vacuum or compression increased in direct proportion to the steam pressure employed. The volume flow was in inverse proportion to the weight of air acted upon, so that a jet-pump operating as an air exhauster was superior to that of an air compressor. Applications of the steam jet-pump were described including propelling dispatch

tubes, the raising of water, evaporation of sugar and liquids, such as juices, by boiling water at low pressures (*i.e.* evaporative cooling), and the pumping and distribution of gases.

2.7. Jet-pump refrigeration

Parsons and Le Blanc invented jet-pump refrigeration in 1901 according to Jordan and Priester [1]. Systems were mainly used where a steam supply was available, such as cooling in cargo ships, but the majority of cooling systems in the early 1900s were ice making machines using absorption refrigeration methods. Carrier [29] observed that steam jet-pump refrigeration was revived in 1928 in the United States for comfort cooling in buildings and introduced into railway coaches in 1932, where the exhaust steam could be utilised. Steam jet-pump refrigeration declined in popularity because vapour compression systems and new CFC based refrigerants increased operational efficiency and greatly reduced the size of plant. However, since the 1980s interest has grown with increasing concern about the ozone depleting properties of CFC/HCFC refrigerants and the need to reduce carbon dioxide emissions. A heat driven cycle was seen as an opportunity to utilise waste heat or renewable sources of energy.

2.8. Applications of jet-pump refrigeration

Al-Khalidy [30, 31] presented papers on solar powered air conditioning and refrigerating machines using R-113 as the refrigerant. Experimental results for the system were described, which showed that a variation in entrainment ratio and COP occurred with condenser pressure. Jet-pumps can operate either in a choked or an unchoked condition, as described by Chow and Addy [32]. Entrainment ratio is approximately constant for changes in condenser pressure up to a critical pressure, under the choked flow regime. In contrast, entrainment ratio decreases with increases in condenser pressure, under the unchoked flow regime, as observed from the results. The difference between the two flow regimes is that

secondary flow is accelerated to sonic velocity at the location of the minimum area between the primary jet and the wall in the choked flow regime. Changes in conditions upstream of this location, therefore, cannot be transmitted downstream and affect the inlet conditions. This phenomenon was not discussed in the relevant papers. Chow and Addy [32], in discussing the performance of a jet-pump in both the choked and unchoked flow regimes, showed that the unchoked flow could occur due to, either the geometry of the jet-pump, or excessive outlet conditions. The jet-pump used in the experiments is known as a constant area jet-pump because the mixing between the two primary and secondary streams takes place in a shroud of constant area. The annular area for secondary flow may be too small to allow secondary flow to attain sonic velocity.

Shchetinina *et al* [33] described experimental results from a solar powered jet-pump refrigeration and air conditioning machine. It was shown that the intensity of incident solar radiation determined the generator temperature level, with the ambient temperature having only a small effect. The collector heat lag smoothed out any small fluctuations in solar radiation intensity. It was found that the COP of the system was 0.10 - 0.12 at an evaporation temperature of 10 °C, a condenser temperature of 40 °C and a generator temperature 75 - 80 °C. Air cooled condensers were sensitive to ambient temperature changes and so high fan power consumption was required to maintain jet-pump operation. Water cooled condensers were recommended to reduce the electrical energy input.

Petrenko and Shchetinina [34] presented results for a 1 kW jet-pump air conditioning system. One set of tests were carried out in which a heat exchanger transferred heat from a solar collector fluid to the refrigerant, and a second set of tests were carried out in which the refrigerant boiled directly inside the solar collector tubes. The first set of tests showed that the system operated at a COP of 0.23 and an overall efficiency including the collector efficiency of 0.07. The second set of tests showed that the system operated at a COP of 0.39 and an

overall efficiency of 0.16. It was shown that an evaporation temperature of 8 - 12 °C could be attained at an overall efficiency of 0.12 - 0.16 over 5 hours a day.

Sokolov and Hershgal [35] described a solar powered compression enhanced jet-pump cycle for air conditioning, shown in Figure 2.8. This consisted of a vapour-compression sub-cycle and a jet-pump sub-cycle coupled by an intercooler.

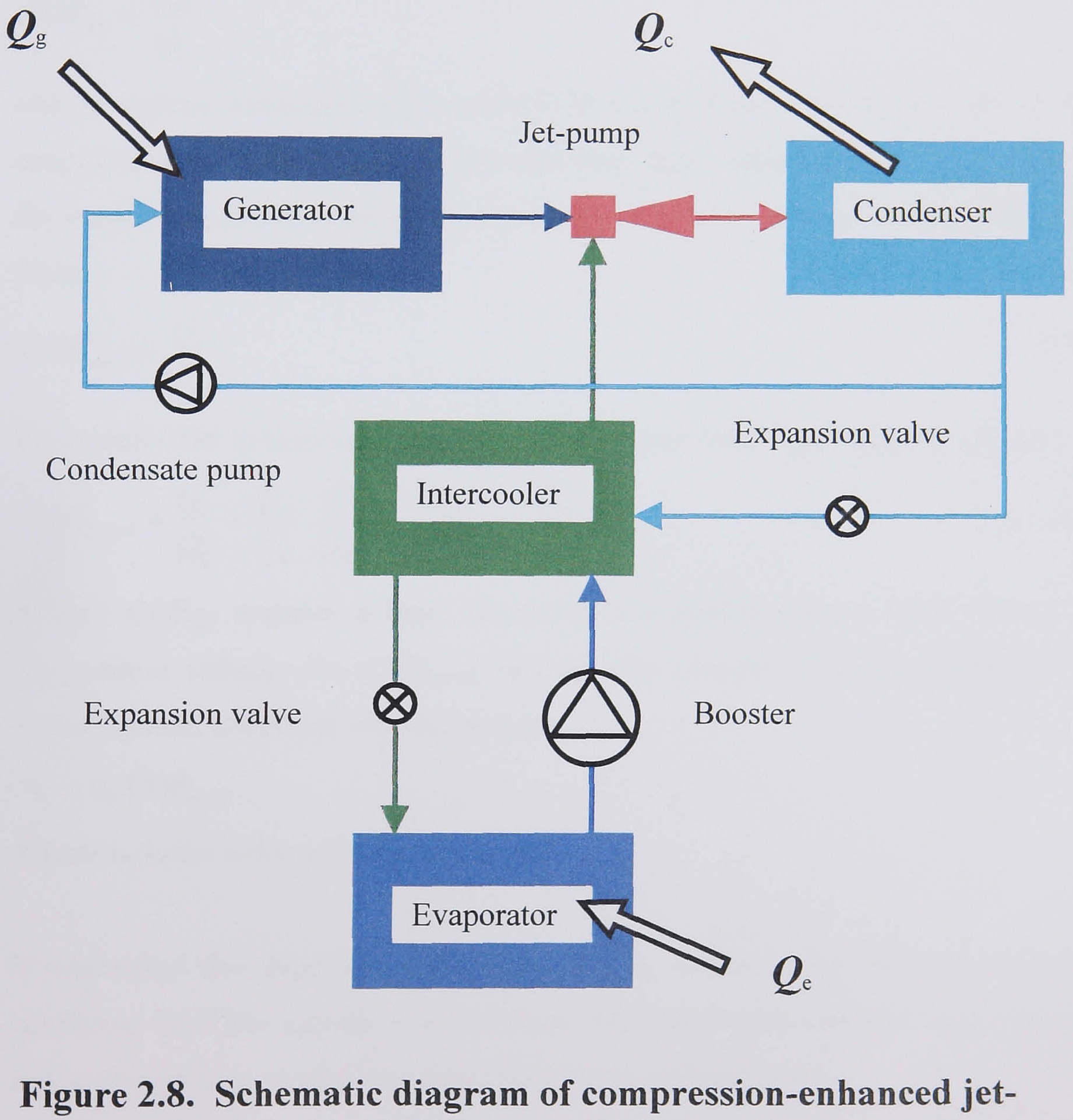

Figure 2.8. Schematic diagram of compression-enhanced jet-pump cycle, Sokolov and Hershgal [35].

The COP of a jet-pump cycle is the ratio of the evaporator cooling load to the generator heat input and the work associated with pumps and fans. The work input is usually neglected as it is small compared with the generator heat load.

$$\mathrm{COP} = \frac{Q_e}{Q_g} \tag{2.8}$$

Sokolov and Hershgal [35] defined the COPs of the two sub-cycles to allow for the interaction of the two sub-cycles, and analyse their influence on overall performance. The jet-pump sub-cycle COP was defined as the ratio of the intercooler heat load Q_{int} to the generator heat input Q_g,

$$\mathrm{COP}_{eje} = \frac{Q_{int}}{Q_g} \tag{2.9}$$

and the vapour-compression sub-cycle COP could be described by the ratio of the evaporator heat load Q_e to the intercooler heat input, which acts as a condenser in the vapour compression sub-cycle and as an evaporator in the jet-pump sub-cycle. Thus,

$$\mathrm{COP}_{comp} = \frac{Q_e}{Q_{int}} \tag{2.10}$$

The actual COP is therefore, the ratio of evaporator load to generator heat input.

$$\mathrm{COP}_{actual} = \frac{Q_e}{Q_g} = \frac{Q_{int}}{Q_g}.\frac{Q_e}{Q_{int}} = \mathrm{COP}_{eje} \times \mathrm{COP}_{comp} \tag{2.11}$$

A high COP_{eje} requires a high intercooler temperature, but a high intercooler temperature reduces the COP_{comp} because the booster work is increased. An overall system efficiency was defined as,

$$\eta_s = \eta_c.\mathrm{COP}_{actual} \tag{2.12}$$

Where η_c is the solar collector efficiency.

It was noted that high generator temperatures, desirable for high system COP conflicted with the reduction in collector efficiency with elevated temperatures, and so design curves were presented for system optimisation.

It should be emphasized that COP_{comp} does not represent the coefficient of performance of the actual vapour-compression sub-cycle, which would be the ratio of the evaporator cooling load to the booster work input, but it is used to investigate the mutual interaction between the two sub-cycles.

Sun [36] presented design procedures for a solar powered combined jet-pump vapour compression cycle and experimental results from a steam jet-pump. Experimental results from a steam jet-pump showed that increases in evaporator temperature raised the critical condenser pressure and entrainment ratio for a given generator temperature. An increase in critical condenser pressure allowed the jet-pump to operate at higher condenser pressures without losing its action. It was shown that the solar collector area required increased with an increase in condenser and evaporator temperature, and decreased for increases in solar collector and intercooler temperature.

Sun [37] described a jet-pump vapour compression system and analysed suitable refrigerant pairs. A suitable refrigerant pair based on a generator temperature of 90 °C, condenser temperature of 40 °C, intercooler temperature of 30 °C, and an evaporator temperature of 5 °C was identified as R718 [water] for the jet-pump sub-cycle and R21 [dichlorofluoromethane] for the vapour compression sub-cycle. It was shown that the system could operate with a COP above 0.6 for the above conditions, comparable with single effect absorption systems.

Lund and Søe [38] described a jet-pump refrigeration plant driven by heat from a district heating scheme. A 200 kW demonstration plant was described. A steam generator provided the motive steam at 77 °C, a flash evaporator operated between 9 °C and 16.5 °C, a combined dry and evaporative condenser was used to reduce water consumption. It was found that the yearly average COP was 1.38 compared with a yearly average COP of 4.6 for a conventional plant and 0.78 for the single effect absorption plant. The high COP is due to the low condensing temperature required in Denmark and the higher entrainment ratio achieved at higher evaporator temperatures at part-load. This system showed that district cooling using waste heat can be successfully employed in environments not generally associated with cooling demand.

2.9. Enhancement of jet-pump performance

Jet-pump cooling systems would be much more likely to be commissioned if they could demonstrate similar overall thermodynamic performance, or life-cycle costs of conventional cooling systems, so the enhancement of performance has produced some novel research and development projects, as described below.

Sokolow and Hershgal [39, 40] described a compression enhanced jet-pump which was shown earlier in Figure 2.8. The enhanced jet-pump refrigeration cycle uses a mechanical booster to increase the pressure in the evaporator, so increasing the saturation temperature of the jet-pump cycle, and the system COP. An intercooler operating between the evaporator and condenser provides a means of reducing pressure and flow fluctuations between the jet-pump and booster sub-cycles and separates lubricant from the jet-pump sub-cycle. It was proposed that the COP of the system should reflect the economic benefits of using heat input to the generator supplied at very little or no cost, so a COP_{mech} was introduced. The COP of a heat powered refrigeration cycle was shown to be the ratio of the refrigeration load to the generator heat and total work input, but Sokolov and Hershgal [39] argued that if the generator heat input was from waste heat or a renewable source then the actual COP should be the ratio of the refrigeration load to the total work input, including pumps and compressors, reflecting the economic advantages of using low-grade heat.

$$COP_{mech} = \frac{Q_e}{W} \tag{2.13}$$

Procedures were described by Sokolov and Herschgal [39] to optimise the performance of the enhanced jet-pump system. Sokolov and Herschgal [40] described the design and test results of two parallel jet-pump systems. The first system provided an evaporation load of about 2 kW and the second system provided an evaporation load of about 3 kW. It was shown that less than 0.5 kW of work input was required to provide refrigeration of 3 kW, and just over 0.2 kW of work input was required to provide refrigeration of 2 kW. The system was shown

to work smoothly and largely trouble free. It could also provide year round utilisation if space or water heating were to be incorporated into the design. The work of Sokolov and Hershgal [35, 39, 40] stimulated interest in jet-pumps when it was seen that COPs could be boosted to the equivalent of single and double effect vapour-absorption systems and conventional vapour-compression systems when losses, part-load performance are taken into account, and that such systems could be justified economically when utilising low-grade heat such as waste heat of renewable resources.

Eames and Aphornratana [41] described a system that combined a jet-pump with a Lithium Bromide absorption system in order to increase the COP of a conventional single effect absorption cycle. Figure 2.9 shows a schematic diagram of the jet-pump/absorption cycle. High-pressure refrigerant vapour was evolved in the generator and provided the motive stream to drive the jet-pump. Refrigerant vapour was entrained from the evaporator and compressed by the jet-pump to the condenser pressure. The jet-pump provided an additional cooling effect to that of the absorption process, increasing the system COP. Experimental results from a small scale test rig showed that the system could deliver a COP comparable with double effect absorption cycles but using less complex equipment. The Lithium Bromide-water system cannot be used for TIS because it has a lower operational limit of about 5 °C, but it may be possible to couple the jet-pump and the vapour-absorber in series to boost the performance of the jet-pump TIS system. This will be discussed when the performance of the jet-pump has been established from the testing.

Eames *et al* [42] described the results of a 3 kWc gas fired jet-pump-absorption air conditioning system. It followed on from Eames and Aphornratana [41] by presenting results from a large scale test rig. The COP was found to be more than 60 % higher than a conventional single effect absorption cycle. The generator operated at about 200 °C causing large heat losses. It was concluded that with

improved insulation, the system could deliver a COP of between 0.8 and 1.0, comparable with double effect absorption systems.

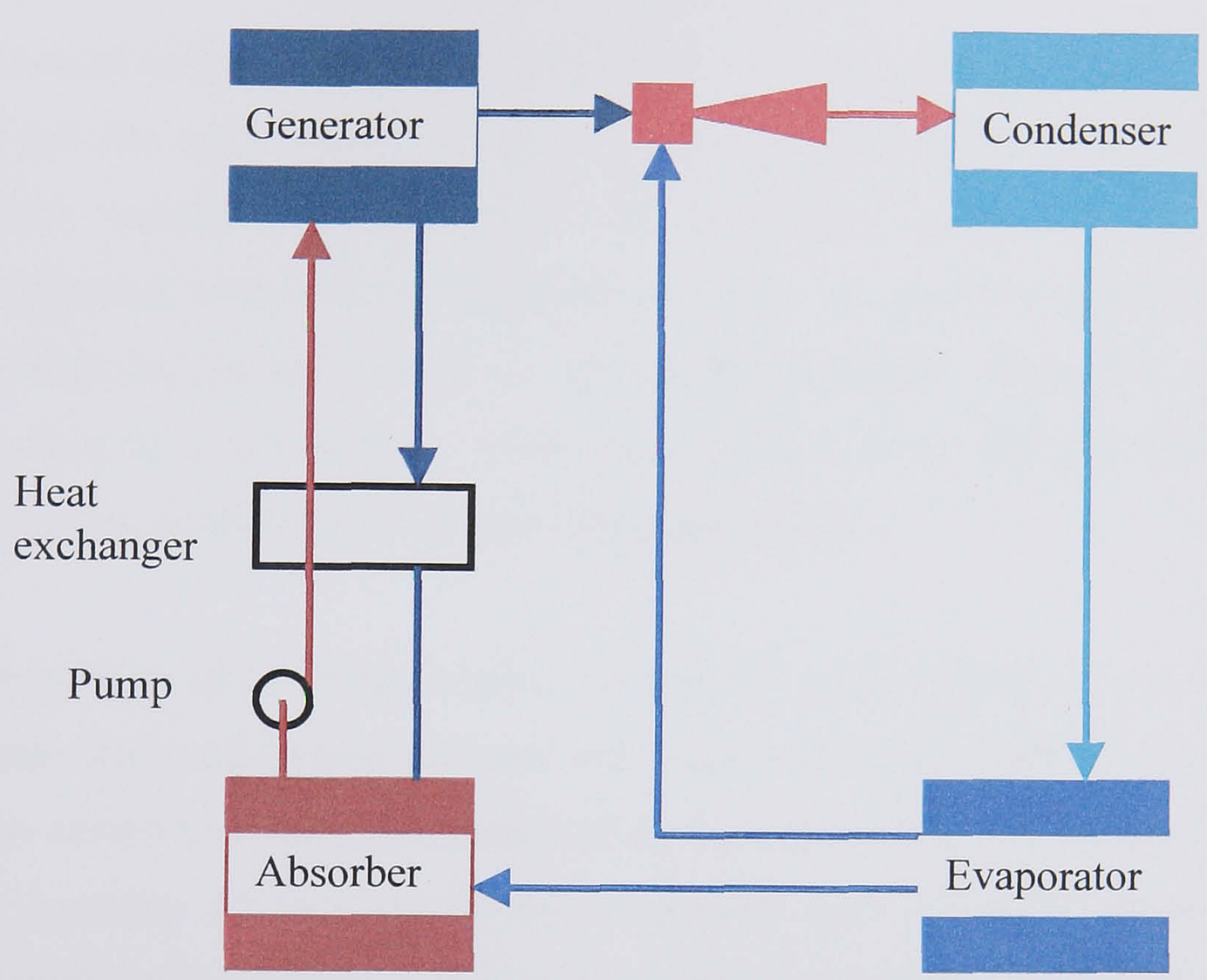

Figure 2.9. Combined ejector/absorption refrigeration cycle, Eames and Aphornratana [41].

2.10. Conclusions

In reviewing TIS, it was shown that most chillers operated at 50 % part load for most of the time and 30 % at some point in the cooling cycle. The review showed how important load shifting together with heat recovery was in reducing the total energy input to a building. The review of encapsulated TIS showed that much research had been carried out on conventional systems where a cooled glycol solution transfers the coolth to a bed of encapsulated elements, causing freezing of the elements, which are then discharged by passing a higher temperature glycol

over the bed. There were analytical and numerical solutions to the solidification of a sphere undergoing cooling and the freezing of a semi-infinite ice layer due to sublimation from the solid surface, but no references to the freezing of a sphere by sublimation.

Practical systems using vacuum freezing methods were highlighted in desalination of sea and mine water, and the cooling of foodstuffs. Experimental vacuum ice slurry systems were described, but most used vacuum pumps, or proposed mechanical water vapour compressors such as axial, or radial compressors to provide the vacuum. None of the systems included a jet-pump to provide the vacuum in a TIS system, which shows that vacuum freezing using a jet-pump remains a novel method for providing an ice store.

The review of jet-pump cooling showed the wide variety of systems using low-grade heat such as solar thermal and waste heat to drive the refrigeration cycle. It was shown how the performance of a jet-pump cooling system could be enhanced by boosting the pressure in the evaporator with a vapour compressor and by operating the jet-pump in conjunction with an absorption cycle. All of the systems described, were designed to provide comfort cooling but could be applicable to jet-pump TIS.

Chapter 3. Test rig construction

3.1. Introduction

This thesis is concerned with analysing the operational characteristics of a low-grade heat driven jet-pump TIS system, and investigating improvements in performance by the use of jet-pumps of different geometries, and a convergent-divergent throat design. This Chapter describes the construction of the test rig that was built to carry out the experimental programme.

The test rig consisted of four main elements shown in a block diagram in Figure 3.1.

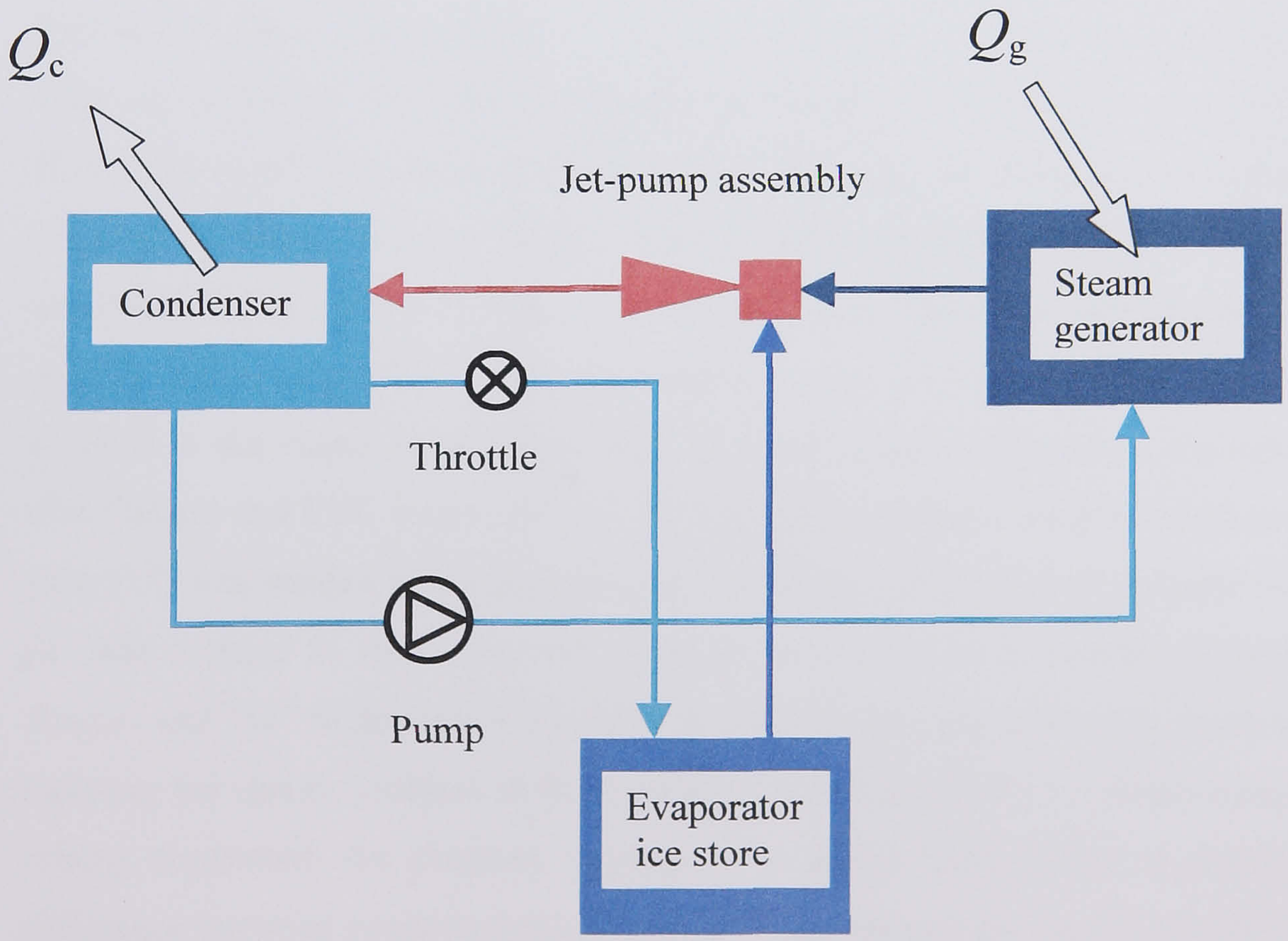

Figure 3.1. Block diagram of the jet-pump TIS test rig.

It consists of an evaporator/ ice store, a condenser, a steam generator and a jet-pump assembly. A heat load applied to the steam generator evolves steam, which is fed to the jet-pump assembly. The action of the jet-pump causes cooling in the evaporator and ice formation below the triple point of water. The vapour from the generator and the evaporator are mixed and compressed in the jet-pump and the combined flow is condensed. Most of the condensate is fed back to the generator via a pump, with the remainder returned to the evaporator through a throttle valve.

Temperature and pressure measurements were carried out and mass flows determined from calibrated vessels, so that the performance characteristics of the jet-pump TIS system could be evaluated.

3.2. Evaporator

Figure 3.2 shows a photograph of the test rig with an accompanying schematic diagram in Figure 3.3, and the legend in Table 3.1. The evaporator and heat exchanger system consisted of an evaporator, a storage vessel, a heat exchanger, a circulation pump, various pipes, fittings and measuring apparatus. A glass evaporator vessel (12) 300 mm inside diameter and 500 mm in height was sealed at both ends using PTFE seals and stainless steel plates (13). The plates were secured to the vessel by stainless steel 16 mm hexagonal fasteners, through cast iron flanges and PVC inserts (14). A 78 mm inside diameter stainless steel suction pipe (15) was welded to the top stainless steel plate and a 150 mm diameter flange (2) was welded to the outlet end. Four 20 mm hexagonal fasteners joined the flanges and "O" rings sealed the joint. A pressure tapping point was provided to measure the vapour pressure in the evaporator chamber (EVP). 6 mm polyurethane tubing connected the pressure tapping to a gauge (16) which measured the difference between condenser pressure (CVP) and evaporator pressure (EVP), and

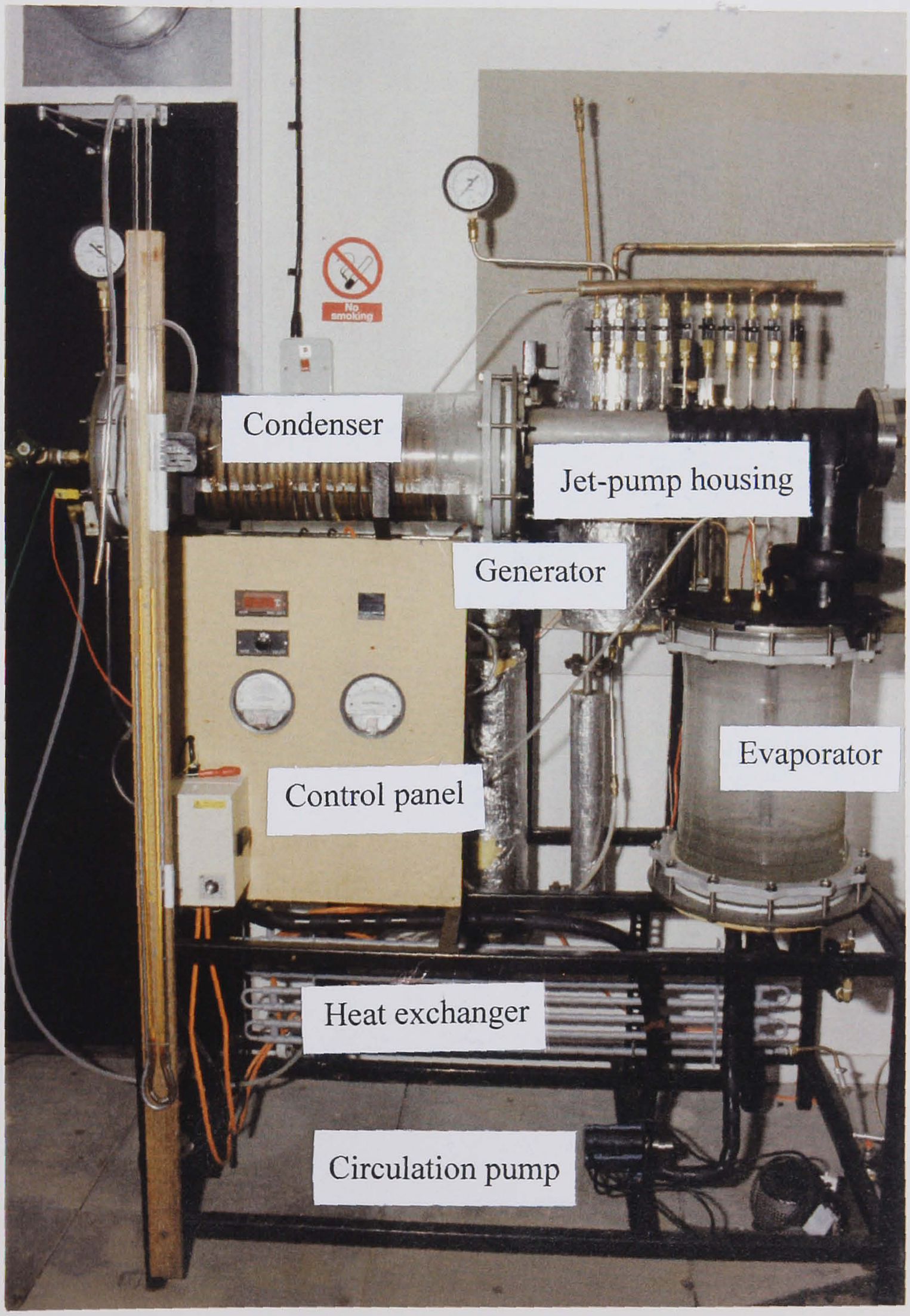

Figure 3.2. Photograph of the jet-pump TIS test rig

Table 3.1. Drawing legend of Figure 3.2.			
1. Suction pipe-jet-pump section	14. Flanges, bolts and inserts	27. Condenser vessel	40. Generator temperature cut-out
2. Flange, seals, and bolts-jet-pump section	15. Suction pipe-evaporator section	28. Plates and seals	41. Thermocouple selector
3. Jet-pump insert housing	16. Differential pressure gauge-condenser/evaporator	29. Flanges, bolts and seals	42. Thermocouple indicator
4. Primary nozzle flange	17. Storage vessel	30. Cooling coil	—— Evaporator circuit
5. Flange, seals, bolts-condenser	18. Plates and seals	31. Flow meter	—— Heat load circuit
6male-male connector	19. Flanges, bolts and inserts	32. Pressure gauge	—— Storage circuit
7. Plug seal	20. Circulation pump	33. Manometer	—— EVP evaporator

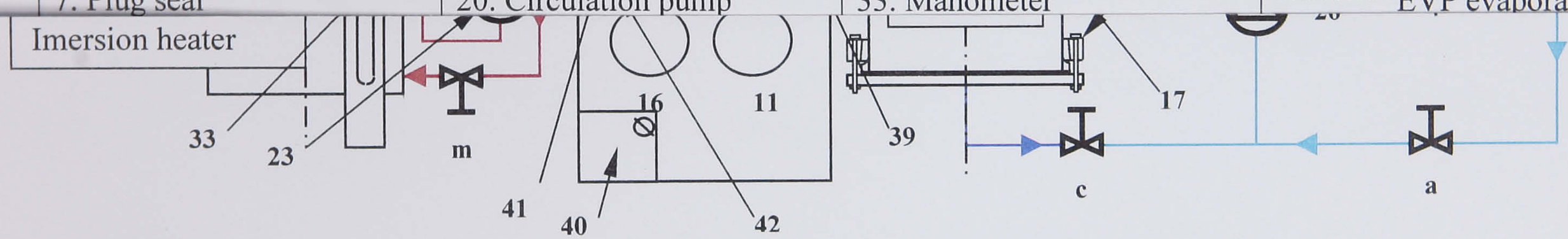

Figure 3.3. Flow diagram of the jet-pump TIS test rig.

another gauge (12) was used to measured the difference between jet-pump wall pressure (JWP) and the evaporator pressure (EVP).

Nickel-chromium/nickel-aluminium (type K) thermocouples were used to measure the temperature; both at the top of the evaporator chamber and in the liquid water in the bottom of the vessel. A 6 mm copper tube and ball valve (k) connected the evaporator to the condenser so that some of the condensate could be returned to the evaporator. A glass storage vessel (17), 300 mm diameter and 300 mm in height was sealed at both ends using PTFE seals and stainless steel plates (18). The plates were secured to the vessel by 16 mm stainless steel hexagonal fasteners, through cast iron flanges and inserts (19). Refrigerant-water was circulated from the bottom of the evaporator to the top by a gear pump (20) and delivered through a spray nozzle (21). The delivery side was arranged so that water could be pumped through a heat exchanger (26) when valves a and e were open and when valves b, c, and d closed. The heat exchanger (26) could be by-passed when valves a and b were open and valves c, d and e closed. Water could be pumped from the evaporator to the storage vessel by opening valves a, c and d, and closing valves b and e. The evaporator could be re-filled by opening valves b and c and closing valves d and e. Thermal insulation, 25 mm in thickness, was used to cover the glass vessel and the stainless steel end plates. Tubular insulation, 12 mm in thickness, was used for the pipework. A 3 kW water heater (22) was used to provide a heat load to the evaporator. A centrifugal pump (23) circulated water through the heat exchanger (26), and a control valve (n) was used to vary the flow. The flow was determined by a calibrated variable area flow meter (24). Warm water at the top of the heater tank (25) was drawn into the suction side of the pump and cold return water entered the base of the tank through a stop valve (m). A header tank (27) was fitted to allow for expansion of water, to prevent the water level dropping below the inlet, and to provide a high suction head. A contra-flow tube-in-tube heat exchanger (26) transferred heat from the heater to the evaporator circuit. Nickel-chromium/nickel-aluminium (type K) thermocouples were used to

measure water temperatures at inlet to and exit from both sides of the heat exchanger in order to determine the heat transfer between the two sides.

3.3. Condenser

The condenser system, shown in Figure 3.2, included a condenser, a heat exchanger, a pump, a condensate measuring vessel, pipes, fittings and measuring equipment. A glass condenser vessel, 200 mm inside diameter glass (27) and 700 mm in length was sealed at both ends by PTFE seals and stainless steel plates (28), and were secured by stainless steel 16 mm hexagonal fasteners, through cast iron flanges and PVC inserts (29). The jet-pump housing (3) was connected to the condenser by four 20 mm hexagonal fasteners, and sealed by an "O" ring (5). A water cooled coil (30), 15 mm outside diameter and 15 m in length, was wound to form a 150 mm diameter coil, 600 mm in length. The coil ends protruded through one stainless steel end plate and were sealed by compression fittings. A globe valve (l) was fitted to the outlet side (CWO) tube. A calibrated variable area flow meter (31) was incorporated into the inlet side (CWI) of the cooling circuit, with a flow control valve (p) in line and upstream of the meter. The pressure within the condenser was adjusted by varying the flow of cooling water through the coil. A pressure gauge (32) and a mercury manometer (33) connected to the line (CP) were used to measure the condenser pressure. 6 mm polyurethane tubing connected the condenser line to a pressure gauge (16) measuring the difference between condenser pressure (CVP) and evaporator pressure (EVP). A nickel-chromium/nickel-aluminium (type K) thermocouple was used to measure the saturation temperature in the condenser. A glass vessel (34) 80mm inside diameter and 500 mm in height, was calibrated and used to measure condensate flow. PTFE seals and stainless steel plates sealed the glass vessel (35), and were secured by 6 mm hexagonal fasteners, through cast iron flanges and PVC inserts (36). A diaphragm pump (37) was used to return condensate to the generator via a condensate measuring vessel. With valves f and h open and valves g and i closed condensate could be pumped from the condenser to the measuring vessel. With

valves h and g open and valves f and i closed condensate could be pumped into the generator. A pressure gauge (38) was fitted to determine the pressure in the measuring vessel as the pressure had to be intermediate between the condenser and generator pressure.

3.4. Jet-pump assembly

The suction pipe (15) in Figure 3.2, which connected the jet-pump assembly to the evaporator, was manufactured from 78 mm inside diameter stainless steel pipe. The suction pipe was connected to the evaporator by 150 mm flanges (2) welded to the pipe and fastened by four 20 mm bolts, sealed by an "O" ring between the flanges. The suction pipe was welded to the 78 mm inside diameter stainless steel jet-pump housing (3) as shown in Figure 3.2. A 150 mm diameter flange (4) was welded to the jet-pump housing to connect the primary nozzle assembly and allow access to the primary nozzle. The detailed design and manufacture of the primary nozzles is described in Chapter 4.3.2. The steam supply was fed to the primary nozzle via a ball valve (j). A stainless steel tube 78 mm in diameter (3), was used to house inserts manufactured to test the variation in geometry and the convergent-divergent throat. Three jet-pump inserts of different geometries were manufactured from aluminium bar stock, and a convergent-divergent throat was manufactured from an epoxy resin. The detailed design and manufacture of the aluminium and epoxy resin sections are described in Chapter 4 and 7, respectively. The wall static pressure along the jet-pump could be measured at ten pressure tapping points. Each tapping point had a ball valve (q) and they were connected to a common copper manifold (10) 25 mm in diameter and 400 mm in length. 3/16" copper tubes were brazed to the manifold and compression fittings connected the tubes to the valves. The details of the pressure tapping assembly is described in Chapter 4. The manifold was connected to one side of a differential pressure gauge (11). The other side was connected to the evaporator. A 150 mm diameter flange (5) was welded to the end of the jet-pump housing to connect it to the condenser. Thermal

insulation 25 mm in thickness was used on the suction pipe and part of the jet-pump housing.

3.5. Generator

Figure 3.3 shows the main components in the generator section. A stainless steel vessel 90 mm diameter and 600 mm in height was manufactured to house two 3.5 kW electric element heaters. The heaters were mounted on a 84 mm flange and placed inside the vessel bolted to the opposite flange. The electrical supply to the heaters was connected via an on-off temperature controller (42). This was also used as a safety device to prevent the generator from exceeding a set temperature. The electrical supply was connected to the heaters and a proportional temperature controller (39) via junction boxes. During operation, one heater was energized throughout the experiments, whilst the other heater was switched on and off by the controller in order to maintain a constant temperature in the generator. A nickel-chromium/nickel-aluminium (type K) thermocouple was sited in the base of the steam separator to measure the saturation temperature in the generator. A stainless steel vessel 165 mm diameter and 650 mm in length with welded end plates performed the function of a steam separator. It acted as an accumulator to even out any small fluctuations in steam generation, separated any wet vapour and provided a stagnation vapour space. A 35 mm stainless steel pipe connected the top of the heater section and the steam separator via a 114 mm flange, and a 22 mm stainless steel pipe connected the bottom of the heater section with the steam separator via a 95 mm flange. The stainless steel vessels acted as two legs of a thermosyphon reboiler. The vessel containing the heater elements provided the hot leg and the steam separator provided the cold leg.

Valve labels refer to Figure 3.2.

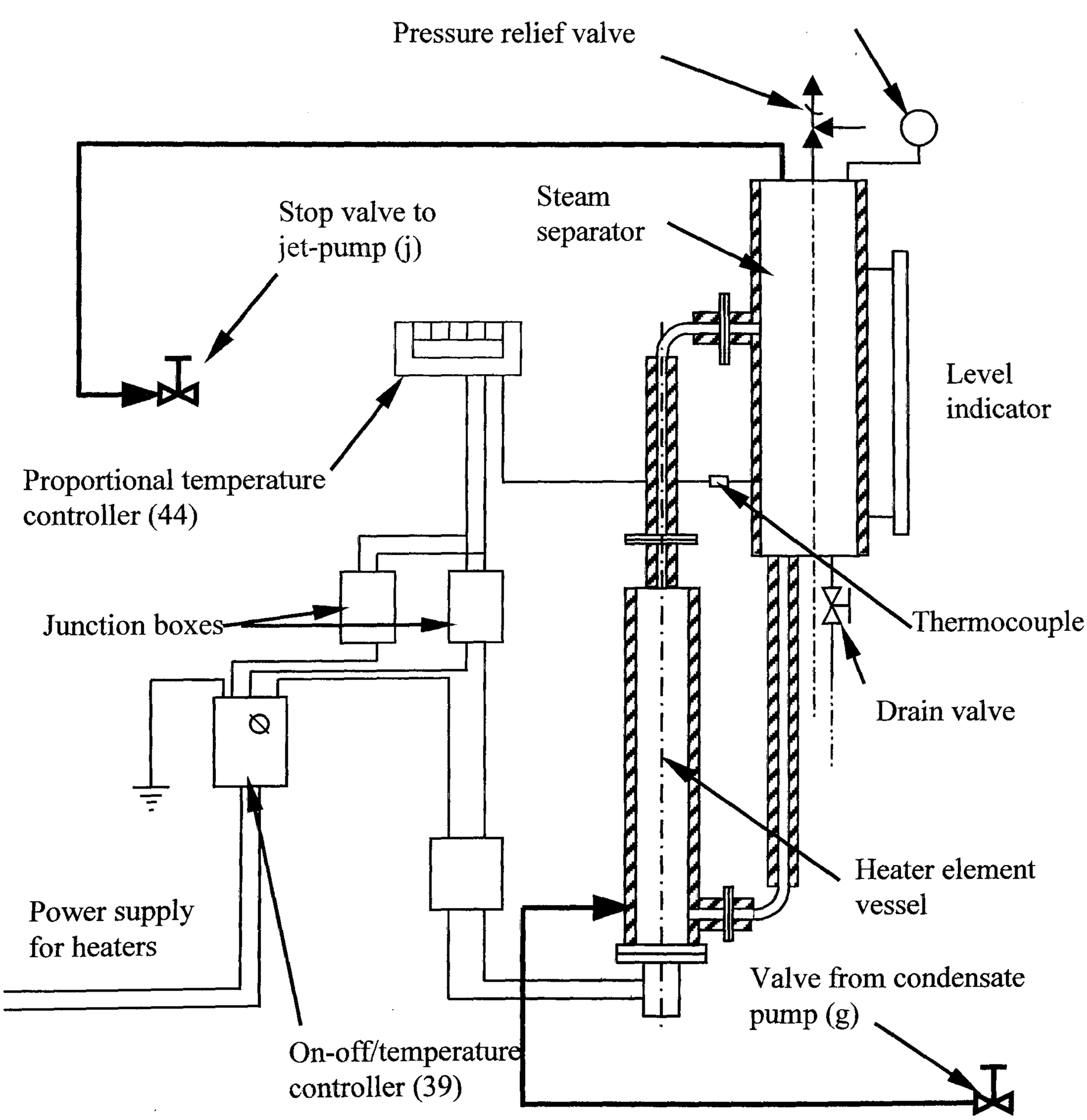

Figure 3.3. Diagram of generator section

The difference in density between the water in the hot and cold legs driving the circulation in the thermosyphon boiler. Thermal insulation, 25 mm in thickness, was used on the stainless steel vessels and connecting pipe-work. A calibrated sight glass 12 mm diameter and 445 mm in length was fitted to determine the water level in the steam separator. A pressure gauge was fitted to provide a pressure measurement of the vapour in the generator, and a pressure relief valve was fitted to protect the generator from operating at excessive pressures. A drain valve was fitted to the steam separator to enable the vessel to be drained. When under vacuum pressures it also provided a means of filling the vessel. A 12 mm insulated copper pipe connected the steam separator to a 20 mm ball valve (j) in the jet-pump assembly. A diaphragm pump delivered condensate from a measuring vessel shown in Figure 3.2 (36) via a ball valve (g).

3.6. Conclusions

This chapter described the construction of the test rig used to satisfy the aims and objectives of this research project. The rig consisted of four basic sections; a generator, a condenser, an evaporator and a jet-pump assembly. A heat load could be applied to the evaporator by a heater via a heat exchanger to maintain a steady-state when testing the jet-pump, and when discharging the encapsulated ice store. The overall system allowed measurements of primary and condensate mass flow, ice storage and heat transfer, providing data for assessing the performance of the jet-pump under the four different experimental programmes; jet-pump calibration, spray ice and encapsulated ice TIS and convergent-divergent performance enhancement.

Chapter 4. Jet-pump performance

4.1. Introduction

The optimisation of the jet-pump TIS system is important because the jet-pump cycle has a COP of less than half that of competitive comfort cooling systems such as vapour absorption and vapour-compression plant. Testing was carried out over a range of part-load conditions in order to optimise the jet-pump design for changes in condenser conditions. This is important because jet-pump entrainment is known to be approximately constant for changes in condenser conditions. It was decided to design and manufacture three jet-pump geometries in order to assess the variation in performance. This chapter describes the performance characteristics of the jet-pump, the procedure used to design the three geometries used in the jet-pump TIS system, and the test results.

4.2.1. Jet-pump operating characteristics

Figure 4.1 shows a schematic diagram of a jet-pump with the symbols referred to in the analysis below. Eames *et al* [53] showed that the actual COP of a jet-pump can be defined as a function of three dimensionless parameters; entrainment ratio, nozzle pressure ratio, and pressure lift ratio. Entrainment ratio is the ratio of secondary mass flow $\dot{m}_s$ to primary mass flow $\dot{m}_p$.

$$\omega = \frac{\dot{m}_s}{\dot{m}_p} \tag{4.1}$$

Nozzle pressure ratio is the ratio of primary stagnation pressure P_i to secondary stagnation pressure P_o.

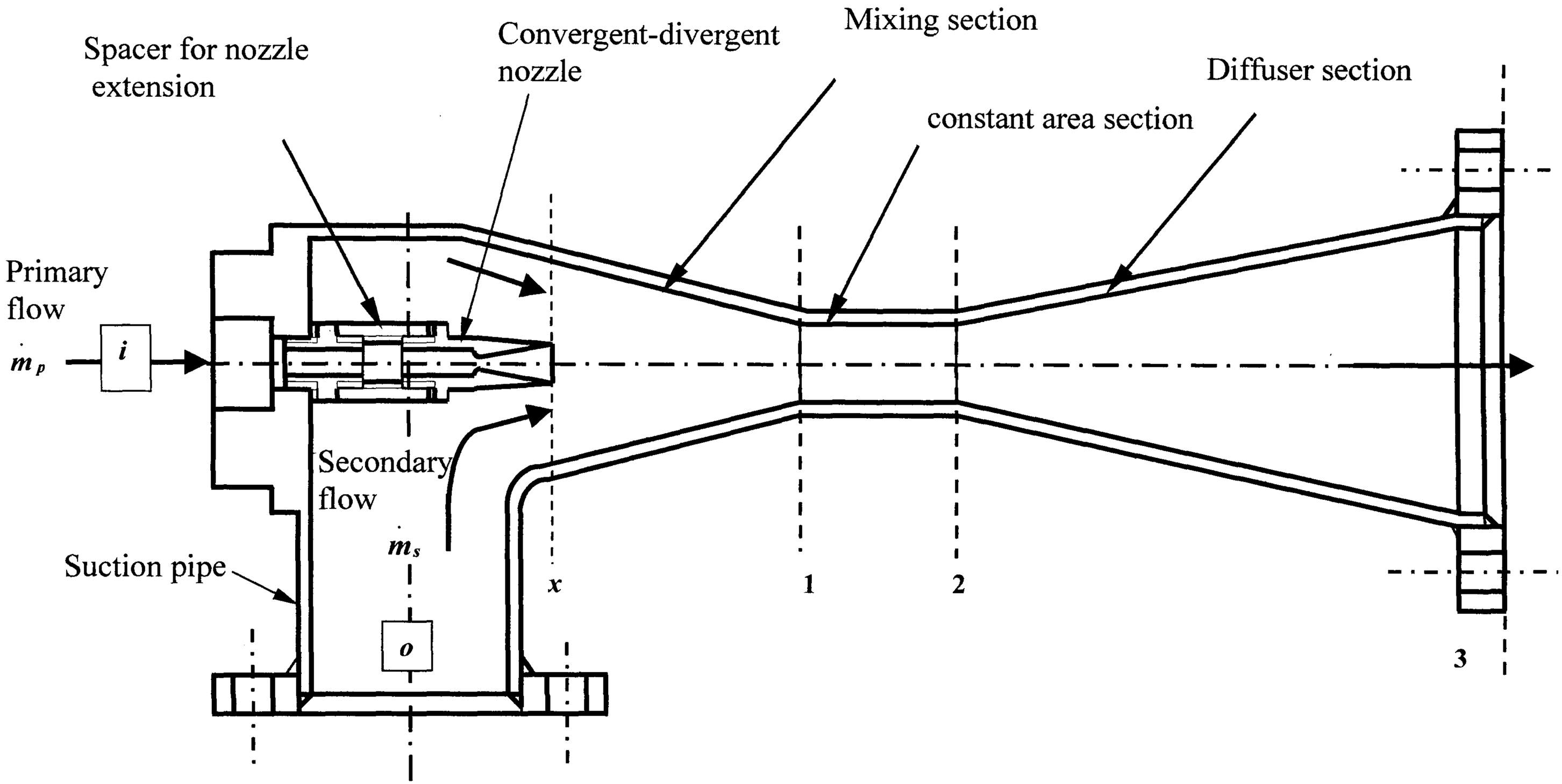

Figure 4.1. Schematic diagram of jet-pump

$$N_n = \frac{P_i}{P_o} \tag{4.2}$$

Pressure lift ratio is the ratio of diffuser outlet to secondary stagnation pressures. Pressure lift ratio will vary with condenser operating conditions up to a critical point. A one-dimensional analysis will only provide a solution at this critical point and will be known as the critical pressure lift ratio. Therefore, the critical pressure ratio is the ratio of the critical condenser pressure P_3* to the secondary stagnation pressure P_o.

$$N_s* = \frac{P_3*}{P_o} \tag{4.3}$$

In the present case, the generator and evaporator pressures, P_i and P_o are fixed, and therefore, the nozzle pressure ratio is constant. Therefore the COP of the jet-pump refrigerator becomes a compromise between entrainment ratio and critical pressure lift ratio. A high entrainment ratio is desirable because COP increases proportionately with entrainment ratio, but it was found experimentally that a high entrainment ratio can only be attained at the expense of a low critical pressure lift ratio. The design method for determining the geometries of the three jet-pumps is described in the next section.

4.2.2. Jet-pump design analysis

The jet-pump geometries were designed using a one-dimensional analysis described originally by Keenan *et al* [44] and modified by Eames *et al* [45]. The energy, momentum and continuity equations are applied from inlet to outlet to give the flow conditions through the jet-pump.

The conservation of energy for a one-dimensional adiabatic process between states 1 and 2 in a horizontal plane is

$$\sum \dot{m}_1 \left(h_1 + \frac{U_1^2}{2} \right) = \sum \dot{m}_2 \left(h_2 + \frac{U_2^2}{2} \right) \tag{4.4}$$

Conservation of linear momentum is

$$P_1 A_1 + \Sigma \dot{m}_1 U_1 = P_1 A_1 + \Sigma \dot{m}_2 U_2 \tag{4.5}$$

The continuity equation is

$$\Sigma \rho_1 U_1 A_1 = \Sigma \rho_2 U_2 A_2 \tag{4.6}$$

where $\dot{m}$ is mass flow, h is specific enthalpy, U is velocity, P is pressure, ρ is density and A is area.

4.2.3. Assumptions made in the one-dimensional analysis

The primary and secondary streams are assumed to have the same molecular weight and the same ratio of specific heats. The primary $\dot{m}_p$ and secondary $\dot{m}_s$ streams are assumed to be supplied at zero velocity in state i and o, respectively. The velocity at 3 is assumed to be zero. The primary and secondary streams mix at constant pressure between x and 1. Losses are taken into account by applying isentropic efficiencies to the primary nozzle, and diffuser and a momentum loss coefficient to the mixing chamber. The mixing of the two streams is assumed to be complete before the normal shock wave that occurs in the constant area section and transverse shocks may occur between 1 and 2. Finally, it was assumed that the vapour behaves as a perfect gas.

4.2.4. Outlet stagnation state T_3

The temperature of the flow at the outlet to the diffuser when it is decelerated to rest adiabatically is known as the stagnation temperature. It is found by applying the conservation of energy between primary and secondary, and outlet stagnation states to give;

$$\dot{m}_p h_i + \dot{m}_s h_o = \left(\dot{m}_p + \dot{m}_s \right) h_3 \tag{4.7}$$

The specific enthalpy is defined as

$$h = C_{pv} T \tag{4.8}$$

where C_{pv} is the specific heat of vapour at constant pressure, and T is the absolute temperature. Applying Equation 4.8, dividing through by $\dot{m}_p C_{pv}$, and rearranging gives;

$$T_i + \omega T_o = (1+\omega)T_3 \tag{4.9}$$

Equation 4.9 shows that outlet stagnation temperature is constant for any given inlet condition in an adiabatic nonisentropic flow.

4.2.5. State of primary and secondary streams at *x-x*

Eames *et al* [45] determined the velocity of the primary and secondary streams at the primary nozzle exit plane *x-x* by applying the conservation of energy between *i-x* and *o-x* such that the primary flow velocity at *x-x* is

$$U_{px} = \sqrt{2\eta_p (h_i - h_{ix})} \tag{4.10}$$

where η_p is the primary nozzle isentropic efficiency. The secondary flow velocity at *x-x* is

$$U_{sx} = \sqrt{2(h_o - h_{ox})} \tag{4.11}$$

Perfect gas relations can be applied to Equations 4.10 and 4.11.

Specific heat at constant pressure is defined as,

$$C_{pv} = \frac{kR}{k-1} \tag{4.12}$$

where R is the characteristic gas constant and k is the isentropic index of compression/expansion. The isentropic relationship between pressure and temperature ratios between states 1 and 2 is,

$$\frac{T_1}{T_2} = \left(\frac{P_1}{P_2}\right)^{\frac{k-1}{k}} \tag{4.13}$$

The speed of sound at the local static temperature is defined as,

$$c = \sqrt{kRT} \tag{4.14}$$

The local Mach number is defined as,

$$\mathrm{M} = \frac{U}{c} \tag{4.15}$$

Equations 4.10 and 4.11 can be expressed in terms of Mach numbers and pressure ratios by applying Equations 4.8 and 4.12 to 4.15, as shown by Eames *et al* [45]. The local Mach number of the primary stream at nozzle exit plane *x-x* is found from Equation 4.16.

$$\mathrm{M}_{px} = \sqrt{\frac{2\eta_p}{(k-1)}\left(\left(\frac{P_i}{P_x}\right)^{\frac{k-1}{k}} - 1\right)} \tag{4.16}$$

where P_x is the static pressure at the exit plane *x-x*. The local Mach number of the secondary stream at the nozzle exit plane *x-x* is found from Equation 4.17.

$$\mathrm{M}_{sx} = \sqrt{\frac{2}{(k-1)}\left(\left(\frac{P_o}{P_x}\right)^{\frac{k-1}{k}} - 1\right)} \tag{4.17}$$

The local primary and secondary stream Mach numbers can be compared to the flow at sonic velocity where the Mach number is unity so that both are expressed in terms of one variable called the critical Mach number. Eames *et al* [45] showed that primary and secondary flow Mach numbers could be converted into critical Mach numbers by using Equation 4.18.

$$\mathrm{M}^* = \frac{\sqrt{(k+1)\frac{\mathrm{M}^2}{2}}}{\sqrt{1+(k-1)\frac{\mathrm{M}^2}{2}}} \tag{4.18}$$

where M* is the critical Mach number. The derivation of M* in terms of M is described in Appendix A.

4.2.6. State of mixed stream at section 1

Applying the conservation of momentum between *x* and 1,

$$\phi_m(\dot{m}_p U_p + \dot{m}_s U_s) = \dot{m}_1 U_1 \tag{4.19}$$

$$U_1 = \left(\frac{\phi_m (U_p + \omega U_s)}{1 + \omega} \right) \tag{4.20}$$

Where ϕ_m is the mixing chamber momentum loss coefficient. The state of the combined stream at 1 in terms of critical Mach numbers is given by Equation 4.21,

$$M_1^* = \frac{\phi_m \left(M_{px}^* + \omega M_{sx}^* \sqrt{\tau} \right)}{\sqrt{(1 + \omega\tau)(1 + \omega)}} \tag{4.21}$$

where τ is defined as the ratio of inlet stagnation temperatures,

$$\tau = \frac{T_o}{T_i} \tag{4.22}$$

Appendix B shows how Equation 4.21 was derived from Equation 4.20. The critical Mach number found from Equation 4.21 is then converted back into the local Mach number upstream of the shock wave by using Equation 4.23,

$$M = \frac{\sqrt{2M^{*2}}}{\sqrt{(k+1) - M^{*2}(k-1)}} \tag{4.23}$$

4.2.7. State of mixed stream after shock process

The mixed stream is decelerated from supersonic to subsonic velocity by a normal shock wave between sections 1 and 2, and the Mach number is given by Equation 4.24.

$$M_2 = \frac{\sqrt{2 + (k-1)M_1^2}}{\sqrt{(k-1) + 2kM_1^2}} \tag{4.24}$$

The pressure rise across a normal shock wave is given by Equation 4.25.

$$\frac{P_2}{P_1} = \frac{1 + kM_1^2}{1 + kM_2^2} \tag{4.25}$$

4.2.8. State of mixed stream at outlet

The pressure rise across the subsonic diffuser is given by Equation 4.26.

$$\frac{P_3{}^*}{P_2} = \left[\frac{(k-1)\eta_d M_2^2}{2} + 1\right]^{\frac{k}{k-1}} \tag{4.26}$$

Where η_d is the diffuser isentropic efficiency. The critical pressure lift ratio across the jet-pump is then found from Equation 4.27. The assumption of constant pressure mixing from x to 1, gives $P_1 = P_x$, therefore the critical pressure lift ratio is

$$\frac{P_3{}^*}{P_o} = \left(\frac{P_3{}^*}{P_2}\right)\left(\frac{P_2}{P_x}\right)\left(\frac{P_x}{P_o}\right) = N_S{}^* \tag{4.27}$$

The static pressure P_x at the nozzle exit plane x-x is not known, but an iterative scheme can be used to calculate the critical pressure lift ratio for a range of exit static pressures and so find the optimum value. Appendix C describes a program which was written to calculate the critical pressure lift ratio for an assumed entrainment ratio. The program also calculates the jet-pump geometry, the equations of which are described below. The selection of primary nozzle and diffuser isentropic efficiencies and the momentum loss coefficient used in the calculation procedure are a matter for judgement, but ESDU [46] give general guidelines. The design procedure will use 0.85, 0.8 and 0.9 for the primary nozzle and diffuser isentropic efficiencies and momentum loss coefficient, respectively.

4.3.1. Jet-pump geometry

The primary nozzle throat area, primary nozzle exit area and diffuser throat are determined by applying the continuity equation, and the conservation of energy and momentum between stagnation and local states. The relationship between the stagnation states P_0, T_0 and local condition M gives the area at that point as shown in Equation 4.28.

$$A = \frac{1}{M}\frac{\dot{m}}{P_0}\left[\frac{RT_0}{k}\left(1 + \frac{k-1}{2}M^2\right)^{\frac{k+1}{k-1}}\right]^{\frac{1}{2}} \tag{4.28}$$

The primary nozzle throat area can be calculated by setting the local Mach number to unity and entering the generator stagnation states P_i and T_i.

The ratio between the primary nozzle exit and throat areas can be found from Equation 4.29.

$$\frac{A_x}{A_t} = \frac{1}{\mathrm{M}_{px}}\left[\frac{2}{(k+1)}\left(1+\frac{(k-1)}{2}\mathrm{M}_{px}{}^2\right)^{\frac{k+1}{2(k-1)}}\right] \tag{4.29}$$

The ratio between the primary nozzle to diffuser throat areas can be found from Equation 4.30.

$$\frac{A_t}{A_2} = \left[\frac{\mathrm{N_s}^*}{\mathrm{N_p}}\sqrt{\frac{1}{(1+\omega)(1+\omega\tau)}}\right]\left[\frac{\left(\frac{P_2}{P_3}\right)^{\frac{1}{k}}\sqrt{1-\left(\frac{P_2}{P_3}\right)^{\frac{k-1}{k}}}}{\left(\frac{2}{k+1}\right)^{\frac{1}{k-1}}\sqrt{1-\left(\frac{2}{k+1}\right)}}\right] \tag{4.30}$$

4.3.2. Assumptions made in the detailed jet-pump design

The previous sections described the design procedure based on a one-dimensional analysis, but further performance assumptions have to be made in order to establish the design of the jet-pump in detail. This section describes the performance assumptions that have been made, and the designs that followed.

A generator stagnation temperature of 120 °C and an evaporator stagnation temperature of 5 °C were chosen as representative of the low grade heat available (80 °C - 140 °C), and the chilled water supply requirements of a building. The jet-pump used in the TIS tests was assumed to operate at the maximum condenser temperature of 30 °C, typical of the peak cooling season ambient conditions. An entrainment ratio of 0.3 was assumed for these operating conditions.

4.3.2. Primary nozzle design

In order to establish the dimensions of the primary nozzle, a cooling load of 750 W was assumed at an evaporator temperature of 5 °C. The cooling load is found from Equation 4.31.

$$\dot{Q}_{\mathrm{e}} = \dot{m}_{\mathrm{e}}\left(h_{g,Te} - h_{\mathrm{f},Tc}\right) \tag{4.31}$$

where $h_{\mathrm{g},Te}$ is the specific enthalpy of saturated vapour at the evaporator temperature and $h_{\mathrm{f},Tc}$ is the specific enthalpy of saturated liquid at the condenser saturation temperature. If it is assumed that at steady-state, the evaporation rate is equal to secondary mass flow then secondary mass flow is

$$\dot{m}_{\mathrm{s}} = \frac{\dot{Q}_{\mathrm{e}}}{\left(h_{g,Tg} - h_{\mathrm{f},Tc}\right)} \tag{4.32}$$

The specific enthalpy of saturated vapour at the generator saturation temperature is 2707 $\mathrm{kJ.kg^{-1}}$, and the specific enthalpy of saturated liquid at the condenser saturation temperature is 125.7 $\mathrm{kJ.kg^{-1}}$. Therefore, secondary mass flow is

$$\dot{m}_{\mathrm{s}} = \frac{750}{(2707 - 125.7)}$$

$$\dot{m}_{\mathrm{s}} = 0.291\mathrm{g.s^{-1}}$$

Entrainment ratio was defined by Equation 4.1, thus, rearranging in terms on primary mass flow gives

$$\dot{m}_{\mathrm{p}} = \frac{\dot{m}_{\mathrm{s}}}{\omega} \tag{4.33}$$

$$\dot{m}_{\mathrm{p}} = \frac{0.3}{0.291}$$

$$\dot{m}_{\mathrm{p}} = 0.970\mathrm{g.s^{-1}}$$

The primary nozzle throat area can now be determined from Equation 4.28 by setting the Mach number to unity. At a generator temperature of 388 K, the stagnation pressure P_i is 1.985 bar. For dry saturated steam the characteristic gas constant R is 461.5 $\mathrm{J.kg^{-1}.K^{-1}}$ and the isentropic index of compression/expansion k

is 1.3, according to Rogers and Mayhew [47]. Therefore, the primary nozzle throat area is

$$A_t = \frac{\dot{m}}{P_i}\left[\frac{RT_i}{k}\left(1+\frac{k-1}{2}\right)^{\frac{k+1}{k-1}}\right]^{\frac{1}{2}} \tag{4.34}$$

$$A_t = \frac{0.970\times10^{-3}}{1.985\times10^{5}}\left[\frac{461.5\times393}{1.3}\left(1+\frac{0.3}{2}\right)^{\frac{2.3}{0.3}}\right]^{\frac{1}{2}}$$

The primary nozzle throat diameter is

$$d_t = \sqrt{\frac{4A_t}{\pi}} \tag{4.35}$$

d_t =1.993 mm

A primary nozzle throat diameter of 2 mm will be used. The ratio of the primary nozzle exit to throat areas is given by Equation 4.29.

$$\frac{A_x}{A_t} = \frac{1}{\mathrm{M}_{px}}\left[\frac{2}{(k+1)}\left(1+\frac{(k-1)}{2}\mathrm{M}_{px}{}^2\right)^{\frac{k+1}{2(k-1)}}\right] \tag{4.29}$$

The result of calculations using the design procedure described in section 4.2 give a primary flow Mach number at the nozzle exit plane *x*-*x* of 3.762, therefore the primary nozzle area ratio is

$$\frac{A_x}{A_t} = \frac{1}{3.762}\left[\frac{2}{2.3}\left(1+\frac{0.3}{2}3.762^2\right)^{\frac{2.3}{0.6}}\right]$$

The diameter of the primary nozzle at the exit plane *x*-*x* is

$$d_x = \sqrt{d_t{}^2\frac{A_x}{A_t}} \tag{4.36}$$

d_x = 8.5 mm

A throat diameter of 2 mm and an exit diameter of 8.5 mm are the dimensions of the design nozzle for the operating conditions described earlier, and will be referred to as Nozzle No 1. Figure 4.2 illustrates the main features of the primary nozzle.

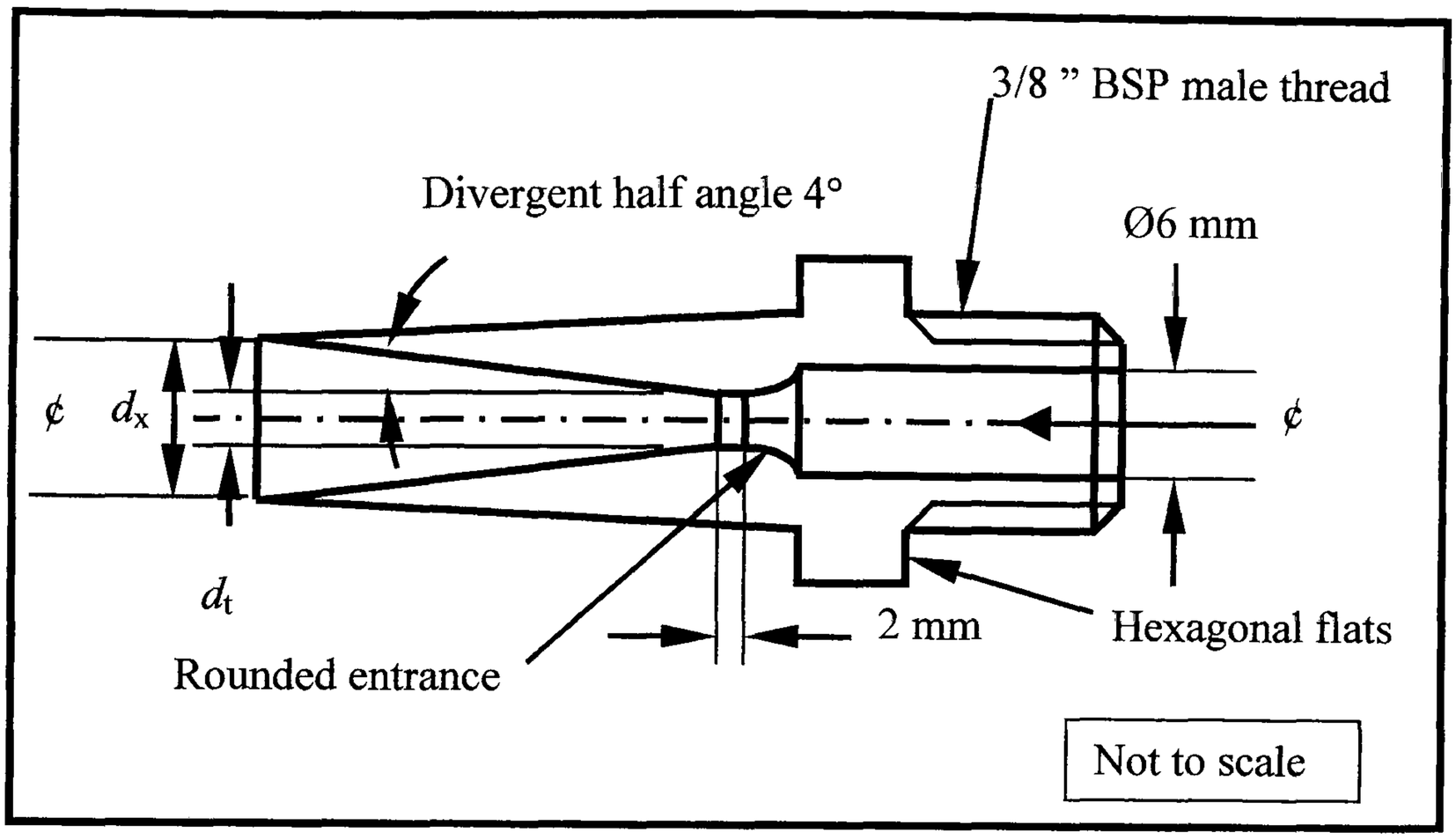

Figure 4.2. Diagram of primary nozzle

The primary pressure ratio at the design point is 227, but experiments are also to be carried out using an over-expanded nozzle in order to investigate the effect of over-expansion on jet-pump performance. The design nozzle pressure ratio of the over-expanded nozzle will be double that of Nozzle No 1, thus giving a N_p of 454. The same procedures were used to determine the exit diameter of the over-expanded nozzle and it was found to be 10.8 mm. An exit diameter of 11 mm will be used. The over-expanded nozzle will be referred to as Nozzle No 2. Both nozzles used a smooth, rounded entrance to the throat and a 4° divergent half angle.

4.3.3. Jet-pump geometries

Three geometries were designed and manufactured to give a range of cooling capacities and critical pressure lift ratios. All of the designs operated at the same inlet stagnation conditions, namely, generator and evaporator saturation temperatures of 120 °C and 5 °C, respectively. An assumed entrainment ratio on 0.3 has already been referred to with respect to peak cooling load conditions, but

two other values were chosen to test the system for different operating conditions. First, a high entrainment ratio to provide enhanced cooling below the peak, and second, a low entrainment ratio to provide higher pressure lift ratios that would be required if the system operated in hot and humid climates. Entrainment ratios of 0.1, 0.3 and 0.5 were, therefore, chosen to provide a range of cooling capacities. Table 4.1 summarises the flow conditions found from the design procedure described in Section 4.2 and the geometry of the three jet-pump designs found from Section 4.3.

Table 4.1. Flow conditions and diffuser geometry for the three jet-pump designs

ω	0.1	0.3	0.5
N_s*	7.44	4.74	3.44
A_d	49	81	121
D_2	14	18	22

The specification of section lengths and angles are a matter judgement because of the wide variety of operating conditions and uses to which jet-pumps can be applied. Published experimental data and manufacturers recommendations have been brought together by ESDU and other Standards organisations in order to produce general design guidelines. ESDU [46] give a range of recommended lengths based on diffuser throat diameter and Table 4.2 shows the assumed ratios and lengths of the sections used in this case for the design of the three test geometries. The labels in Table 4.2 refer to the diagram of the jet-pump assembly shown in Figure 4.3.

Table 4.2. Detailed geometry of the three test jet-pump designs

D_2 (mm)	A (mm)	B (mm)	C (mm)	D (mm)
	$2.75D_2$	$7.5\ D_2$	$2.5D_2$	$12D_2$
14	35	105	38.5	168
18	45	136	49.5	216
22	55	165	60.5	264

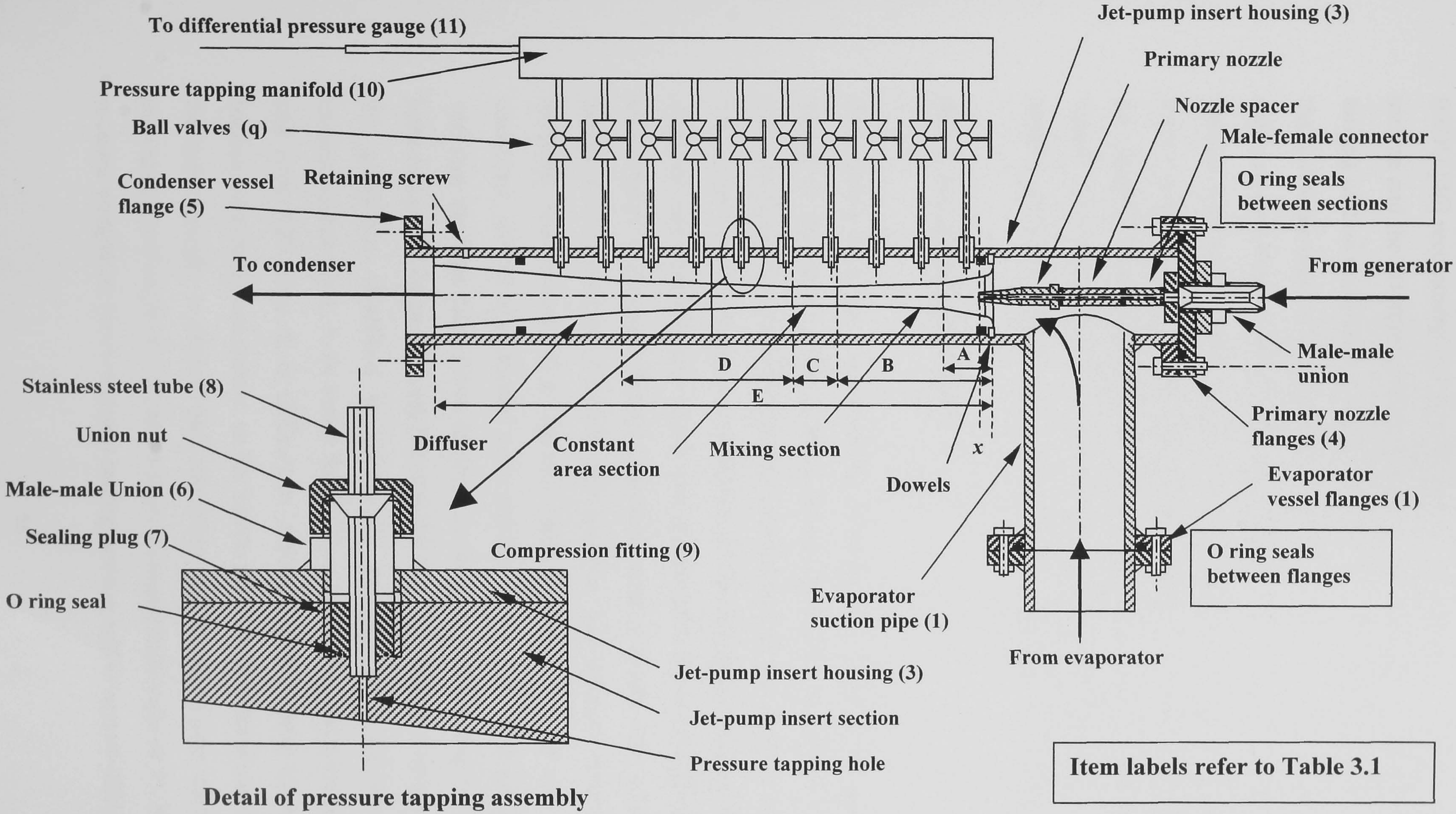

Figure 4.3. Schematic diagram of jet-pump assembly

ESDU [46] recommend that double taper cones are used in the convergent mixing section and the divergent diffuser section in order to smooth the flow through the mixing section and reduce losses in the diffuser. A half angle of 11° was used in the first taper cone in the convergent mixing section so as to maximise the cross sectional area between the primary jet and the wall. A half angle of 1.5° was used beyond $2.75D_2$ to smooth the flow into the diffuser throat and reduce turbulent losses. A half angle of 3° was used in the first taper cone in the divergent diffuser for a length $12D_2$, which gave an overall length of 495.5 mm. All three jet-pump inserts were designed to have an overall length of 500 mm, therefore, the two smaller geometry designs used a divergent cone half angle of 6° beyond $12D_2$.

4.3.4. Jet-pump assembly

The suction pipe was connected the evaporator to the jet-pump housing (3) as shown in Figure 4.3. The primary nozzle assembly consisted of a 150 mm diameter flange (item 4 in Figure 3.2), primary nozzle, spacer, connector and seals. The primary nozzles were machined from 25 mm hexagonal section brass bar. The upstream end of the primary nozzle was connected to the spacer-piece by a 10 mm male thread. 10 mm male/female spacers of varying lengths were manufactured to permit the adjustment of nozzle exit position. The primary nozzle and spacer assembly was fastened to a 150 mm diameter flange by a 10 mm male/female connector, and 10 mm bonded seals provided sealing between components. The 150 mm diameter flange was fastened to the jet-pump housing by four 20 mm bolts and sealed by an "O" ring between the two flanges. Three jet-pump inserts of the geometries described in Tables 4.1 and 4.2 were manufactured from aluminium bar stock, to fit inside the stainless steel tube, and were sealed at each end with "O" rings. It is difficult to machine long internal tapers accurately because of cutting tool chatter, so the inserts were made in three parts to minimize the taper length; a central part including the constant area section, a short convergent half angle of 1.5°, and a short divergent half angle of 3°. The two other sections completed the convergent mixing section and divergent diffuser, and "O"

rings were used to seal the joints. The stainless steel housing was also used to contain a convergent-divergent throat jet-pump whose design and manufacture is described in Chapter 7. Two 6 mm dowels at the upstream end and three 6 mm retaining screws at the downstream end held the inserts in position. The static pressure along the jet-pump could be measured at ten pressure tapping points. They were situated at 40 mm intervals starting 15 mm from the jet-pump insert entrance. 5 mm male/male connectors were screwed into the jet-pump housing and welded in place. A plug was screwed into a 10 mm female tapped hole in the jet-pump insert to provide a seal. A 5 mm stainless steel tube passed through the connector and plug, with the sharp end resting on a flat surface machined in the jet-pump insert. The tube was secured by compression fittings at the valve and welded connectors. A hole, 1.5 mm diameter was drilled through the aluminium insert to measure the static pressure at the inner wall, the measuring point on the inner surface of the jet-pump being sharp edged and smooth.

4.4. Test results

A range of jet-pump geometries were designed and manufactured to examine the change in performance at part-load. Initially, testing was carried out to calibrate the jet-pumps and compare their performance with those assumed at the design stage. Once the jet-pumps had been calibrated, the results were used to make recommendations for improving the performance and control of the jet-pump over a range of operating conditions. This is important because of the relatively low performance of a jet-pump compared to other competing cooling systems. The experimental methodology and the test results are described below.

4.4.1. Experimental method

Referring to Figure 3.2, before testing, the test rig was evacuated by a vacuum pump to remove non-condensable gases. After evacuation, the generator heaters

were switched on until the water reached the desired temperature. An imersion heater in the hot water tank (24), that provided the heat load for the evaporator was also switched on until the temperature reached the desired value. When the generator temperature reached the test level, the refrigerant water re-circulation pump (22) was started and the flow to the evaporator was delivered to the spray nozzle (23) via the heat exchanger (28). The steam-valve to the primary nozzle (j) was then opened and all temperatures and pressures recorded. When the evaporator vapour temperature approached the test temperature, the heat load simulator centrifugal pump (25) was started, and the flow through the heat exchanger (28) varied until the temperature in the evaporator was equal to the required test temperature. The hot water flow to the heat exchanger was adjusted to maintain a steady-state temperature in the evaporator. The water levels in the evaporator and generator were then recorded and a stopwatch started. Each test run continued until the refrigerant-water level in the evaporator reached a predetermined lower limit, then the water level in the evaporator and the generator and time interval was recorded. The measured change in level with time enabled measurement of secondary and primary flows to be made. Entrainment ratio was then calculated from these data. With the generator and evaporator conditions held constant, entrainment ratio was found to be approximately constant for changes in condenser pressure up to the critical condenser pressure; that is the condenser pressure at which flow reversal was found to occur and the jet-pump became unstable. Higher condenser pressures cause the entrainment ratio to decrease rapidly to zero. At higher condenser pressures reversal of primary flow back into the evaporator vessel was found to cause an increase in pressure and temperature. This effect was used to determine the critical condenser pressure over a range of nozzle pressure ratios and diffuser area ratios. Critical condenser pressures were established by reducing the flow through the cooling coil until the pressure and temperature in the evaporator began to rise, which indicated that the condenser pressure had increased beyond its critical condenser pressure and flow reversal back to the evaporator had taken place. The flow through the condenser cooling coil was then increased slowly until the jet-pump operation had been re-

established and pressures and temperatures returned to steady-state values. Once this had been achieved the maximum pressure was taken to be the critical condenser pressure.

With the jet-pump operating at steady-state conditions, static pressure measurements were taken along the length of each diffuser from ten pressure tapping points (10) shown in Figure 3.2 and 4.2. Before each pressure distribution test all of valves (q) were closed. At the start of each test the first valve downstream of the mixing section entrance was opened and the pressure measured by an analogue differential pressure gauge (11). After the pressure was recorded, the first valve was shut and the next valve downstream opened. In each case, the static pressure was allowed to become steady before being recorded. The procedure was repeated over the length of the diffuser until the wall static pressure distribution with axial position had been measured.

4.5. Findings

Figure 4.4 shows the results of entrainment ratio and condenser saturation pressure measurements taken at a constant generator saturation temperature of 120 °C and a range of evaporator saturation temperatures. At constant evaporator conditions, the entrainment ratio appeared to be approximately constant for variations in condenser pressure up to the critical condenser pressure P_3*. This result confirmed that the "constant capacity" assumption made in the introduction was reasonable to the accuracy of the flow measurements. According to Huang et al [48], the "constant capacity" phenomenon characteristic of jet-pumps is caused by choking of secondary flow in the mixing chamber. One-dimensional analyses of a jet-pump give reasonable agreement with actual performance but cannot be used to analyse part-load performance. Bagster and Munday [49] described a semi-empirical theory to explain choking in a jet-pump in order to model part-load performance.

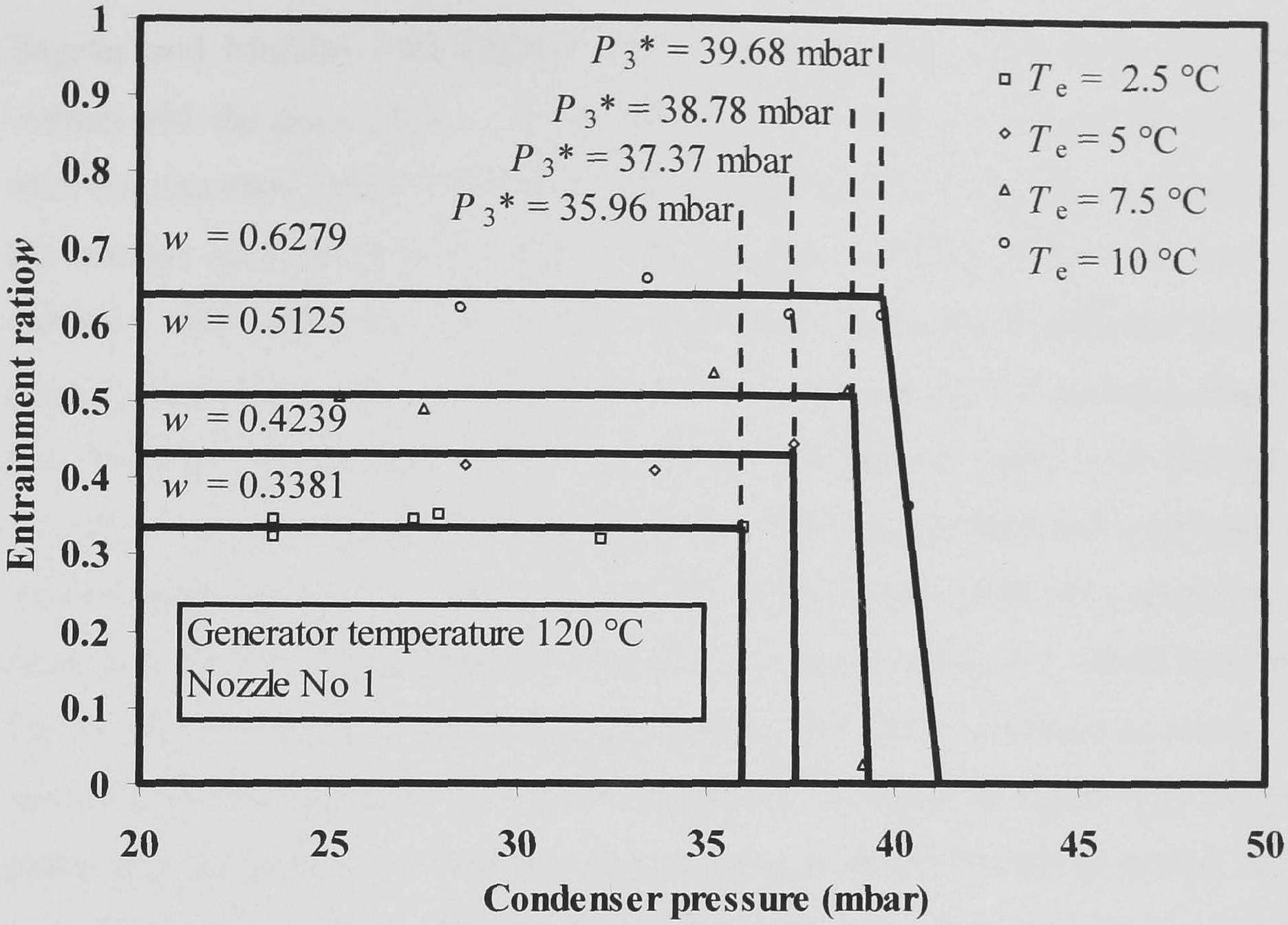

Figure 4.4. Variation in entrainment ratio with condenser pressure at constant evaporator temperatures.

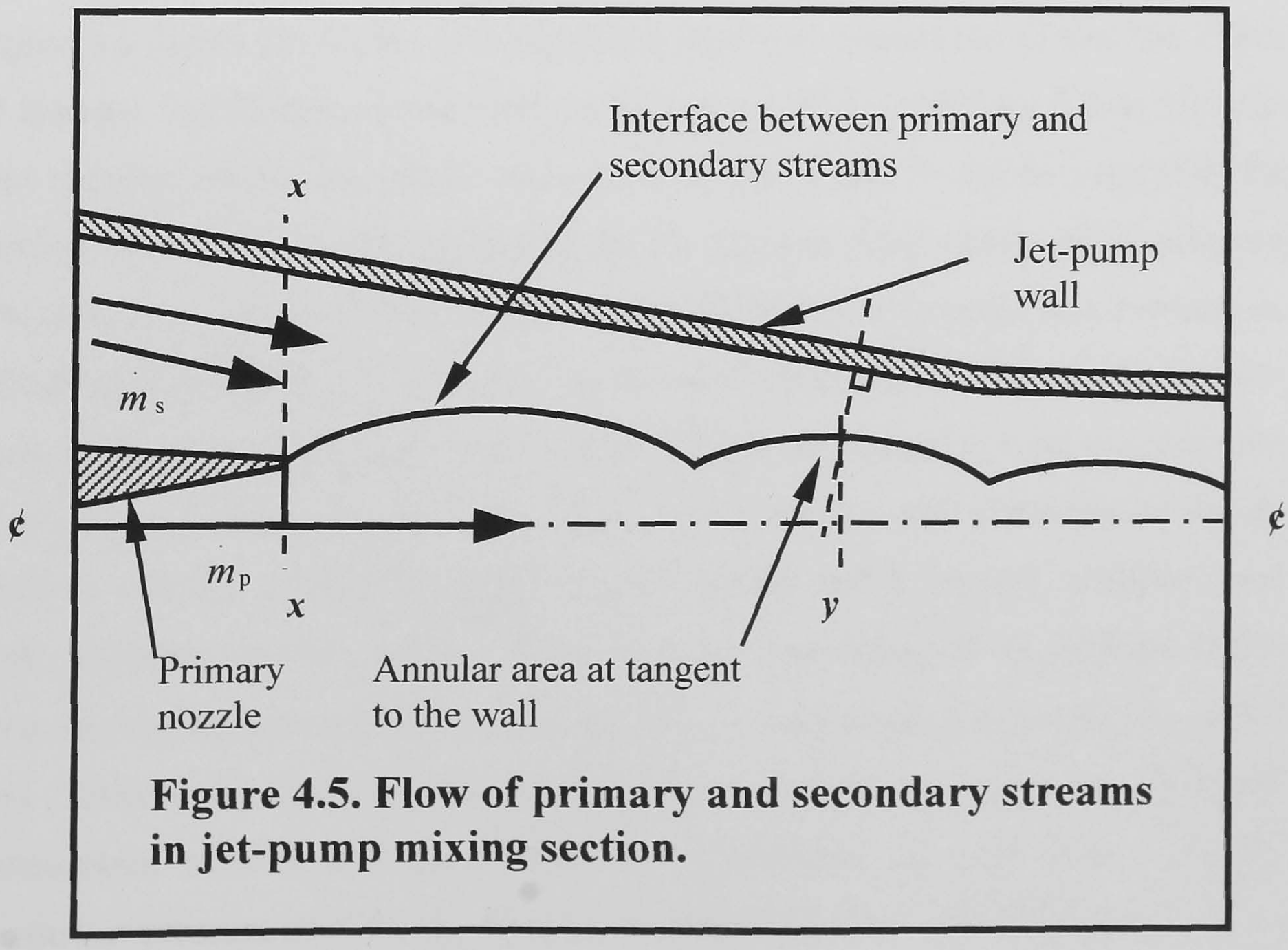

Figure 4.5. Flow of primary and secondary streams in jet-pump mixing section.

Bagster and Munday [49] suggested that when the secondary flow came into contact with the primary jet at the nozzle exit, the two streams did not immediately mix, but remained distinct. Figure 4.5 shows how the secondary flow expands into the annular area between the primary jet and the wall. The primary jet tends to exhibit a node anti-node behaviour as the pressure in the jet changes so that it is equal to that of the surroundings at the interface between the two streams. Bagster and Munday [49] proposed that the primary jet and the duct wall formed a convergent duct through which the secondary flow accelerated and continued to expand until it reached sonic velocity. The two streams were then assumed to begin mixing. The point at which secondary flow reached Mach 1 would be where the annular area between the primary jet and the wall was a minimum and could be used to calculate secondary flow more accurately, as shown in Figure 4.5. The jet-pump was designed to provide an entrainment ratio of 0.3 but the measured value was found to be 0.4239. The critical pressure lift ratio decreased from a design value of 4.74 to 4.30, which resulted in a reduction in critical condenser pressure from 4133 Pa to 3750 Pa.

Figure 4.6 shows the results of a sensitivity analysis, carried out to find the effect of changes in efficiencies and loss coefficient on flow conditions. Each variable was changed whilst the others were fixed at unity, and it can be seen that the mixing section loss coefficient had by far the greatest effect upon critical pressure lift ratio. A change in mixing section loss coefficient of 0.7 results in a decrease in critical pressure lift ratio of more than two and a half times. This shows that the most likely cause of the difference between theory and practice is an overestimate of momentum losses in the converging mixing section. An overestimate would result in a lower velocity and Mach number at the end of mixing, a higher local static temperature and specific volume, and an over-sizing of the diffuser throat area, causing an increase in entrainment ratio. A momentum loss coefficient of 0.9 was assumed for the mixing chamber, but re-calculations using the measured entrainment ratio and a momentum loss coefficient of 0.94 give a critical condenser pressure of 3750 Pa, close to the measured value of 3737 Pa.

The design procedure for calculating the diffuser throat area was simplified by assuming that the constant area section extended back to the primary nozzle. constraining the total throat area to be equal to the sum of the primary nozzle exit area and secondary area. This would also tend to over-estimate the annular area for secondary flow. It would be possible to calculate the entrainment ratio more accurately, but would require finite difference techniques such as the method of characteristics to find the flow conditions and radius of the primary jet downstream of the nozzle exit, and so determine the minimum area and theoretical throat. This would give a better approximation to actual values but would be much more complex.

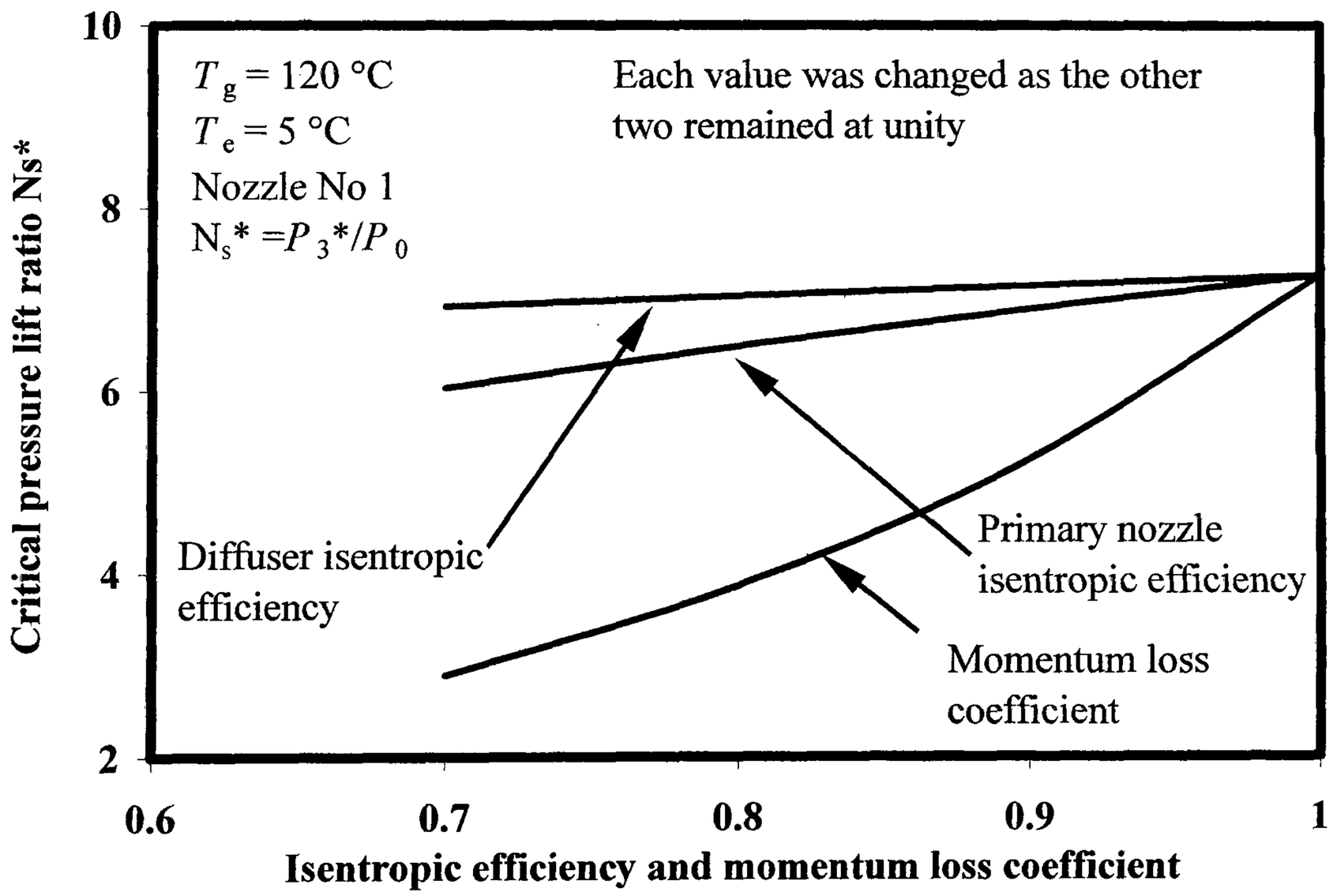

Figure 4.6. Results of a sensitivity analysis of isentopic efficiencies and a momentum loss coefficient

The measured entrainment ratio was approximately 40 % higher than that envisaged at the design stage, but the pressure lift ratio had decreased by approximately 10 %. This shows that for very small changes in pressure lift ratio,

much larger increases in entrainment ratio are attainable. Equation 4.28 described the cross-sectional area of a duct where the stagnation conditions and the local Mach number was known. It was assumed that the secondary flow expands adiabatically from the stagnation conditions in the evaporator and at the theoretical throat the Mach number is unity. If Equation 4.28 were re-arranged in terms of the mass flow, then the relationship between the stagnation conditions, throat area and secondary flow can be seen.

$$\dot{m}_s = \frac{AP_o}{\sqrt{T_o}}\left(\frac{R}{k}\left(1+\frac{k-1}{2}\right)\right)^{-\frac{1}{2}} \tag{4.37}$$

Equation 4.37 shows that secondary flow is proportional to the theoretical throat area, evaporator stagnation pressure and inversely proportional to the square root of the evaporator stagnation temperature. This shows that secondary flow increases with stagnation conditions, as can be seen from Figure 4.4. It was shown in the design section, that the pressure lift ratio would decrease with an increase in entrainment ratio. Pressure lift ratio was reduced from 4.92 to 3.23 for an increase in evaporator saturation temperature from 2.5 °C to 10 °C. This would be equivalent to an increase in the chilled water supply temperature. The critical condenser pressure increased by approximately 10 % over the same chilled water temperature range, which corresponded to a saturation temperature range of approximately 1.5 °C. This shows that the variation in chilled water temperature is not an appropriate method of controlling the jet-pump with respect to condenser conditions. However, entrainment ratio can be enhanced by approximately 50 %, thus, changes in the cooling requirements of a building could be partially met by varying the chilled water supply temperature. It would not normally be possible to use this control strategy in TIS systems because the evaporator saturation conditions will be fixed during evaporative freezing, but the discussion will show how the calibration tests at part-load could be used to enhance jet-pump TIS performance.

At evaporator saturation temperatures of 2.5 °C and 5 °C it was not possible to measure entrainment ratio beyond the critical condenser pressure because secondary flow became unstable. The difference between choked flow and zero flow must be small, and if this design were used in a practical jet-pump refrigerator then it would be inadvisable to operate it at the critical condenser pressure because of the loss of action with a small increase in condenser pressure. In practice, a jet-pump will operate at a lower condenser pressure than the design point to give a margin of error for unforeseen changes in operating conditions.

Figure 4.7 show results of tests carried out using an over-expanded nozzle and will be used in comparison with Figure 4.4. Nozzle No 1 was designed to fully expand to the static pressure of the surrounding vapour at an evaporator saturation temperature of 5 °C. The entrainment ratio at 5 °C was found to be 0.3476, approximately 20 % less than was found using nozzle No 1. Nozzle No 2 had an extended length and a larger exit area than nozzle No 1, causing the primary flow to continue to expand compared to the flow in nozzle No 1. At the nozzle exit, the static pressure of the jet is lower than the surroundings, and the primary stream leaves the nozzle in a series of oblique shock waves. If the difference in pressure is great enough then a normal shock wave can form in the primary nozzle, increasing losses and possibly causing flow separation. The oblique shock waves tend to cause the primary jet to bulge out, restricting secondary flow. If the only consequence of using an over-expanded nozzle were to restrict secondary flow, then it would seem reasonable to assume that a higher pressure lift ratio could be achieved because of the inter-related behaviour of entrainment ratio and pressure lift ratio. Experimental results showed that critical condenser pressure was approximately 3488 Pa compared with 3737 Pa using nozzle No 1, showing that the over-expanded nozzle caused a decrease in critical condenser pressure and critical pressure lift ratio. It is thought that over-expansion caused an increase in momentum losses in the mixing section.

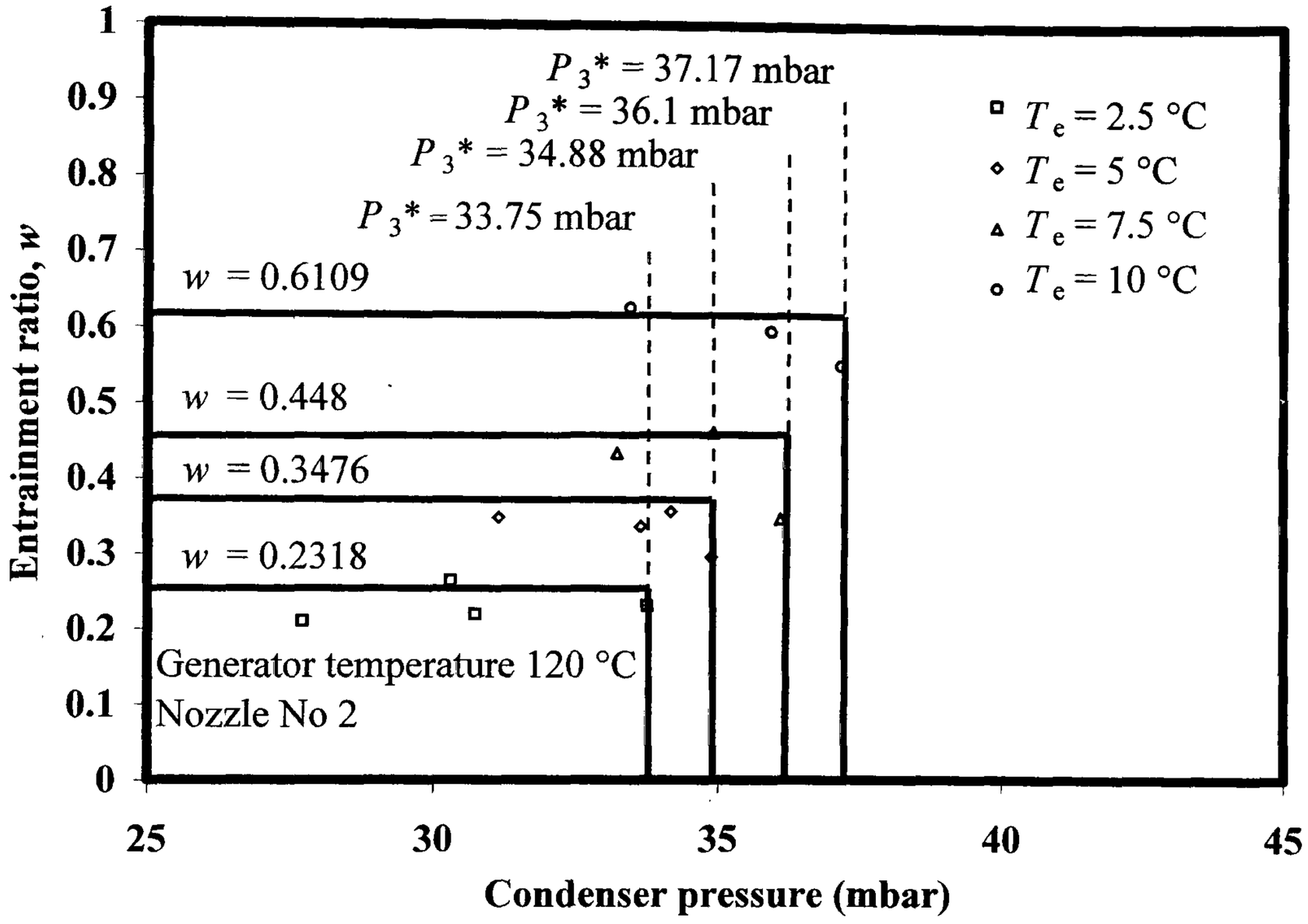

Figure 4.7. Variation in entrainment ratio with condenser pressure at constant evaporator temperatures.

The calculation procedure described in Appendix C was modified and used to input the entrainment ratio and vary the momentum loss coefficient until the measured pressure lift ratio was output. A loss coefficient of 0.875 gave the correct critical pressure lift ratio for the given inlet conditions. This suggested that there is approximately a 7 % increase in losses in the mixing chamber due to over-expansion of the primary flow. The results shown in Figure 4.7 at the other evaporator saturation temperatures showed the same trend as observed in Figure 4.4. An increase in evaporator saturation temperature increased entrainment ratio and critical condenser pressure but reduced critical pressure lift ratio. Figure 4.7 showed that an over-expanded nozzle reduced both entrainment ratio and critical condenser pressure compared to the fully expanded nozzle. Of course, at conditions greater than the design point both nozzles were over-expanded, but Nozzle No 1 was superior in terms of entrainment ratio, pressure lift ratio and critical condenser pressure.

Pressure tapping points were used to measure the wall static pressure downstream of the nozzle exit plane, and the pressure distribution using the two test primary nozzles can be seen in Figures 4.8 and 4.9.

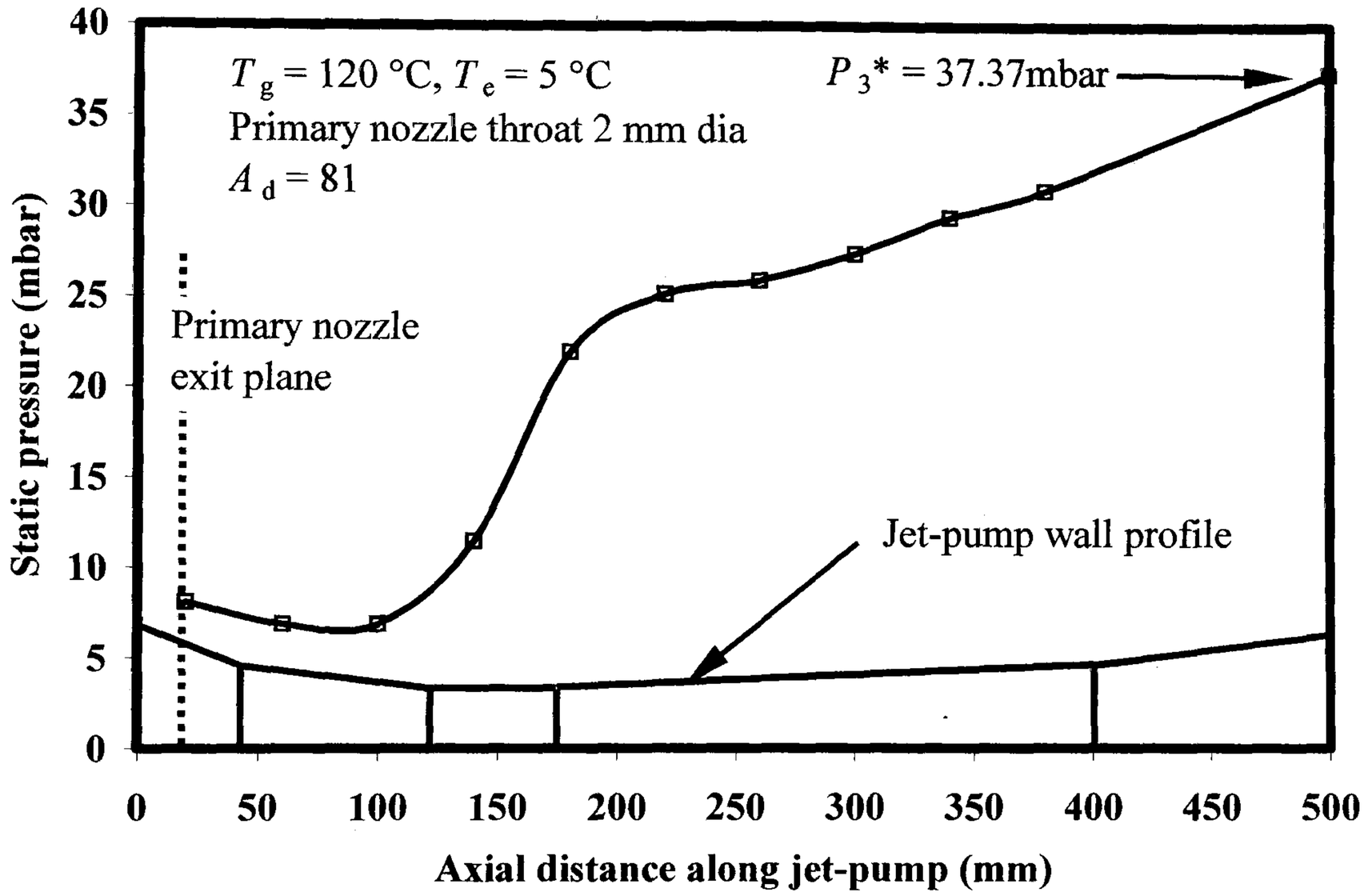

Figure 4.8. Static pressure distribution using primary nozzle No 1.

In Figure 4.8, The static pressure decreased in the convergent section from the entrance to the second tapping point, suggesting that the secondary stream may have expanded for some distance downstream of the primary nozzle exit plane.

This observation was consistent with convergent duct theory by Bagster and Munday [49]. The 'theoretical throat' within the entrainment region must occur near to the entrance of the second taper cone. This may also explain the difference between the design entrainment ratio of 0.3 and the measured value of 0.4239. It is well known that secondary flow is very sensitive to inlet geometry. Any sharp bends, surface roughness, restrictions or obstructions can cause significant losses, but the large annular area at the entrance may reduce any losses due to restriction

in the flow. The large first half angle of 11° may enhance the theoretical area, increasing secondary flow, allowing a rapid acceleration to sonic velocity, and providing a smooth entrance into the second taper cone. Experimental results showed that critical condenser pressure was approximately 3488 Pa compared with 3737 Pa using nozzle No 1, showing that the over-expanded nozzle caused a decrease in critical condenser pressure and critical pressure lift ratio. It is thought that over-expansion caused an increase in momentum losses in the mixing section. Figure 4.8 shows the data linked by a continuous curve, but it appears from pressure measurements at tapping points No 2 and No 3 that constant pressure mixing occurs in the second taper cone up until the entrance to the constant area diffuser throat. The pressure had risen at tapping point No 4, but it was assumed that the pressure rise started at the throat entrance. The pressure rose steadily through the throat, and not a discontinuous step change that would be seen if the static pressure had risen across a normal shock wave. The actual shock process is a complex three-dimensional phenomenon that Chin *et al* [50] studied using computational fluid dynamic analysis. At the critical condenser pressure, the shock wave occurs at the exit to the constant area throat. In three dimensions, there is a shock point close to the centre-line of the throat. The static pressure is highest at the centre, with a pressure front propagated in three-dimensions. When the flow is choked, the pressure front and the static pressure at the entrance to the throat are equal. The static pressure then increases downstream of the entrance to the throat because of the pressure front presented by the shock.

Figure 4.9 shows the wall static pressure distribution from tests using nozzle No 2. Unlike the results in Figure 4.8, constant pressure mixing downstream of the primary nozzle exit plane was observed. This showed that there was no expansion of the secondary stream, so the minimum area must have occurred close to the nozzle exit. At the nozzle exit, the annular area for secondary flow was large, and should have given higher mass flow compared to any position downstream of that point, but the jet may expand almost perpendicularly to the nozzle axis. This could occur because of oblique shock waves caused by over-expansion of the primary

jet. This restriction and the momentum losses caused a reduction in entrainment ratio and pressure lift ratio, as discussed earlier.

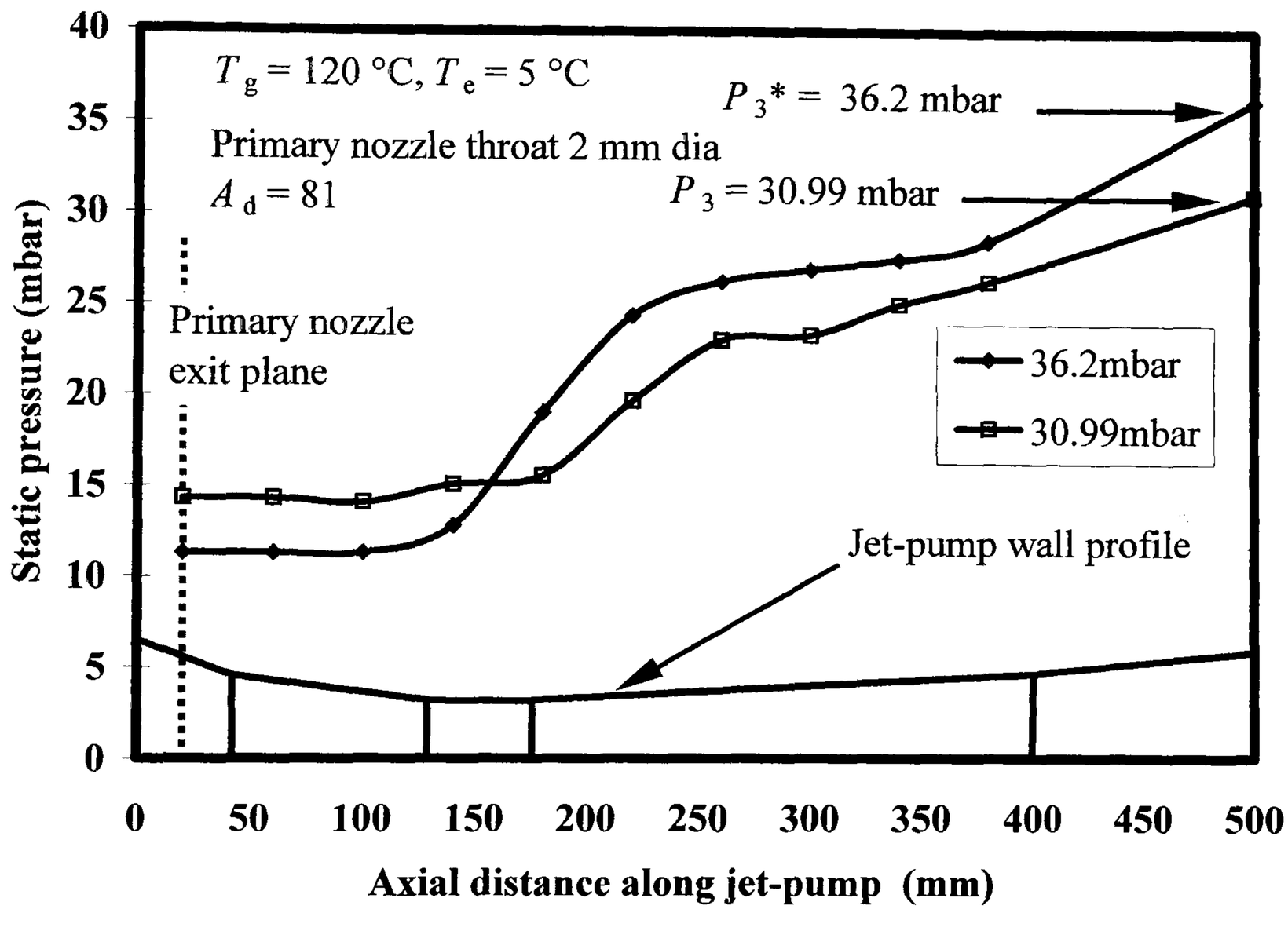

Figure 4.9. Static pressure distribution using Nozzle No 2.

Two pressure distribution curves are presented on the same diagram for comparison. The curve labeled 36.2 mbar showed the results of measurements at the critical condenser pressure. The pressure rise appeared to begin at the entrance to the diffuser throat, as was observed in Figure 4.8. The second curve was measured when the condenser pressure was at 30.99 mbar. The static pressure began to rise further downstream than that found at the critical condenser pressure. It was mentioned in discussing the results from Figure 4.8, that it was thought that the shock wave occurred at the exit from the constant area section, but at condenser pressures below the critical pressure the shock wave is thought to move downstream and into the subsonic diffuser. Figure 4.9 shows that the shock wave does move into the subsonic diffuser where the mixed stream accelerates, increasing the Mach number upstream of the shock and increasing the static

pressure rise across the shock. There is a loss in stagnation pressure across a normal shock wave, thus the strength of the shock increases with position downstream and the losses also increase. The shock wave moves downstream until the static pressure of the mixed stream at the exit of the diffuser is equal to the outlet pressure.

4.6. Variable geometry results

Figure 4.10 shows how the critical pressure lift ratio N_s* changes with diffuser throat area ratio A_d and nozzle pressure ratio N_n.

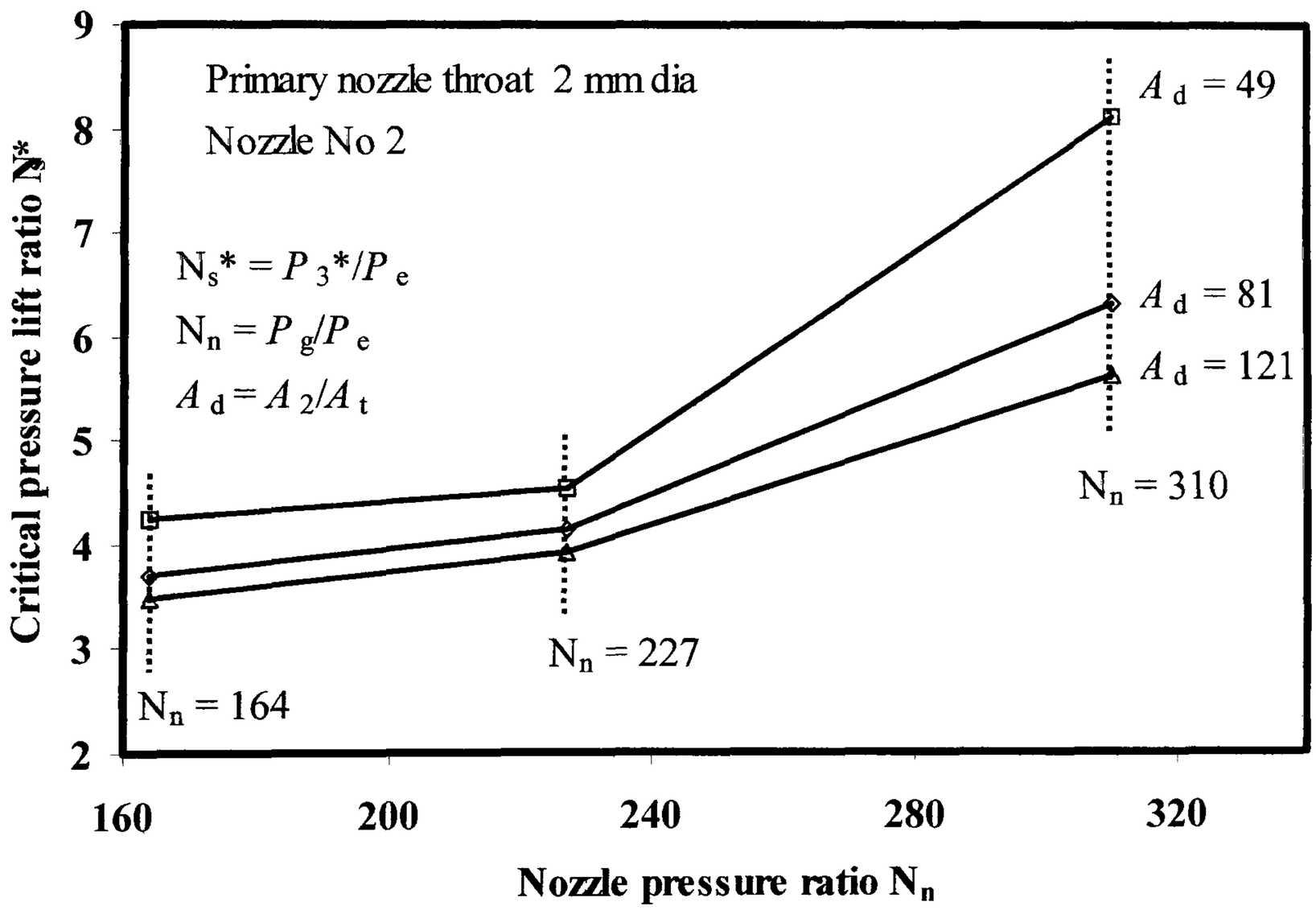

Figure 4.10. Variation in critical pressure lift ratio with nozzle pressure ratio at different diffuser geometries

An increase in A_d at constant N_n allowed an increase in secondary mass flow through the annular area between the primary jet and the wall, increasing entrainment ratio. For constant generator and evaporator conditions, N_s* decreased

with an increase in entrainment ratio because the stagnation temperature at outlet was lower, as can be seen from Equation 4.9, shown again below.

$$T_i + \omega T_o = (1+\omega) T_3 \tag{4.9}$$

The relationship between local Mach number and static temperature and outlet stagnation temperature is given by Equation 4.38.

$$\frac{T_3}{T_1} = 1 + \frac{k-1}{2} \mathrm{M}_1^{\,2} \tag{4.38}$$

Isentropic compression would yield a pressure lift ratio given by Equation 4.39.

$$\frac{P_3}{P_1} = \left(1 + \frac{k-1}{2} \mathrm{M}_1^{\,2}\right)^{\frac{k-1}{k}} \tag{4.39}$$

The actual pressure rise is much less than this because of losses due to friction and the shock process in the constant area section. This shows that the reduction in stagnation temperature because of an increase in entrainment ratio with A_d will cause a decrease in pressure lift ratio. All three geometries were designed to operate at a N_n of 227. As N_n increased from 164 to 227, primary flow also increased. An increase in primary flow entrains more secondary vapour, increasing both entrainment ratio and outlet stagnation temperature. N_s* increased because of the increase in stagnation temperature, but the increase was small because of the increase in entrainment ratio. At the design N_n, the flow through the diffuser throat was choked and secondary flow at a maximum. Further increases in N_n caused an increase in primary flow, but the combined mass flow had reached a maximum, restricting secondary flow and reducing entrainment ratio. An increase in N_n and a decrease in entrainment ratio had the effect of increasing N_s* much more rapidly. An increase in N_n from 227 to 310 at a constant A_d of 81 increased N_s* from 4.153 to 6.308; approximately a 50 % increase in N_s*. N_s* increased from 6.308 to 8.104, as the A_d was reduced from 81 to 49. The restriction in flow at lower A_d allowed the jet-pump to operate at higher ambient conditions, but would result in a decrease in entrainment ratio and cooling capacity.

Figure 4.11 shows the variation in entrainment ratio and pressure lift ratio with changes in A_d at a constant nozzle pressure ratio of 227.

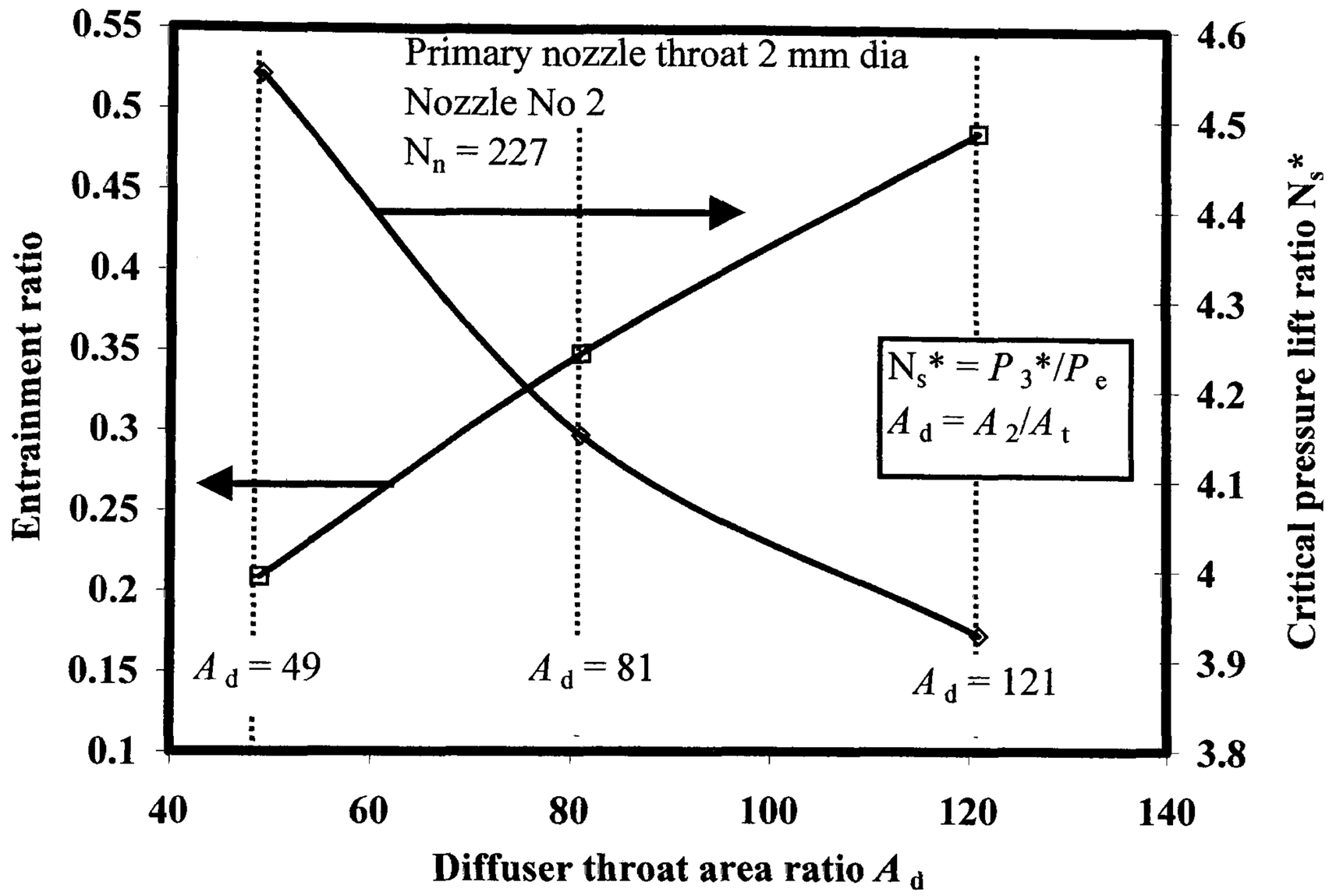

Figure 4.11. Variation in entrainment ratio and critical pressure lift ratio with area ratio

Entrainment ratio appeared to increase approximately linearly with A_d. An increase in A_d from 49 to 121 more than doubles entrainment ratio (2.33 times) and causes a reduction in N_s* by about 15 %. This shows that very small changes in N_s* can substantially increase entrainment ratio and cooling capacity. This was also noticed when chilled water supply temperatures were increased. By increasing A_d from 49 to 81 entrainment ratio increased by about one and a half times, with a consequent reduction in critical pressure of less than 10 %.

If a low-grade heat supply were available 24-hours per day, then the enhancement of cooling capacity by only a small decrease in N_s* could be taken advantage of. A small A_d jet-pump could be designed to deliver cooling of refrigerant-water during the day. A large A_d jet-pump could then be designed to make ice during non-office

hours. The low condensing conditions allow enhanced coolth storage, and discharge of the ice store would reduce the required cooling capacity of the small A_d jet-pump. If the ice store were discharged in response to the building's cooling requirements, then the small A_d jet-pump could operate at approximately constant capacity, thus maximising its performance. The system could consist of two separate jet-pumps and evaporators, where one operates as a jet-pump TIS and the other as a jet-pump refrigerator. The jet-pump TIS system could operate as an encapsulated ice store as will be described in Chapter 6. Alternatively, a single evaporator/ice store could be used to provide cooling of the refrigerant water during the day-time, and have an ice storage capability, as will be described in Chapter 5. Two jet-pumps would operate in parallel; a large A_d jet-pump would be used to provide the ice storage, and a small A_d jet-pump would be used to cool the refrigerant water as in jet-pump refrigeration. During non-office hours, ice could be continually produced on a plate or internal wall, as will be described in Chapter 5. The ice would be occasionally freed from the surface and stored in a vessel under the evaporator. During office hours, the small A_d jet-pump would cool incoming refrigerant-water from the building and direct the chilled water to the ice tank. The coolth stored in the ice tank could be supplied as an ice/brine slurry, thus enhancing the heat transfer coefficient, or as chilled water in a conventional TIS discharge system. Again, the small A_d jet-pump could be optimised by using the ice store to provide variation in output in response to the cooling load.

Figure 4.12 shows the variation in critical pressure lift ratio with primary pressure ratio N_p for changes in jet-pump geometry. The three jet-pump geometries tested were designed to operate at a nozzle pressure ratio N_n of 227, and primary pressure ratio peaked at about that point in all three curves. As N_p was increased, N_s* also increased because the flow was not choked. Entrainment ratio and cooling capacity therefore increased with primary pressure ratio.

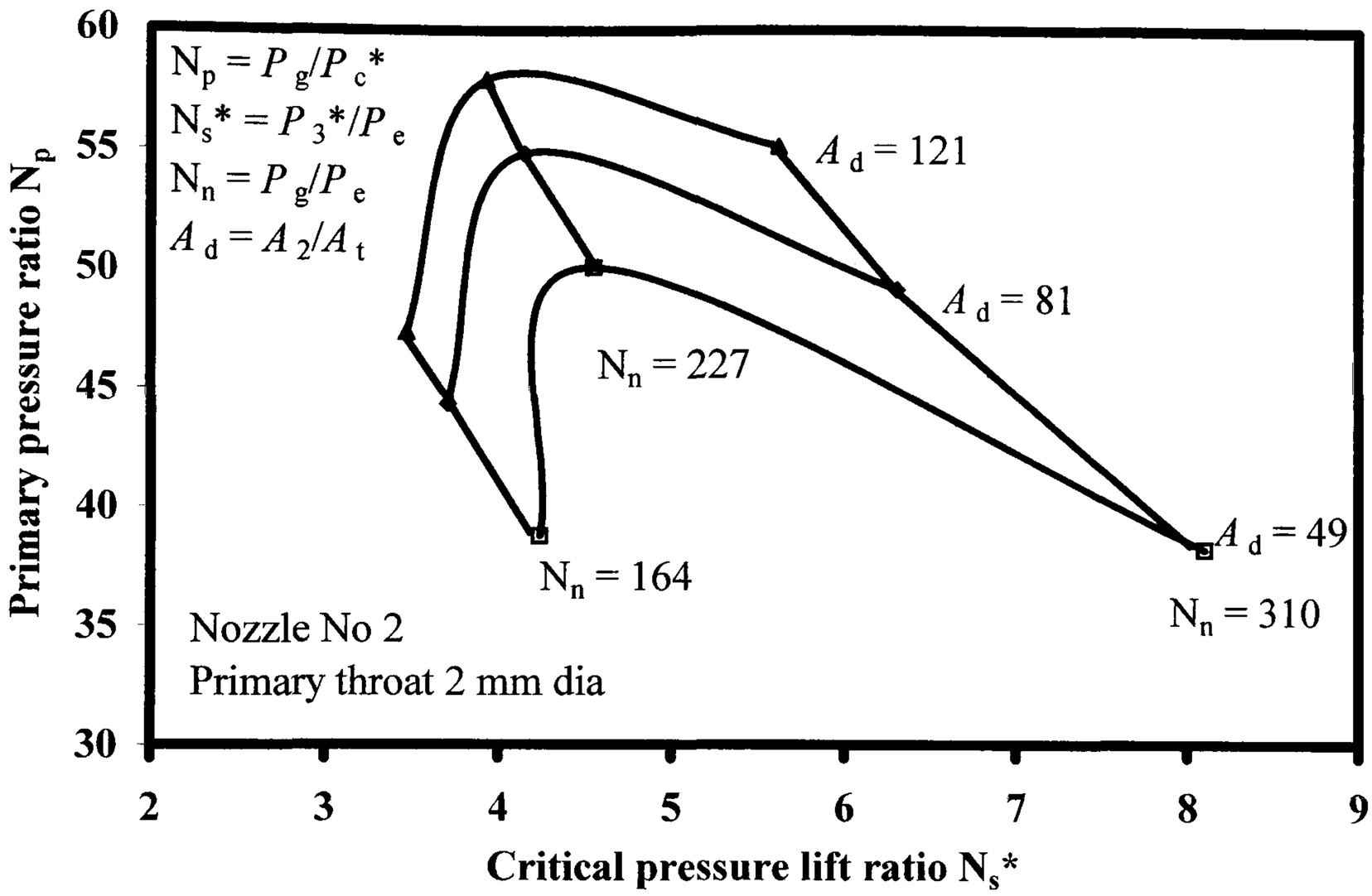

Figure 4.12. Variation in critical pressure lift ratio with primary pressure ratio for three diffuser throat area ratios.

For a constant N_n, an increase in A_d increased entrainment ratio but reduced N_s^*, which caused an increase in N_p. At the design point, the flow through the jet-pump was choked, and primary pressure ratio reached a maximum. Beyond the design point, entrainment ratio decreased because of choking, which caused a rapid increase in N_s^*. This was also seen in Figure 4.11 where there was only a small increase in N_s^* up to the N_n of 227, and then a rapid increase in N_s^* beyond that point.

A single jet-pump would be constrained to operate at the maximum ambient conditions to avoid a loss of action above critical condenser conditions, but if the generator temperature could be varied, then a small increase would allow the jet-pump to operate at higher ambient conditions. The heat input to the generator may be at a fixed temperature, but if it could be varied by as little as 5 °C, then the jet-pump could be under-designed to take advantage of the boost in critical condenser pressure. If the temperature range were between 115 °C and 120 °C then the jet-pump should be designed to operate at the lower temperature. The maximum cooling capacity would be at 115 °C, but if the ambient conditions rose above the

critical point then the generator temperature could be raised by 5 °C, cooling capacity would fall because of choking, but the critical condenser pressure would increase by about one and a half times. A disadvantage of designing a jet-pump to operate at a lower nozzle pressure ratio is that cooling capacity and COP are less than the optimum, but a small difference allows a large margin of error and the system can respond to higher than normal ambient temperatures.

4.7. Discussion

The results from Figures 4.4 and 4.7 showed that a possible control strategy for jet-pump refrigerators would be to allow the chilled water temperature to rise, which would increase entrainment ratio and cooling capacity, and decrease the critical pressure lift ratio. This is not an option in jet-pump TIS systems because the evaporator saturation conditions will be approximately constant whilst a change of phase is taking place. The principle of enhancing jet-pump performance by increasing evaporator conditions and reducing critical pressure lift ratio was used by Sokolov and Hershgal [35] to boost the COP of a jet-pump refrigerator. A compressor was used to boost the suction pressure of the jet-pump cycle to an intermediate pressure between the evaporator and condenser pressures. The jet-pump, therefore, had the advantage of operating at a higher evaporator pressure and a lower pressure lift ratio. Water is the refrigerant in the steam jet-pump TIS system, but compression enhancement is not practicable because of the high specific volume at low pressures. However, if the jet-pump were to pump low-pressure vapour to an intermediate pressure then the entrainment ratio would be increased because of the low pressure lift ratio. Another system in series with the jet-pump could then complete the compression to the desired outlet pressure. It was shown in the literature survey that water vapour-compression systems, such as a radial type described by Andersen and Fleming [27], could be used for evaporative freezing. A jet-pump could reduce the electrical energy input to the system by reducing substantially the compression ratio of the compressor and increasing the suction pressure, so reducing the power requirement. The reduction

in the jet-pump pressure lift ratio then allows it to operate at a higher entrainment ratio and COP, thus reducing the heat input requirement from the generator. A heat driven vapour absorption system such as lithium bromide/water, described by Eames and Aphornatana [41], could boost the performance of a jet-pump TIS system. Lithium bromide/water systems are limited to operating above the freezing point, but the system could be used as a second stage of a heat driven TIS system. If it is assumed that the jet-pump TIS system saturation pressure was at approximately 500 Pa and the intermediate pressure was 1227 Pa then the critical pressure lift ratio would be approximately 2.5 and an entrainment ratio of 0.8 could be achieved. The entrainment ratio of a jet-pump TIS system operating between an evaporator/ice store and a condenser during ice storage would be between 0.1 and 0.3, therefore, the average entrainment ratio could be boosted by around four times, so increasing the cooling capacity of the evaporator/ice store.

4.8. Conclusions

In this chapter, the jet-pump test rig was calibrated to find its operational characteristics. The results were used to analyse the performance at part-load conditions, make recommendations on improving and optimising jet-pump refrigeration systems, and apply that information to the TIS system.

If the generator temperature could be varied over a small range, then the jet-pump should be under-designed so that when the peak cooling load and peak condenser operating conditions are at a maximum, any increase in ambient temperature above the design point could be met by a small increase in generator temperature.

If the chilled water supply temperature could be varied, than it should be at the maximum when the peak cooling load occurs in order to take advantage of a higher entrainment ratio. At part-load, the chilled water supply temperature can be allowed to decrease, so reducing the cooling capacity of the jet-pump. A variation

in entrainment ratio of between 20 % and 50 % could be achieved depending on the temperature range.

The two simple strategies described above, allow the jet-pump to meet variations in cooling load and ambient conditions over a small temperature range compared to the whole cooling season and will be over-sized at times other than the peak. The cooling capacity can be doubled for only a 10 % reduction in critical pressure lift ratio, by operating a jet-pump with a larger diffuser area ratio. As peak cooling demand occurs over a small proportion of the total cooling cycle, whether daily or over a cooling season, performance at part-load is enhanced. This is in contrast with vapour-compression systems, which have to be designed to meet the peak cooling requirements but are operating at part-load for most of the time. A jet-pump system is therefore, more compatible with a building's cooling cycle, and the control strategy of varying generator temperature over a small temperature range and operating jet-pumps of different capacities in response to ambient temperature changes is simple.

The conclusions made about variations in generator temperature and geometry can be applied directly to jet-pump TIS because they involve varying generator temperature and geometry to give a flexible response to changes in cooling requirements and ambient conditions. It was also proposed that the increase in cooling capacity with chilled water temperature could be applied to a fixed temperature system such as in TIS, by employing an intermediate system between the evaporator and condenser; the closer the intermediate temperature is to the evaporator the higher the cooling capacity. Which is analogous to increasing the cooling capacity by raising the chilled water temperature.

Tests were carried out on two primary nozzles to examine the effect of over-expansion of the primary jet on the performance of the jet-pump. The performance of the over-expanded nozzle was inferior in terms of both entrainment ratio and pressure lift ratio.

Chapter 5. Spray ice TIS

5.1. Introduction

Spray ice TIS has three novel features. The use of low-grade heat to store ice for comfort cooling applications, the coupling of a jet-pump with an ice store using an evaporative freezing process, and nucleation and ice formation on a vertical surface. The first feature is a general application that could reduce the pollution attributable to the comfort cooling of a building, but its use, in practice, would be dependent on the successful operation of the second two features.

The performance parameters that will be used to analyse the spray ice TIS system are coolth storage rate, cooling capacity and system COP. Coolth storage rate is directly related to jet-pump secondary flow, and so its performance can be determined in terms of ice storage rate. Cooling capacity can be used to compare spray ice TIS with encapsulated ice TIS systems, and COP can be used to compare the jet-pump TIS system with other ice storage and cooling systems. This chapter initially describes the simplifying assumptions and the models used in establishing the performance parameters. The experimental method is then described and the test results presented.

5.2.1. Spray ice TIS

When a liquid enters a vessel which is at a pressure lower than the equilibrium saturation vapour pressure, a small proportion of the liquid is flashed off as vapour, causing the rest of the liquid to cool to the saturation temperature of the surrounding vapour. The principle of flash evaporation was used to cool water in the evaporator to below its equilibrium freezing temperature, and so create a thermal ice store. It was estimated that the flight time of the droplets between exit from the spray nozzle and the impact on the evaporator wall would be too short for

freezing to take place, so nucleation and ice crystal growth after impact was assumed to be the more likely process. This assumption was tested during the project.

5.2.2. Flash evaporative cooling

Liquid-water enters the evaporator/ice store through a spray nozzle that breaks the liquid into a fine mist of small droplets, enhancing the surface area available for heat and mass transfer. Figure 5.1 shows a single liquid droplet in surrounding vapour. A force balance on a single liquid droplet on an equatorial plane gives

$$\frac{\pi d^2}{4}\Delta P = \pi d\sigma \tag{5.1}$$

$$\Delta P = \frac{4\sigma}{d} \tag{5.2}$$

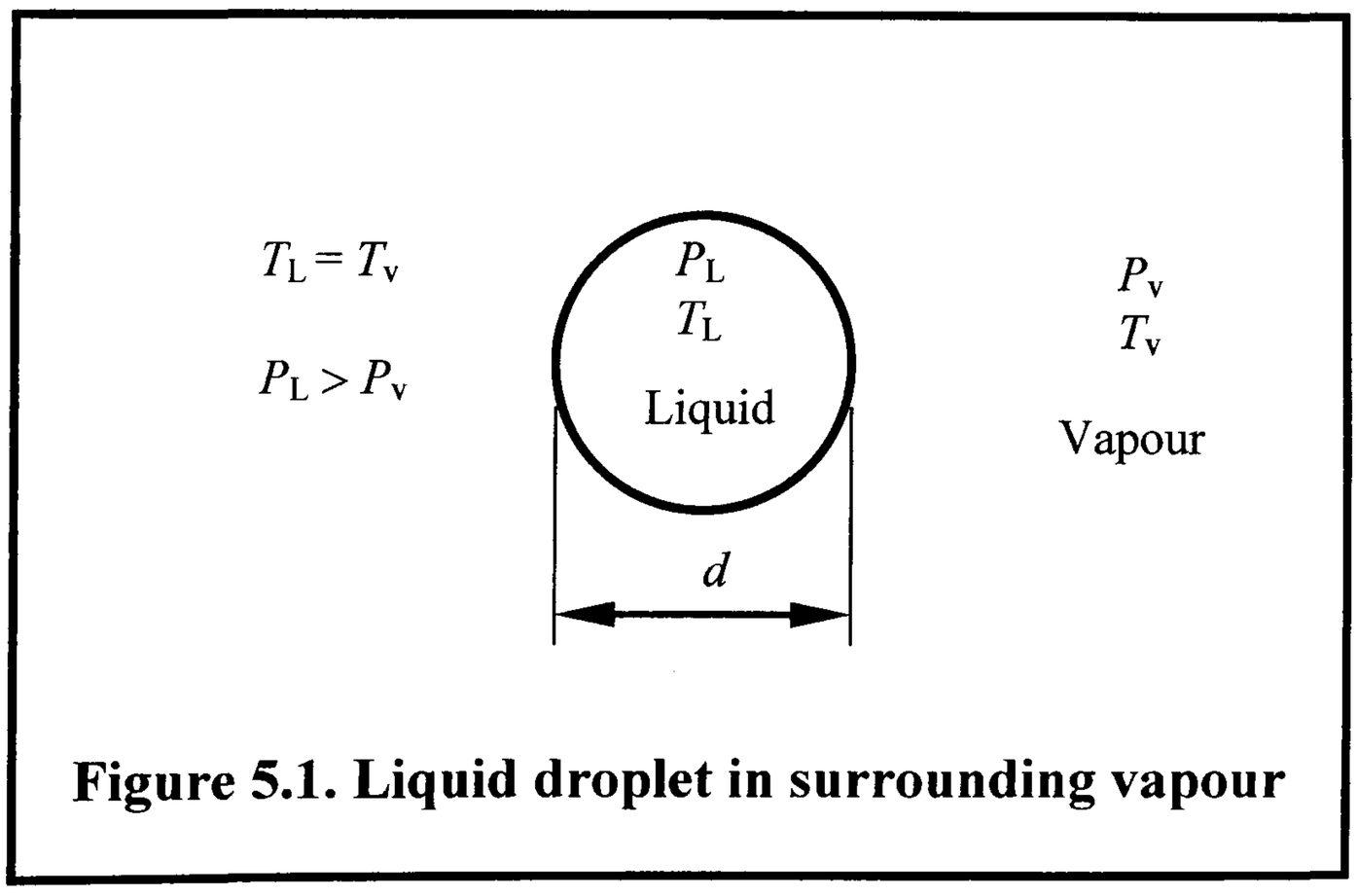

Figure 5.1. Liquid droplet in surrounding vapour

where ΔP is the excess pressure of the liquid droplet with respect to the vapour pressure, σ is the surface tension and d is the droplet diameter. If a single liquid droplet is in thermal equilibrium ($T_L = T_v$) with the surrounding vapour, then it must be supercooled with respect to the saturation temperature of the droplet because of the difference in pressure. When the liquid droplet enters the evaporator/ice store, it is not in thermal equilibrium because the temperature of the

liquid is greater than the saturation temperature in the evaporator. The pressure difference between the liquid droplet and the surrounding vapour drives the evaporation process and causes sensible cooling of the droplet, but the flow through the nozzle will produce a variation in droplet sizes, causing differences in ΔP and evaporation rates. It is assumed that the mean size distribution of the droplets produces an average evaporation rate, and that this value causes the rest of the liquid-water from the spray nozzle to be cooled sensibly by an amount ΔT.

It is assumed the freezing of the liquid in the evaporator is achieved adiabatically, as described by Eames *et al* [51]. It follows that the sensible cooling undergone by the liquid-water will be equal to the latent cooling due to evaporation.

$$h_{\mathrm{fg}}\,\dot{m}_{\mathrm{e}} = \dot{m}_{w}\,C_{\mathrm{pw}}\Delta T \tag{5.3}$$

where $\dot{m}_{\mathrm{e}}$ is the mass evaporation rate, $\dot{m}_{\mathrm{w}}$ is the mass flow of liquid-water cooled by evaporation, h_{fg} is the latent heat of vaporisation, C_{pw} is the specific heat capacity of liquid-water and ΔT is the difference in temperature between the liquid entering the evaporator and the saturation temperature of the surrounding vapour.

A mass balance on the spray nozzle flow shows that the mass flow leaving the nozzle is equal to the sum of the mass flow impacting on the wall and the evaporation rate.

$$\dot{m}_{\mathrm{spray}} = \dot{m}_{\mathrm{w}} + \dot{m}_{\mathrm{e}} \tag{5.4}$$

where is $\dot{m}_{\mathrm{spray}}$ the flow leaving the spray nozzle. Solving for in $\dot{m}_{\mathrm{e}}$ Equation 5.3 and substituting back into Equation 5.4 gives;

$$\dot{m}_{\mathrm{spray}} = \dot{m}_{\mathrm{w}}\left(1+\frac{C_{\mathrm{pw}}\Delta T_{\mathrm{F}}}{h_{\mathrm{fg}}}\right) \tag{5.5}$$

Eames *et al* [51] performed an energy balance on a unit mass of liquid-water arriving at the surface of the evaporator in a supercooled condition undergoing adiabatic freezing, giving

$$\dot{m}_{\mathrm{i}}\,h_{\mathrm{if}} = \dot{m}_{\mathrm{i}}\,C_{\mathrm{i}}\Delta T_{\mathrm{F}} + (\dot{m}_{\mathrm{w}} - \dot{m}_{\mathrm{i}})C_{\mathrm{pw}}\Delta T_{\mathrm{F}} \tag{5.6}$$

where $\dot{m}_i$ is the ice storage rate, h_{if} is the latent heat of ice fusion, C_i is the specific heat capacity of ice, and ΔT_F is the degree of supercooling, defined as the difference between the equilibrium freezing temperature T_F and the vapour saturation temperature T_v. Rearranging in terms of the mass flow of water gives;

$$\dot{m}_w = \frac{\dot{m}_i (C_{pw} - C_i)\Delta T_F}{C_{pw}\Delta T_F} \tag{5.7}$$

Substituting back into Equation 5.5 gives;

$$\dot{m}_{spray} = \frac{\dot{m}_i (C_{pw} - C_i)\Delta T_F}{C_{pw}\Delta T_F}\left(1 + \frac{C_{pw}\Delta T_F}{h_{fg}}\right) \tag{5.8}$$

Rearranging in terms of the ratio of the ice storage rate to the mass flow leaving the spray nozzle gives;

$$\frac{\dot{m}_i}{\dot{m}_{spray}} = \frac{C_{pw}\Delta T_F}{\left(1 + \frac{C_{pw}\Delta T_F}{h_{fg}}\right)\left(h_{if} + \left(C_{pw} - C_i\right)\Delta T_F\right)} \tag{5.9}$$

Eames et al [52] showed that for constant spray nozzle flow, the ice storage rate increased with the degree of supercooling undergone by the liquid-water.

5.2.3. Cooling capacity

Under adiabatic vacuum freezing conditions the coolth stored as ice is equal to the latent cooling due to evaporation, thus

$$\dot{m}_i h_{if} = \dot{m}_e h_{fg} \tag{5.10}$$

Substituting thermodynamic values at 0 °C into Equation 5.10 gives

$$\dot{m}_i = \frac{2500}{333.5}\dot{m}_e \tag{5.11}$$

$$\dot{m}_i = 7.5\,\dot{m}_e \tag{5.12}$$

The coolth stored is given by Equation 5.13,

$$\dot{Q}_i = \dot{m}_i h_{if} \tag{5.13}$$

It will be assumed that the spray ice TIS system is used in phase with a building's cooling requirements, so that ice is being continually manufactured and its coolth discharged. Therefore, the cooling capacity will be

$$Q_{\mathrm{i}} = \dot{Q}_{\mathrm{i}}\,\Delta t \tag{5.14}$$

where Δt is the time duration of jet-pump operation.

5.2.4. Coefficient of performance

The coefficient of performance of a jet-pump TIS system can be determined by measuring either jet-pump or ice storage characteristics. The coefficient of performance of the jet-pump is the ratio of the evaporator cooling load to the total heat and work input.

$$\mathrm{COP} = \frac{\dot{Q}_{\mathrm{e}}}{\dot{Q}_{\mathrm{g}} + \dot{W}} \tag{5.15}$$

Where Q_{e}, Q_{g} and W are the evaporator cooling load, the heat input to the vapour generator and the work input of pumps and fans, respectively. The work input is usually neglected because it is small compared to the heat input to the generator. In the spray ice TIS system there is no cooling load, but evaporation below the triple point temperature causes a change of phase to ice, thus the COP can be determined for the TIS system by measuring the coolth storage rate.

$$\mathrm{COP} = \frac{\dot{Q}_{\mathrm{i}}}{\dot{Q}_{\mathrm{g}}} \tag{5.16}$$

It is assumed that the saturation conditions in the evaporator/ice store approach steady-state because evaporative cooling below the triple point temperature causes the release of latent heat during ice formation at a constant temperature.

During adiabatic evaporative freezing, the coolth stored is assumed to be approximately equal to the cooling due to evaporation because of the steady-state

assumption. An alternative description of COP in terms of evaporation rates can be used.

$$\mathrm{COP} = \frac{\dot{m}_{\mathrm{e}}\, h_{\mathrm{fg}}}{\dot{Q}_{\mathrm{g}}} \tag{5.17}$$

It is assumed that the generator is maintained at a constant temperature, providing approximately constant primary mass flow, therefore, the maximum heat input to the generator would occur if condensate were fed back to the generator at the same rate as the primary flow. The heat required to raise steam from the saturated liquid temperature of the condensate to the saturated vapour temperature of the generator is thus given by Equation 5.18.

$$\dot{Q}_{\mathrm{g}} = \dot{m}_{\mathrm{p}}\left(h_{\mathrm{g},T\mathrm{g}} - h_{\mathrm{f},T\mathrm{c}}\right) \tag{5.18}$$

where $\dot{m}_{\mathrm{p}}$ is the primary mass flow. $h_{\mathrm{g},T\mathrm{g}}$ and $h_{\mathrm{f},T\mathrm{c}}$ were defined in Chapter 4.

$$\mathrm{COP} = \frac{\dot{m}_{\mathrm{e}}\, h_{\mathrm{fg}}}{\dot{m}_{\mathrm{p}}\left(h_{\mathrm{g},T\mathrm{g}} - h_{\mathrm{f},T\mathrm{c}}\right)} \tag{5.19}$$

Secondary flow will be approximately equal to the evaporation rate, under the steady-state assumption. Therefore, the evaporation rate is replaced by secondary flow in Equation 5.19 to give

$$\mathrm{COP} = \frac{\dot{m}_{\mathrm{s}}}{\dot{m}_{\mathrm{p}}} \frac{h_{\mathrm{fg}}}{\left(h_{\mathrm{g},T\mathrm{g}} - h_{\mathrm{f},T\mathrm{c}}\right)} \tag{5.20}$$

The ratio of secondary to primary mass flow was defined in Chapter 4 as the entrainment ratio, thus the performance of the jet-pump TIS system can be estimated by measuring mass flows, and comparisons with ice storage measurements can be made.

$$\mathrm{COP} = \omega \frac{h_{\mathrm{fg}}}{\left(h_{\mathrm{g},T\mathrm{g}} - h_{\mathrm{f},T\mathrm{c}}\right)} \tag{5.21}$$

The assumption that secondary flow can be used to determine ice storage characteristics was examined during testing.

5.3. Spray ice TIS test results

The objective of testing the spray ice TIS system was to determine its performance characteristics at the design point and at part-load, to examine the simplifying assumptions made in modeling the process, and analyse its practicability as an ice storage system. This chapter describes the experimental method and the results of the tests.

5.3.1. Experimental method

Before testing, the rig shown in Figure 3.2, was evacuated by a vacuum pump to remove non-condensable gases. After evacuation, the heaters were switched on until the water in the generator reached the desired test temperature. The water levels in the evaporator and generator and the initial evaporator liquid and vapour temperatures were noted. The stop valve (f) in the condenser line was opened so that water could flow through the condenser cooling coils, then the circulation pump (22) was started. Once the flows were at steady-state the stop valve to the primary nozzle (j) was opened and a stop-watch started to record the time interval. Temperatures and pressures were recorded every two minutes and the time when the vapour and liquid temperatures reached 0 °C and ice began to form was noted. Testing continued as ice built up on the wall of the vessel until the water level in the evaporator reached a lower limit. The valve to the primary nozzle was then shut, and the re-circulation pump switched off. The water level in the evaporator and time were then recorded. The water level was once again recorded when all of the ice had melted. The time duration between the beginning of freezing and the end of the test, and height difference gave an estimate of the ice storage rate. The level in the generator sight glass was recorded at various intervals during ice storage and an estimate of primary mass flow was made from the height difference, time interval and a calibration coefficient. An estimate of ice storage rate enabled the cooling capacity to be determined, and measurement of primary flow provided an estimate of generator heat input so that the COP of spray ice TIS

could be determined. This section describes the results of samples taken from the test rig and the performance of the jet-pump ice store that was estimated from them.

5.3.2. Ice storage rate

The results of experimental measurements of ice storage rate during spray ice TIS are shown in Figure 5.2.

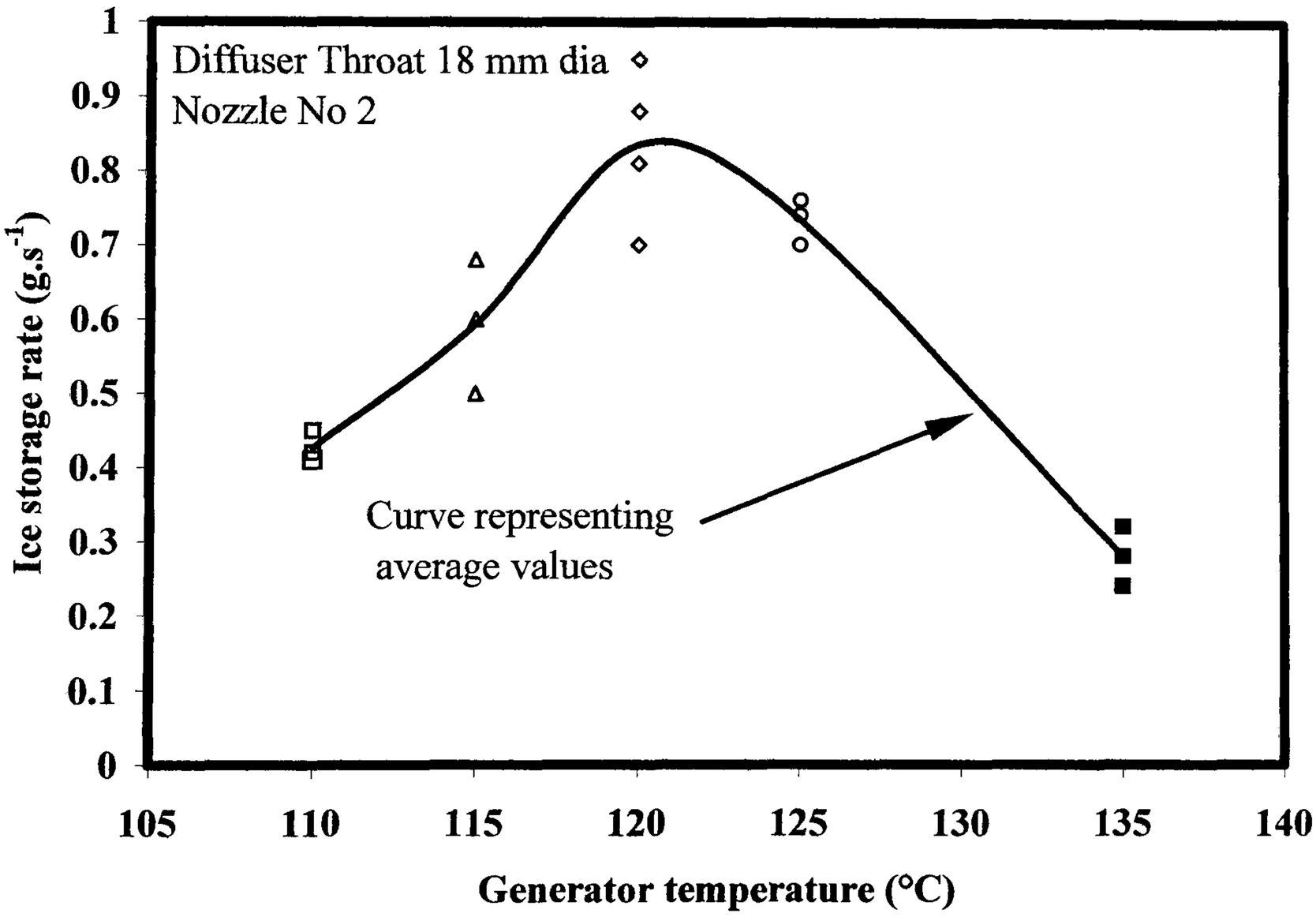

Figure 5.2. Variation in ice storage rate with generator temperature at a spray nozzle flow of 10.1 $g.s^{-1}$

The diagram shows that ice storage rates varied with generator temperature and that they reached a maximum at around 120 °C. The average ice storage rate at a generator temperature of 120 °C was 0.84 $g.s^{-1}$. The ice storage rate peaks at approximately

120 °C because secondary flow is choked at this point. The effect of choking was observed when discussing the part-load performance of jet-pumps in Chapter 4. As the generator saturation temperature increases from 110 °C to 120 °C both primary and secondary flow increase, causing an increase in ice storage rates. At 120 °C the combined primary and secondary flow that can pass through the diffuser throat has reached a maximum, as shown by the peak in ice storage rates. Beyond this point, primary flow increases but secondary flow falls off rapidly because of choking, as seen from the ice storage rate values. Figure 5.2 showed that the ice storage rate is dependent on secondary flow, and therefore, will always be at a maximum at the choked condition.

Table 5.1. Ice storage rate, standard error and range at a spray nozzle flow of 10.1 $g.s^{-1}$.

T_g (°C)	110	115	120	125	135
	0.42	0.5	0.7	0.7	0.24
	0.45	0.6	0.88	0.74	0.32
	0.41	0.68	0.81	0.76	0.28
			0.95		
Average ($g.s^{-1}$)	0.43	0.59	0.84	0.73	0.28
Standard error ($g.s^{-1}$)	0.05	0.22	0.21	0.08	0.10
Range ($g.s^{-1}$)	0.04	0.18	0.25	0.06	0.08

Table 5.1 shows the data presented in Figure 5.2 and lists the average ice storage rates, the standard error and the range of these data. At a generator temperature of 120 °C the percent standard error was ± 25 % and the range was 36 % of the minimum value. The experimental results show that nucleation and ice storage on a vertical surface was successful and repeatable, but there was a large data spread. There were thought to be two main causes of the large spread of data. Errors due to uncertainties introduced by the method of sampling, and actual differences in ice storage rate due to variations in saturation conditions. The time duration of each test differed and so there may have been variations in ice storage rates due to these differences. The raw data are presented in Appendix F. At a generator saturation temperature of 120 °C and ice storage rates of 0.7 $g.s^{-1}$, 0.88 $g.s^{-1}$

0.81 $g.s^{-1}$ and 0.95 $g.s^{-1}$, the water levels measured after melting were 45 mm, 55 mm, 19 mm and 12 mm, respectively. The uncertainty of the first two samples is approximately 2 % but the difference in ice storage rate is 25 %. The uncertainty increases for the third and fourth samples to between 5 % and 8 %. If the spread of data were mainly because of the difference in height then the first two samples would be close and the latter two would cause the spread of data, but the data show that the spread does not depend on the difference in height measurement. A second source of uncertainty in the sampling method was due to a short delay between stopping the test and measuring the level. The steam flow to the jet-pump was cut off and insulation was partly removed to enable measurement of the height of the liquid-water, causing rapid melting. Any delay in measurement increased inaccuracies in the ice storage rate calculations, but the time lapse was approximately constant, and so the error introduced would be relative to the uncertainty of each sample. Again, the uncertainty would be reduced over the longer test duration, but the spread of data is large compared to the uncertainty.

The rate of ice formation is dependent on the evaporation rate, assuming adiabatic evaporative freezing, and this is dependent on the secondary flow induced by the jet-pump. Equation 5.22 shows that secondary flow is proportional to stagnation pressure and inversely proportional to the square root of stagnation temperature.

$$\dot{m}_s \alpha \frac{P_o}{\sqrt{T_o}} \tag{5.22}$$

As the temperature in the evaporator reaches the freezing point of water, ice begins to form on the inner surface of the vessel. The saturation pressure continues to fall until the evaporation rate and secondary flow become approximately equal, and a steady-state is established. If the steady-state evaporator saturation pressure and temperature varies with each test then the average ice storage rate will also vary. It is thought that this is the main cause for the spread of data.

During testing it was found that higher ice storage rates were obtainable when the flow through the spray nozzle was reduced. Tests were originally carried out at a

maximum spray nozzle flow of 10.1 $g.s^{-1}$, but the average ice storage rate increased to 1.12 $g.s^{-1}$ at a spray nozzle flow of 9 $g.s^{-1}$. Figure 5.3 shows the change in ice storage rate at a spray nozzle flow of 9 $g.s^{-1}$. This shows that the average ice storage rate was increased by approximately 33 % when the flow through the spray nozzle was reduced to 9 $g.s^{-1}$.

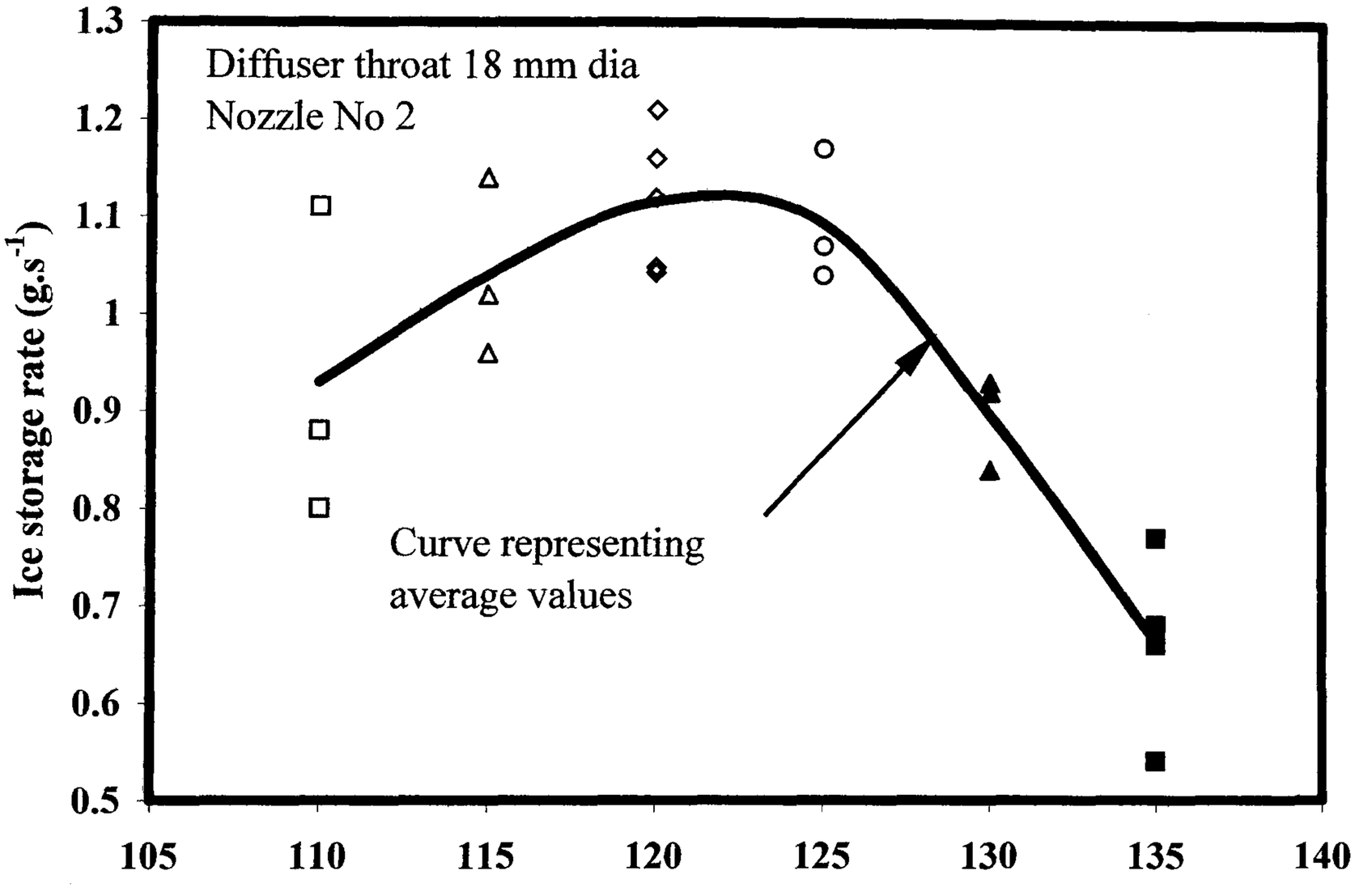

Figure 5.3. Variation in ice storage rate with generator temperature, at a spray nozzle flow of 9 $g.s^{-1}$

Table 5.2 shows the ice storage data presented in Figure 5.3, together with the average value, the standard error and the range of the experimental results at a spray nozzle flow of 9 $g.s^{-1}$. Again, the results show a large spread of data about the average and a large range. At a generator temperature of 120 °C the percent standard error was ± 6 % and the range was 15 % of the minimum value. The error and range of the data were smaller compared with the data from testing at a spray nozzle flow of 10.1 $g.s^{-1}$.

Table 5.2. Ice storage rate, standard error and range at a spray nozzle flow of 9 $g.s^{-1}$						
T_g (°C)	110	115	120	125	130	135
	1.11	0.96	1.21	1.17	0.93	0.54
	0.8	1.14	1.05	1.04	0.84	0.77
	0.88	1.02	1.16	1.07	0.92	0.66
			1.04			0.68
			1.12			
Average ($g.s^{-1}$)	0.93	1.04	1.12	1.09	0.89	0.66
Standard error ($g.s^{-1}$)	0.39	0.22	0.072	0.21	0.21	0.16
Range ($g.s^{-1}$)	0.31	0.18	0.17	0.13	0.09	0.23

Analysis of the data presented in Table 5.1 indicated that errors in the measurement of water level were small compared to the experimental error and range of the data. It was noticed that the cooling of the liquid-water in the evaporator/ice store from the initial steady-state temperature at the start of the test, to the freezing point temperature was more rapid during testing at a spray nozzle flow of 10.1 $g.s^{-1}$. If the rate of cooling is more rapid then it is possible that the saturation pressure at which the steady-state condition is established will vary as shown by the results. However, if as is assumed, the rate of cooling is reduced then the establishment of a steady-state condition will be more consistent. This is seen in Figure 5.3 in a range of generator saturation temperatures from 115 °C to 130 °C. At generator temperatures of 110 °C and 135 °C the percent relative errors increase to between 30 % and 40 %, which is consistent with a variation in saturation conditions during each test. The corresponding data in Figure 5.2 appears to have a lower spread but the average ice storage rate is lower and so the percent relative errors are between 12 % and 35 %. A further factor that may effect the spread of the data with respect to the saturation conditions is the assumption that, under adiabatic evaporative freezing conditions, approximately 7.5 kg of ice would be formed per kg of liquid-water evaporated, as described by Equation 5.12, shown gain below.

$$\dot{m}_i = 7.5\dot{m}_e \tag{5.12}$$

Assuming that secondary flow is approximately equal to the evaporation rate during ice storage, then a small difference in secondary flow due to differences in

saturation conditions would magnify the difference in the ice storage rate by a factor of 7.5. This would lead to a large spread of ice storage data for only a small difference in secondary flow.

If the ice storage rate is dependent on spray nozzle flow as shown by the results then the system may vary over the operational life of such plant because of pump wear, the fouling of pipes and fittings and the blockage of nozzles. The variation in ice storage rate would make ice production by spray ice methods impractical because of the variation in ice storage rates for the same nominal spray nozzle flow.

The performance of the jet-pump spray ice TIS system was determined from the averages of the ice storage rate data in order to analyse its average performance and compare it with the encapsulated ice TIS system described in Chapter 6.

5.3.3. Evaporative freezing analysis

The average ice storage rates and spray nozzle flows were entered into Equation 5.9 in order to obtain an estimate of the degree of supercooling undergone by the liquid-water and the saturation temperature in the evaporator/ice store.

Thermodynamic values at 0 °C were substituted into Equation 5.9 to give,

$$\frac{\dot{m}_{\mathrm{i}}}{\dot{m}_{\mathrm{spray}}} = \frac{4.21\Delta T_{\mathrm{F}}}{\left(1+\frac{4.21\Delta T_{\mathrm{F}}}{2500}\right)(333.5+2.24)\Delta T_{\mathrm{F}}} \tag{5.23}$$

Solving for the degree of supercooling, and substituting the measured ice storage rate at a spray nozzle flow of 9 $g.s^{-1}$ suggests that the droplets were supercooled to a saturation temperature of -11 °C. At a spray nozzle flow of 10.1 $g.s^{-1}$, the solution to Equation 5.23 suggests that the droplets were supercooled to a saturation temperature of approximately -6 °C. This shows that the coolth storage rate increases with a decrease in saturation conditions, but it is well known that the

performance of the jet-pump decreases with saturation conditions. The results show that adiabatic evaporative freezing of the liquid droplets, as described by Eames *et al* [52], does not adequately model the freezing process during spray ice TIS.

Flash evaporation is commonly used in jet-pump refrigeration systems because the droplets produced by the spray jet present a large surface area for evaporation, heat transfer is by direct contact between the liquid droplets and the surrounding vapour, and only a small percentage of the water is evaporated to cool the remainder. It was thought that flash evaporation provided the main cooling effect in the spray ice TIS system and so Equation 5.9 was derived.

When the supercooled droplets impact on the vessel wall they coalesce and form a falling film. Ice crystals nucleate and grow, producing a layer of ice at the vertical surface. As the latent heat is released, the falling film reverts to the equilibrium freezing temperature. No further ice formation can occur unless there is additional evaporation to the surroundings. However, the falling film presents a large surface area for further evaporation, therefore it is subsequently assumed that evaporation from both the spray nozzle flow and the falling film contribute to the coolth stored as ice.

Figure 5.5 shows the variation in temperature and vapour pressure in the evaporator/ice store at a spray nozzle flow of 9 $g.s^{-1}$. At the start of ice formation the saturation pressure in the evaporator was assumed to be at the triple point pressure 611 Pa (T_{sat} = 273 K), but the total pressure was approximately 740 Pa because of non-condensable gases in the evaporator. At the end of the test the measured vapour pressure was approximately 550 Pa (T_{sat} = 271.7 K), and it was assumed that this represented the saturation pressure, because of the removal of non-condensable gases during the test. This value was entered into Equation 5.24, below, to give an estimate of the ice storage rate attributable to evaporative freezing from the supercooled droplets.

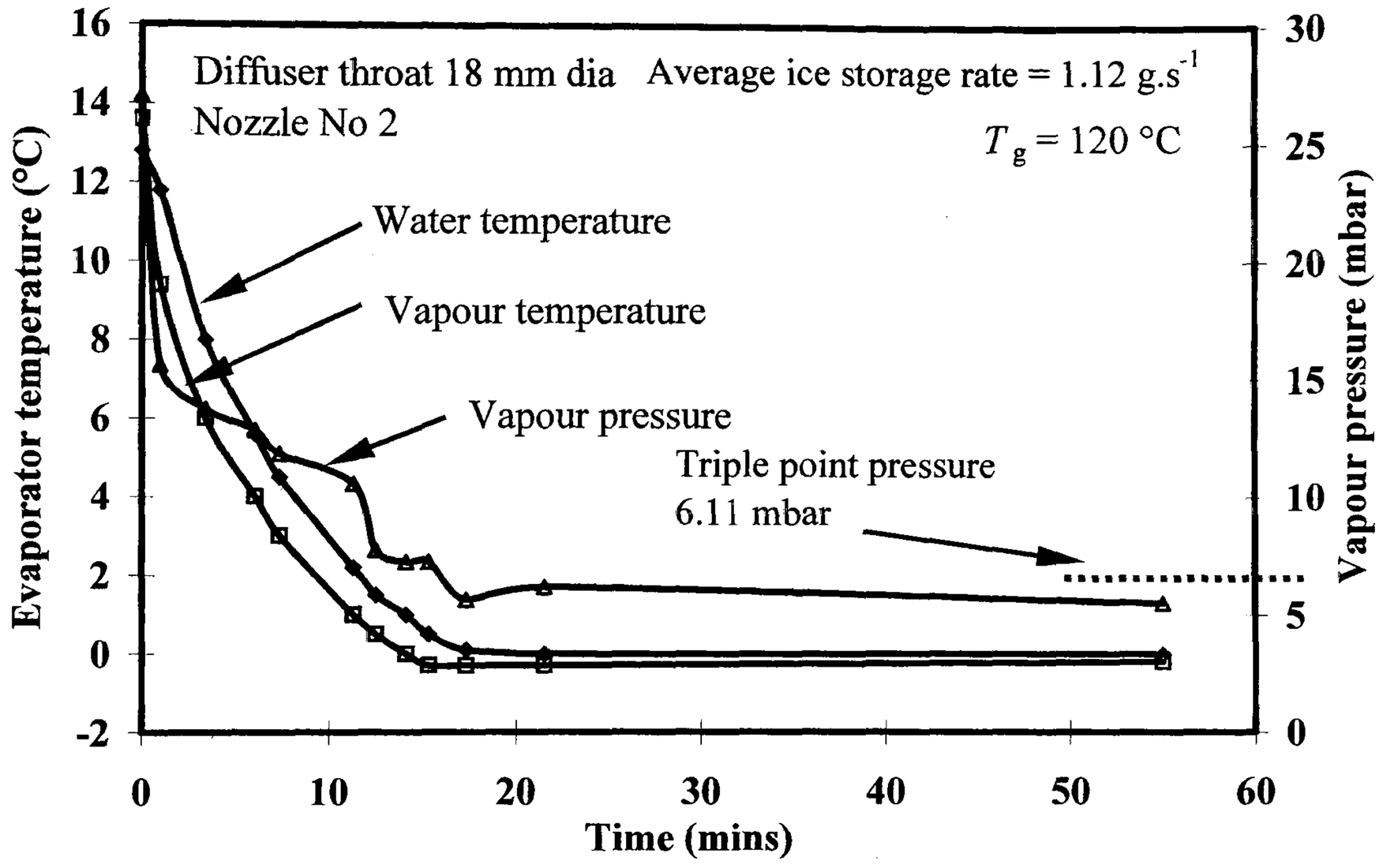

Figure 5.4. Variation in evaporator temperature and vapour pressure with time at a spray nozzle flow of 9 g.s^{-1}.

$$\dot{m}_i = \frac{\dot{m}_{spray} \times 4.21 \Delta T_F}{\left(1 + \frac{4.21 \Delta T_F}{2500}\right)(333.5 + 2.24)\Delta T_F} \tag{5.23}$$

$$\dot{m}_i = \frac{9 \times 10^{-3} \times 4.21 \times 1.3}{\left(1 + \frac{4.21 \times 1.3}{2500}\right)(333.5 + 2.24) \times 1.3}$$

$$\dot{m}_i = 0.113 \text{g.s}^{-1}$$

The estimated rate of ice formation due to evaporation from the supercooled droplets was approximately 9 % of the total found experimentally. This indicates that most of the ice formed during spray ice TIS testing was due to evaporation from the falling film.

5.3.4. Coolth storage rate

The average coolth storage rate was calculated to enable the results to be compared with encapsulated ice TIS, and is given by Equation 5.13,

$$\dot{Q}_{\mathrm{i}} = h_{\mathrm{if}}\, \dot{m}_{\mathrm{i}} \tag{5.13}$$

At a spray nozzle flow of 10.1 $g.s^{-1}$ the average ice storage rate was 0.835 $g.s^{-1}$. Therefore,

$$\dot{Q}_{\mathrm{i}} = 333.5 \times 0.835$$

$$\dot{Q}_{\mathrm{i}} = 280 \text{ W}$$

and at a spray nozzle flow of 9 $g.s^{-1}$ the average ice storage rate was 1.12 $g.s^{-1}$. Giving

$$\dot{Q}_{\mathrm{i}} = 333.5 \times 1.12$$

$$\dot{Q}_{\mathrm{i}} = 373.5 \text{W}$$

It was observed that ice crystal nucleation took place on the inner vertical surface of the evaporator/ice store from the height of impact of the spray nozzle flow to the level of the liquid-water in the bottom of the vessel. The ice layer then grew radially inward as water at the solid/liquid interface changed phase to ice. It was possible that the liquid-water droplets either froze in flight, or remained liquid until impacting on the vessel wall. If nucleation had occurred in flight then the appearance of the ice layer would have been glassy, and less even. This confirms the assumption that the droplets remained liquid until impact.

In unpurified water, nucleation is initiated from foreign particles in suspension, or on an insoluble foreign surface, but for nucleation to occur, an individual ice crystal has to grow to a critical size and overcome a free energy barrier between it and the surrounding liquid, according to Hobbs [52]. It is known that small droplets can undergo high degrees of supercooling prior to nucleation because the number of nucleating sites is reduced with a decrease in volume. When a droplet

comes in contact with an insoluble foreign surface and an ice-like cluster is bonded on one side by a surface and on the other by the liquid, the cluster will have a lower free energy than an independent cluster. Therefore it was assumed that nucleation would occur on the vertical surface because small liquid droplets could undergo high degrees of supercooling before nucleation, but when an individual liquid droplet impacted on an insoluble foreign surface, the free energy barrier to nucleation would be lowered, initiating macroscopic ice crystal growth.

5.3.5. Entrainment ratio

Equation 5.12 showed that approximately 7.5 kg of ice was formed per kg of liquid water evaporated, therefore an estimate of evaporation rate could be made from ice storage rate data.

$$\dot{m}_e = \frac{1}{7.5}\dot{m}_i \tag{5.24}$$

$$\dot{m}_e = 1.12 \times \frac{1}{7.5}$$

$$\dot{m}_e = 0.149 \text{ g.s}^{-1}$$

Table 5.3 shows the sample data of primary mass flow at a range of generator temperatures. Primary flow at 120 °C was estimated to be 1.057 $g.s^{-1}$, compared to a theoretical value of 0.977 $g.s^{-1}$ showing that the measured value was 8 % higher than that calculated by Equation 4.37. The throat of the primary nozzle was measured and found to be 2.02 mm in diameter, increasing the throat area by 2 %. The mass flow was therefore also increased by 2 % because of the proportional relationship with throat area. The calculated mass flow was found to be 0.997 $g.s^{-1}$, which was 6 % less than the estimate from the experiments.

Table 5.3. Primary mass flow at varying generator temperatures			
T_g	110 °C	120 °C	130 °C
	0.78	1.06	1.38
	0.78	1.04	1.37
	0.76	1.04	1.39
	0.76	1.06	1.35
	0.76	1.06	1.44
	0.76	1.08	1.39
Average ($g.s^{-1}$)	0.767	1.057	1.381
Standard error ($g.s^{-1}$)	± 0.011	± 0.016	± 0.032

The calculated result was based on a one-dimensional compressible flow theory assuming that the steam behaved as a perfect gas and obeyed the relationship, $Pv^{1.3}$ = constant. Eames *et al* [43] showed that the theory could predict mass flow to within 5 %, and that it tended to under-estimate the actual value. This conclusion is confirmed from the results shown above. The results show that a simple one-dimensional compressible flow theoretical model can predict the flow within 6 % of the actual value, and therefore, can give good estimates of primary flow in a low-grade heat powered jet-pump.

At steady-state, the evaporation rate is approximately equal to secondary flow, therefore, an estimate of entrainment ratio can be made from measurements of ice storage rate. Entrainment ratio is found from Equation 4.1.

$$\omega = \frac{\dot{m}_s}{\dot{m}_p} \tag{4.1}$$

The entrainment ratio was, therefore,

$$\omega = \frac{0.149}{1.057}$$

$$\omega = 0.141$$

The uncertainty of the result was calculated using the error analysis described in Appendix D. The percent relative error of the entrainment ratio was approximately

14 %, and was dominated by the error propagated by the large spread of ice storage data about the average.

5.3.6. Coefficient of performance

Assuming that the coolth stored is equal to the evaporator load, the COP of the TIS system can be found from Equation 5.16.

$$\mathrm{COP} = \frac{\dot{Q}_{\mathrm{i}}}{\dot{Q}_{\mathrm{g}}} \tag{5.16}$$

The coolth storage rate was estimated to be 373.5 W. The generator heat input can be found from Equation 5.18 below.

$$\dot{Q}_{\mathrm{g}} = \dot{m}_{\mathrm{p}}(h_{\mathrm{g},Tg} - h_{\mathrm{f},Tc}) \tag{5.18}$$

Experimental measurements of primary mass flow and condenser liquid temperature are shown in Table 5.4.

Table 5.4. Primary mass flow, condenser temperature, and COP at T_g = 120 °C.

	$\dot{m}_{\mathrm{p}}$	T_{c}	$h_{\mathrm{f},Tc}$	COP
	1.06	26	108.9	0.135
	1.04	28	117.3	0.139
	1.04	20	83.9	0.137
	1.06	21	92.2	0.135
	1.08	20	83.3	0.137
Average ($g.s^{-1}$)	1.057			0.136
Standard error ($g.s^{-1}$)	0.016			0.019

The specific enthalpy of saturated liquid and the calculated coefficient of performance are also shown. The COP is less than the optimum value because the primary nozzle is over-expanded, causing a bulging out of the primary jet at the exit plane, restricting secondary flow and incurring higher losses in the mixing chamber, as was described in Chapter 4. A COP of 0.136 during spray ice TIS is

low compared to other heat driven cooling systems. Rose *et al* [53] showed that single effect ammonia/water TIS systems could operate at COPs of between 0.4 and 0.7, and an experimental silica gel absorber-desorber described by Hisaki *et al* [13] operated at a COP of 0.4. Electrically driven ice storage systems have COPs of between 3 and 5, according to Brady [5], but this would be reduced to less than unity when inefficiencies of supply and part-load performance are taken into account. The low COP is a major disadvantage of jet-pump cooling systems, because a large boiler would be required to provide the primary steam flow, and steam consumption would be high. As in jet-pump refrigeration, spray ice TIS may only be applicable if there is a demand for cooling and a low-grade heat supply is already available, such as from existing CHP systems.

In analysing the growth of an ice layer on a vertical surface, it was suggested that two different cooling mechanisms occurred simultaneously; discharge of coolth from supercooled droplets and conduction through a falling film. An investigation into the nucleation and ice layer growth of a falling film in absence of flash evaporative freezing could establish its performance in comparison with the tests described in this report. Nucleation may occur at a lower saturation pressure and temperature, causing a lower COP, but the ice storage rate may be more consistent, in the absence of variability due to the spray nozzle flow. However, as was shown in discussing the growth of the ice layer, a solid surface can provide many nucleating sites for ice crystal growth. This may cause nucleation to occur at a higher saturation pressure and temperature, increasing COP with respect to spray ice TIS. If TIS driven by evaporation from a falling film were successful then it may be applied to existing dynamic TIS systems that use refrigerated plates to build up an ice layer. A jet-pump could be used to enhance the ice storage rate, thus increasing the cooling capacity of an existing dynamic TIS system.

5.4. Part-load performance

Figures 5.2 and 5.3 showed that the average ice storage rate varied with generator temperature, and a maximum value was observed at approximately 120 °C. It was concluded that the ice storage rate peaked because of the choking phenomenon that occurred in the diffuser throat. Ice storage rate was, therefore, dependent on the flow entrained by the jet-pump. The coolth storage rate and COP at part-load conditions were determined, and the results presented in Figure 5.5, below.

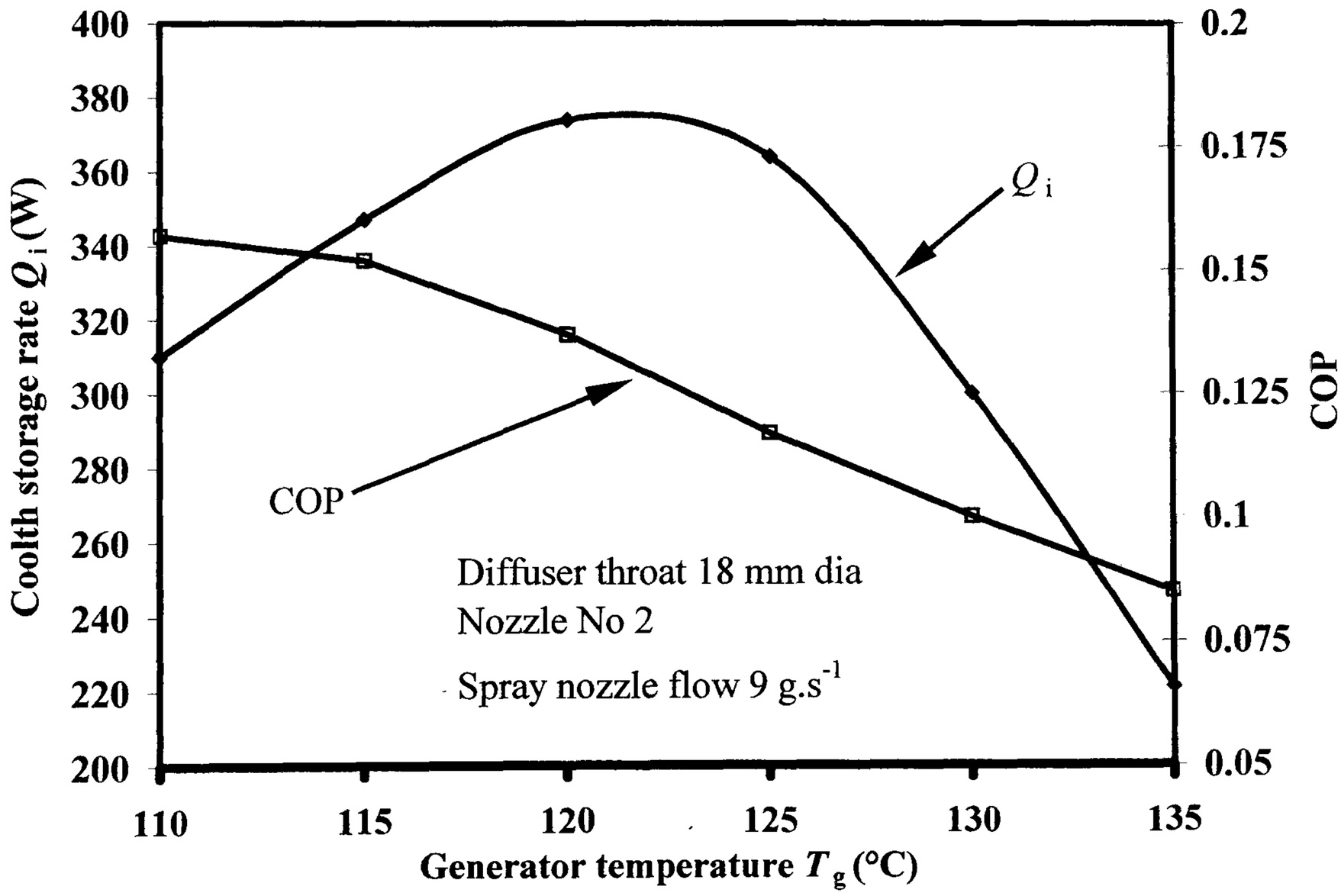

Figure 5.5. Variation in coolth storage rate and COP with generator temperature.

As would be expected, the coolth storage rate peaked at the choked condition where the maximum was found to be 373.5 W at 120 °C. Over the interval of 110 °C to 135 °C, however, the COP was observed to decrease with increases in generator temperature. It would normally be expected that coolth storage rate and COP would peak at similar inlet conditions, because of the reduction in secondary

flow below the choked condition. Figure 5.6 shows the change in secondary flow at evaporator saturation temperatures of 5 °C and 10 °C, and the change in primary flow with a variation in the generator saturation temperature.

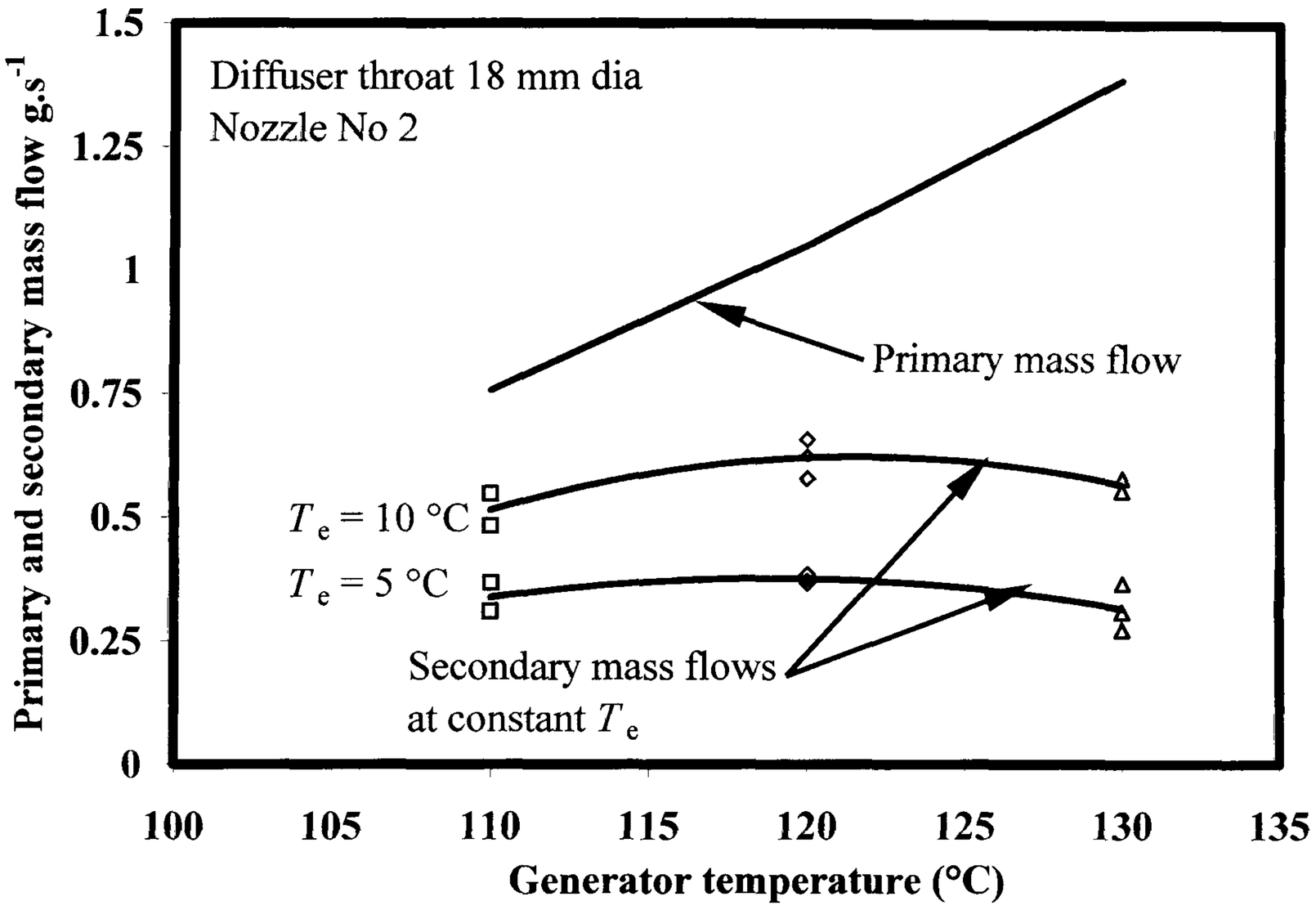

Figure 5.6. Variation in primary and secondary flow with generator temperature at constant evaporator temperatures.

Primary flow is proportional to the stagnation pressure and inversely proportional to the square root of the stagnation temperature, as shown by Equation 5.25.

$$\dot{m}_p \alpha \frac{P_i}{\sqrt{T_i}} \tag{5.25}$$

There was only a small difference in secondary flow with a change in generator saturation temperature, especially at lower evaporator temperatures, but primary mass flow decreased by a larger margin. The more rapid reduction in primary flow compared with secondary flow would cause an increase in entrainment ratio and COP as the generator saturation temperature decreased below the choked condition The COP may increase with a reduction in generator saturation temperature because of the inlet geometry of the jet-pump. The jet-pump mixing section

consisted of a double taper cone, the first half angle cone of which was 11°. This is slightly larger that recommended (5° to 10°) and may have allowed the secondary stream to accelerate more smoothly, reducing the losses due to friction and turbulence. In Chapter 4, it was concluded that the losses in the mixing section were over-estimated, causing a larger entrainment ratio than expected. The difference in peaks between secondary flow and entrainment ratio is probably peculiar to this design, but if the generator temperature could be varied practically in a jet-pump TIS system then a reduction in cooling requirements could be met by a decrease in the generator saturation temperature. This would increase the COP, reduce the heat input to the generator, and energy use in response to a decrease in evaporator cooling requirements. The test results cannot be used to make conclusions about minimising losses by optimising the first half angle taper cone, but the use of a double taper cone appears to have increased secondary flow by reducing momentum losses and restrictions to flow.

In the encapsulated ice TIS tests, the generator temperature will be fixed at 115 °C so that the COP can be increased without reducing coolth storage rate substantially. The coolth stored, and COP were 347 W and 0.274, respectively.

5.5. Conclusions

During freezing, the evaporator saturation pressure and temperature approached a steady-state condition because of the transfer of latent heat when changing phase to ice. Cooling capacity was dependent upon the secondary flow entrained by the jet-pump and that depended upon the saturated conditions and the annular area through which secondary flow could pass. The ice storage rate was therefore, found to be approximately equal to the adiabatic evaporative freezing rate.

Nucleation and ice crystal growth on a vertical surface was found to be a practical method of ice storage, and only limited by the flow conditions described above. There was a large data spread however, because of the method of measuring ice

production, and variations in the saturation conditions in the evaporator with size distribution of the water droplets. This may make spray ice TIS unreliable as a practical long term storage system, but a falling film in the absence of flash evaporation may provide a more predictable system.

Two evaporative freezing processes were identified which occurred simultaneously. Nucleation and growth of an ice layer due to the discharge of coolth stored in supercooled spray droplets, and further ice layer growth due to evaporative freezing from the falling film. Approximately 90 % of ice stored was formed by evaporation from the falling film.

The assumption that approximately 7.5 kg of ice was formed per kg of liquid evaporated was shown to give a reliable estimate of either ice storage rate for a measured secondary flow, or evaporation rate for a measured ice storage rate. This depended upon the assumption that evaporation rate could be assumed equal to secondary mass flow, which was shown to be valid during the change of phase.

The COP during spray ice TIS was just below 0.15 which was low compared to other cooling systems, but the utilisation of waste heat, low first cost and minimal maintenance may make the system more competitive, especially when the reduction in emissions attributable to cooling systems are taken into account.

The cooling capacity was limited to the maximum secondary flow possible, and this reached a peak at the design point where secondary flow was choked, but it was found that the COP increased as the generator temperature decreased. This was thought to be characteristic of the large first half taper cone angle and the use of a double taper cone mixing section. This characteristic could be used to reduce the steam consumption of the thermal (ice) store if the required cooling capacity decreased.

Chapter 6. Encapsulated ice TIS

6.1. Introduction

Jet-pump encapsulated ice TIS is a novel method of ice storage which utilises sublimation freezing to solidify an encapsulated ice store using a gel system that optimises the surface area for heat and mass transfer, and so requires experimental analysis to determine its optimum operating characteristics. The performance parameters that will be used to analyse the encapsulated ice TIS system are coolth storage rate, cooling capacity and COP. Coolth storage rate is directly related to jet-pump secondary flow, and so the performance of the jet-pump can be determined in terms of ice storage rate. Cooling capacity can be used to compare encapsulated ice TIS with spray ice TIS results found in Chapter 7, and COP can be used to compare the jet-pump TIS system with other ice storage and cooling systems. This chapter describes the simplifying assumptions and the models used in establishing the performance parameters. The use of the spherical capsules is another novel feature of the system, and this section also describes how they were designed and manufactured. Finally, the experimental method is described and test results are presented.

6.2.1. Sublimation freezing

The liquid-water in the evaporator/ice store is frozen by sublimation from the surface of a solidifying ice layer. Once the liquid-water has solidified, a higher temperature solution is passed through the store to discharge it. The surface area available should be maximised to enhance the heat and mass transfer processes during both freezing and melting, so that a bed of spherical capsules was identified as the most appropriate storage method because of the high surface area to volume ratio.

Encapsulated ice storage systems normally use plastic spheres partially filled with water, as shown by Arnold [15] and Eames *et al* [16], but a hydroscopic polymer gel system developed by Sanken Setsubi Kogyo Ltd of Japan was able to absorb about 100 times its own mass of water. This allowed water in an evaporator/ice store to be held in suspension and presented a large surface area for heat and mass transfer. They can be formed to any shape; spherical, cylindrical and rectangular beds have been experimented with. The system has been tested under conventional encapsulated TIS conditions, and by using a vacuum pump to cause evaporative freezing, but has not been used in conjunction with a jet-pump refrigeration system. A large number of small diameter copper capsules were, therefore, manufactured to form a bed of encapsulated elements in the jet-pump evaporator/ice store to analyse the novel system. The design of the capsules is described in this chapter.

A bed of encapsulated elements undergoes four cooling regimes during jet-pump TIS. Entrainment of vapour by the jet-pump causes evaporative cooling of the bed of capsules in the evaporator/ice store. When the temperature of the bed of capsules reach the equilibrium freezing temperature they do not freeze immediately, but continue to be sensibly cooled, supercooling the elements. Once ice crystal nucleation begins, the temperature of the bed of capsules reverts to the equilibrium freezing temperature. When the temperature reaches 0 °C, the coolth stored sensibly has been released and further ice formation occurs by the formation and growth of an ice shell at the interface between the vapour and water in the capsules. Sublimation from the shell surface causes further ice formation until the elements have solidified. The freezing process was based on the solidification of a liquid droplet as described by Hobbs [52], thus it was assumed that the same basic process occurred during the solidification of the liquid-water contained in the individual capsules. When all of the capsules have solidified the temperature will begin to fall because sublimation from the solid surface will cause sensible cooling of the capsules below the equilibrium freezing temperature. This will result in a further decrease in mass.

6.2.2. The sensible cooling regime

A difference in pressure and temperature between the liquid and vapour phases causes continual sensible cooling of the liquid-water, but the contents of the evaporator/ice store including the copper capsules that contain the gel, the glass vessel and the stainless steel end plates, are also cooled, and so must be taken into account, as shown by Houška *et al* [25]. The heat capacity of the vessel and capsules is assumed to be constant so can be represented by Equation 6.1.

$$m_v C_v = m_{gl} C_{gl} + m_{ss} C_{ss} + m_{cu} C_{cu} \tag{6.1}$$

where m is the mass and C is the specific heat capacity. The subscripts v, gl, ss, and cu refer to the overall vessel, glass evaporator vessel, stainless steel end plates and copper capsules, respectively. Assuming that the evaporative cooling process is adiabatic, then the sensible cooling undergone by the liquid-water and vessel will be equal to the latent cooling due to evaporation.

$$\Delta m_e h_{fg} = \left(m_w C_{pw} + m_v C_v\right)\Delta T \tag{6.2}$$

where Δm_e is the mass evaporated, m_w is the mass of liquid-water contained in the bed of capsules, and ΔT is the change in temperature due to the mass evaporated. As in spray ice TIS, a small proportion of the total mass is evaporated, cooling the remaining water, therefore, the mass contained in the encapsulated ice TIS system after evaporation is the difference between the initial mass and the mass evaporated.

$$m_w = m_0 - \Delta m_e \tag{6.3}$$

where m_0 is the initial mass of liquid-water contained in the bed of capsules. Substituting back into Equation 6.2 gives;

$$\Delta m_e h_{fg} = \left(\left(m_0 - \Delta m_e\right)C_{pw} + m_v C_v\right)\Delta T \tag{6.4}$$

$$\Delta m_e \left(h_{fg} + C_{pw}\mathrm{d}T\right) = \left(m_0 C_{pw} + m_v C_v\right)\Delta T \tag{6.5}$$

$$\Delta m_e = \frac{(m_0 C_{pw} + m_v C_v)\Delta T}{h_{fg} + C_{pw}\Delta T} \tag{6.6}$$

Equation 6.6 shows the mass evaporated in sensibly cooling the liquid-water and vessel by a temperature difference ΔT. Sensible cooling will continue until the liquid-water temperature reaches 0 °C.

6.2.3. The supercooling regime

On reaching 0 °C, a change of phase does not occur spontaneously but ice crystals must reach a critical size before macroscopic ice formation can occur. Once nucleation is achieved a small quantity of the liquid-water freezes, according to Hobbs [52]. As ice growth continues, the temperature of the liquid-water reverts to the equilibrium freezing temperature. The coolth stored as ice is equal to the coolth released by the supercooled liquid.

$$m_{\mathrm{iF}} h_{\mathrm{if}} = \left(m_{\mathrm{F}} C_{\mathrm{pw}} + m_{\mathrm{v}} C_{\mathrm{v}}\right)\Delta T_{\mathrm{F}} \tag{6.7}$$

where ΔT_{F} is the degree of supercooling, m_{iF} is the mass of ice formed and m_{F} is the mass of liquid-water contained in the evaporator/ice store when nucleation begins and the temperature starts to rise. The mass frozen during the reversion to the equilibrium freezing temperature is, therefore,

$$m_{\mathrm{iF}} = \frac{(m_{\mathrm{F}} C_{\mathrm{pw}} + m_{\mathrm{v}} C_{\mathrm{v}})\Delta T_{\mathrm{F}}}{h_{\mathrm{if}}} \tag{6.8}$$

6.2.4. The latent cooling regime

It is assumed that the ice crystal growth in the supercooling regime forms a shell between the liquid and vapour phases, and that sublimation from the solid shell causes a growth of the shell. This is assumed to occur from the as the capsules revert to the equilibrium freezing temperature.

The latent cooling due to sublimation from the surface of the bed of capsules is equal to the coolth stored as ice, thus

$$m_{\mathrm{sub}} h_{\mathrm{sub}} = m_{\mathrm{isub}} h_{\mathrm{if}} \tag{6.9}$$

where h_{sub} is the latent heat of sublimation m_{sub} is the mass sublimated from the ice shell, and m_{isub} is the mass of ice formed due to sublimation. Sublimation from the surface causes the growth of an ice shell such that the coolth stored as ice is equal to the cooling due to sublimation. Therefore,

$$m_{sub} = \frac{h_{if}}{h_{sub}} m_{isub} \tag{6.10}$$

The latent heat of ice fusion at 0 °C is 333.5 kJ.kg^{-1} and the latent heat of sublimation is 2838 kJ.kg^{-1}, therefore, substituting the values into Equation 6.10 gives,

$$m_{sub} = \frac{333.5}{2838} m_{isub} \tag{6.11}$$

$$m_{isub} = 8.5 m_{sub} \tag{6.12}$$

Mass is sublimated at the interface between the solid and vapour resulting in a decrease in mass contained in the capsules, but sublimation causes an inward growth of the ice shell. When the ice shell has solidified, the difference between the mass at the start of shell growth and at solidification will be,

$$m_{isub} = m_L - m_{sub} \tag{6.13}$$

where m_L is the mass of liquid-water contained in the capsules at the start of sublimation freezing. Substituting back into Equation 6.12 gives,

$$m_{sub} = \frac{m_L - m_{sub}}{8.5} \tag{6.14}$$

$$m_{sub}(8.5+1) = m_L \tag{6.15}$$

$$m_{sub} = \frac{1}{9.5} m_L \tag{6.16}$$

Equation 6.16 shows that there is a reduction in liquid-water mass of approximately 10 % during sublimation freezing.

6.2.5. Sensible cooling of the ice store

When the liquid-water in the bed of capsules has solidified, the action of the jet-pump continues to induce sublimation from the surface of the ice spheres,

resulting in a decrease in cooling capacity of the ice store. Again, assuming adiabatic conditions in the evaporator/ice store, the latent cooling induced by sublimation will be equal to the sensible cooling undergone by the bed of capsules.

$$\Delta m_{sub} h_{sub} = (m_i C_i + m_v C_v)\Delta T \tag{6.17}$$

where m_i is the mass of ice in the evaporator/ice store after sensible cooling by an amount ΔT. The mass of ice is the difference between the mass at solidification and the mass sublimated. Thus

$$m_i = \sum m_i - \Delta m_{sub} \tag{6.18}$$

where Σm_i is the mass of ice found from Equation 6.8 and 6.13 at the completion of solidification of the liquid-water contained in the capsules. Substituting back into Equation 6.17 and solving for the mass sublimated gives

$$\Delta m_{sub} = \frac{(\sum m_i C_i + m_v C_v)\Delta T}{h_{sub} + C_i \Delta T} \tag{6.19}$$

Equation 6.19 will be used to estimate reductions in cooling capacity after the ice store has been fully charged.

6.3.1. Cooling capacity

The cooling capacity of the ice store is found from Equation 6.20, below.

$$Q_i = \sum m_i h_{if} \tag{6.20}$$

The mean coolth storage rate over the latent cooling period is then found from Equation 6.21, below.

$$\dot{Q}_i = \frac{Q_i}{\Delta t} \tag{6.21}$$

where Δt is the time duration of the charge cycle. The cooling capacity and the mean coolth storage rate can then be compared with the results from spray ice TIS testing.

6.3.2. Coefficient performance

The coefficient of performance of the encapsulated ice TIS system is the ratio of the coolth stored as ice to the heat input to the generator, neglecting the work of pumps, etc.

$$\mathrm{COP} = \frac{Q_{\mathrm{i}}}{Q_{\mathrm{g}}} \tag{6.22}$$

The energy input to the generator during ice storage is found from Equation 5.18. The energy input over the charge period Δt is, thus

$$Q_{\mathrm{g}} = \dot{Q}_{\mathrm{g}}\,\Delta t \tag{6.23}$$

The COP of the encapsulated ice TIS system in terms of jet-pump measurements can be found by using Equation 5.16. Under adiabatic freezing conditions, the coolth stored as ice is assumed to be equal to the cooling due to sublimation, thus

$$\mathrm{COP} = \frac{\dot{m}_{\mathrm{sub}}\, h_{\mathrm{sub}}}{\dot{Q}_{\mathrm{g}}} \tag{6.24}$$

Assuming steady-state conditions in the evaporator/ice store, the mass sublimated will be approximately equal to the mass of vapour entrained by the jet-pump.

$$\mathrm{COP} = \frac{\dot{m}_{\mathrm{s}}}{\dot{m}_{\mathrm{p}}} \frac{h_{\mathrm{sub}}}{(h_{\mathrm{g},Tc} - h_{\mathrm{f},Tc})} \tag{6.25}$$

$$\mathrm{COP} = \omega \frac{h_{\mathrm{sub}}}{(h_{\mathrm{g},Tg} - h_{\mathrm{f},Tc})} \tag{6.26}$$

Equation 6.26 can be used to find the COP from jet-pump measurements, to compare it with the results found from ice storage capacity estimates, and to examine the steady-state assumption.

6.4. Encapsulated ice TIS discharge cycle

Once the charge cycle had been completed, water from a storage vessel was returned to the evaporator/ice store and re-circulated via a heat exchanger, where a

heat load was applied to it. The coolth discharge rate was determined by using the calibrated flow from the re-circulation pump, measuring the temperature of the re-circulation flow as it entered the evaporator, and the temperature of the water in the base of the evaporator/ice store. The results were used to compare the coolth charged and discharged, thus checking the simplifying assumptions used during ice storage.

Results of the discharge of a bed of spherical capsules 40 mm in diameter were obtained from Sanken Setsubi Kogyo Ltd, for comparison with the capsules used in the tests described in this thesis. The two systems could be compared because the inlet temperature and the flow of coolant were approximately the same. The coolth discharge rates and diameters would be different, therefore it was decided to compare the two sets of results by calculating the coolth flux.

$$\dot{q} = \frac{\dot{Q}}{SA} \tag{6.27}$$

where $\dot{q}$ is the coolth flux, and SA is the total surface area of the bed of encapsulated elements. The ratio of surface area to volume of a bed of encapsulated elements may be described as

$$\frac{SA}{V} = \frac{4\pi r_i^{\,2} N_{\mathrm{T}}}{\frac{4}{3}\pi r_i^{\,3} N_{\mathrm{T}}} \tag{6.28}$$

where V is the total volume of the bed of elements, r_{i} is the capsule radius and N_{T} is the number of capsules. Volume can be substituted by the ratio of mass to density (m/ρ). Giving the surface area in terms of total mass, density, and capsule radius in Equation 6.29.

$$SA = \frac{3m}{\rho r_i} \tag{6.29}$$

6.5. Capsule design and manufacture

This section describes the design method that was used to maximise the mass and the surface area available for heat and mass transfer. The first part of the analysis determined the design cooling capacity using an assumed secondary flow and charge phase duration. Once the cooling capacity was calculated, the best combination of capsule size and number was determined. The mass of the polymer granules required in the individual capsules was then calculated, followed by the choice of material and method of manufacture.

Assuming steady-state conditions in the evaporator/ice store, the sublimation rate will be approximately equal to secondary flow. The action of the jet-pump induces sublimation from the surface of the water-gel in the capsules, causing the release of latent heat and ice crystal growth. The heat released by the liquid-water when changing phase to ice is equal to the cooling due to sublimation from the solid surface. Therefore,

$$\dot{Q}_{sub} = \dot{m}_{sub}\, h_{sub} \tag{6.30}$$

It was assumed that the jet-pump could operate at an entrainment ratio of between 0.2 and 0.3, so an average entrainment ratio of 0.25 was used. In Chapter 4, it was shown that at a generator saturation temperature of 120 °C and a primary nozzle throat diameter of 2 mm, the primary mass flow was found to be approximately 1 $g.s^{-1}$, giving a secondary flow of approximately 0.25 $g.s^{-1}$. A charge period of 60 minutes was assumed to give adequate time for steady-state measurements. Therefore the design cooling capacity for the test rig would be,

$$Q_{sub} = \dot{m}_{sub}\, h_{sub} \Delta t \tag{6.31}$$

$$Q_{sub} = 0.25 \times 10^{-3} \times 2838 \times 10^{3} \times 60 \times 60$$

$$Q_{sub} = 2566 \text{ kJ}$$

If it is assumed that the cooling caused by sublimation is equal to the heat released in changing phase to ice, then

$$Q_{sub} = m_i h_{if} \tag{6.32}$$

Therefore,

$$m_i = \frac{Q_{sub}}{h_{if}} \tag{6.33}$$

The mass of ice contained in the evaporator/ice store at the end of the charge phase is

$$m_i = \frac{2556}{333.5}$$

$$m_i = 7.664 \text{ kg}$$

There is a reduction in liquid-water during sublimation of approximately 10 % and a reduction by evaporation during the initial sensible cooling period. It is assumed that the total decrease in mass is 15 % over both periods to give an initial mass capacity of

$$m_0 = 1.15 \times m_i \tag{6.34}$$

$$m_0 = 1.15 \times 7.664$$

$$m_0 = 8.814\text{kg}$$

The packing of spherical capsules in an evaporator vessel was assumed to start with a single sphere at the centre of the vessel, then a ring of 6 spheres would surround the central one. This would continue with successive rings of spheres surrounding the previous ones, with each ring containing 6 more spheres. Equation 6.35 describes the number of spheres N that would be contained in a single layer with n number of rings.

$$N = 1 + 6(1 + 2 + \ldots + \text{n}) \tag{6.35}$$

This can be simplified to Equation 6.36.

$$N = 1 + 6\left(\frac{1}{2}\text{n}(\text{n}+1)\right) \tag{6.36}$$

If the radius r is measured from the centre of the evaporator to the perimeter of the outer ring of spheres, then the overall radius can be found from Equation 6.37.

$$r = d_{cap}\left(\frac{1}{2} + \text{n}\right) \tag{6.37}$$

where d_{cap} is an individual capsule diameter. Rearranging in terms of the number of rings,

$$n = \left[\frac{r}{d_{cap}} - \frac{1}{2} \right] \tag{6.38}$$

The number of rings is an integer whose value will be the nearest whole number below the absolute result. It was assumed that there was no close packing of the spheres, so that the number of rows was simply a divisor of the assumed maximum height and the sphere diameter.

$$N_R = \left[\frac{H}{d_{cap}} \right] \tag{6.39}$$

Again, the number of rows N_R is an integer whose value will be the nearest whole number below the absolute result. The total number of capsules is, therefore

$$N_T = N_R \times N \tag{6.40}$$

The mass of water contained in the beds was calculated from Equation 6.41.

$$m_0 = \frac{4}{3} \pi r_i^3 \rho_L N_T \tag{6.41}$$

where r_i is the inside radius of the individual capsule assuming a 1mm capsule shell thickness.

The size and number of capsules were varied with the constraint that the maximum height of the bed would be 0.4 m. Three sizes of capsule (20 mm, 25 mm and 30 mm) were considered to meet the required mass capacity. Table 6.1 describes the results of the calculations performed using Equations 6.38, 6.36, 6.39, 6.40 and 6.41.

Table 6.1. Determination of totals number of capsules and mass capacity for various sphere diameters.

d_{cap} (mm)	20	25	30
n	6	5	4
N	127	91	61
N_R	20	16	13
N_T	2450	1456	793
m_0 (kg)	7.391	8.119	9.116

Table 6.1 will give the capacity for a given size and number of capsules, and it shows that the capsule size closest to the design requirement is the 25 mm diameter sphere. However, Table 6.1 also shows that the capacity will be increased by about 12 % if 30 mm diameter spheres were used. Hiromi [54] used the ratio of the volume of the capsules to the total volume of the vessel to define an ice packing factor, shown below.

$$\mathrm{PF} = \frac{2}{3}\frac{D_v^{\,3} N_T}{d_{cap} H} \tag{6.42}$$

Where D_v is the vessel diameter, and H is the height of the bed of capsules in the vessel. In this case, the height is just the diameter of the individual capsules multiplied by the number of rows N_R. The values were entered into Equation 6.42 and the packing factor for the three capsule sizes were 0.363, 0.421 and 0.407 with respect to the 20 mm, 25 mm and 30 mm diameter capsules. The packing factor should be maximised, and so it was concluded that the 25 mm diameter capsules would be used, as they gave the design cooling capacity and the highest packing factor of the three. 1500 capsules were manufactured to give an overall mass of 8.364 kg.

Figure 6.1 shows a diagram of an individual capsule and Figure 6.2 shows a photograph of the bed of capsules in the evaporator/ice store. Copper was chosen as the most appropriate material of construction for the capsules because it is ductile, allowing half-spheres to be easily formed by pressing from a sheet, it is corrosion resistant in water, and has high thermal conductivity, thus reducing resistance to heat transfer. Seven holes, 3 mm in diameter were punched into each of the copper half-spheres prior to pressing, to allow water in the evaporator to come into contact with the polymer granules and absorb water. The holes also allowed evaporation and sublimation to proceed during the charge phase, and heat transfer from the bed to the surrounding liquid-water during the discharge phase. The capsule consisted of two hemispheres, the outer one 27 mm outside diameter and the inner one 25 mm outside diameter.

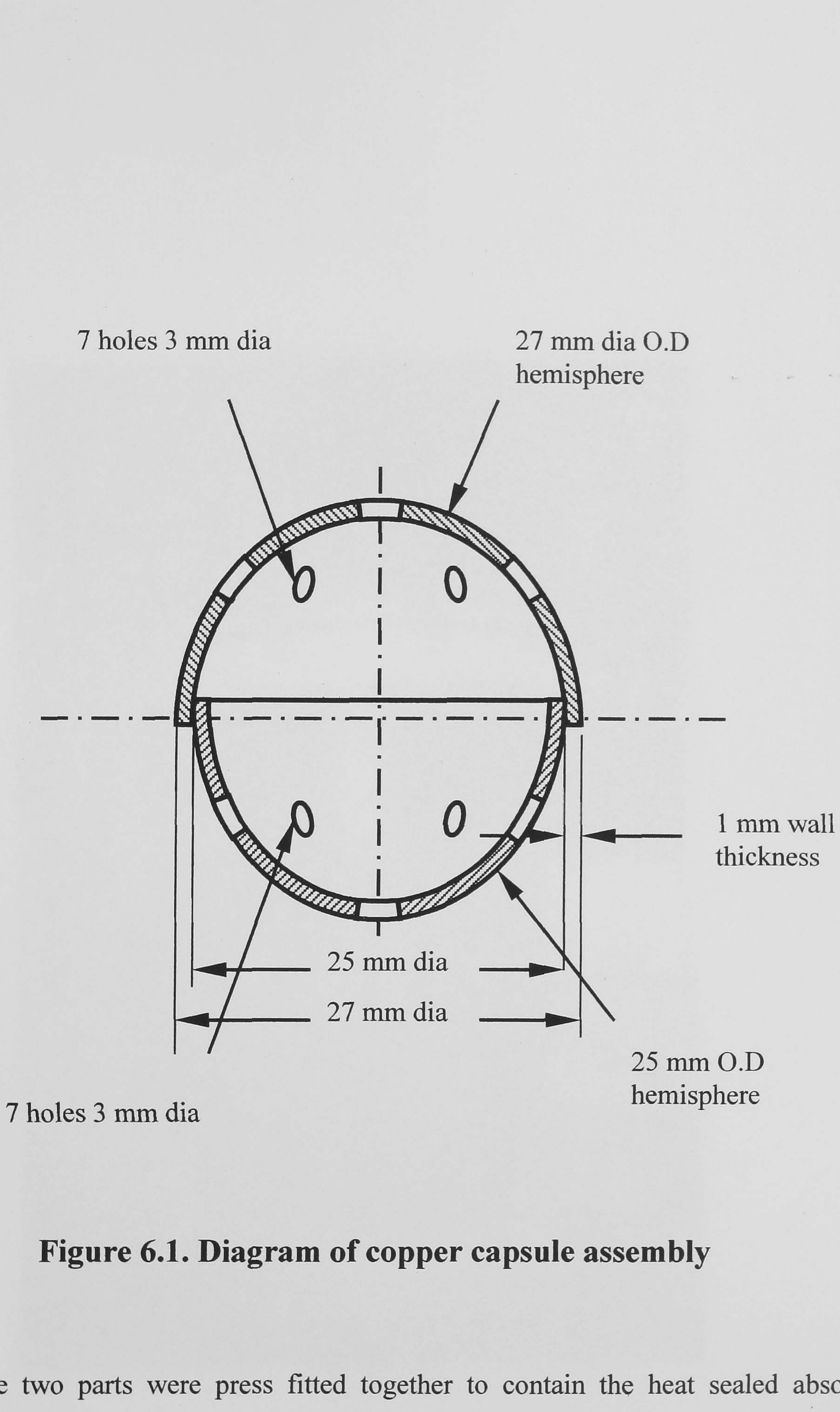

Figure 6.1. Diagram of copper capsule assembly

The two parts were press fitted together to contain the heat sealed absorbent sachets containing the polymer granules. Each capsule contained a mass of water of

$$m_{cap} = \frac{m_0}{1500} = \frac{8.364}{1500} = 5.576\text{g}$$

Figure 6.2. Photograph of the bed of capsules in the evaporator/ice store

The polymer granules were assumed to absorb approximately 100 times their own mass of water, therefore 55.76 mg of polymer granules was used in each sachet.

6.6. Encapsulated ice TIS test results: charge cycle

The objective of testing the encapsulated ice TIS system was to establish its operating characteristics, to examine the simplifying assumptions, to compare the results with spray ice TIS and other systems and to evaluate its use in a practice. This chapter describes the experimental method and the results of the tests.

6.6.1. Experimental Method: charge cycle

Referring again to Figure 3.2, before each test, water was pumped from the storage vessel (17) to the evaporator (12) until the level was above the bed of ice storage capsules. They were then allowed to soak overnight so that the polymer granules could absorb their maximum amount of water. On the morning of the test, excess water was pumped from the evaporator chamber to the storage vessel. The generator vessel was then filled and the heater in the heat load simulator (22) was switched on. Once excess water had been removed from the evaporator, the test rig was evacuated by a vacuum pump. When the evacuation procedure had been completed the generator heater elements were switched on. Once the generator water temperature had reached the required value, cooling water was allowed to flow through the coils (30) in the condenser and the primary steam valve (j) was opened. A stop-watch was started and the temperature of the water/ice in the gel at the top, in the middle and at the bottom of the bed of capsules were recorded at one minute intervals, together with vapour pressures and temperatures. The mass of water evaporated was estimated by calculating the evaporation required to cause a decrease in water temperature over one minute intervals and summing this over the sensible cooling period. The mass of ice formed as the supercooled liquid transferred the coolth as latent heat was estimated from the difference between the equilibrium freezing temperature and the minimum measured temperature and

calculated from Equation 6.12. The mass sublimated during latent cooling was estimated from the difference between the original mass, the mass evaporated and initial ice formation, and calculated from Equation 6.21. The mass of ice formed was found from Equation 6.18 using the estimated mass of sublimated water, and the cooling capacity was determined from Equation 6.22. Primary flow was estimated by observing the difference in water level of a sight glass mounted on the generator steam drum. An estimate of the mass of liquid-water evaporated and ice sublimated over the charge cycle enabled an estimate of cooling capacity and average ice storage rate to be made for comparison with spray ice TIS. COP was then determined from both jet-pump measurements and ice storage capacity estimates to compare the two methods. COP was also used to compare encapsulated ice TIS with spray ice TIS and other competitive TIS systems. This section describes the results of tests carried out on the experimental rig and the performance of the jet-pump ice store that was estimated from them.

6.6.2. The sensible cooling regime

1500 spherical capsules 22 mm inside diameter were constructed to hold the heat sealed sachets containing the polymer granules. A sample of 100 capsules was taken to make an estimate of the mass of liquid-water absorbed by the polymer system. The overall mass of the copper capsules, absorbent sachets and polymer granules was measured in a dry condition, and then the sample was allowed to fully absorb water. The mass was measured and the difference between the wet and dry samples gave an estimate of the mass absorbed by the 1500 capsules. The sample of 100 capsules was 1.6624 kg dry and 2.2136 kg wet. The error in the estimate of the initial mass will be neglected because the errors in evaporation and sublimation are orders of magnitude greater. The total mass of water absorbed by 1500 capsules was estimated from Equation 6.43.

$$m_0 = (m_{\text{wet}} - m_{\text{dry}}) \times 15 \tag{6.43}$$

where m_{dry} is the mass of the dry sample and m_{wet} is the mass of the wet sample. The difference between the wet and dry samples was multiplied by 15 to give an estimate of the liquid-water contained in the bed of 1500 capsules.

$$m_0 = (2.2136 - 1.6624)\times 15$$

$$m_0 = 8.268 \text{ kg}$$

The mass contained in the evaporator was approximately 1 % less than the mass calculated from Equation 6.42 in the design section. The assumption that the polymer absorbed approximately 100 times its own mass of water at the design stage has been validated, and gives an accurate prediction of liquid-water contained in the evaporator/ice store.

Figure 6.3 shows the variation in evaporator vapour pressure and liquid-water. The temperature in the bottom gel capsule (T_3) during the charge phase.

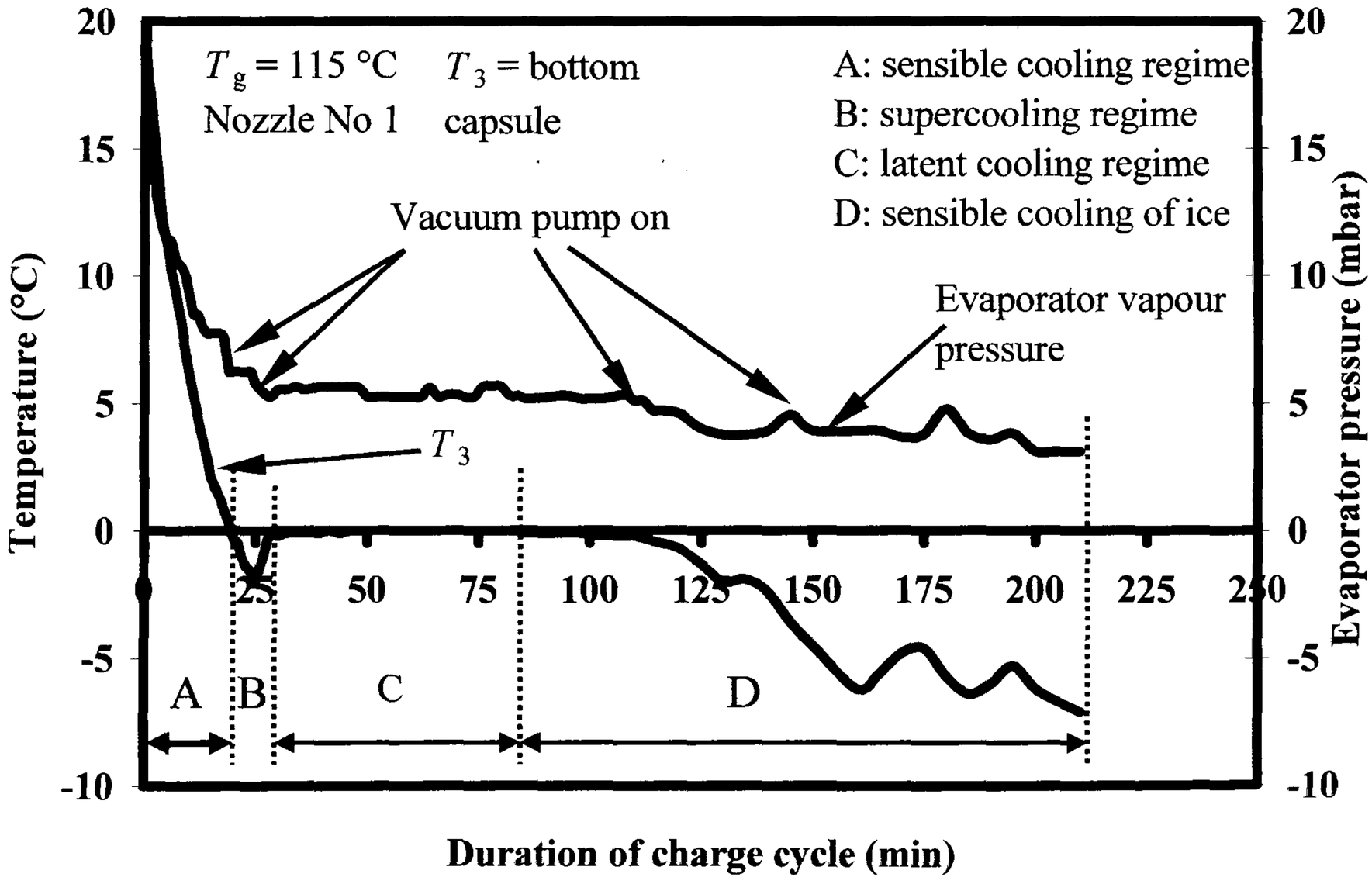

Figure 6.3. Variation in vapour presure and water temperature during the charge cycle.

It was shown in the discussion of spray ice TIS results, that secondary flow decreased with a lowering of vapour pressure, and it can be seen that the pressure measured in the evaporator was between 500 Pa and 550 Pa throughout the latent heat transfer period. This compared with approximately 550 Pa at the end of spray ice TIS at the higher coolth storage rate, showing that the saturation conditions during spray ice TIS were approximately the same under encapsulated ice TIS testing.

The pressure measured in the evaporator was within 6 % of the saturated pressure corresponding to the measured vapour temperature, showing that the presence of non-condensable gases in the evaporator/ice store was negligible. It was found that non-condensables could be removed from the base of the evaporator because the water was retained in the gel and excess water could be pumped away to the storage vessel. The removal of non-condensables was difficult before testing in spray ice TIS, even if an evacuation point at the top of the evaporator vessel was used. It is thought that the vapour and non-condensables stratify, with the non-condensables occupying a layer at the base of the vessel. It was noticed that the vapour pressure during spray ice manufacture slowly decreased as the test continued, as was shown in Figures 5.4 and 5.5. The turbulent action of the spray jet may, over time, cause some of the non-condensables to mix with the vapour and become entrained by the primary flow. It was assumed that the measured pressures at the end of the tests were approximately at the saturation pressures because of the continual withdrawal of non-condensables during the test.

The evaporator liquid-water temperature was recorded over 1 minute intervals and so was used to estimate the reduction in liquid-water from the bed of capsules over the sensible cooling period using Equation 6.6.

$$\Delta m_e = \frac{(m_0 C_{pw} + m_v C_v)\Delta T}{h_{fg} + C_{pw}\Delta T} \tag{6.6}$$

The vessel heat capacity was assumed to be constant but the average specific heat capacity of water over the measured liquid-water temperatures and average latent

heat of vaporisation at the vapour temperature were used. At each interval the mass m_0 was re-evaluated and a new estimate made. Equation 6.1 shows how the vessel heat capacity was calculated.

$$m_v C_v = m_g C_g + m_{ss} C_{ss} + m_c C_c \tag{6.1}$$

Table 6.2. Mass and specific heat capacity of materials in evaporator vessel

m_c (kg)	m_{ss} (kg)	m_g (kg)	C_c ($kJ.kg^{-1}.K^{-1}$)	C_{ss} ($kJ.kg^{-1}.K^{-1}$)	C_g ($kJ.kg^{-1}.K^{-1}$)
24.853	19.075	15.220	0.39	0.44	0.99

Table 6.2 shows the masses and specific heat capacities of the materials that are cooled in the evaporator as liquid-water is evaporated. The masses were determined using calibrated digital scales with a resolution of ±1 g, and the specific heat capacities were taken from Calvert and Farrer [55]. Again, the errors due to the measurement of masses will be neglected because of the small relative error compared with the mass evaporated and sublimated. Substituting the values into Equation 6.1 gives

$$m_v C_v = (15.220 \times 0.99) + (19.075 \times 0.44) + (24.853 \times 0.39)$$

$$m_v C_v = 33.235 \text{ kJ.kg}^{-1}$$

Table 6.3. Estimates of masses and errors.

	Δm_e	m_{iF}	m_{sub}	m_{isub}	Δm_{sub}	Σm_i
R_1 (kg)	0.529	0.395	0.776	6.596	0.114	6.991
ε_R (kg)	0.257	0.056	0.007	0.059		0.115
ε_P (%)	49	12	0.9	0.9	$\Delta m_{sub} \ll 0.1$	1.6
R_2 (kg)	0.504	0.395	0.773	6.571	0.114	6.966
ε_R (kg)	0.011	0.049	0.032	0.272		0.321
ε_P (%)	2	14	4	4	$\Delta m_{sub} \ll 0.1$	4.6

Table 6.3 shows the estimates of the masses used to determine the cooling capacity of the encapsulated TIS store and the errors due to the uncertainties introduced by sampling and arithmetic operations, where R is the result of a sample, ε_R is the relative error and ε_P is the percent relative error. The error analysis is described in Appendix D.

Figure 6.3 showed that the liquid temperature reached 0 °C at approximately 18 minutes and continued to decrease until it reached -2 °C. At approximately 24 minutes the temperature began to revert to 0 °C, indicating that nucleation and macroscopic ice crystal growth had begun. The result R_1 of the mass evaporated was estimated over one minute intervals and summed over the 24 minute sensible cooling period, and was estimated to be

$\Delta m_e = 0.529$ kg

Table 6.3 shows that the percent relative error was approximately 49 %. The temperature difference over a one minute interval was less than 1 °C after about 5 minutes into the test, but the uncertainty due to the temperature measurement was ± 0.25 °C, causing a large error. Table 6.3 shows a second set of results R_2, using an estimate of the mass evaporated over a single 24 minute period as the liquid-water temperature decreased from 17 °C to -2°C, using average specific heat capacity and specific heat of vaporisation values. The error analysis included errors in assuming an average specific heat capacity.

$$\Delta m_e = \frac{(m_0 C_{pw} + m_v C_v)\Delta T}{h_{fg} + C_{pw}\Delta T} \tag{6.6}$$

$$\Delta m_e = \frac{(8.268 \times 4.198 + 33.235)19}{2480 + (4.198 \times 19)}$$

$\Delta m_e = 0.504$ kg

There was approximately a 5 % difference in the estimate of mass evaporated, but the error was reduced to approximately 2 % and will be used in subsequent calculations. This showed that approximately 6 % of the liquid-water had been evaporated during the sensible cooling regime, compared to an assumed value of 5 %. The table also shows that the large error in the evaporation estimate results in only a small error in the subsequent estimates of ice storage capacity. This is because the mass evaporated is small relative to the mass of ice stored.

6.6.3. The supercooling regime

Pressure and temperature continued to fall after reaching 0 °C, causing further sensible cooling below the equilibrium freezing point until the vapour temperature reached -1.8 °C at 24 minutes. The temperatures in the top, middle and bottom capsules were -1.8 °C, -1.9 °C and -2.0 °C respectively, and the measured vapour pressure was 524 Pa. According to Hobbs [52], a supercooled liquid is in an energetically favourable state for it to crystallise, but this cannot be achieved discontinuously. A small crystal embryo is, however, in an energetically unfavourable state because of the ice crystal's large surface area to volume ratio and the positive free energy associated with its interface with the liquid. There is, therefore, a free energy barrier to be overcome before freezing can commence which is only surmounted by thermal fluctuations in the liquid. Ice crystals are continually growing and melting as the temperature falls, until they reach a critical size, which allows them to overcome the free energy barrier. The experimental results showed that this occurred at approximately -2 °C. The temperature then increased and reached 0 °C at 28 minutes.

Eames and Adref [16] described experimental results from studies of a sphere 70 mm in diameter and observed supercooling of -4.3 °C. Arnold [15] described an encapsulated ice storage system using 77 mm diameter capsules, that underwent approximately -7 °C of supercooling. The degree of supercooling in the jet-pump TIS tests was much lower than that found in conventional encapsulated TIS systems. Heterogeneous nucleation is a process in which ice crystals form and grow from foreign particles suspended in the liquid. Most liquids contain impurities, so it is the most common form of nucleation. A decrease in volume reduces the number of foreign particles to a small proportion of a sample, and a decrease in diameter from 70 mm to 22 mm reduces the volume of an individual capsule by over 95 %. Therefore it would be expected that the temperature at which nucleation occurred would be lower, causing the saturation conditions in the evaporator/ice store, and the rate of solidification to be reduced. The water-

polymer gel structure appears crystalline and so may present many nucleating sites, and thus, initiating nucleation at a reduced degree of supercooling. This shows that the polymer gel system may enhance the performance of the jet-pump TIS system compared with a similar system that consisted of capsules partially filled with water only by operating at higher saturation conditions.

The coolth stored sensibly due to supercooling caused ice crystal growth until the temperature reached 0 °C. The mass of ice formed during this period was calculated from Equation 6.8.

$$m_{iF} = \frac{(m_w C_{pw} + m_v C_v)\Delta T_F}{h_{if}} \tag{6.8}$$

The mass of liquid-water in the evaporator at the end of the supercooling period is the difference between the initial mass and the amount evaporated. The mass of ice formed was therefore,

$$m_{iF} = \frac{((m_0 - \Delta m_e)C_{pw} + m_v C_v)\Delta T_F}{h_{if}} \tag{6.44}$$

$$m_{iF} = \frac{((8.268 - 0.504) \times 4.21 + 33.235) \times 2}{333.5}$$

$$m_{iF} = 0.395 \text{ kg}$$

6.6.4. The latent storage regime

During the charge period water sublimates directly from solid to vapour causing ice fusion. The mass of water sublimated was given by Equation 6.16, therefore,

$$m_{sub} = \frac{1}{9.5} m_w \tag{6.16}$$

The mass of water at the start of sublimation is the difference between the initial estimate, the mass evaporated and the mass crystallised in reverting to 0 °C. The mass sublimated is, therefore,

$$m_{sub} = \frac{(m_0 - \Delta m_e - m_{iF})}{9.5}$$

$$m_{sub} = \frac{(8.268 - 0.504 - 0.395)}{9.5}$$

$m_{sub} = 0.776$ kg

The mass sublimated during the latent cooling period was approximately 9 % of the original mass, and so any large errors in estimating sublimation will cause only small errors in ice storage capacity. Equation 6.13 gives the mass of ice formed,

$m_{isub} = 8.5\ m_{sub}$ (6.12)

$m_{isub} = 6.596$ kg

The overall reduction in liquid-water by evaporation and sublimation was approximately 15 %, but this represented an estimate based on thermodynamic properties, temperature and time measurements. The coolth stored will be compared to the coolth discharged to examine the accuracy of the estimates.

6.6.5. Sensible cooling of the ice store

Once the evaporator/ice store was fully charged, the experiment continued so that the effect of sublimation on ice storage capacity could be analysed. Figure 6.3 showed that the temperature of the ice in the capsules continued to fall from 84 minutes to 210 minutes. The temperature of the bottom capsule (T_3) decreased to approximately -7 °C in that time, but with increases in temperature on three occasions. During the test, non-condensables built up in the condenser and caused the condenser pressure to exceed the critical pressure. The jet-pump would cease to entrain vapour from the evaporator/ice store, and further increases in pressure may cause a reversal of primary flow back into the evaporator/ice store, resulting in a rapid increase in pressure and temperature. Decreases in evaporator pressure can be seen in Figure 6.3, which correspond to occasions when a vacuum pump was used to remove non-condensables from the condenser. This also resulted in a decrease in temperature as the jet-pump regained its action. The saturation pressure in the evaporator fell from approximately 520 Pa to 310 Pa during this period. A reduction of this magnitude would cause a large decrease in secondary

flow because its proportional relationship with the saturation conditions in the evaporator/ice store. The mass sublimated can be estimated from Equation 6.19.

$$\Delta m_{sub} = \frac{(\sum m_i C_i + m_v C_v)\Delta T}{h_{sub} + C_i \Delta T} \tag{6.19}$$

Substituting values of thermodynamic properties into Equation 6.19 gives

$$\Delta m_{sub} = \frac{(((0.395 + 6.596) \times 1.9) + 33.235) \times 7}{2838 + (1.9 \times 7)}$$

$\Delta m_{sub} = 0.114\text{kg}$

The estimate of mass sublimated resulted in a 2 % decrease in ice stored.

6.6.6. Cooling capacity

Cooling capacity was determined for both the charge period, and the total test duration, including the reduction due to sublimation. The charge period will be used to establish a mean coolth storage rate, so that jet-pump and ice store performance can compared and the results contrasted with those found in spray ice TIS testing. The overall cooling capacity will be used to compare it with the discharge measurements, so that assumptions made for the charge cycle can be tested.

The cooling capacity during ice storage was found from Equation 6.20, thus;

$$Q_i = \sum m_i h_{if} \tag{6.20}$$

At the end of the latent cooling period, the ice stored in the capsules was the sum of the ice formed during both the supercooling and latent cooling regimes.

$$\sum m_i = m_{iF} + m_{isub} \tag{6.45}$$

$\sum m_i = 0.395 + 6.596$

$\sum m_i = 6.991\text{kg}$

Therefore cooling capacity is,

$Q_i = 6.991 \times 333.5$

$Q_i = 2331\text{kJ}$

6.6.7. Average coolth storage rate

Figure 6.4 shows the change in temperature in the top, middle and bottom capsules during freezing. It can be seen that the temperature in the top and middle capsules start to decrease at about the same time. This is at approximately 76 minutes. The time duration for sublimation freezing is therefore 52 minutes.

The estimated mass of ice stored during sublimation freezing was entered into Equation 6.20 to give

$$Q_{\mathrm{i}} = 6.596 \times 333.5$$

$$Q_{\mathrm{i}} = 2200 \text{ kJ}$$

The average coolth storage rate is

$$\dot{Q}_{\mathrm{i}} = \frac{Q_{\mathrm{i}}}{\Delta t} \tag{6.22}$$

$$\dot{Q}_{\mathrm{i}} = \frac{2200}{52 \times 60}$$

$$\dot{Q}_{\mathrm{i}} = 705\mathrm{W}$$

The mean coolth storage rate during spray ice TIS was 347 W, which was approximately 50 % less than that found in encapsulated ice TIS. There are two main reasons for the difference in coolth storage rate. First, the nozzle used in the encapsulated ice TIS tests had a smaller exit area compared with that used in spray ice TIS testing. Results from Chapter 4 showed that an over-expanded nozzle would restrict secondary flow and cause an increase in losses in the mixing section. Second, approximately 8.5 kg of ice is formed per kg of ice sublimated, compared to 7.5 kg of ice formed per kg of water evaporated.

6.6.8. COP

The COP was determined from measurements of both ice storage and jet-pump testing to provide a check for previous ice storage data, to investigate the

relationship between jet-pump and ice store and compare the two methods of performance measurement. The COP of the thermal ice store is calculated from Equation 6.22.

$$\text{COP} = \frac{Q_{\text{i}}}{Q_{\text{g}}} \tag{6.22}$$

and heat input to the generator is calculated from Equation 5.18.

$$\dot{Q}_{\text{g}} = \dot{m}_{\text{p}}(h_{\text{g},Tg} - h_{\text{f},Tc}) \tag{5.18}$$

The generator and condenser liquid temperatures were 115 °C and 20 °C respectively, which correspond to a specific enthalpy of saturated vapour of 2699 kJ.kg^{-1} and a specific enthalpy of saturated liquid of 84 kJ.kg^{-1}. Table 6.4 shows the samples of primary flow taken during the charge period. The average primary mass flow was 0.968 g.s^{-1}.

Table 6.4. Measured primary mass flow

	ΔH (mm)	Δt (min)	$\dot{m}_{\text{p}}$ (g.s^{-1})
1	89	32.42	0.9852
2	126	42.42	1.0660
3	144	53.42	0.9675
4	55	21.00	0.9399
5	91	36.33	0.8989
6	82	31.00	0.9493
Average			0.9678
Standard error			±0.073
Calibration factor, F_{p} = 0.3589E-3 g/mm: $\dot{m}_{\text{p}} = F_{\text{p}} \frac{\Delta H}{\Delta t}$			

$$Q_{\text{g}} = 0.968 \times (2699 - 84) \times 52 \times 60$$

$$Q_{\text{g}} = 7898 \text{ kJ}$$

The COP from ice storage measurements is therefore,

$$\text{COP} = \frac{2200}{7898}$$

$$\text{COP} = 0.279$$

This will be compared with the COP found from jet-pump measurements, which is a function of entrainment ratio.

6.6.9. Entrainment ratio

The COP of the jet-pump TIS system was determined from measurements of entrainment ratio using Equation 6.26.

$$\mathrm{COP} = \omega \frac{h_{\mathrm{sub}}}{h_{\mathrm{g},Tg} - h_{\mathrm{f},Tc}} \tag{6.26}$$

Secondary mass flow was determined during the change of phase by measuring the mass of vapour leaving the generator at constant generator temperature and the mass of condensate collected. The measurement of condensate mass flow is shown in Table 6.5. Secondary flow is the difference between condensate and primary mass flows.

$$\dot{m}_{\mathrm{s}} = \dot{m}_{\mathrm{c}} - \dot{m}_{\mathrm{p}} \tag{6.46}$$

$$\dot{m}_{\mathrm{s}} = 1.2131 - 0.968$$

$$\dot{m}_{\mathrm{s}} = 0.245 \mathrm{g.s}^{-1}$$

Table 6.5. Measured condensate mass flow

	ΔH (mm)	Δt (min)	$\dot{m}_{\mathrm{c}}$ (g.s^{-1})	Error
1	679	45.53	1.2131	$\pm$ 0.0229
Calibration factor, F_{c} =4.8805E-5 g/mm : $\dot{m}_{\mathrm{c}} = F_{\mathrm{c}} \frac{\Delta H}{\Delta t}$				

Entrainment ratio was found from Equation 4.1,

$$\omega = \frac{\dot{m}_{\mathrm{s}}}{\dot{m}_{\mathrm{p}}} \tag{4.1}$$

$$\omega = \frac{0.245}{0.968}$$

$$\omega = 0.253$$

The percent relative errors of the secondary flow and entrainment ratio were calculated according to the procedure described in Appendix D, and were found to be approximately 7 % and 6.5 %, respectively.

The estimated entrainment ratio during spray ice TIS was 0.158, which was approximately 40 % less than during encapsulated ice TIS. The entrainment ratio is higher because the primary flow is restricted by over-expansion of the primary flow, and an increase in losses in the mixing section.

The COP based on jet-pump measurements is

$$\mathrm{COP} = \omega \frac{h_{\mathrm{sub}}}{(h_{\mathrm{g},Tg} - h_{\mathrm{f},Tc})} \tag{6.26}$$

The latent heat of sublimation at 0 °C is 2838 $\mathrm{kJ.kg^{-1}.K^{-1}}$, thus

$$\mathrm{COP} = 0.253 \times \frac{2838}{(2699 - 84)}$$

$$\mathrm{COP} = 0.275$$

This is about 1.5 % greater than the COP found from entrainment ratio measurements. The determination of COP from ice storage measurements depended on the identification of the time to complete solidification, but this is difficult to determine accurately. However, the measurement of secondary flow is simple and provides a practical method for determining the ice storage characteristics over the charge period.

The COP during spray ice TIS was 0.152 which is approximately 40 % less than that found from encapsulated ice TIS because of the restriction of secondary flow with over-expansion. It was shown that there was a reduction in the average coolth storage rate of approximately 50 %, 40 % of which was attributable to the restriction in flow. There was a further 10 % difference because of the higher ice storage rate due to sublimation freezing. The large losses due to restriction in flow show that it is important to use a nozzle close to the design operating conditions, especially when the COP is inherently low. The results show that encapsulated ice

especially when the COP is inherently low. The results show that encapsulated ice TIS is superior to spray ice TIS because, for the same nominal secondary flow, the average coolth storage rate is enhanced through sublimation freezing.

The literature review highlighted a model of the solidification of a semi-infinite layer by Yeh and Cheng [22], where the heat released in freezing water at the solid-liquid interface is transferred by conduction across the ice layer and then released as the heat of sublimation at the solid-vapour interface. The vapour temperature decreases over time as the ice layer thickness increases. In the case of a solidifying spherical capsule, the ice layer is finite, and there will only be a small reduction in vapour temperature and pressure over the charge period. However, Figure 6.3 showed that the temperature of the frozen capsules began to decrease before complete solidification, therefore, the vapour pressure and temperature fall because of the sensible cooling of the solidified proportion of the bed. The small-scale ice store used in the experiments only experiences a small decrease in vapour pressure and temperature during the charge phase. A large-scale system may undergo a large reduction in pressure and temperature over the charge period, causing a reduction in ice storage rate and COP.

6.7. Coolth discharge cycle

The objective of measuring the coolth discharged was to compare it with the coolth stored, in order to validate the estimate that was based on thermodynamic relations at the triple point, and the assumption that the freezing process was adiabatic. A secondary objective was to use the data to compare the discharge characteristics with a water-polymer gel system consisting of larger diameter spherical capsules. This section describes the experimental method of the discharge cycle and the results of the tests.

6.7.1. Experimental method

Referring to the diagram of the test rig in Figure 3.2, when the charge test had been completed, water from the storage vessel (17) was delivered to the evaporator (12). With valve (d) closed, the storage vessel was exposed to atmospheric pressure so that the pressure difference could be used to refill the evaporator more rapidly via valves (a) and (c), than by the circulation pump (22). Once the evaporator water level was above the bed of capsules, valve (c) was shut and water from the evaporator was re-circulated by the pump (20) through the heat-exchanger (26) via valves (c) and (k). The centrifugal pump (23) was started, delivering water from the heat load simulator (22) to the heat exchanger. The circulation pump flow was kept constant whilst the heat load flow varied by valve (n) to maintain an approximate constant inlet temperature. Pump flows were calibrated, temperatures in the bed of ice capsules, and temperature into and out of the heat exchangers were recorded at two-minute intervals. Testing continued until the temperature of the bottom capsule reached that of the surroundings. The measurement of temperatures and flows enabled an estimate of coolth discharge to be made, thus allowing the simplifying assumptions described in Section 6.7 to be tested and also enabling a comparison of the discharge rates of the bed of 22 mm diameter and 40 mm diameter capsules. This section describes the results from the discharge cycle and the comparisons made between charge and discharge cycles and different diameter capsules.

6.7.2. Cooling capacity

Figure 6.4 shows the variation in water temperature in the top and bottom capsules during the charge and discharge cycles.

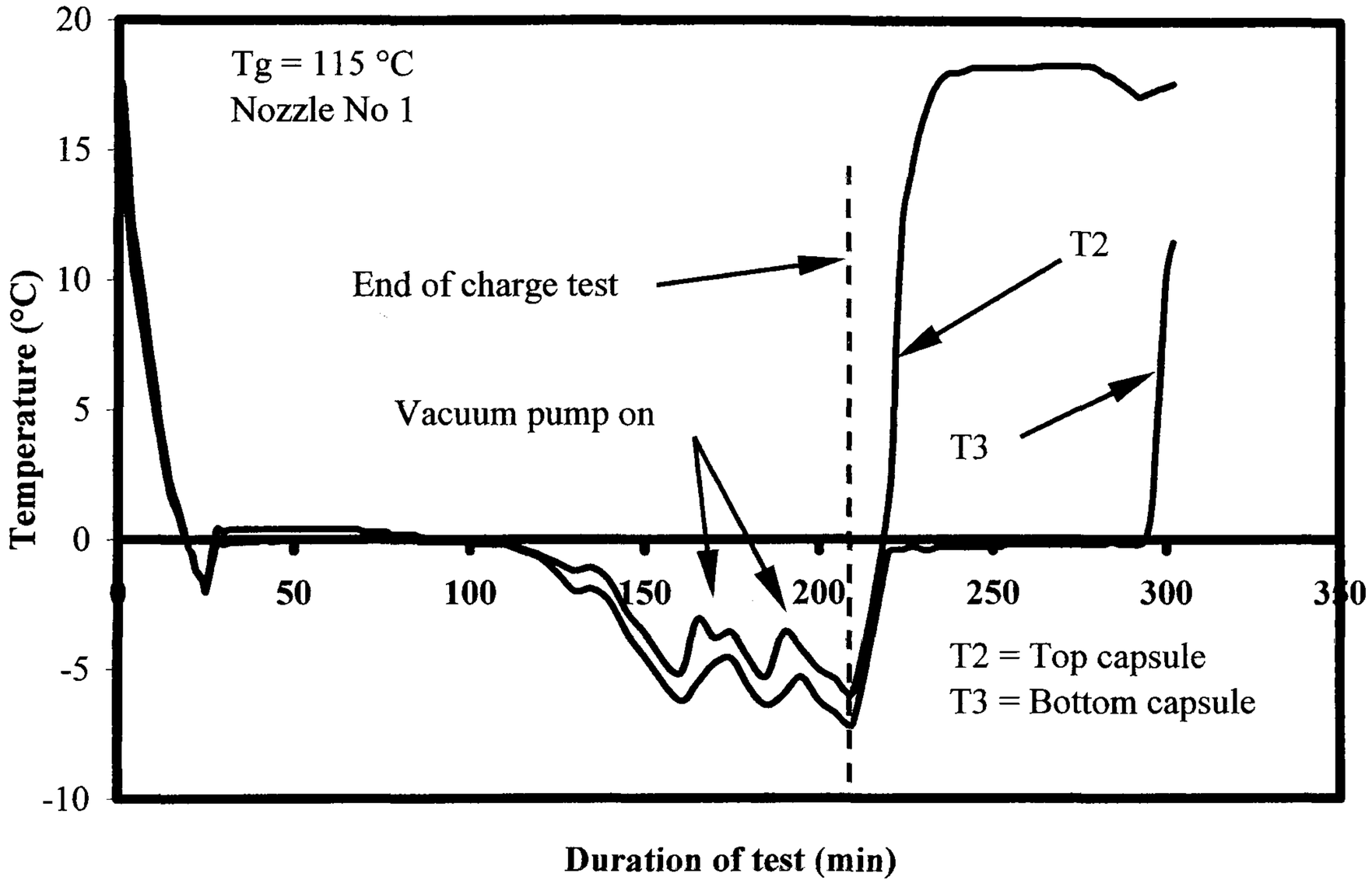

Figure 6.4. Variation in water temperature during the charge and discharge phases.

Once the change of phase had been completed, ice was sensibly cooled to -7.1 °C in the bottom capsule by sublimation. There was approximately a 1 °C difference in temperature between the top and bottom capsule, with the temperature difference increasing with time, showing that there was a difference in cooling rates through the bed. There was about a 10-minute interval between the end of the charge test and the start of ice store discharge due to refilling of the evaporator and bringing the heat transfer fluids in the heater and chiller circuits to a steady-state condition. The temperature of the top gel capsule was 1.5 °C at the start of discharge, then rapidly increased until it reached the temperature of the surrounding vapour. The temperature inside the bottom capsule in the

evaporator/ice store remained at freezing point for approximately 74 minutes, before beginning to rise.

Figure 6.5 shows the change of temperature vertically through the bed. T_2, T_6, T_3 are the temperatures of elements in the top, mid-section, and bottom of the bed. T_8 shows the temperature of surrounding water at the base of the evaporator vessel, and T_{10} records the temperature of the surrounding water at the mid-section of the

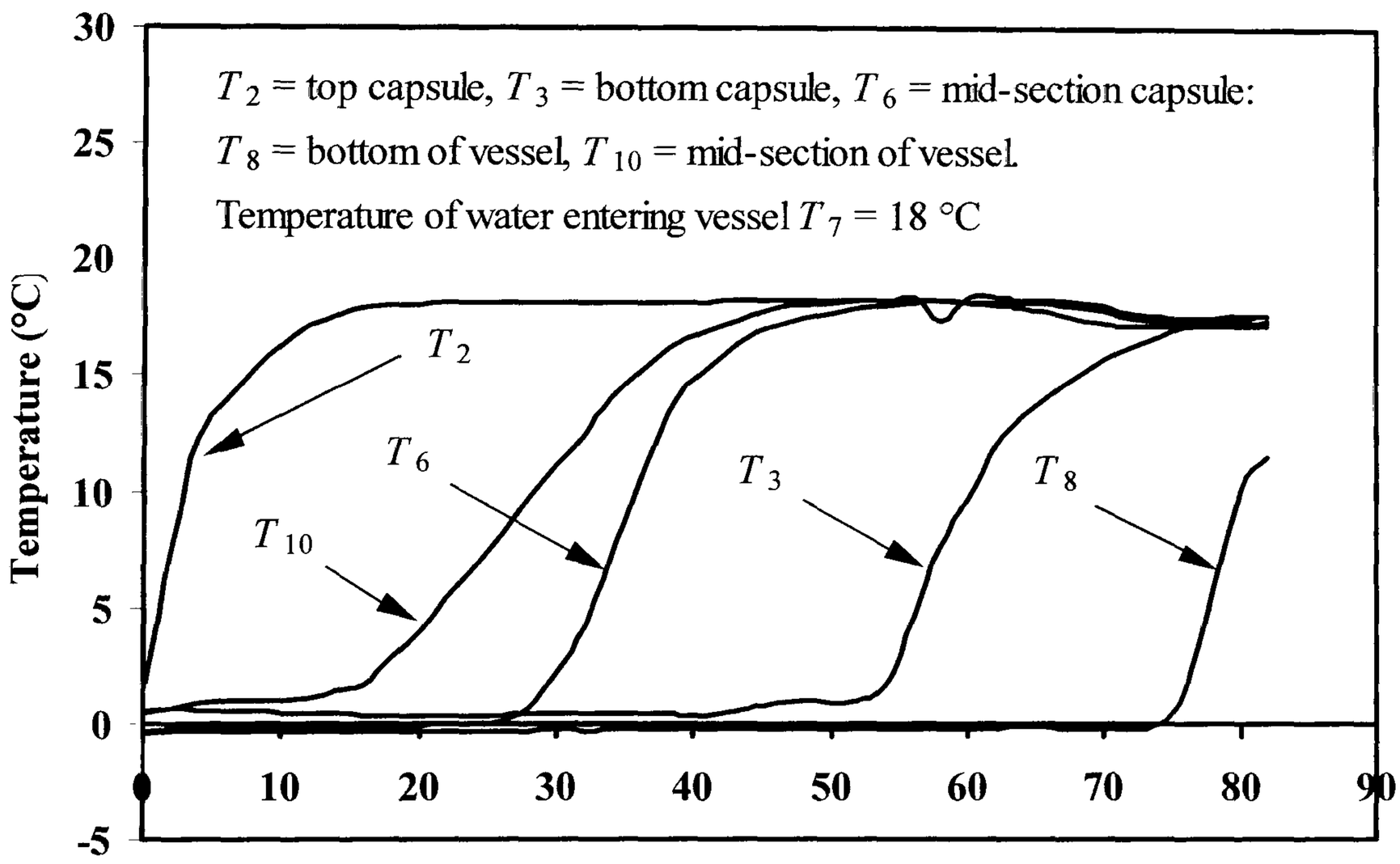

Figure 6.5. Variation in water temperature through the bed during ice store discharge.

vessel. It can be seen that there was stratification of temperature through the bed during discharge as the ice in the capsules melted from the top down. The capsules remained at the equilibrium freezing temperature until most of the ice had melted and then increased sharply as the liquid elements transferred their remaining coolth sensibly. The points at which the elements in the top, mid-section and bottom had completely melted, indicated by a rise in temperature, was not linearly

related with time. The temperature of the top element began to rise at the start of the discharge test, the mid-section element began to rise after 28 minutes and the bottom element rose at 74 minutes.

At 56 minutes, the temperature at the base of the evaporator vessel had reached approximately 5 °C, but a proportion of the bed of elements was still frozen, thus, there was still cooling capacity but it may not be possible to usefully discharge the remainder. This is a common problem with static TIS systems, whether ice-on-pipe or encapsulated. This may indicate an advantage of spray ice TIS, in that ice is continually being produced and stored in a water/ice slurry vessel, then a slurry mix of ice and brine is delivered to the building, or district cooling system. Potentially, all of the ice manufactured by the jet-pump spray ice TIS could be discharged so eliminating the losses in being unable to fully discharge an ice store in encapsulated ice TIS. Spray ice TIS could also be used out of phase with the building's cooling load so that a water/ice mix is built-up overnight then discharged as slurry during the day.

Figure 6.6 shows the temperature of water entering the evaporator through the spray nozzle and in the bottom of the evaporator. The inlet temperature remained at approximately 18 °C, whilst the base temperature remained at 0 °C for 54 minutes and then began to rise. Heat transfer was determined at two-minute intervals using the temperature difference ($T_7 - T_8$) in Figure 6.7, the calibrated mass flow through the heat exchanger and the average specific heat capacity of water.

Figure 6.7 shows the heat transfer during the discharge period. The approximately constant coolth discharge rate for the majority of the cycle is characteristic of TIS systems. The temperature in the evaporator/ice store remains approximately constant as the latent heat stored as ice is released whist melting. The coolth discharge rate begins to fall at approximately 56 minutes, which coincides with the rise in temperature of the water in the base of the vessel (T_8) in Figure 6.6. The

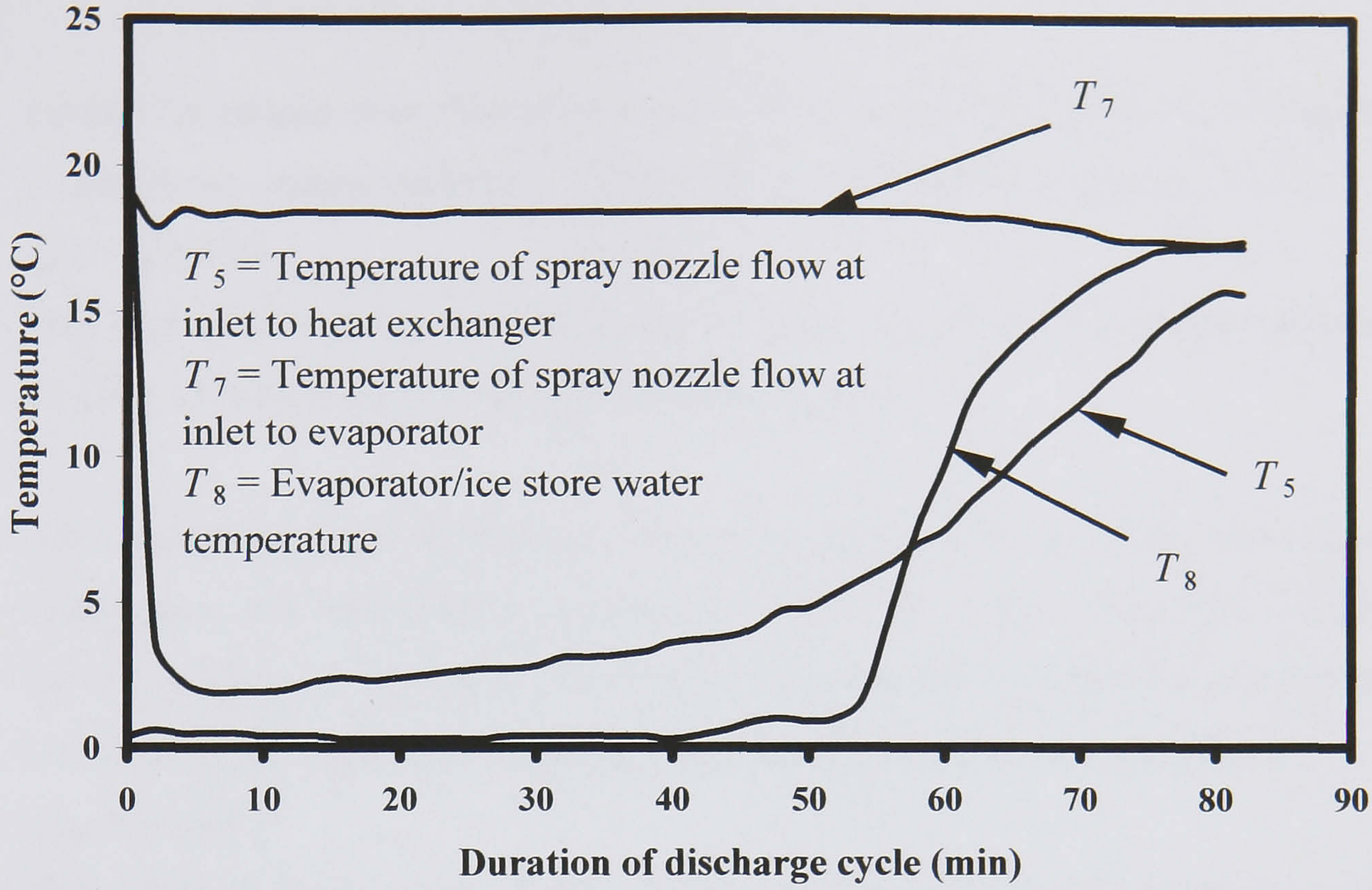

Figure 6.6. Variation in temperature on chiller side of heat exchanger

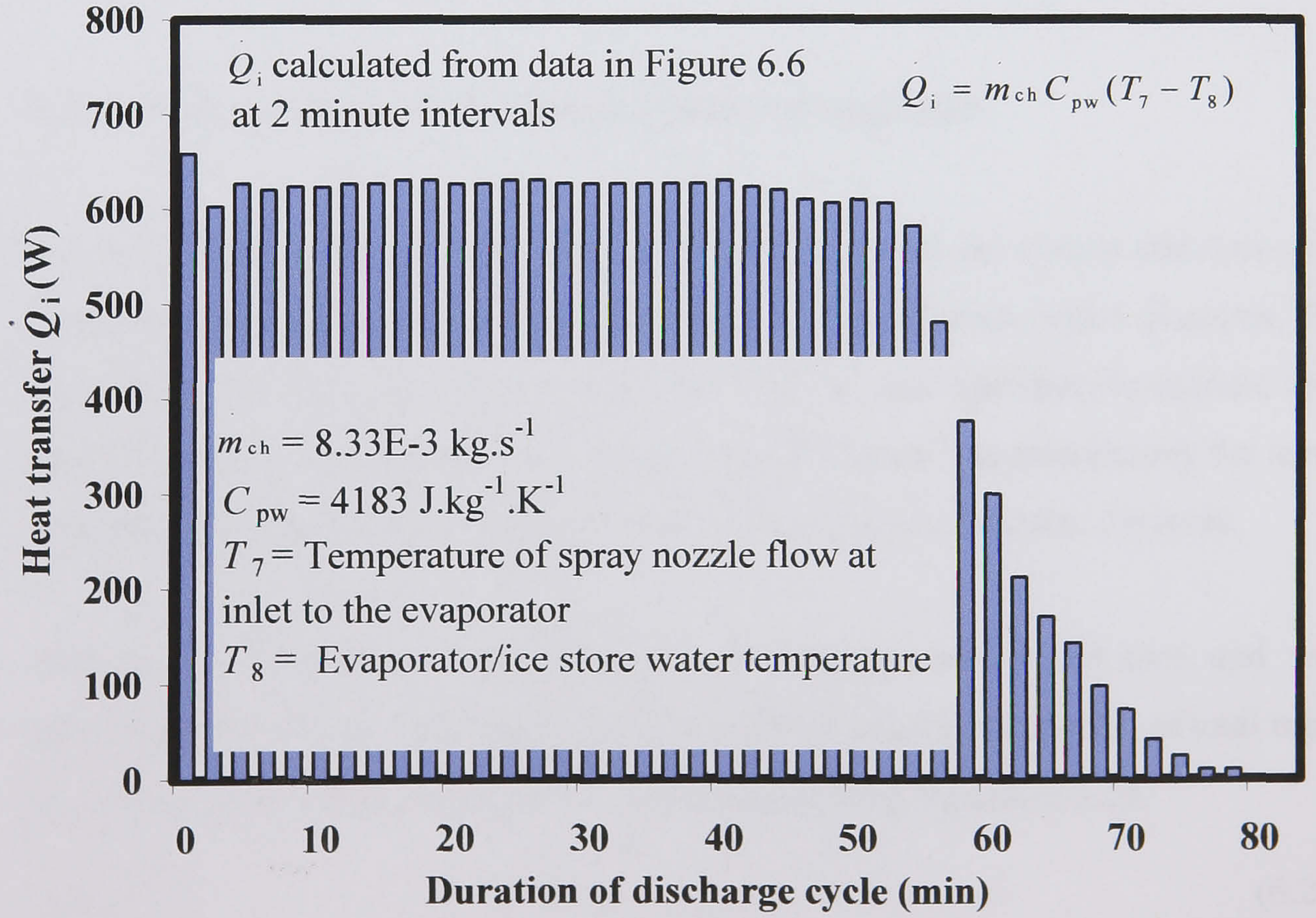

Figure 6.7. Heat transfer from the bed of encapsulated elements

coolth discharged over this period was determined by summing the calculated values at two-minute intervals. The total coolth discharged was estimated to be

$Q_{dis} = 2327$ kJ

The total coolth stored was estimated to be 2331 kJ compared to a coolth discharge of 2327 kJ, which was a difference of approximately 3 %.

This shows that good estimates of cooling capacity could be made from simple evaporation and sublimation relationships. The base water temperature reached 10 °C, as shown in Figure 6.7, at about 60 minutes, but a proportion of elements were still frozen. The coolth discharged up to that period was estimated to be

$Q_{dis} = 2194$ kJ

This shows that approximately 6 % of the coolth stored in the charge phase would have remained frozen if discharge had been halted at that point. It was mentioned earlier, that spray ice TIS may be advantageous over encapsulated ice TIS because an ice store may be more fully discharged using an ice/brine slurry.

6.7.3. Comparison with 40mm diameter capsules

Hiromi [54] carried out experiments on the same polymer gel system that was used in the encapsulated ice TIS tests. The capsules were 40 mm inside diameter, the total mass was 9 kg, the surface area was 1.37 m^2, and the specific surface area was 170 $m^2.m^{-3}$. The flow through the bed was 0.5 $l.min^{-1}$, approximately the same as the re-circulation flow in the tests on the 22 mm inside diameter capsules.

The average coolth discharge rate remained approximately constant and was approximately 333 W. The surface area of a bed of spherical capsules of total mass m, density ρ_L and capsule radius r_i was calculated from Equation 6.29.

$$SA = \frac{3m}{\rho_L r_i} \tag{6.29}$$

For a total mass of 9 kg, radius of 0.02 m and density of 1000 kg.m^{-3}, the surface area of the 40 mm diameter spheres was

$$SA = \frac{3 \times 9}{1000 \times 0.02}$$

$$SA = 1.350 \text{ m}^2$$

The total surface area given in the specification was 1.37 m^2 which is only 1.5 % greater than that found from Equation 6.29.

For a total mass of 7.177 kg and radius of 0.011 m, the surface area was

$$SA = \frac{3 \times 7.177}{1000 \times 0.011}$$

$$SA = 1.957 \text{ m}^2$$

Heat flux is calculated from Equation 6.27.

$$\dot{q} = \frac{\dot{Q}}{SA} \tag{6.27}$$

The heat flux from the 40 mm diameter spheres at an average coolth discharge rate of 333 W and flow through the bed of 0.5 l.min^{-1} is

$$\dot{q} = \frac{333}{1.350}$$

$$\dot{q} = 247 \text{W.m}^{-2}$$

and the heat flux from the 22 mm diameter spheres at an average coolth discharge rate of 628 W and flow through the bed of 0.5 l.min^{-1} is

$$\dot{q} = \frac{628}{1.957}$$

$$\dot{q} = 322 \text{W.m}^{-2}$$

This shows that that heat transfer is enhanced by approximately 30 % when the diameter of a bed of spherical capsules is reduced from 40 mm to 22 mm.

A bed of smaller capsules enhances coolth charge and discharge rates because of the increase in specific surface area, but there is a lower limit to the practical size of sphere used. The polymer absorbs approximately 100 times its mass of water,

increasing the errors in manufacture with a decrease in individual capsule volume. A sphere is ideal for heat and mass transfer, but it may not provide the maximum surface area for a given vessel, because the rows may not conform to the optimum packing arrangement, and other geometries may pack together more efficiently, presenting greater overall surface area. It may be advantageous to pack different geometries in the same bed. For instance, it may be advantageous to have cylindrical capsules around the outer wall, then small diameter spheres close to the cylinders and larger diameter spheres in the bulk of the bed.

6.8. Discussion

The results from the experimental rig showed that the COP was around 0.2 during encapsulated ice TIS, which is low compared with other heat powered TIS systems and conventional vapour-compression TIS. Encapsulated ice TIS can only operate in separate charge and discharge phases, but the test rig was designed to operate at condenser temperature of 30 °C. A practical encapsulated ice store would operate at off-peak periods, typically, 7.00 pm to 7.00 am. Ambient temperatures would be in the region of 10 °C to 15 °C, depending upon the time and date. The lowest average wet bulb temperature in July at Kew, UK was 12.3 °C, according to CIBSE [56]. A jet-pump TIS system constrained to operate at a condenser pressure corresponding to a wet bulb temperature of 15 °C could reduce the critical pressure lift ratio, increasing entrainment ratio and boosting COP. If the jet-pump ice storage system were to be designed to operate at 1704 Pa (T_{sat} = 15 °C) then the desired pressure lift ratio given the same inlet conditions would be 3.1. Appendix E shows that a jet-pump designed for a pressure lift ratio of 3.1 would be able to operate with an entrainment ratio of 0.7275 and a COP of 0.7913. COP is increased by more than three times when operating at reduced ambient conditions and is equivalent to a single effect ammonia/water TIS absorption system and a vapour-compression chiller when losses and part-load performance are taken into account. An outlet pressure of 1704 Pa is a conservative choice as it assumes an average minimum temperature in July. A cooling season from the beginning of

May to the end of August would result in lower condensing temperatures (an entrainment ratio of unity may be possible). A range of jet-pumps delivering cooling capacity according to variations in condenser conditions throughout the cooling season, as was suggested in Chapter 4, could optimise the overall system COP, and so make it competitive with other systems.

6.9. Conclusions

Experimental results have revealed a number of characteristics when a jet-pump is coupled to an encapsulated ice store.

The coolth storage rate was approximately double that found in spray ice TIS testing. Approximately 40 % of the difference was due to the restriction in flow and increases in momentum losses in the mixing section. It is important that any over-expansion of the primary flow is minimised to maximise COP. A further 10 % of the difference was due to sublimation freezing, which shows that encapsulated ice TIS is superior to spray ice TIS in terms of coolth storage rates.

An encapsulated ice TIS is superior to a spray ice TIS when shifting the cooling load to off-peak periods, because of the enhanced cooling capacity due to sublimation freezing, but such systems can only operate in separate charge and discharge cycles. Spray ice TIS may be more suitable when the heat source is in synchronisation with the cooling requirements of a building, or a district.

Encapsulated ice TIS systems experience difficulties in fully discharging the coolth, in this case approximately 6 % was left frozen, but spray ice TIS can discharge the coolth by supplying an ice/brine slurry, and so may be advantageous if the remaining stored coolth is large.

The COP was between 0.2 and 0.3, which is low compared to other competitive cooling and TIS systems, but an encapsulated ice TIS designed for low ambient

conditions experienced at off-peak periods could match the performance of other systems and take advantage of the its simple operation and low maintenance.

The assumption that 8.5 kg of ice was formed per kg of ice sublimated from surface provided a good estimate of cooling capacity during the charge phase. Only a simple estimate of the mass evaporated in the first cooling regime was needed because it was only a small proportion of the total mass frozen.

As under evaporative freezing conditions, measurement of secondary mass flow could give a good estimate of ice storage rate. This assumes that the sublimation rate is approximately equal to secondary mass flow, which is valid over short time intervals (30 minutes) during the change of phase to ice. Although the experimental results showed approximately steady-state conditions in the evaporator over the charge period, static pressure was observed to decrease slowly with time. This would reduce the performance of a jet-pump used in charging a large capacity ice store over time.

The use of spherical water/gel capsules maximised the surface area available for heat and mass transfer and it was shown that a reduction in diameter from 40 mm to 22 mm increased the heat flux by approximately 30 %. The granular structure of the polymer gel may initiate ice crystal nucleation at lower degrees of supercooling, allowing the jet-pump system to operate at higher saturation conditions compared to a capsule partially filled with water only.

Chapter 7. The convergent-divergent jet-pump

7.1. Introduction

The convergent-divergent throat jet-pump was designed to eliminate the shock wave characteristic of jet-pump systems, and to examine the performance of a jet-pump manufactured from a plastic material. If the shock wave could be eliminated then losses could be reduced and higher performance achieved for the same inlet conditions, and if a jet-pump were manufactured from a plastic material then, in principle, a large number of units could be made from a single mould, reducing first cost. A convergent-divergent throat jet-pump is difficult to manufacture, so is not practical if the jet-pump were to be machined, but the inverse of a convergent-divergent throat can be machined easily, so can provide a convenient former in a plastic moulding system. The reduction in cost and the increase in performance could increase the use of jet-pumps in heat powered refrigeration in general, and jet-pump TIS in particular. This chapter describes the design and manufacture of the convergent-divergent jet-pump. The experimental method and the test results are then described and analysed in order to meet the objectives.

7.2.1. Design of the convergent-divergent jet-pump

A diagram of the convergent-divergent jet-pump is shown in Figure 7.1. The primary and secondary streams are assumed to have the same molecular weight and the same ratio of specific heats. The primary $\dot{m}_p$ and secondary $\dot{m}_s$ streams are assumed to be supplied at zero velocity in state *i* and *o*, respectively. The primary and secondary streams mix at constant pressure between *x* and 1. Losses are taken into account by applying isentropic efficiencies to the primary nozzle, and diffuser and a momentum loss coefficient to the mixing chamber. The mixing of the two streams is assumed to be complete before reaching section 1.

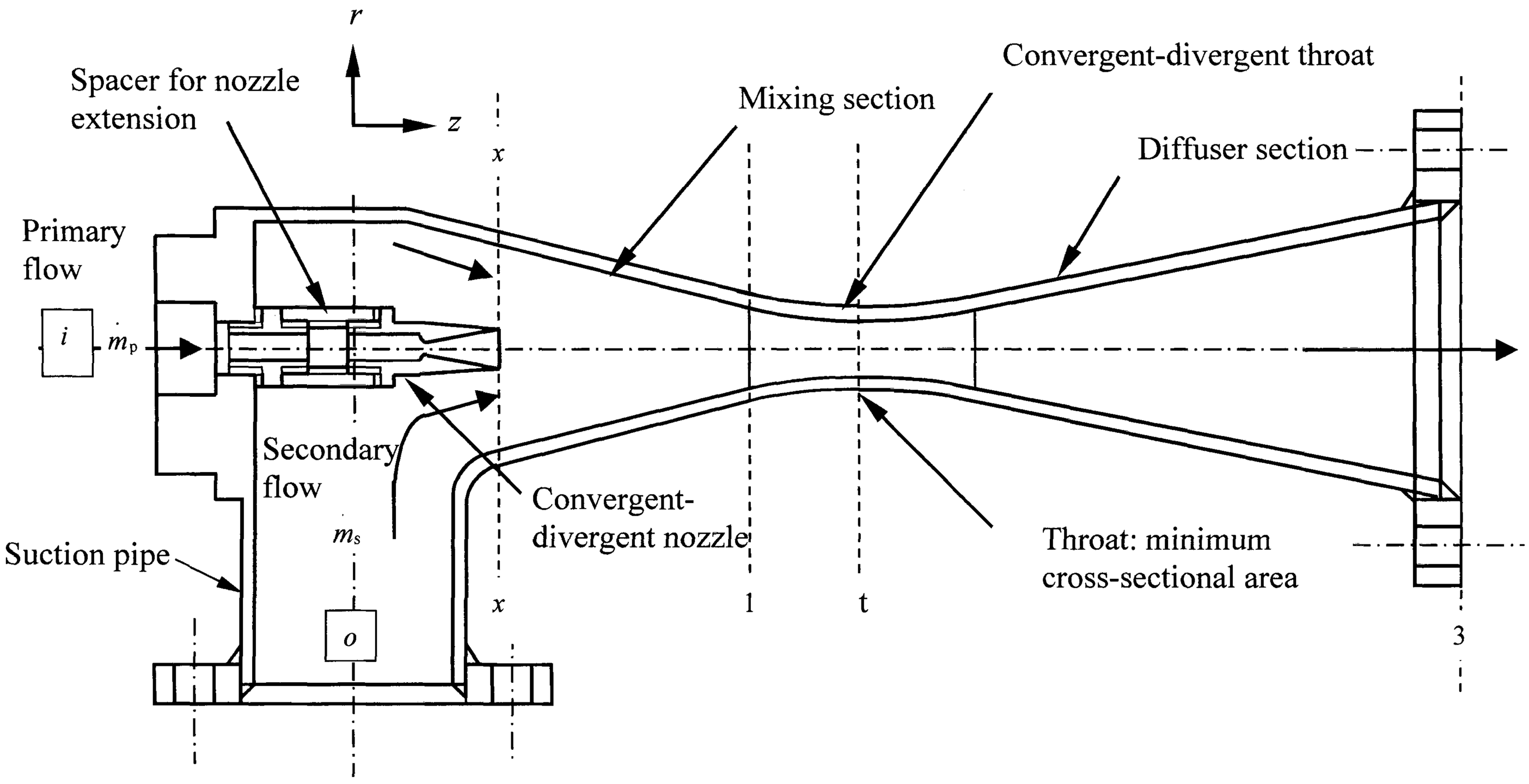

Figure 7.1. Schematic diagram convergent-divergent throat jet-pump

It is assumed that the vapour behaves as a perfect gas. It is assumed that the static pressure of the mixed stream rises linearly downstream of section 1. The diffuser cone half angle is not allowed to exceed 4° in order to prevent possible flow separation.

7.2.3. States at nozzle exit plane *x*-*x* and after mixing at 1

The inlet geometry up to section 1 is the same as the jet-pump designed for a diffuser area ratio of 81, which was described in Chapter 4. Thus, the Mach number at section 1 is found from Equations 4.21 and 4.23 after pressure lift optimisation.

7.2.4. State between 1 and 3

The outlet stagnation temperature T_3 is found from Equation 4.9, and the stagnation pressure P_3^* is found from Equation 4.13. The relationship between and local and stagnation temperatures and Mach number is found from Equation 4.38, shown again below.

$$\frac{T_3}{T_1} = \left(1 + \frac{k-1}{2} \mathrm{M}_1^{\,2}\right) \tag{4.38}$$

The difference between static pressure at the end of constant pressure mixing and at the outlet is divided into a number of stations between 1 and 3 so that the static pressure increases linearly with distance. The static temperature is re-calculated using Equation 4.13 and the local Mach number is found from Equation 4.38. The area at that station is then calculated from Equation 4.28, shown again below, by inserting the combined mass flow, the local Mach number and outlet stagnation conditions.

$$A = \frac{m}{\mathrm{M}}\left[\frac{RT_0}{k}\left(1 + \frac{(k-1)}{2}\mathrm{M}^2\right)^{\frac{k-1}{k+1}}\right]^{\frac{1}{2}} \tag{4.28}$$

The calculation procedure continues downstream at each station giving a constantly changing cross-sectional area with distance downstream. The minimum area at the throat can be calculated by setting the Mach number in Equation 4.28 to unity. Upstream of the throat supersonic flow decelerates with convergence, and downstream of the throat subsonic flow decelerates with divergence. The calculation procedure continues downstream until the change in radius with axial distance equals 4°. The length of the diffuser is extended at a half angle of 4° until the velocity at exit from the diffuser is less than 30 $m.s^{-1}$, because the length would tend to infinity for a velocity of zero to be achieved.

7.3. Construction of the convergent-divergent section

The dimensions of the double taper cone angle convergent mixing section were the same as described in Chapter 4. The end of the convergent mixing section was 136 mm downstream of the entrance, and this point was the zero datum point for the convergent-divergent section. Table 7.1 shows the variation in flow conditions and radius with position downstream of the zero datum point. The minimum radius at the throat was 7.42 mm and the axial position of the throat was 88 mm downstream from the zero datum point and therefore, 224 mm downstream from the entrance to the mixing section. Downstream of the throat, the radius increased until the change in angle with distance was greater than 4°. This occurred between 200 mm and 220 mm, so that the diffuser half angle downstream of this point was kept constant at 4°. The diffuser length was extended to 350 mm to give an outlet velocity of less than 30 $m.s^{-1}$. The overall length of the jet-pump insert was, therefore, 476 mm.

Table 8.1.Dimensions of convergnet-divergent jet-pump and flow conditions.

z	*P*	*U*	*T*	M	*r*
0	871.9	684.0919	242.8469	1.769953	8.9281
20	1247.511	618.1857	265.4333	1.53467	8.183126
40	1623.121	560.727	283.2593	1.350387	7.764954
60	1998.732	507.7891	298.1448	1.193876	7.531861
80	2374.342	457.118	311.0113	1.053597	7.429591
100	2749.953	407.0587	322.3956	0.922452	7.44079
120	3125.564	356.0464	332.6397	0.795019	7.573707
140	3501.174	302.1415	341.9764	0.665878	7.87047
160	3876.785	242.1313	350.5717	0.527386	8.45392
180	4252.395	168.2744	358.5484	0.362628	9.786506
200	4396.382	127.99	361.6891	0.274758	11.185
220	4484.127	100.4948	363.3423	0.215242	12.5835
240	4535.601	80.35986	364.3006	0.17189	13.982
260	4566.354	65.55349	364.8691	0.14011	15.3805
280	4585.539	54.36124	365.2223	0.116132	16.779
300	4597.954	45.70479	365.4503	0.097609	18.1775
320	4611.037	34.32296	365.69	0.073277	20.976
340	4614.964	30.08374	365.7618	0.064221	22.3745
350	4617.769	26.64837	365.8131	0.056883	23.773

The insert used in the jet-pump test rig was to be manufactured from an epoxy resin to test the practicality of using plastic as a material in a jet-pump system and to observe any difference in performance. The epoxy resin system consisted of a resin and a range of hardeners for different applications. A mould consisted of two formers that fitted together at the minimum area location, and an outer sleeve of a greater diameter than that of the insert tube in the test rig. The two central formers were manufactured from aluminium and were machined using the co-ordinates described in Table 7.1. A mild steel sleeve fitted around the former and was split down the seam to assist in removal after the resin had set. Figure 7.2 (a) shows a photograph of the two halves of the former together with the outer steel tube, resin, hardener and release agent. Figure 7.2 (b) shows the two half formers joined to provide the convergent-divergent profile.

An epoxy resin was selected because it was simpler to use in a laboratory environment. Epoxy resins are cold cure thermoset plastics, so can be mixed at ambient conditions, compared to hot cure plastics that require granules to be elevated above their melting point before being directed to the moulds. This would have required specialist equipment and added cost. Shrinkage of the cold cure resin was negligible, so did not need to be taken into account at the design stage. The two central formers and the inside of the steel tube were cleaned and polished to remove grease and dirt and to increase surface smoothness. A release agent was applied to the two central formers and the inside of the sleeve to help in the removal of the section from the mould. The two half formers were joined and the sleeve placed over them. A seal was fitted to the split and three clamps secured the sleeve around the central former. Silicone sealant was used to seal joints at the base of the mould and to provide a further seal to the vertical split. The mass of resin required to fill the mould was approximately 2 kg, and the proportion of resin to hardener was 2 to 1. A deep, shallow tray was used to mix the resin and hardener, so that the time between mixing and setting was maximised and air bubbles introduced during mixing could be eliminated. The first attempt used a

Figure 7.2 (a) Photograph of the two half-formers, sleeve and the epoxy resin system.

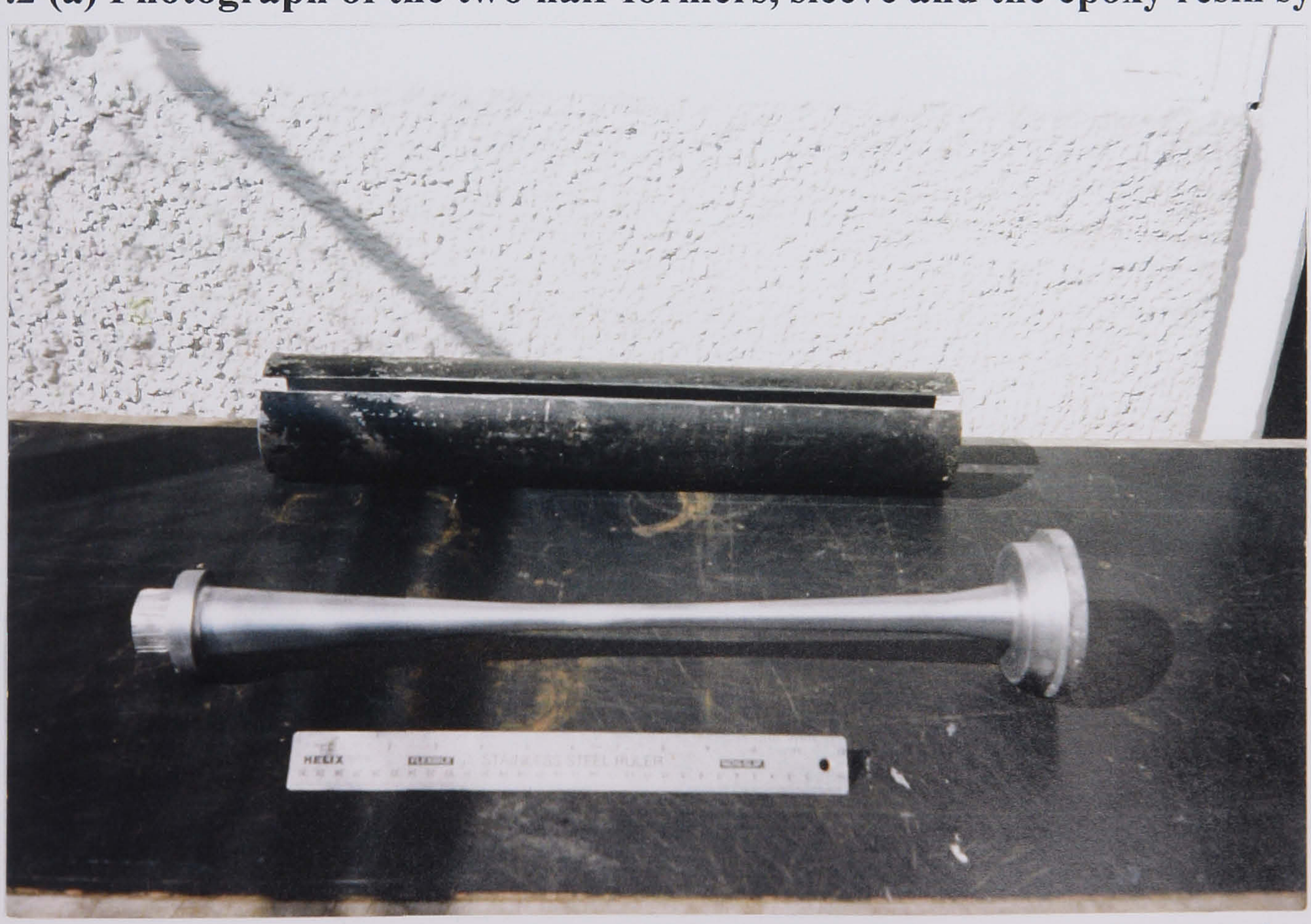

Figure 7.2 (b) Photograph of the assembled half-formers and outer sleeve.

fast hardener, which once fully mixed, took approximately 15 minutes to begin to set (called pot life). The reaction between the resin and hardener caused exothermic heating, leading to temperatures of up to 100 °C as the mixture set. It was found that there was too little time for small air bubbles trapped in the resin during mixing to be removed. As the temperature rose, the air bubbles expanded and moved due to convection currents. The resin section was constrained to fit inside a constant diameter tube, resulting in a variation in section thickness with axial distance. As in any casting, a good design has approximately constant thickness so that the transfer of heat from the resin to the surroundings is fairly constant. Different rates of cooling cause stresses to build up in the section. Two of the attempts resulted in cracking of the section. A slow hardener was used in subsequent tests to reduce the exothermic reaction and increase pot life. The last section manufactured was satisfactory but air bubbles were still evident at the surface of the former. The section was bored out approximately 10 mm larger than the diameter of the former, then a much smaller quantity of resin/hardener was made. This gave a smooth section for testing. Figure 7.3 shows a photograph of the completed epoxy resin section held in a centre lathe whilst the outer diameter was being turned down to fit into the test rig insert tube.

7.4. Test results

The main objective of manufacturing and testing the convergent-divergent throat jet-pump was to find out whether the shock process in a conventional jet-pump could be reduced or eliminated, and thus increase the pressure lift ratio for the same inlet conditions. If the shock wave could be eliminated then the COP could be boosted and a jet-pump TIS system may be more competitive with other systems. A secondary objective was to manufacture a jet-pump from a thermoset plastic, and examine its suitability for use in a practical system.

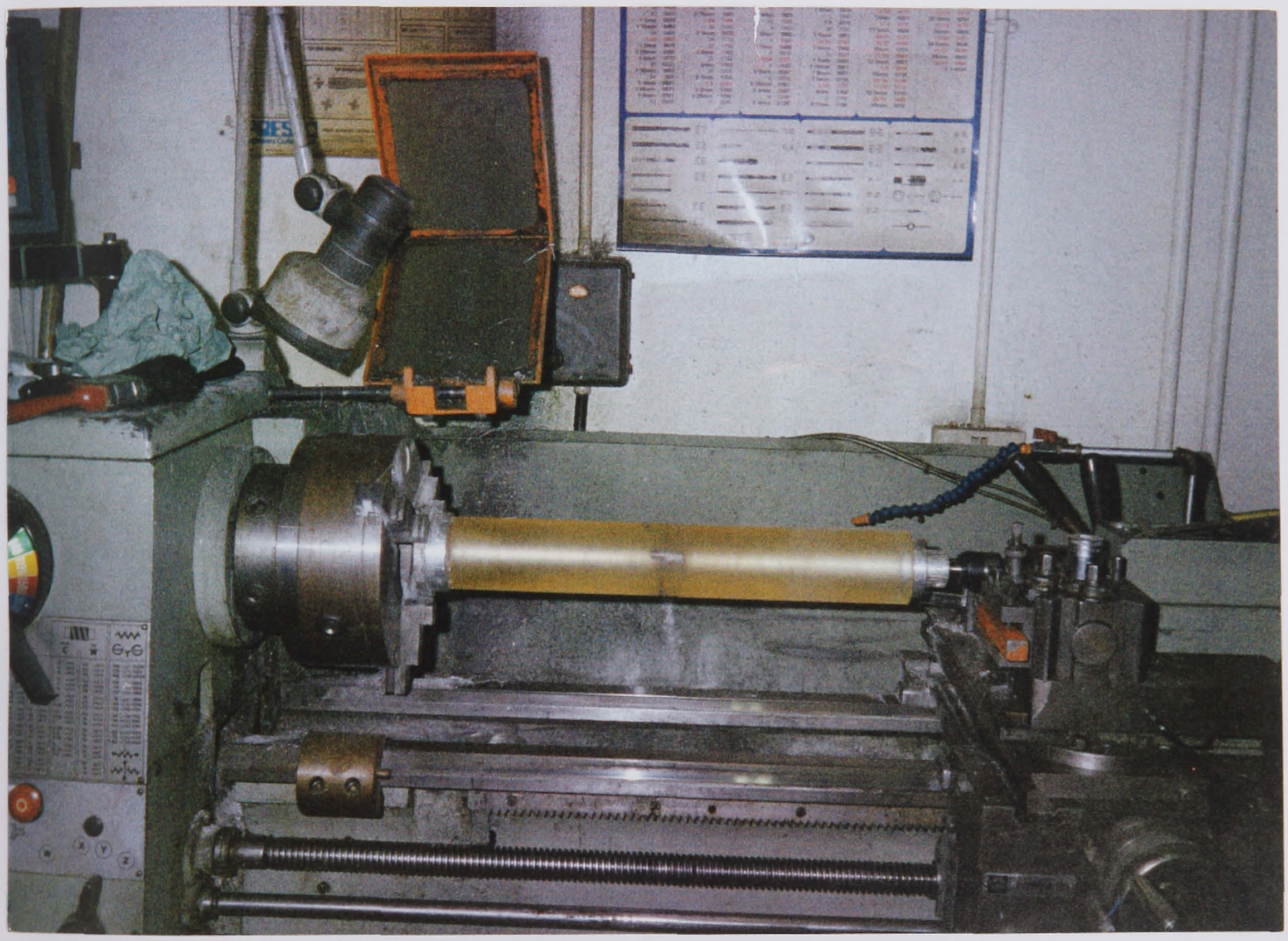

Figure 7.3. Photograph of the epoxy resin section being machined to fit into the jet-pump housing

7.4.1. Experimental method

Testing of the convergent-divergent throat jet-pump followed the procedure described in Chapter 4, except that method of determining secondary flow was modified. A condensate measuring vessel was introduced into the test rig in Figure 3.2, during encapsulated ice TIS and convergent-divergent jet-pump testing. Condensate was collected in the bottom of the condenser vessel (22). The level in the condenser was marked and the time noted, and after a period of time the condensate that had collected was pumped from the condenser vessel to the condensate measuring vessel (36). Pumping continued until the level in the condenser reached that of the marker. The level in the condensate measuring vessel was noted before and after pumping so that an estimate of condensate flow could be made, given the time interval and calibration coefficient. Secondary flow was then determined from the estimated primary and condensate flows.

7.4.2. Convergent-divergent throat jet-pump performance

Figures 7.4 and 7.5 show the measured entrainment ratio and condenser pressures from tests on the 18 mm diameter throat jet-pump and the convergent-divergent throat jet-pump, respectively. Both sets of results were carried out at a constant generator saturation temperature of 120 °C and an evaporator temperature of 5 °C. Figure 7.4 shows that the entrainment ratio was 0.4239 and the critical condenser was 3737 Pa. Pressures beyond that point caused jet-pump operation to become unstable, with reversal of primary flow into the evaporator, causing a rapid rise in evaporator pressure and temperature.

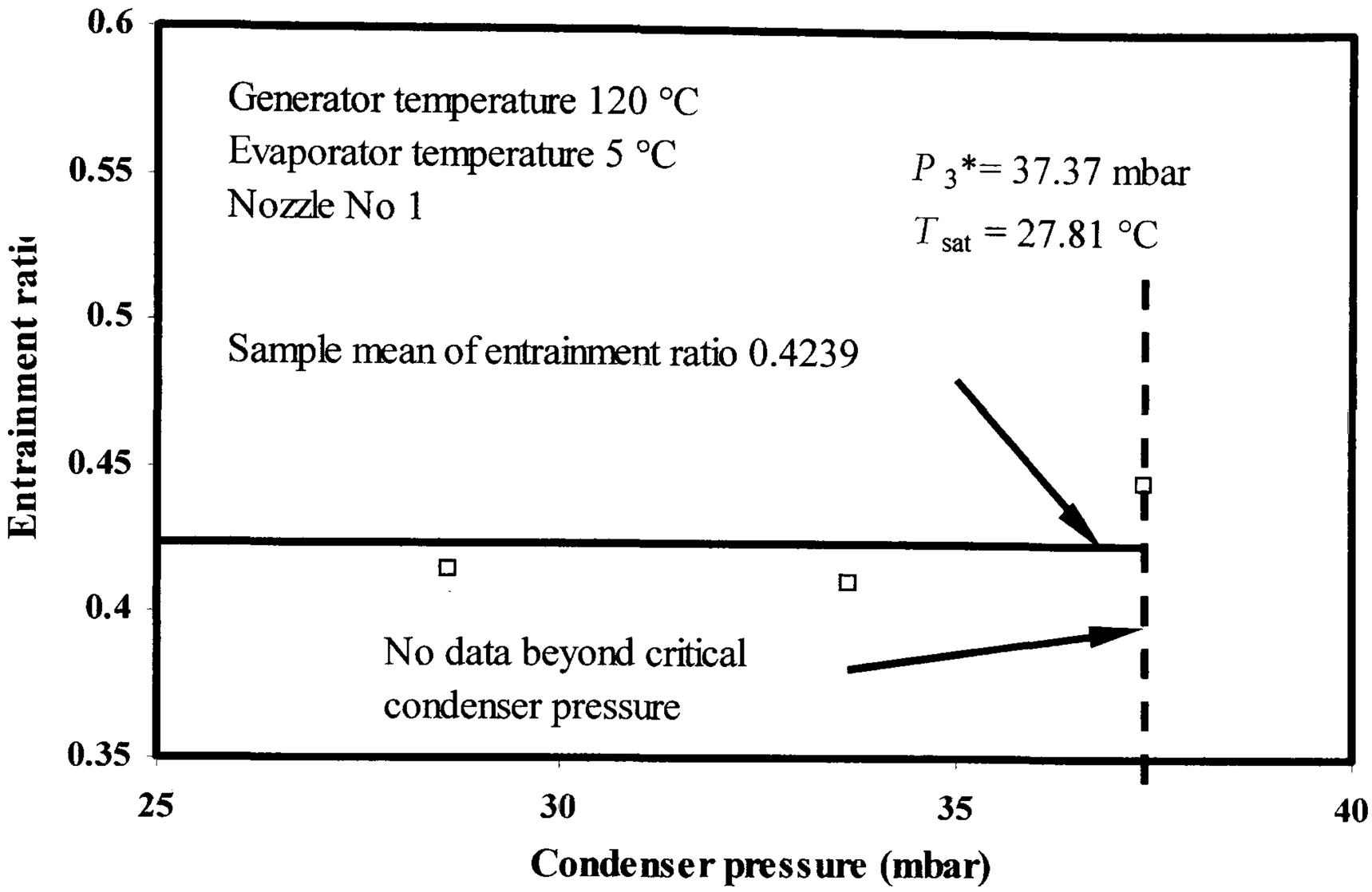

Figure 7.4. Variation in entrainment ratio with condenser pressure in 18 mm dia jet-pump throat.

Figure 7.5 shows that the entrainment ratio was not constant as in Figure 7.4, but varied with condenser pressure. The maximum entrainment ratio was 0.4642 at a condenser pressure of 35.71 mbar, and the minimum entrainment ratio was 0.2851 at a condenser pressure of 31.82 mbar. The range of the entrainment ratio data was, therefore, 63 % of the minimum value. All of the data show variations in entrainment ratio with condenser pressure, but values appear to form peaks and troughs as the condenser pressure is reduced from the maximum condenser pressure. The maximum condenser pressure was found to be approximately 46.43 mbar, at an entrainment ratio of 0.3444, which is 26 % less than the maximum measured value. The variation in entrainment ratio with condenser pressure shows that secondary flow was not choked in the jet-pump mixing section, and therefore did not reach sonic velocity. For choking to occur, secondary flow must be accelerated to Mach 1, and this would occur at the minimum area for secondary flow.

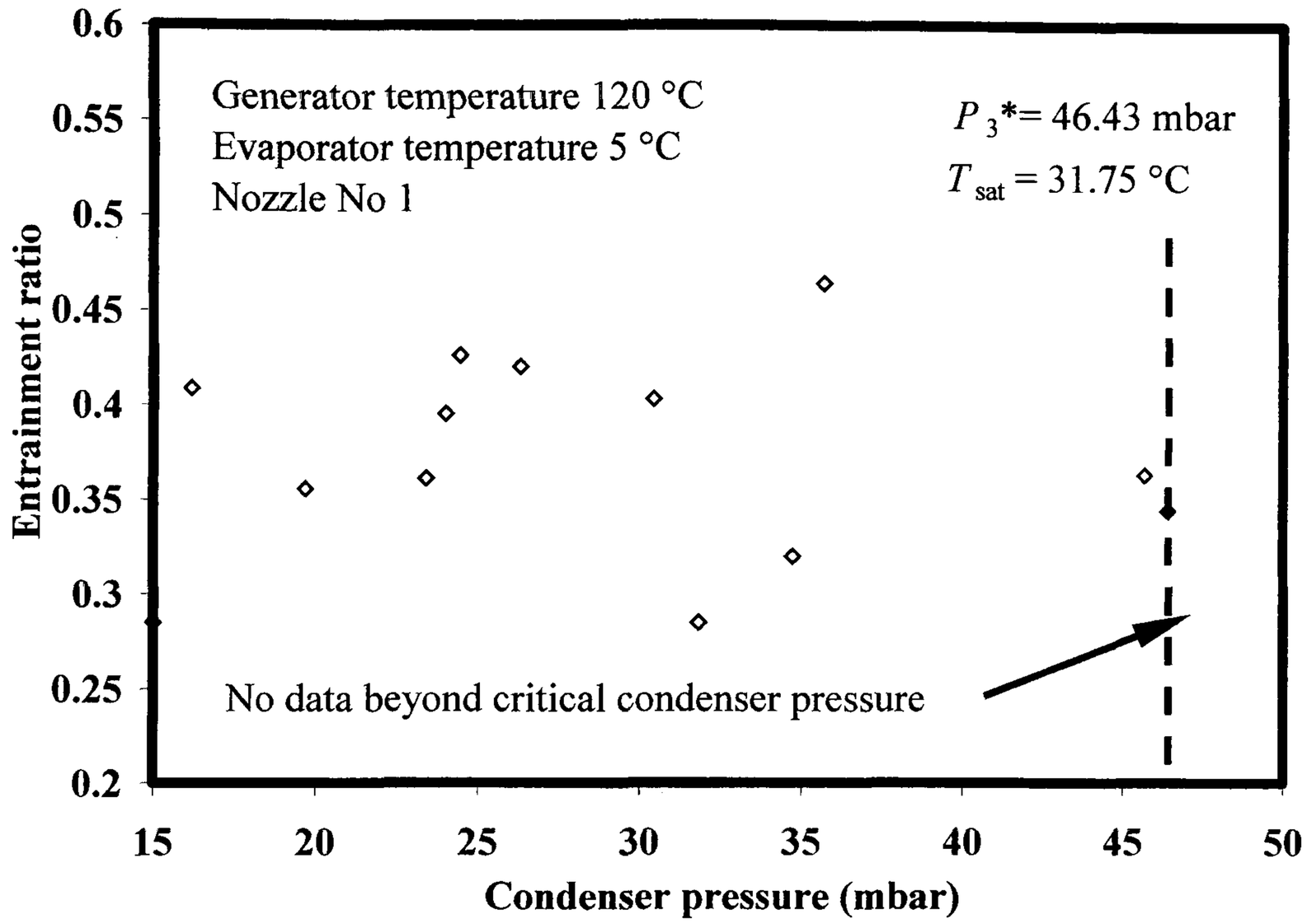

Figure 7.5. Variation in entrainment ratio with condenser pressure in the convergent-divergent duct.

Addy [57] described the conditions for choked and unchoked flow in a jet-pump with a varying geometry shroud by defining two non-dimensional parameters and presenting their relationship on a performance surface. The main features of the flow phenomena in a variable area shroud jet-pump are described below.

It was shown in Chapter 4 that the entrainment ratio of the jet-pump could be described in terms of nozzle pressure ratio N_p and pressure lift ratio N_s, but Addy [57] defined two similar non-dimensional variables for the analysis of jet-pump performance. The reciprocal of N_p, referred to as the secondary stagnation pressure ratio N_{sp}.

$$N_{sp} = \frac{P_0}{P_i} \tag{7.3}$$

and the outlet to primary stagnation pressure ratio, N_{is},

$$N_{is} = \frac{P_3}{P_i} \tag{7.4}$$

Therefore, entrainment ratio is redefined a

$$\omega = f(N_{sp}, N_{is}) \tag{7.5}$$

when the flow is unchoked and

$$\omega = f(N_{sp}) \tag{7.6}$$

when the flow is choked.

The operational characteristics of a jet-pump in terms of these non-dimensional parameters can be shown on a three-dimensional solution surface, illustrated in Figure 7.6.

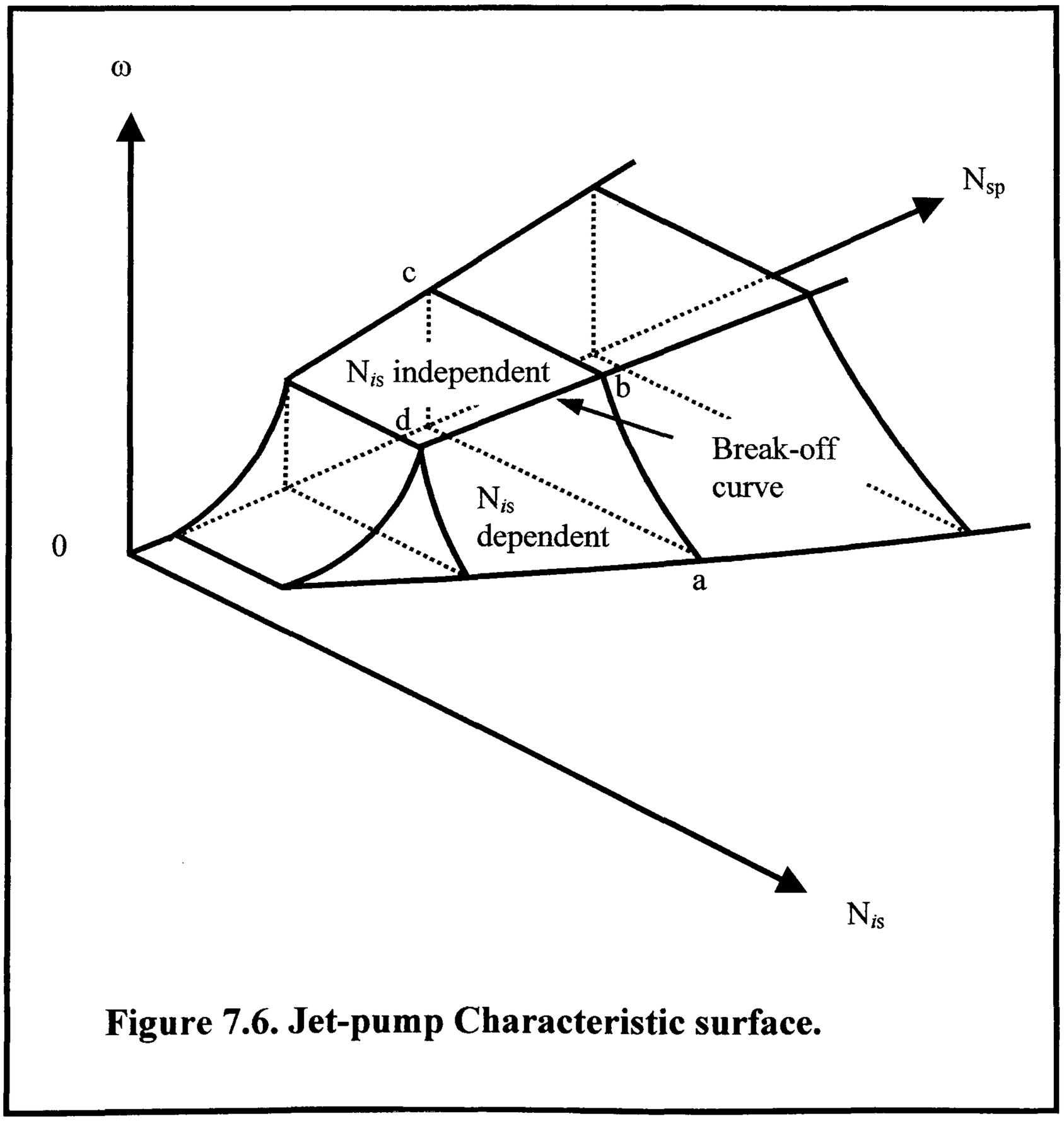

Figure 7.6. Jet-pump Characteristic surface.

Figure 7.6 shows a break-off curve that separates the two flow regimes, which depend on whether secondary flow is choked. Additionally, Addy [57] showed that the interaction of the primary and secondary streams may be divided into three general flow mechanisms; "zero flow", "small secondary flow" and "moderate to high secondary flow".

In the first flow regime secondary flow is zero. The primary jet expands to the wall of the jet-pump and an oblique shock system at the wall effectively seals off secondary flow from the outlet conditions, according to Addy [57]. There may be some diffusion of secondary flow across the primary jet boundary, but backflow within the jet-pump maintains the "zero flow" condition. In the "small secondary flow" regime, secondary fluid may diffuse across the primary jet boundary, but the primary jet detaches from the wall, allowing secondary flow between the primary jet and the wall. Secondary flow is then a combination of entrainment and the mutual interaction between the primary and secondary streams, but predominantly an entrainment process.

At "moderate to high secondary flows", the primary and secondary streams remain essentially distinct and recompression is predominantly an interaction between two separate flows with a small component of mixing between the two streams. The transition from one flow regime to another is not clearly defined, but will be continuous.

The plane (a-b-c-d), in Figure 7.6, represents the variation in entrainment ratio for changes in outlet conditions at constant N_{sp}. The "zero flow" condition, at point a, establishes the minimum mechanical energy required to maintain the oblique shock system at the jet-pump wall. As N_{is} is reduced, the strength of the oblique shock mechanism is insufficient to maintain contact with the wall and the jet detaches from it. Two distinct flow streams then exist, with recompression accomplished depending on the flow regime. Entrainment ratio increases as N_{is}

decreases until choking of secondary flow occurs and the flow conditions become independent of N_{is}.

Figure 7.7 shows the variation in the ratio of wall static pressure to primary stagnation pressure ratio, N_z, with axial distance to illustrate the transition from the N_{is} dependent to the N_{is} independent condition. As N_{is} decreases from the "zero flow" condition, entrainment ratio increases because the area available for secondary flow increases. Consequently, the constraint that the primary and secondary streams coexist in the cross sectional area of the jet-pump has a modifying effect on the primary flow field.

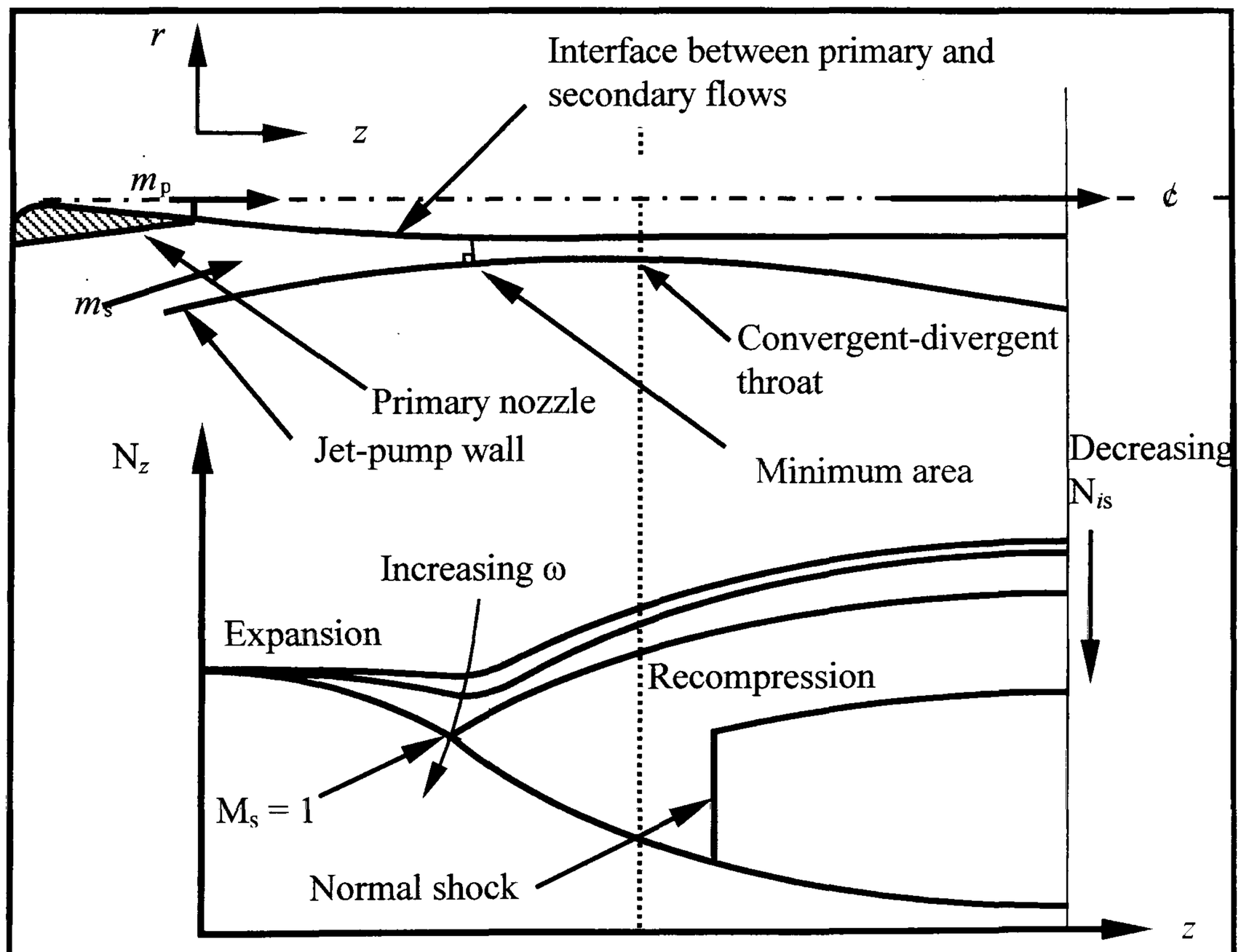

Figure 7.7. Variation in wall static pressure distribution with outlet conditions.

Secondary flow is assumed to expand isentropically from the evaporator stagnation state, causing a reduction in N_z and acceleration of the secondary stream to a maximum velocity where the flow area is a minimum. The primary and secondary streams are then recompressed to the outlet condition, N_{is}, downstream of this point. The area available for secondary flow and the entrainment ratio will vary until the boundary condition at the outlet is met. As N_{is} decreases further, the axial position at which the minimum area occurs moves upstream until the minimum area changes to give the entrainment ratio necessary to meet the boundary condition at outlet. The maximum velocity also increases with an increase in minimum area and when this reaches sonic velocity, secondary flow is choked. This condition corresponds to the point labeled (b) on the break-off curve in Figure 7.6 and labeled $M_s = 1$ in Figure 7.7, where M_s is the Mach number of the secondary stream. The break-off curve represents the condition that separates the flow regimes that are dependent and independent of N_{is}, and is a saddle point with two isentropic solutions. Figure 7.7 illustrates the two solutions, which can only be obtained by satisfying their respective outlet boundary conditions. At any N_{is} between the two isentropic solutions, secondary flow will continue to expand beyond the convergent-divergent throat and into the diffuser. Recompression is then achieved through a normal shock process located in the diffuser. As N_{is} decreases along the (b-c) line, the position of the shock will move downstream to satisfy the outlet boundary condition.

The test results did not reveal any data indicating choking in the jet-pump and so it is assumed that the geometry of the jet-pump was such that sonic velocity was not achieved over the operating range of the condenser.

It was observed in tests on the conventional jet-pump that the static pressure decreased downstream of the primary nozzle exit plane in agreement with the theory described by Bagster and Munday [49]. It was proposed that the primary jet and the wall provided a convergent duct through which the secondary flow

expanded, remaining essentially distinct, and accelerated to sonic velocity at the minimum area between the primary jet and the wall. The two streams would then mix at constant pressure and be recompressed across a shock system at the constant area section and in the subsonic diffuser. In contrast, the results from the convergent-divergent tests suggest that the secondary stream was not choked and therefore, did not reach sonic velocity. The consequence of replacing a constant area throat with a convergent-divergent design is to move the position of the minimum area downstream of the original location and change the flow conditions from a choked to an unchoked regime.

In the design procedure, it was assumed that the two streams mixed at constant pressure between the primary nozzle exit plane and the entrance to the constant area section. It was assumed that the flow at this section could be treated as one distinct stream and the continuity, momentum and energy equations could be solved in one-dimension to give a change in geometry for changes in flow conditions. The experimental results indicate that secondary flow was not choked, and therefore, the velocity of the secondary stream at the throat would be less than at the minimum area location. The flow in the convergent part of the duct would be highly non-uniform and so a one-dimensional treatment of the combined flow may not be valid for designing a jet-pump geometry because the modification to the geometry changes the minimum area location, and in this case changes the flow regime from choked to unchoked.

However, the one-dimensional procedure may be used to determine a variable geometry, then a two-dimensional technique used to determine the flow conditions for the given geometry. The geometry could then be varied until choking is achieved in the jet-pump. The two-dimensional procedure could use the method of characteristics to calculate the primary flow field and an inviscid one-dimensional analysis to calculate the secondary flow field with a superimposed mixed flow regime to take into account the viscous interaction of the shear layer where the two

streams combine, as described by Addy [57]. Computational fluid dynamics packages have been used recently in the study of jet-pumps, such as Rifatt *et al* [58] and Chin *et al* [50], and so could be used to determine the flow conditions for a geometry suggested by the one-dimensional analysis.

Figure 7.7 indicated that entrainment ratio would continually rise with a decrease in N_{is} until choking occurred, but Figure 7.5 suggested that the change in entrainment ratio with N_{is} had the appearance of peaks and troughs. The primary jet exhibits a node anti-node behaviour as it emerges from the nozzle and into the surroundings. Keenan *et al* [46] and Royds and Johnson [59] showed similar peaks and troughs in entrainment ratio with changes in the position of the primary nozzle with respect to the constant area entrance. Similarly, a number of peaks and troughs in vacuum pressure were observed when the position of the primary nozzle was varied with respect to the diffuser throat, as shown by Watson [60] in a study of steam jet-pumps in the production of a vacuum. It was thought that the variation in entrainment ratio coincided with changes in secondary flow area corresponding to nodes and anti-nodes of the primary jet.

Royds and Johnson [61] showed that the wavelength of a cylindrical free jet was

$$\lambda = 1.306 d_x \sqrt{M_{px}^{\ 2} - 1} \tag{7.6}$$

where d_x is the primary nozzle exit diameter and M_{px} is the Mach number of the primary flow at the nozzle exit. For an exit diameter of 8 mm and a primary flow Mach number of 3.762, the wavelength of the primary stream is 37.9 mm. This shows the approximate distance between two peaks, therefore a trough would be approximately 19 mm from the peak. This could be the reason that entrainment ratio appears to rise and fall in a number of peaks and troughs with a change in condenser pressure. As the condenser pressure decreases from its maximum value, the location of the minimum area will move upstream. The peak in entrainment ratio will then correspond to the anti-node section of the primary jet, and the trough will correspond to the node. The minimum area would then move upstream

in a series of peaks and troughs as the condenser pressure is reduced. For this to occur, the anti-nodes of the primary jet at the peak entrainment ratios must also be coincident with the minimum area for secondary flow.

The variation of entrainment ratio in the form of peaks and troughs may be characteristic of a convergent-divergent throat in the unchoked flow regime, because some studies of jet-pump performance, such as Al-Kalidy [31], have shown variations in entrainment ratio with condenser conditions, but with a monotonic increase in entrainment ratio with reductions in condenser pressure. The design of the jet-pump described by Al-Kalidy [30] showed that the primary nozzle exit plane was close to the constant area section and that all of the mixing would take place in the tube. The minimum area for secondary flow would be close to the primary nozzle and remain in the same position for changes in outlet conditions, but a reduction in static pressure at the minimum area location would allow greater expansion of secondary flow with a consequent increase in entrainment ratio. The primary jet would adjust its flow field so that the boundary conditions that both streams coexisted in the constant area duct and the static pressure at the interface was equal were satisfied. In contrast, it is thought that the curvature of the mixing section and the change in the primary flow field with outlet conditions allows the minimum area to be coincident with the nodes and anti-nodes of the primary jet.

In some circumstances it may be useful to be able to vary entrainment ratio with condenser pressure, such as a cooling system which is designed for the maximum outlet conditions, but which operates below that for most of the time. The cooling capacity could then be increased beyond the design point by reducing the condenser operating pressure. However, Figure 7.7 illustrates that the entrainment ratio, and therefore the COP will be less than at the choked condition and so will not be maximised. The entrainment ratio of the convergent-divergent jet-pump has a large variation for small changes in outlet conditions, and so is unreliable for

practical operation. However, if a geometry could be designed to establish a choked flow regime then its performance would be superior to a conventional jet-pump because the shock process would be eliminated at the design outlet conditions.

The convergent-divergent jet-pump was designed assuming that the two streams would mix at constant pressure, as in the case of the conventional jet-pump. This assumption resulted in the design of the mixing section with the same inlet geometry between the entrance and section 1, as the conventional jet-pump. The two streams were then assumed to be recompressed continuously in the convergent-divergent throat and discharged at the outlet conditions through the diffuser. The results show that this assumption is incorrect, because the change in geometry downstream of the mixing section changes the location of the minimum area and the flow regime in the mixing section.

7.5. Conclusions

The main objective of the experiments was to determine if the normal shock process associated with jet-pump recompression could be eliminated, thus increasing its performance. But some unexpected results were obtained with a change in the design of the throat.

The assumption that the primary and secondary streams are mixed and can be considered a single stream is not justified, because the reduction in geometry downstream of the original minimum area changes the location of the minimum area.

The replacement of a constant area throat with a convergent-divergent design changed the flow from a choked to an unchoked condition, but the peak

entrainment ratio and the critical condenser pressure was higher than the 18 mm throat jet-pump. However, small variations in pressure lift ratio caused large changes in entrainment ratio. This would make the performance of such a system unpredictable over its operational range.

Entrainment ratio is less than the maximum when the flow is unchoked, but the one-dimensional procedure for determining the geometry of the jet-pump assumes that the flow is already choked, and so does not adequately predict the local flow conditions of the jet-pump in the convergent section.

Entrainment ratio varied over a large range in a series of peaks and troughs, thought to be associated with the interaction between the swelling and contracting of the primary flow downstream of the nozzle exit and the geometry of the wall.

The epoxy resin insert was tested successfully, showing that a jet-pump could be manufactured using injection moulding techniques, enabling a large number of standard capacity units to be produced from a single mould, and potentially reducing first cost.

Chapter 8. Conclusions

This chapter will begin by summarising the previous chapters of the thesis, re-stating the aims and objectives of the study. An overview of the literature, the theoretical background and the test rig construction will also be made. Following the summary, the conclusions made from the test results will be brought together to assess the individual test results with the objective of studying the novel jet-pump TIS system. Limitations to the study will then be discussed, and recommendations for further study made.

8.1 Summary

Thermal (ice) storage (TIS) systems are used to shift the cooling demand of a building to off-peak periods by using electrical energy at off-peak periods to make ice, then discharging the coolth during the day. TIS systems can reduce harmful emissions by allowing chiller plant to operate at close to their full load capacity, but they still contribute to high emissions because the overall energy consumption can be similar. It was proposed that heat powered refrigeration systems could use waste-heat or renewable sources of energy to cool buildings and the combination of heat powered refrigeration and TIS could greatly reduce the emission of harmful gases. Jet-pump refrigeration was identified as the most promising combination of refrigeration system and ice store. Water is both the refrigerant and the storage medium, so is not harmful to the environment, heat and mass transfer are direct, increasing the efficiency of the ice store and the jet-pump is simple in construction and has few moving parts, so requires little maintenance. Two novel methods of TIS were developed to enable a jet-pump and an ice store to be coupled. Spray ice TIS would create an ice store using flash evaporative freezing, and build a layer of ice on the inner surface of the evaporator vessel. Encapsulated ice TIS would use sublimation freezing to solidify a bed of spherical capsules containing a novel polymer gel system. The jet-pump has a low coefficient of

performance compared with other competitive cooling and TIS systems, and cannot normally respond to changes in outlet conditions, so it was proposed to test three jet-pump geometries at the design operating point and at part-load in order to make recommendations for optimisation of jet-pump performance. The greatest loss causing mechanism in a jet-pump is a thermodynamic shock in the diffuser throat. The only method of eliminating the shock would be to use a convergent-divergent section instead of a constant area section. A novel convergent-divergent design manufactured from an epoxy resin was proposed to investigate any enhancement in performance.

The objectives of the study were to experimentally test the jet-pump TIS concept in the laboratory. A test rig was devised to allow the two methods of jet-pump TIS to be analysed, and to investigate the performance of the jet-pump using the three geometries and the convergent-divergent design at the operating point and at part-load.

8.2. Literature review

In reviewing TIS, it was shown that most chillers operated at 50 % part load for most of the time and 30 % at some point in the cooling cycle. TIS systems were shown to increase energy consumption because of their lower COP, and it was therefore, important to utilise heat recovery, energy storage and cold air distribution it order to reduce the overall energy consumption of a building.

The review of encapsulated TIS showed that much research had been carried out on conventional systems where a cooled glycol solution transferred the coolth to a bed of encapsulated elements, causing freezing of the elements, which were then discharged by passing a higher temperature glycol over the bed. There were analytical and numerical solutions to the solidification of a sphere undergoing cooling and the freezing of a semi-infinite ice layer due to sublimation from the solid surface, but no references to the freezing of a sphere by sublimation. The

information on the discharge of encapsulated bed of elements was relevant to the experimental investigation.

The review of vacuum freezing revealed practical systems that already use the technique for the desalination of sea-water and mine water, and the cooling of foodstuffs. Experimental vacuum ice slurry systems were described, but most used vacuum pumps, or proposed mechanical water vapour compressors such as axial or radial compressors to provide the vacuum. Electrical energy input would be required to drive these systems, so would not reduce primary energy input, on the contrary, energy input would be increased because the coefficients of performances tend to be lower than for conventional ice storage systems. None of the systems included a jet-pump to provide the vacuum, which shows that vacuum freezing using a jet-pump remains a novel method for providing an ice store, so it is important to investigate the operational characteristics of the jet-pump ice store and the mechanisms of vacuum freezing.

A model of one-dimensional sublimation from an ice layer was described, but the liquid and vapour temperatures decreased with time because of the assumption of a semi-infinite ice layer. A spherical capsule would freeze with very little change in temperature, so may not be applicable to encapsulated ice storage. The model assumed a constant rate of sublimation and described how an ice front grew in thickness but reduced in original position due to sublimation. These concepts could be applied to a spherical water/ice capsule undergoing vacuum freezing.

The review of jet-pump cooling showed the wide variety of systems using low-grade heat such as solar thermal and waste-heat to drive the refrigeration cycle. It was shown how the performance of a jet-pump cooling system could be enhanced by boosting the pressure in the evaporator with a vapour compressor and by operating the jet-pump in conjunction with an absorption cycle. All of the systems described, were designed to provide comfort cooling but could be applicable to jet-pump TIS.

8.3. Test rig construction

The test rig consisted of four main elements, an evaporator, a condenser, a steam generator and the jet-pump assembly. Temperature and pressure measurements were carried out and mass flows determined from calibrated vessels. The results were used to test analyse the performance of the jet-pump TIS system.

8.3.1. Evaporator

The evaporator consisted of a glass vessel 300 mm diameter and 500 mm in height. The evaporator was connected to the jet-pump assembly by a stainless steel tube 78 mm inside diameter. During spray ice TIS testing, a gear pump circulated water from the base to the top of the vessel, delivering it through a spray nozzle. An ice layer then formed on the inner surface of the vessel. During jet-pump calibration and convergent-divergent testing, a heat load provided by a 3 kW heater was applied to the circulation flow, via a heat exchanger, in order to maintain a steady-state in the evaporator/ice store. A centrifugal pump circulated water through the heat exchanger, and the flow was determined by a calibrated variable area flow meter. 1500 spherical elements 22 mm inside diameter were manufactured to contain a hydroscopic polymer gel system, which was able to retain water in suspension. After the polymer system had absorbed the maximum amount of water, any excess could be pumped to a glass storage vessel, which was 300 mm in diameter and 300 mm in height. During discharge, water was pumped through a heat exchanger and distributed over the bed of capsules. The water heater was used to simulate an air-conditioning heat load during discharge.

8.3.2. Condenser

The condenser consisted of a 200 mm diameter glass vessel and 700 mm in length. A copper tube, 15 mm diameter and 15 m in length, was wound to form a cooling coil. The condenser pressure was varied by adjusting the flow through the cooling coil. An 80 mm diameter glass vessel, 500 mm in height was calibrated and used

to measure condensate flow. A diaphragm pump delivered condensate from the condenser to the measuring vessel, and from the measuring vessel to the generator.

8.3.2. Generator

The generator consisted of a stainless steel vessel 90 mm diameter and 600 mm in length, housing two 3.5 kW electric element heaters. During operation of the test rig, the generator temperature was controlled by a proportional temperature controller. One heater was energized throughout the experiments, whilst the other heater was switched on and off in order to maintain a constant generator temperature. A stainless steel vessel 165 mm diameter and 650 mm in length performed the function of a steam separator. A calibrated sight glass was used to determine steam flow. An insulated copper tube connected the steam separator to a ball valve in the jet-pump assembly. A diaphragm pump was used to refill the generator with condensate.

8.3.3. Jet-pump assembly

A stainless steel suction pipe connected the jet-pump assembly to the evaporator. The primary nozzle assembly consisted of a flange, primary nozzle, spacer, connector and seals. Two primary nozzles with a 2 mm throat diameter were manufactured from 25 mm hexagonal section brass bar. Nozzle No 1 had an exit diameter of 8.5 mm and nozzle No 2 had an exit diameter of 11 mm. The three jet-pump geometries were constructed from aluminium bar stock and machined to fit into a jet-pump housing of 78 mm inside diameter. A convergent-divergent throat jet-pump was manufactured from an epoxy resin and fitted inside the jet-pump housing.

All pressures were determined be differential pressure gauges and a mercury manometer, and temperatures were determined by Type "K" thermocouples. The generator and condensate measuring vessel were calibrated to enable the determination of mass flows. All glass vessels were sealed with stainless steel

plates and PTFE inserts, and all vessels, plates and connecting tubing were thermally insulated.

8.3.4. Spherical capsules

Polymer granules were placed in heat sealed absorbent sachets, and then the sachets were placed inside the capsules. 1500 spherical capsules approximately 22 mm inside diameter were manufactured from copper, with a number of holes punctured to allow water to come into contact with the polymer granules. The capsules consisted of two hemispheres, one fitting inside the other, which were then press fitted together.

8.4. Conclusions

Testing was carried out in four phases. In the first phase, three jet-pump geometries were tested at constant inlet conditions so that the designs could be calibrated and that the differences in performance with geometry analysed. In the second and third phases, the performance of the jet-pump TIS systems (spray ice and encapsulated ice TIS) were examined so that the characteristics of the individual systems could be evaluated and the two systems compared. In the fourth phase, a convergent-divergent throat jet-pump was manufactured from an epoxy resin and tested in order to establish if the shock process characteristic of conventional jet-pump was eliminated and quantify the enhancement of performance.

Entrainment ratio, and therefore, COP can be increased by over 50 % for increases in evaporator saturation conditions (2.5 °C to 10 °C). The critical condenser pressure is reduced by approximately 10 %, showing that large increases in entrainment ratio can be achieved for only small reductions in critical condenser pressure by varying the chilled water supply temperature. However, the small change in critical condenser pressure makes variations in chilled water supply

temperature with respect to condenser operating conditions inappropriate as a control strategy.

The large increase in entrainment ratio with reductions in pressure lift ratio can be applied to jet-pump TIS systems by using a jet-pump to create an ice store, but operating it in series with a second system. The jet-pump would then discharge to an intermediate pressure and temperature, reducing the pressure lift ratio and boosting the entrainment ratio and COP. The COP could be boosted by 3 to 4 times, making it comparable to other chiller and TIS systems.

The choking phenomenon is important in the performance of the jet-pump. At operating conditions below the choked condition, entrainment ratio and pressure lift ratio both increase slowly. At the choked condition, secondary flow, and therefore, cooling capacity is a maximum. Beyond the choked condition, entrainment ratio decreases, but critical pressure lift ratio increases substantially. Only a small increase beyond the choked condition can allow the jet-pump to operate at higher ambient conditions, therefore, if the generator temperature has a small operational range, then the jet-pump should be designed for the lower value. The cooling capacity will be slightly lower than the optimum, but if the condenser pressure should increase beyond the critical pressure, then the generator temperature can be increased. The entrainment ratio and cooling capacity would decrease, but the critical pressure lift ratio would increase to enable operation at higher ambient conditions.

Entrainment ratio increases proportionally with diffuser area ratio A_d. A doubling of entrainment ratio is achieved by a reduction in the critical pressure lift ratio of only about 15 %. The jet-pump system must be able to operate when the ambient conditions are at their peak but most of the cooling cycle, daily and seasonal, is less than that peak. The entrainment ratio could be greatly enhanced for a small decrease in ambient conditions by operating a jet-pump with a larger A_d.

It was found that an over-expanded nozzle was inferior to a fully expanded nozzle because of a restriction in flow due to over-expansion, and an increase in momentum losses in the mixing section.

During spray ice TIS testing, evaporator saturation pressure and temperature became approximately steady-state because of the transfer of latent heat when changing phase to ice. Cooling capacity was dependent on the secondary flow entrained by the jet-pump and that depended on the saturated conditions and the annular area through which secondary flow could pass. The saturation conditions decreased with an increase in spray nozzle flow because the degree of supercooling increased with flow, reducing the steady-state pressure and temperature. At lower spray nozzle flows, evaporation from the spray was lower because of the reduction in the degree of supercooling, but the total evaporation rate was higher because of the higher saturation conditions.

Two ice formation processes occurred simultaneously during spray ice TIS evaporative freezing. Evaporative freezing from coolth stored in supercooled droplets and from a falling film. Between 85 % and 90 % of the coolth stored as ice was formed by evaporation from the falling film.

Nucleation and ice crystal growth on a vertical surface was found to be a practical method of ice storage and was only limited by the flow conditions described above. However, there was a large data spread due to errors in measurement and variations in droplet size distribution of the spray jet. The dominant cause for the spread of data was thought to be differences in the steady-state saturation conditions in the evaporator, and therefore, actual differences in ice storage rate. This, and the variation in ice storage rates with flow through the spray nozzle may make the use of spray ice TIS impractical over the service life of the system.

The coolth storage rate found from spray ice TIS testing was approximately 50 % less that that found in encapsulated ice TIS tests. There was a reduction of

40 % because the primary flow over-expanded, restricting secondary flow and increasing mixing chamber losses. There was a further 10 % difference because, for the same secondary flow, approximately 8.5 kg of ice is formed per kg of water-ice sublimated, compared with 7.5 kg of ice formed per kg of liquid-water evaporated. This shows that encapsulated ice TIS is the superior system based on coolth storage rate.

The performance of the jet-pump TIS system could be determined by either measuring the ice storage rate, to give an average secondary flow, of measuring secondary flow, to give an average ice storage rate. This depended upon the assumption that the evaporation rate could be assumed equal to secondary mass flow, which was shown to be valid during the change of phase.

The COP of the spray ice and encapsulated ice TIS systems were found to be approximately 0.15 and 0.25, respectively. The use of an over-expanded nozzle caused a 40 % reduction in COP because of the restriction of the flow and increases in losses in the mixing chamber. This showed that a primary nozzle should be designed for the fully expanded condition to maximise the system COP.

As under evaporative freezing, measurement of secondary mass flow could give a good estimate of ice storage rate. This assumes that the sublimation rate is approximately equal to secondary mass flow, although the experimental results showed approximately steady-state conditions in the evaporator over the charge period, static pressure was observed to decrease slowly with time. This would reduce the performance of a jet-pump used in charging a large capacity ice store over time. The saturation pressure decreased by about 50 Pa in about one hour of ice storage. The saturation temperature would have decreased by about 1 °C over the charge period, so that flows sampled over, say 30 minutes could be assumed to be at steady-state, thus allowing a prediction in ice storage rate.

The 22mm inside diameter spherical water/gel capsules underwent supercooling of approximately -2 °C, compared to between -4 °C and -7 °C from references to tests on 70 mm inside diameter capsules. The granular structure of the gel appeared to initiate ice crystal nucleation, thus reducing the degree of supercooling undergone by the liquid-water in the bed of capsules. This meant that the steady-state pressure and temperature were higher, increasing the secondary flow and the sublimation rate.

Encapsulated ice TIS systems could only operate in separate charge and discharge cycles, so spray ice TIS would be most advantageous when the coolth and heat source are in synchronization with a building, or a district. Encapsulated ice TIS systems also experience difficulties in fully discharging their stored coolth. This demonstrates an advantage of spray ice TIS, in that the coolth stored can be discharged in an ice/brine slurry, and thus, all of the ice manufactured can be discharged to provide the cooling.

It was shown that if a encapsulated ice TIS system were designed for a dry bulb temperature of 15 °C, the pressure lift could be reduced and COP increased to about 0.8, making in comparable with vapour-compression and single effect ammonia/water ice making system.

The use of spherical water/gel capsules maximised the surface area available for heat and mass transfer and it was shown that a reduction in diameter from 40 mm to 22 mm increased heat flux by about 30 %.

A novel convergent-divergent throat jet-pump designed to eliminate the shock process associated with conventional jet-pumps and increase the pressure lift ratio for the same inlet conditions changed the flow from a choked to an unchoked flow regime. The change in geometry caused the minimum area location to vary and prevented secondary flow from being accelerated to sonic velocity.

Entrainment ratio varied with condenser outlet conditions, but appeared as peaks and troughs. The primary jet exhibits a node anti-node behaviour as it flows downstream of the nozzle exit, and it was thought that the interaction of the primary flow field and the curvature of the jet-pump wall caused peaks corresponding to anti-nodes and the troughs to nodes.

The maximum entrainment ratio and pressure lift ratio were greater than for the conventional jet-pump, but small variations in pressure lift ratio caused large changes in entrainment ratio. This would make the performance of such a system unpredictable over its operational range.

The geometry was designed by assuming that the primary and secondary streams could be treated as a single flow and a one-dimensional analysis applied, but the +results showed that this assumption was not valid.

A convergent-divergent section manufactured from an epoxy resin was tested and operated successfully, proving that a thermoset plastic material can provide a suitable material for jet-pump construction. A single epoxy resin section was manufactured to test the performance of the convergent-divergent jet-pump, but in principle, a large number of sections could be manufactured from a single mould. The injection moulding of jet-pumps, manufactured from a thermoplastic material in mass quantities and various standard capacities, would provide inexpensive, light and mobile units, with the performance advantages over conventional jet-pumps already highlighted above.

The investigation proved the concept of jet-pump TIS. Its use could minimise the electrical energy requirements of a building and allow chillers to operate close to their full-load capacity. Waste-heat could be utilised over 24-hours and year round, increasing the efficiency of the process. The use of multiple geometry jet-pumps and operation at off-peak periods can maximise the performance over a cooling season, and be competitive with other TIS and chiller systems. The mass

production of jet-pumps using injection moulding techniques could reduce substantially the capital cost of the system. All of these factors should encourage the development of such systems, so that the harmful emissions caused by the use of air conditioning systems can be minimised.

8.5. Limitations

8.5.1. Mathematical models

The jet-pump TIS systems described in the thesis were modeled assuming simple evaporative and sublimation freezing, The models allowed for good predictions of ice storage rate and capacity, but did not include the actual heat and mass transfer mechanisms involved. The models assumed that the conditions in the evaporator/ice store approached steady-state, but the vapour saturation pressure was observed to decrease slowly over the test duration. The assumption gives adequate results for average conditions over the tests but over a longer time interval the reduction in saturation conditions could be substantial. Mathematical models of the transient processes taking place would give a more realistic analysis.

8.5.2. Sampling

Temperatures and pressures were recorded manually, so that there was a delay, causing a possible difference between the reading and the time recorded. A data logger should be installed to allow the automatic recording of pressures and temperatures. Ice storage rate during dynamic TIS was determined by measuring the difference in height of water between the end of ice storage and the completion of melting, but errors were introduced because of delays between the end of the test and measurement. An external level indicator could allow the determination of level without the delay in measurement. The mass of water contained in the evaporator at the start of static encapsulated TIS was estimated from a sample of

100 capsules, but it may be possible to automatically measure the mass contained in the evaporator, and so determine the change in mass with time. This could also be used to check the evaporation rate and therefore ice storage rate.

8.5.3. Instrumentation

Evaporator and wall static pressure were recorded by differential pressure gauges, causing an increase in error because of the addition of individual errors. Measurements during static TIS showed that pressures were within 6 % of the saturation pressure, but pressure transducers could be used to back up the analogue pressure measurements.

8.5.4. Testing

There was always evidence of the presence of non-condensable gases during dynamic TIS, so accurate measurement of evaporator vapour pressure was not possible. Evacuation was attempted from the evaporator vessel but there was still evidence of non-condensables because of possible stratification between the vapour and gases. Above the equilibrium freezing temperature saturation pressures can be estimated from the measurement of vapour and liquid temperature, but below the equilibrium freezing temperature the measured temperature was not at the saturation temperature, probably because ice had formed on the probe.

The charge phase test duration was approximately one hour and the saturation pressure fell by about 50 Pa. It was assumed that over this time duration the evaporator saturated conditions were approximately constant. This allowed an estimate of ice storage rate from measured secondary flow, but over longer ice storage periods and for larger capacities, saturation conditions are likely to fall, reducing jet-pump performance. Testing could be carried out using an over-expanded nozzle, so reducing ice storage rate and increasing the time duration of the charge phase.

Tests were carried out on a jet-pump designed to operate at a condensing temperature of 30 °C, but static TIS would operate during non-office hours, so the test results were compared with a theoretical jet-pump operating at a condensing temperature of 15 °C. There were no experimental results to back up the claims, so the actual performance could be different to the theory.

8.6. Recommendations

It was found that some of the ice formed during spray ice TIS took place by evaporation from a film of water flowing down a vertical surface. A test rig could be designed and built to analyse the cooling and freezing processes undergone by a falling film under vacuum freezing conditions. It was shown that the ice formation rate could be determined by measurement of jet-pump secondary flow, and this could be related to the saturation conditions in the evaporator. Water could be pumped from the base of an evaporator vessel to a circular manifold in the top of the vessel. The manifold could be a small bore tube, with a series of small holes drilled to distribute the water evenly and direct it to the wall. There would need to be some heat input to raise the water temperature to above the equilibrium freezing temperature to prevent solidification in the tube, but this could be taken into account when calculating the ice storage rate.

A practical spray ice TIS system would require scrapers or crushers to remove the ice from the surface, but another way of using a jet-pump for dynamic TIS is to form ice crystals in the bulk of an agitated brine solution. A test rig could be designed and built to analyse the vacuum freezing process in an ice/brine slurry and compare it with the results presented here.

In Chapter 4, it was suggested that the jet-pump COP could be enhanced by operating it in series with a separate cooling system. The jet-pump could operate to an intermediate outlet pressure, reducing the pressure lift ratio and boosting the

entrainment ratio. A vapour-absorption or water vapour-compression system could then provide the remaining pressure lift to the required outlet conditions. A small-scale test rig could be built to evaluate the operating characteristics of the system.

A jet-pump could be manufactured to operate at condensing temperatures of between 10 °C and 15 °C, and so test the performance at off-peak conditions. The jet-pump insert could be machined to fit in the current test rig. A small-scale cooling system would be required to reduce the condenser cooling water temperature, and so operate the condenser at the required test temperature and pressure.

It was shown that the pressure in the evaporator was approximately constant over the charge period, with a slight decrease with time, but if the pressure does decrease significantly, performance will decrease. A mathematical model could be developed to predict the cooling and solidification of a bed of encapsulated elements so that prediction of cooling capacity and coolth storage rate could be made for large-scale ice storage systems.

It was suggested in Chapter 7 that the one-dimensional analysis used to design the geometry of the convergent-divergent section did not adequately model the flow of the combined streams and so produced a design in which the flow was unchoked. It is proposed that the simple one-dimensional procedure could be used to produce a preliminary geometry, then a two-dimensional procedure used to predict the actual flow conditions. The geometry could then be altered iteratively, until choking is achieved in the mixing section.

The recommendations show that the novel concept evaluated in this thesis can provide the basis for further research into boosting the performance of the system, and encourage the development of large scale systems that could make substantial reductions in energy use.

References

1. Jordan, R. C, Priester, G. B, Refrigeration and air-conditioning, 1948, Prentice-Hall, Inc.
2. Woolrich, W. R, The men who invented cold, 1967, Exposition Press, Inc. New York.
3. Rule, J, The new age: Ice making for thermal storage, Australian Refrigeration, Air Conditioning and Heating, February 1984, pp. 22-25.
4. Potter Jr, R. A, Weitzel, D. P, King, D. J, Boettner, D. D, ASHRAE RP-766: Study of operational experience with thermal storage systems, ASHRAE Transactions, 1995, Vol 101, No 1, pp. 549-557.
5. Seeley, R. S, District cooling gets hot, Mechanical Engineering, July 1996, pp. 82-84.
6. CIBSE, Ice storage: A guide to the use and application of ice for cool storage, 1994, pp. 19-22.
7. Beyene, A, Guven, H, Jawpat, Z, Lowrey, P, Conventional chiller performances simulation and field data, International Journal of Energy Research, 1994, Vol 18, pp. 391-399.
8. Brady, T. W, Achieving energy conservation with ice-based thermal storage, ASHRAE Transactions, 1994, Vol 100,No 1, pp. 1735-1745.
9. Hittle, D. C, Smith, T. R, Cold strategies and energy consumption for ice storage systems using heat recovery and cold air distribution, ASHRAE Transactions, 1994, No 17, Part 2, pp. 1221-1229.
10. Hisaki, H, Kobayashi, N, Yonezawa, Y, Morikawa, A, Development of ice-thermal storage system using an absorption chiller, ASME International Absorption Heat Pump Conference 1993, Advanced Energy Systems (publication) AES, Vol 31, pp. 439-444.
11. Paul, J, District cooling with "water as refrigerant" combined with energy storage systems, International Institute of Refrigeration, natural working fluids 1998, June 2-5, 1998, Oslo, Norway, Sections B and E, pp. 44-52.
12. Tao, L. C, Generalized numerical solutions of freezing a saturated liquid in

cylinders and spheres, AIChE Journal, 1967, Vol 13, No 1, pp. 165-169.

13. Riley, D. S, Smith, F. T, Poots, G, The inward solidification of spheres and cylinders, International Journal of Heat and Mass Transfer, 1974, Vol 17, pp. 1507-1516.
14. Hill, J. M, Kucera, A, Freezing a saturated liquid inside a sphere, International Journal of Heat and Mass Transfer, 1983, Vol 26, No 11, pp. 1631-1637.
15. Arnold, D, Dynamic simulation of encapsulated ice stores-Part 1: the model, ASHRAE Transactions, 1990, Vol 96, No 1, pp. 1103-1110
16. Eames, I. W, Adref, K, Charging a thermal (ice) store: Results of a theoretical and experimental study, Building Services Engineering Research and Technology, 1996, Vol 17, No3, pp. 109-117.
17. Eames, I. W, Adref, K, Results of an experimental study into the dynamic behaviour of thermal (ice) storage elements during the charging period, CIBSE National Conference, Bournemouth, UK 1998, Oct 18-20, pp. 364-373.
18. Saitoh, T. S, Kato, H, Hoshina, D. C, Theoretical analysis for combined close contact and natural convection melting in ice storage spherical capsule, Proceedings of Intersociety Energy Conservation Engineering Conference, Washington, USA, Aug 11-16, 1996, Vol 3, No 3, pp. 2104-2108.
19. Koretchko, J, Hafela. G, Bench scale study of the vacuum freezing ejector absorption process, Office of Saline Water Research and Development progress report, No 744, November 1971. p.8.
20. El-Nashar, A. M, Solar desalination using the vacuum freezing absorption process, Desalination, March 1984, Vol 49, No 3, pp. 293-319.
21. Cheng, C. Y, Su, Y. F, Hopkins, D. N, Desalination by improved vacuum freezing high pressure melting process, Desalination, Aug 1982, Vol 42, No 2, pp. 141-151.
22. Yeh, H. M, Cheng, C. Y, Solid-liquid multiple phase transformation of water in a vacuum freezing process, Journal of the Chinese Institute of Chemical Engineers, Jan 1991, Vol 22, No 1, pp. 25-28.
23. Yeh, H. M, Cheng, C. Y, Cool thermal storage by vacuum freezing of water with constant volume rate of sublimation, Energy Conversion and

Management, Jan 1992, Vol 33, No 1, pp. 51-57.

24. Dickey, L. C, Evaporation of water from agitated freezing slurries at low pressure, Desalination, May 1996, Vol 104, No 3, pp. 155-163.
25. Houška, M Podloucký, S, Žitný, R, Grée, R, Šesták, J, Dostál, M, Burfoot, D, Mathematical model of the vacuum freezing of liquids, Journal of Food Engineering, 1996, Vol 29, pp. 339-348.
26. Shone, D, Research into slurry ice for mine cooling and the desalination of mine waters, South African Mechanical Engineer, March 1989, Vol 39, No 3 pp. 96-106.
27. Andersen, K, Fleming, B, V, Vacuum ice – A new method for production of large quantities of ice for cooling deep mines, Frigair 1986, Cooling-its vital role in agriculture, mines, factories and buildings, Pretoria, Republic of South Africa, 14-16 April 1986, Vol 1, No 27, p.8.
28. Siemens, C. W, Steam jet for exhausting air, Proceeding of The Institution of Mechanical Engineers, 1872, pp. 97-117.
29. Carrier, W. H, Developments in air-conditioning and refrigeration in the last decade, Proceedings of the Institution of Mechanical Engineers, 1951, Vol 157, pp. 357-361.
30. Al_Khalidy, Nehad, Z. A, Design and experimental investigation of an ejector in an air-conditioning system, ASHRAE Transactions, 1995, Vol 101, No 2, pp. 383-391.
31. Al-Khalidy, Nehad, Z. A, performance of solar refrigerant ejector refrigerating machine, ASHRAE Transactions, 1996, No 2, pp. 58-64.
32. Chow, W. L, Addy, A. L, Interaction between primary and secondary streams of supersonic ejector systems and their performance characteristics, AIAA Journal, April 1964, Vol 2, No 1, pp. 656-695.
33. Schintinina, N. A, Zhadan, S. Z, Petrenko, V. A, Experimental investigation of a solar-ejector freon refrigerating machine, Geliotekhnika, 1987, Vol 23, No 3, pp. 66-69.
34. Petrenko, V. A, Schintinina, N. A, A solar vapour ejection refrigerator testing in air conditioning regime, Proceedings of the 2nd World Renewable Energy

Congress, Reading, UK, Sept 13-18, 1992, pp. 1023-1029.

35. Sokolov, M, Hershgal D, Solar-powered compression-enhanced ejector air conditioner, Solar Energy, Sept 1993, Vol 51, No 3, pp. 183-194.
36. Sun, D. W, Solar powered combined ejector-vapour compression cycle for air conditioning and refrigeration, Energy Conservation and Management, 1997, Vol 38, No 5, pp. 479-491.
37. Sun, D. W, Evaluation of a combined ejector-vapour compression refrigeration system, International Journal of Energy Research, 1998, Vol 22, pp. 333-342.
38. Lund, S, Søe, L, District heating assisted cycle refrigeration plant for process cooling and air condition purposes, Joint meeting of the International Institute of Refrigeration, Natural working fluids 1998, Oslo, Norway, June 2-5 1998, pp. 34-43.
39. Sokolov, M, Hershgal, D, Enhanced ejector refrigeration cycles powered by low-grade heat. Part 2. Design procedures. International Journal of Refrigeration, Nov 1990, Vol 13, No6, pp. 357-363.
40. Sokolov M, Hershgal, D, Enhanced ejector refrigeration cycles powered by low-grade heat. Part 3. Experimental results. International Journal of Refrigeration, Jan 1991, Vol 14, No1, pp. 24-31.
41. Eames, I. W, Aphornratana, S, A novel ejector/absorption cycle refrigerator for building air conditioning, CIBSE National Conference 1995, pp. 96-104.
42. Eames, I. W, Georghiades, M, Tucker, R. T, Gas-fired ejector-absorption cycle technology for building air conditioning, International Heat Powered Cycles Conference 1997, Nottingham, UK, Sept 15-17 1997, pp. 265-275.
43. Eames, I. W, Wu, S, Worall, M, Aphornratana, S, An experimental investigation of steam ejectors for applications in jet-pump refrigerators powered by low-grade heat, Proceedings of the Institution of Mechanical Engineers, 1999, Vol 213, Part A, pp. 351-361.
44. Keenan, J. H, Neumann, E, P, Lustwerk, F. An investigation of ejector design by analysis and experiment, Journal of Applied Mechanics, Sept 1950, pp. 299-309.
45. Eames, I. W, Aphornratana, S, Haider, H, A theoretical and experimental study

of a small scale steam jet refrigerator, International Journal of Refrigeration, 1995, Vol 18, No 6, pp. 378-386.

46. ESDU Item No 86030, Ejectors and jet pumps, design for steam driven flow, ESDU International Ltd, London, Nov 1986, p. 75.
47. Rogers, G. F. C, Meyhew, Y. R, Thermodynamic and transport properties of fluids, 4th Edition, 1988, Blackwell Publishers, Oxford.
48. Huang, B. J, Jiang, C. B, Hu, F, L, Ejector performance characteristics and design analysis of jet refrigeration system, Journal of Engineering for Gas Turbines and Power, July 1985, Vol 107, pp. 792-802.
49. Bagster, D. F, Munday, J. T, The choking phenomenon in ejectors with particular reference to steam jet refrigeration, Thermofluids conference, Hobart, Australia, Dec 1–3 1976, pp. 84-88.
50. Chin, S. B, Eames, I. W, Popov, A, Computational fluid dynamics study of a compressible steam ejector pump design, International heat powered cycles conference 1997, Nottingham, UK, Sept 15-17 1997, pp. 302-310.
51. Eames, I. W, Worall, M, Wu, S, A jet-pump powered thermal (ice) storage system powered by low grade heat for use for comfort cooling for building, Proceedings of the 1998 CIBSE National Conference, Bournemouth, UK, 18-20 October 1998, pp100-113.
52. Hobbs, P. V, Ice physics, Oxford University Press, 1974, pp. 615-625.
53. Rose, D. T, Zuritz, C. A, Perez-Blanco, H, Thermodynamic analysis and pilot plant design for a solar assisted double-effect refrigeration absorption cycle, ASME International Absorption Heat Pump Conference 1993, Advanced Energy Systems (publication) AES, Vol 31, pp 109-115.
54. Hiromi M, Recent research for the gel ice storage, 1998, Internal Technical Report, Kameyama Lab, Sanken Setsubi Kogyo, Co, LTD, p. 13.
55. Calvert, J. R, Farrer, R. A, An engineering data book, 1999, MacMillan Press, Ltd, p. 7.1-7.2.
56. CIBSE guide, Part A, 1986, Weather and solar data, Chapter 2, pp. 2-25.
57. Addy. A, L, The analysis of supersonic ejector systems, AGARDograph No 163 on supersonic ejectors, Nov 1972, pp. 31-103.

58. Riffat, S. B, Gan, G, Smith, S, Computational fluid mechanics applied to ejector heat pumps, Applied Thermal Engineering, 1995, pp. 1-7.
59. Royds, R, Johnson, E, The fundamental principles of the steam ejector, Proceedings of The Institution of Mechanical Engineers, 1941, Vol 145, p. 193-209.
60. Watson, F, R. B, The production of a vacuum in an air tank by means of a steam jet, Proceedings of The Institution of Mechanical Engineers, Feb 1933, Vol 125, pp. 231-300.
61. Royds, R, Johnson, E, Communications on the fundamental principles of the steam ejector, Proceedings of The Institution of Mechanical Engineers, 1941, Vol 146, p. 223-235.

Appendix A: Derivation of M* in terms of M

In compressible flow problems, it is useful to compare local conditions to those of the flow at sonic velocity, where the Mach number is unity. This section describes the derivation of the critical Mach number M* from the local Mach number M.

The local Mach number was defined by Equation 3.9.

(3.9)

and the critical Mach number is defined by Equation A.1.

$$\mathrm{M}^* = \frac{U}{U^*} = \frac{U}{c^*} \tag{A.1}$$

Where U is the local velocity, c is the local speed of sound at the local static temperature T, and U^* is the velocity equal to the sonic velocity c^*.

Applying the conservation of energy between the stagnation and static conditions,

$$h_0 = h_1 + \frac{1}{2}U_1^{\,2} \tag{A.2}$$

For a perfect gas, specific enthalpy is found from Equation 3.2.

$$h = C_{\mathrm{pv}}T \tag{3.2}$$

and the specific heat at constant pressure is found from Equation 3.6.

$$C_{\mathrm{pv}} = \frac{kR}{k-1} \tag{3.6}$$

Equation A.2 becomes

$$\frac{kRT_0}{k-1} = \frac{kRT_1}{k-1} + \frac{U_1^{\,2}}{2} \tag{A.3}$$

The sonic velocity is $\sqrt{kRT}$ from Equation 3.8. Substituting into A.3 for T_0 and T_1 gives

$$\frac{c_0^{\,2}}{k-1} = \frac{c_1^{\,2}}{k-1} + \frac{U_1^{\,2}}{2} \tag{A.4}$$

At sonic velocity, $U = U^* = c$

$$\frac{{c_0}^2}{k-1} = \frac{U^{*2}}{k-1} + \frac{U^{*2}}{2} \tag{A.5}$$

$$U^{*2} = \frac{2}{k+1}{c_0}^2$$

From the definition of critical Mach number from A.1,

$$\mathrm{M}^{*2} = \frac{U^2}{U^{*2}} = \frac{U^2}{\frac{2}{k+1}c_0^{\ 2}} \tag{A.6}$$

Dividing both sides by $\mathrm{M}^2 = \frac{U^2}{c^2}$

$$\frac{\mathrm{M}^{*2}}{\mathrm{M}^2} = \frac{(\mathrm{k}+1)}{2}\frac{\mathrm{c}^2}{{\mathrm{c}_0}^2} \tag{A.7}$$

and dividing Equation A.3 by $\frac{k-1}{c^2}$

$$\frac{{c_0}^2}{c^2} = \frac{k-1}{2}\mathrm{M}^2 + 1 \tag{A.8}$$

Substituting back into A.7 gives

$$\frac{\mathrm{M}^{*2}}{\mathrm{M}} = \frac{k+1}{2} \times \frac{2}{(k-1)\mathrm{M}^2 + 2} \tag{A.9}$$

$$\mathrm{M}^{*2} = \frac{(k+1)\mathrm{M}^2}{1} \times \frac{1}{(k-1)\mathrm{M}^2 + 2} \tag{A.10}$$

Therefore,

$$\mathrm{M}^* = \frac{\sqrt{(k+1)\frac{\mathrm{M}^2}{2}}}{\sqrt{1+(k-1)\frac{\mathrm{M}^2}{2}}} \tag{A.11}$$

This gives the critical Mach number for a given local Mach number, and appears as Equation 4.18 in Chapter 4.

Appendix B: Derivation of M_1* of the mixed stream

Appendix B describes the derivation of the critical Mach number of the mixed stream at 1 in terms of the primary and secondary stream critical Mach numbers, the ratio of stagnation temperatures and the entrainment ratio.

The velocity of the mixed steam was defined by Equation 4.20.

$$U_1 = \frac{\phi_m (U_p + \omega U_s)}{1+\omega} \tag{4.20}$$

Applying the steady flow energy equation between inlet conditions and 1,

$$\dot{m}_{px} C_{pv} T_i + \dot{m}_{sx} C_{pv} T_o = (\dot{m}_{px} + \dot{m}_{sx}) C_{pv} T_1 \tag{B.1}$$

Dividing both sides by $\dot{m}_{px} C_{pv}$

$$T_i + \omega T_o = (1+\omega) T_1 \tag{B.2}$$

Multiplying top and bottom of RHS by U_1^2

$$T_i + \omega T_o = \frac{(1+\omega) T_1}{U_1^2} \frac{\phi_m^2 (U_p + \omega U_s)^2}{(1+\omega)^2} \tag{B.3}$$

$$T_i + \omega T_o = \frac{\phi_m^2 \left(U_p^2 + 2\omega U_p U_s + U_p^2 U_s^2\right) T_1}{1+\omega} \tag{B.4}$$

Multiply top and bottom of RHS by

$$(T_i + \omega T_o)(1+\omega) = \frac{\phi_m^2 kRT_1}{U_1^2} \left[\frac{U_p^2}{kR} + 2\omega \frac{U_p U_s}{kR} + \frac{\omega^2 U_s^2}{kR} \right] \tag{B.5}$$

Dividing through by T_i and defining $\tau = T_o/T_i$

$$(1+\omega\tau)(1+\omega) = \frac{\phi_m^2}{M_1 *} \left[\frac{U_p^2}{kRT_i} + 2\omega \frac{U_p}{\sqrt{kRT_i}} \frac{U_s}{\sqrt{kRT_i}} + \omega^2 \frac{U_s^2}{kRT_i} \right] \tag{B.6}$$

$$(1+\omega\tau)(1+\omega) = \frac{\phi_m^2}{M_1 *} \left[M_p *^2 + 2\omega \frac{U_p}{\sqrt{kRT_i}} \frac{U_s}{\sqrt{kRT_i}} \times \frac{\sqrt{T_o}}{\sqrt{T_o}} + \omega^2 \frac{U_s^2}{kRT_i} \times \frac{T_o}{T_o} \right] \tag{B.7}$$

$$(1+\omega\tau)(1+\omega) = \frac{\phi_m^2}{M_1 *^2} \left[M_p *^2 + 2\omega M_p * M_s * \sqrt{\tau} + \omega^2 \tau M_s * \right] \tag{B.8}$$

$$(1+\omega\tau)(1+\omega) = \frac{\phi_m{}^2}{M_1{}^{*2}}\left[M_p{}^* + M_s{}^* \omega\sqrt{\tau}\right]^2 \tag{B.9}$$

Therefore,

$$M_1{}^* = \phi_m \frac{\left(M_p{}^* + \omega M_s{}^* \sqrt{\tau}\right)}{\sqrt{(1+\omega\tau)(1+\omega)}} \tag{B.10}$$

This gives the critical Mach number of the mixed stream on completion of constant pressure mixing in terms of the critical primary and secondary Mach numbers, entrainment ratio and stagnation temperature ratio, and appears as Equation 4.21 in Chapter 4.

Appendix C: Program to calculate pressure lift and jet-pump geometry

The program described in Appendix C, calculates the pressure lift ratio and jet-pump geometry from the theoretical analysis described in Chapter 4. The program was written in Qbasic, but the calculation procedures can be easily used in other programming languages.

```
CLS
REM Program to calculate pressure lift and jet-pump geometry

REM input section

PRINT " This program calculates the optimum pressure lift and geometry"
PRINT "for given inlet conditions; entrainment ratio, generator and evaporator"
PRINT "temperatures and primary nozzle diameter"
PRINT
PRINT "enter stagnation temperatures"
PRINT
INPUT "for primary stream, Ti=",Ti
PRINT
INPUT "for secondary stream, To=",To
PRINT
PRINT "enter entrainment ratio, w"
PRINT
INPUT "entrainment ratio, w =", w
PRINT
PRINT "enter range for secondary pressure ratio Psx,"
PRINT
INPUT "upper range",upper
PRINT
INPUT "lower range", lower
PRINT
PRINT "enter number of points within the range, including upper"
PRINT "and lower limit at which you would like calculations to be made", steps
PRINT
INPUT "enter primary nozzle throat diameter, dt", dt

Np = 0.85
Nm = 0.9
Nd = 0.85
```

```
Ps=872
Pg=198500

gamma = 1.3
pie = 3.1415927#

IF steps = 1 THEN
     size = 1
  ELSE
     size = (upper-lower)/(steps-1)
END IF

FOR count =1 to steps
  Psx = lower +((count-1)*size)

REM calculation section

  Pxs = 1/Psx
  Msx = SQR((Pxs^((gamma-1)/gamma)-1)*2/(gamma-1))

  Xi = Ti-273
  Pix = Pg*Psx/Ps

  Mpx = SQR((Pix^((gamma-1)/gamma)-1)*2*Np/(gamma-1))

  Mpxcrit = SQR(Mpx^2*(gamma+1)/2)/SQR(Mpx^2*(gamma-1)/2+1)

  Msxcrit = SQR(Msx^2*(gamma+1)/2)/SQR(Msx^2*(gamma-1)/2+1)

  Tor = To/Ti

  M1crit = Nm*(w*Msxcrit*SQR(tor)+Mpxcrit)/SQR(1+w)*(w*tor+1))

  M1 = SQR(2*M1crit^2)/SQR((gamma+1)-(M1crit^2*(gamma-1)))

  M2 = SQR(M1^2*(gamma-1)+2)/SQR(2*gamma*M1^2+(gamma-1))

  P21 = (M1^2*gamma+1)/(M2^2*gamma+1)

  P32 = ((M2^2*(gamma-1)*Nd/2)+1)^(gamma/(gamma-1))

  P23 = 1/P32

  P30 = P32*P21*Psx

REM calculate jet-pump geometry
```

```
Poi = Po/Pi

A = (P30/Poi)*SQR(1/(1+w)*(1+(w*Tor))))
B = P23^(1/gamma)*SQR(1-(P23^(gamma-1)/gamma)))
C = (2./(gamma+1)^(1/(gamma-1))*SQR(1-(2/(gamma+1)))

At2 = A*B/C
At = pie*(dt/2)^2
A2 = At/At2
  D2 = 2*SQR(A2/pie)

REM output section

   OPEN "output.dat"FOR APPEND AS #
   WRITE #1, Psx, M1, P30, D2
   CLOSE #
NEXT count
OPEN "output.dat" FOR INPUT AS #1


DO UNTIL EOF(1)
   INPUT #1, Psx, M1, P30, D2
PRINT USING "###,###",Psx ,M1, P30, D2
LOOP

CLOSE #1

STOP

END

REM nomenclature

REM A2: diffuser throat area (m^2)
REM At2: ratio of primary nozzle throat to diffuser throat area
REM At: primary nozzle throat area (mm)
REM D2: diffuse throat diameter (mm)
REM dt: primary nozzle throat diameter (mm)
REM gamma: index of compression/expansion
REM M1: Mach number before normal shock
REM M1crit: critical Mach number before normal shock
REM M2 Mach number after normal shock
```

REM Mpx: Mach number of primary flow at nozzle exit plane
REM Mpxcrit: critical Mach number of primary flow
REM Msx: Mach number of secondary flow at nozzle exit plane
REM Msxcrit: critical Mach number of secondary flow
REM Nd: diffuser isentropic efficiency
REM Nm: mixing section loss coefficient
REM Np: primary nozzle isentropic efficiency
REM Pg: generator saturation pressure (Pa)
REM Ps: evaporator saturation pressure (Pa)
REM Psx: ratio of evaporator to local pressure at nozzle exit plane
REM P21: pressure ratio across normal shock
REM P32: pressure ratio across diffuser
REM P30: pressure lift ratio between evaporator and condenser
REM Pxs: reciprocal of Psx
REM Ti: generator saturation temperature (K)
REM To: evaporator saturation temperature (K)
REM Tor: ratio of inlet stagnation temperatures
REM w: entrainment ratio

Appendix D. Error analysis and instrument validation

Appendix D describes how the data gathered during testing was processed to take into account errors inherent in testing and observation. The choice of instrumentation, and instrument calibration are also described in this section.

Sources of error

Any experimental procedure is subject to errors, which result in differences between an analytical result and the true value. The errors need to be quantified so that the results can be interpreted correctly.

Discrimination

Discrimination is an error introduced into analytical results because of the smallest interval in which a value can be reliably determined. For instance, a micrometer with a resolution of 0.01 mm cannot be used to determine a value less than that limit. The error introduced is half the discrimination, in this case the error is 0.01 ± 0.005 mm.

Individual error

The error of an individual result is the difference between the result and the true value and is given by Equation D.1.

$$\varepsilon = R - \alpha \tag{D.1}$$

Where ε is the error, R is the result and α is the true value. The error can be positive or negative.

Relative error

The relative error is the error divided by the true value, given by Equation D.2.

$$\varepsilon_R = \frac{\varepsilon}{\lambda} \tag{D.2}$$

The percent relative error is give by Equation D.3.

$$\varepsilon_P = 100\frac{\varepsilon}{\lambda} \tag{D.3}$$

Propagation of errors

When arithmetic operations are carried out, errors due to rounding-off, discrimination, experimental methodology and instrumentation are introduced into the results, increasing the resultant error. The uncertainty of a calculated value can be estimated on the basis of uncertainties in the experimental measurements. The result R is a function of the independent variables $x_1, x_2,\ldots, x_n$. Thus

$R = R(x_1, x_2, \ldots, x_n)$

If ε_R is the uncertainty in the result and $\varepsilon_1, \varepsilon_2,\ldots,\varepsilon_n$ are the uncertainties of the independent variables then the uncertainty of the result is given as Equation D.4.

$$\varepsilon_R^{\,2} = \left[\left(\frac{\partial R}{\partial x_1}\varepsilon_1\right)^2 + \left(\frac{\partial R}{\partial x_2}\varepsilon_2\right)^2 + \cdots + \left(\frac{\partial R}{\partial x_n}\varepsilon_n\right)^2\right] \tag{D.4}$$

Random errors

Random errors are the result of a scattered distribution of sample data about some central value. The errors are introduced by many random factors such as small differences in volume, temperature variations, contamination, and instrumentation fluctuations. The random errors have to be assessed by statistical means to quantify the magnitude of the errors. The mean of a random sample is simply the sum of the individual data divided by the number of samples.

$$\bar{R} = \frac{\sum x_i}{n} \tag{D.5}$$

Where $\bar{R}$ is the random mean, x_i is the individual sample and n is the number of samples. The random variability of a series of independent analytical results is assumed to have a normal distribution about the mean. The scatter of results can be characterised by the standard deviation. The larger the standard deviation the greater the population spread. For a small sample, the sample standard deviation can be found from Equation D.6.

$$s = \sqrt{\frac{1}{n-1}\sum(x_i - \bar{R})^2} \tag{D.6}$$

Where s is the standard deviation of the sample.

The standard error of n independent sample means is

$$S = \frac{s}{\sqrt{n}} \tag{D.7}$$

Confidence limits are used to determine the probability that a proportion of the data lie inside the normal distribution curve. A 95 % confidence limit is used for most applications, which means that there is a 5 % probability that the sample data lie outside the limit. The t-distribution is used to determine the confidence intervals of sample data when the standard deviation is estimated. The confidence interval is obtained from Equation D.8, below.

$$\bar{R} \pm \frac{ts}{\sqrt{n}} \tag{D.8}$$

Where t is the t-distribution. Tables describing the t-distribution for various confidence limits and degrees of freedom can be found in statistical handbooks. Table D.1 shows a range of t-distribution factors for a confidence interval of 95 %. All of the experimental results will be described in the format of Equation D.9, using a confidence limit of 95 % and an appropriate t-distribution.

Table D.1. t-distribution factors at a 95 % confidence interval					
$n-1$	T	n - 1	T	n - 1	t
1	12.7	6	2.45	12	2.18
2	4.3	7	2.36	15	2.13
3	3.18	8	2.31	20	2.09
4	2.78	9	2.26	60	2.00
5	2.57	10	2.26	∞	1.96

Systematic errors

Systematic errors are introduced when there is a consistent tendency for results to be greater or smaller than the true value. Equation D.9 shows the error also known as bias.

$$B = \bar{R} - \alpha \tag{D.9}$$

Where B is an estimate of the bias.

Random and systematic error can be brought together to estimate the accuracy of a set of independent samples.

$$\varepsilon_T = \varepsilon_R + \varepsilon_S \tag{D.10}$$

$$\varepsilon_T = \frac{ts}{\sqrt{n}} + |B| \tag{D.11}$$

Instrumentation

The instruments chosen to measure the temperatures during testing were type "K" thermocouples. The thermocouples were initially calibrated by comparing the temperature measured to that of a known standard temperature, in this case the phase change temperature of water/ice. Table D.2 shows the results of tests of thermocouples used to measure the temperature inside the evaporator. The t factor of 2.78 was used for (n - 1) = 4 degrees of freedom and a confidence limit of 95 %.

Table D.2. Thermocouple validation					
	T_1	T_2	T_3	T_6	T_{10}
1	0.3	-0.2	-0.4	-0.4	-0.1
2	0.0	-0.3	-0.6	-0.1	-0.1
3	0.2	-0.2	-0.3	-0.2	-0.1
4	0.3	-0.4	-0.2	0.0	-0.3
5	0.2	-0.1	-0.3	-0.5	0.0
S	0.122	0.211	0.152	0.207	0.109
$\bar{T}$	0.20 ± 0.16	-0.24 ± 0.25	-0.36 ± 0.18	-0.24 ± 0.25	-0.12 ± 0.13
B	0.19	-0.25	-0.37	-0.25	-0.13
ε_T	0.35	0.50	0.55	0.50	0.26

Pressure gauges

Pressures were determined by a combination of a mercury manometer and analogue pressure gauges.

Condenser

The condenser pressure was determined by observing the difference in height of a mercury manometer and then subtracting the height difference from the known atmospheric pressure. The discrimination was taken to be 1 mm of mercury, which gave an error of ± 0.5 mm. The absolute pressure in the condenser was found from Equation D.11.

$$P = \rho g \mathrm{H} \tag{D.11}$$

Where ρ is mercury density (13620 $kg.m^{-3}$) and g is acceleration due to gravity (9.81 $m.s^{-2}$).

$$P = 9.81 \times 13620 \times 5.0 \times 10^{-4}$$

$$P = \pm 67 \text{ Pa}$$

Evaporator

The evaporator pressure was determined by observing the reading from an analogue differential pressure gauge, graduated in inches of water. The discrimination was taken to be 0.1 inches of water, which gave an error of 0.05 inches of water. The pressure difference was found from Equation D.11.

$$P = \rho g H \tag{D.11}$$

Where ρ is water density (1000 kg.m^{-3}).

$P = 1000 \times 9.81 \times 0.05 \times 25.4 \times 10^{-3}$

$P = \pm 13$ Pa

The pressure gauge gives a pressure difference, therefore, the error from the condenser reading and the error from the differential pressure reading increases the resultant error. The total error is the sum of the individual absolute errors, giving a resultant error of

$P = \pm 80$ Pa

Calibration of vessels

The evaporator, condensate vessel and generator were calibrated by filling the vessels using a calibrated container and measuring the height as the level rose. In each case a calibration curve was obtained representing the change in volume with height.

Condensate measuring vessel

Figure D.1 shows the calibration curve for the 80 mm diameter condensate measuring vessel. A straight line fit to the data resulted in a linear equation shown in Equation D.12.

$$V = 4.8805\ H + 97.581 \tag{D.12}$$

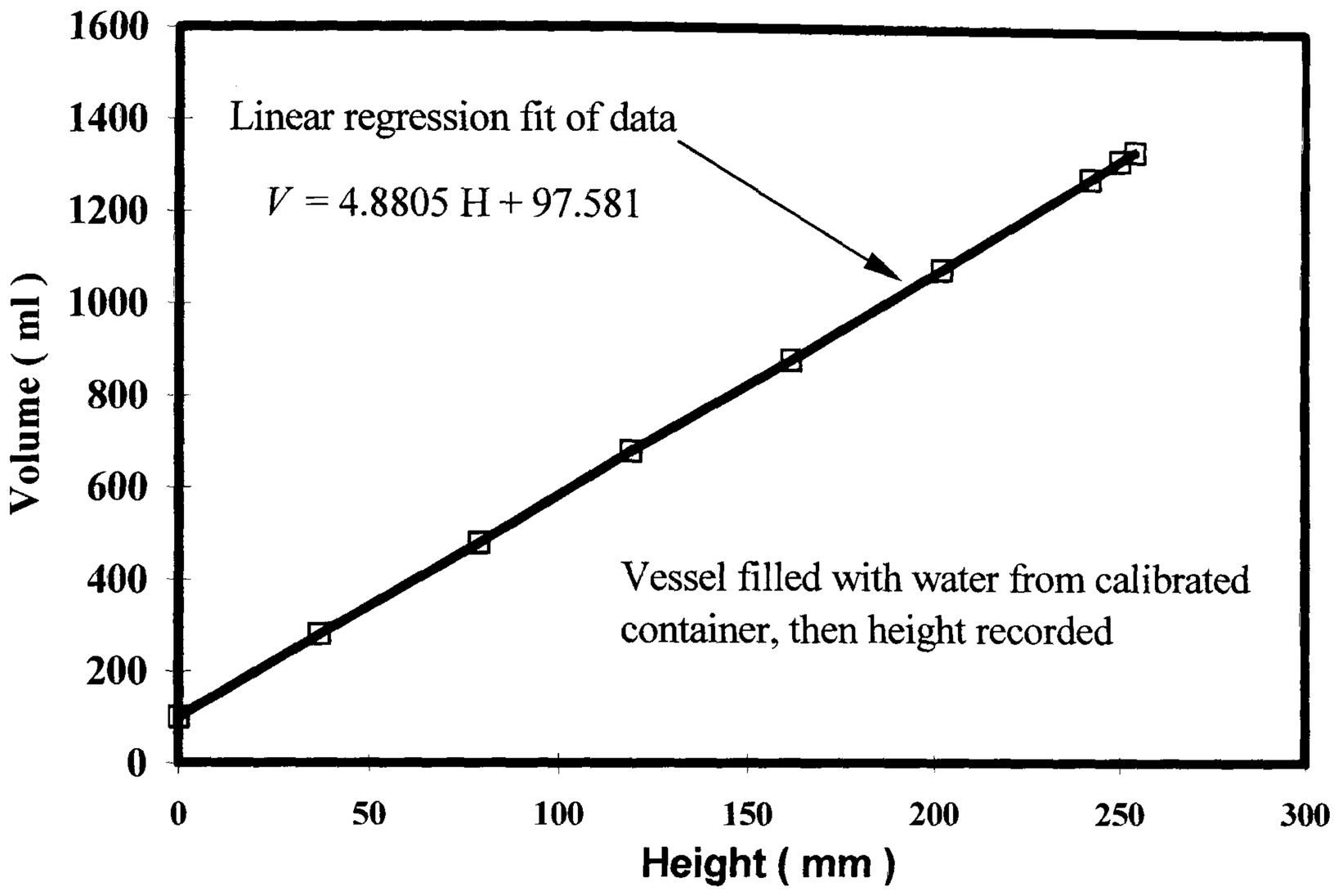

Figure D.1. Calibration of the condensate measuring vessel

Where V is the volume in ml and H is the height in mm. The discrimination of the evaporator vessel was 1 mm which corresponds to an error of ± 0.5 mm.

$$V = AH \tag{D.13}$$

$$V = 0.04^2\pi \times .5.0\times10^{-4}$$

$$V = \pm 2.5 \text{ ml}$$

Generator

Figure D.2 shows the calibration curve for the generator vessel. A straight line fit to the data resulted in a linear equation shown in Equation D.14.

$$V = 21.534\ H + 40.805 \tag{D.14}$$

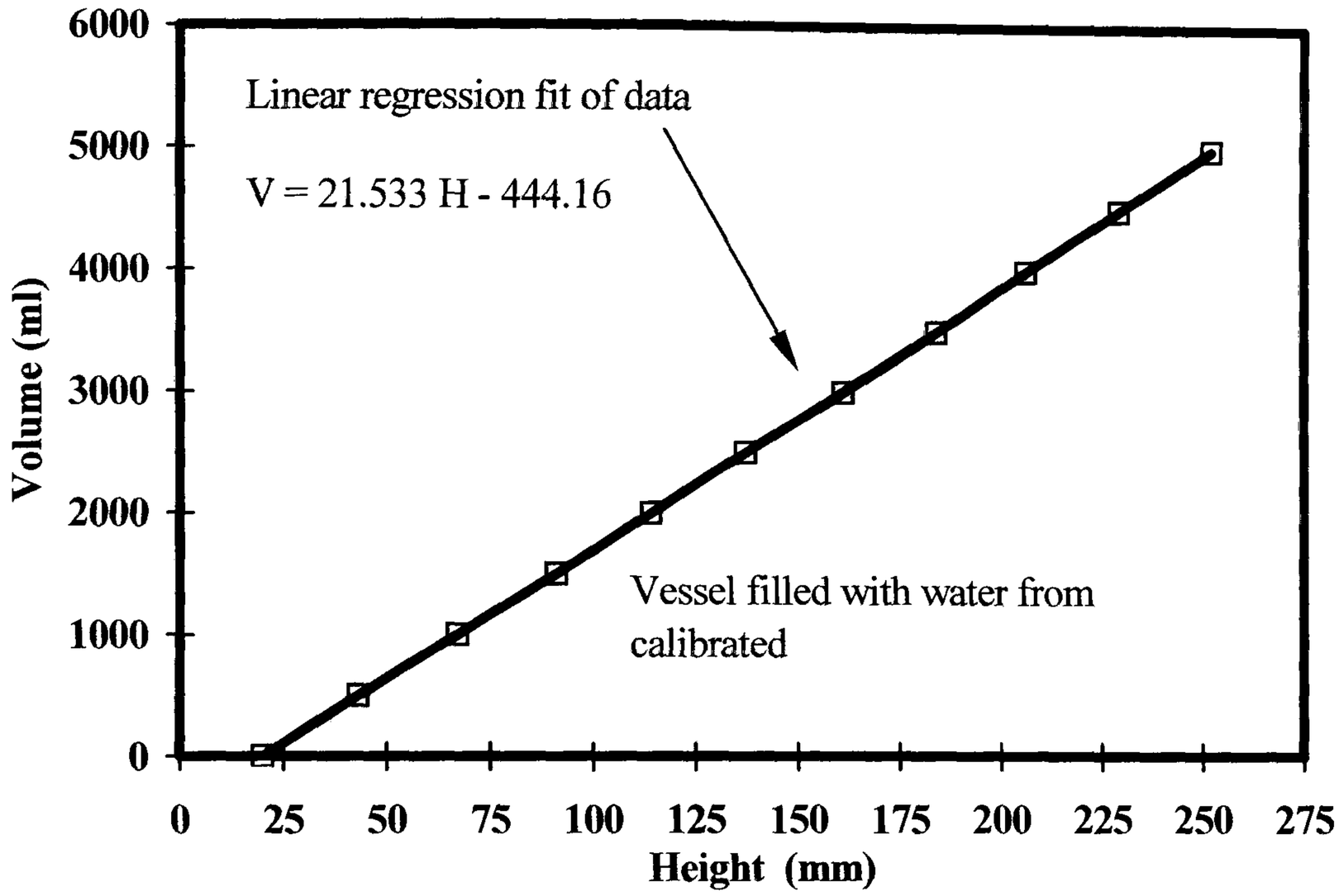

Figure D.2. Calibration of generator vessel

The steam separator, on which the level sight glass is mounted, is 165 mm in diameter. The discrimination of the sight glass attached to the generator vessel was 1 mm, which corresponds to an error ± 0.5 mm

$$V = AH \tag{D.13}$$

$$V = 0.0825^2\ \pi \times .5.0 \times 10^{-4}$$

$$V = \pm\ 11\text{ml}$$

Appendix E. Calculation of COP of jet-pump operating at an ambient temperature of 15 °C.

In Chapter 6, the performance of the encapsulated ice TIS system was determined experimentally, but testing was undertaken during office hours. However, the charge cycle would be operational during off-peak periods, which would allow the jet-pump to operate at much lower ambient conditions. The critical pressure lift ratio N_s* can be reduced, increasing the entrainment ratio and the COP of the jet-pump TIS system. Appendix E describes the estimation of the performance of a jet-pump at reduced ambient conditions.

Figure E.1 shows the assumed operating conditions for a jet-pump under the same inlet stagnation conditions as found from the tests described in Chapter 6, and a minimum ambient pressure and temperature during off-peak periods.

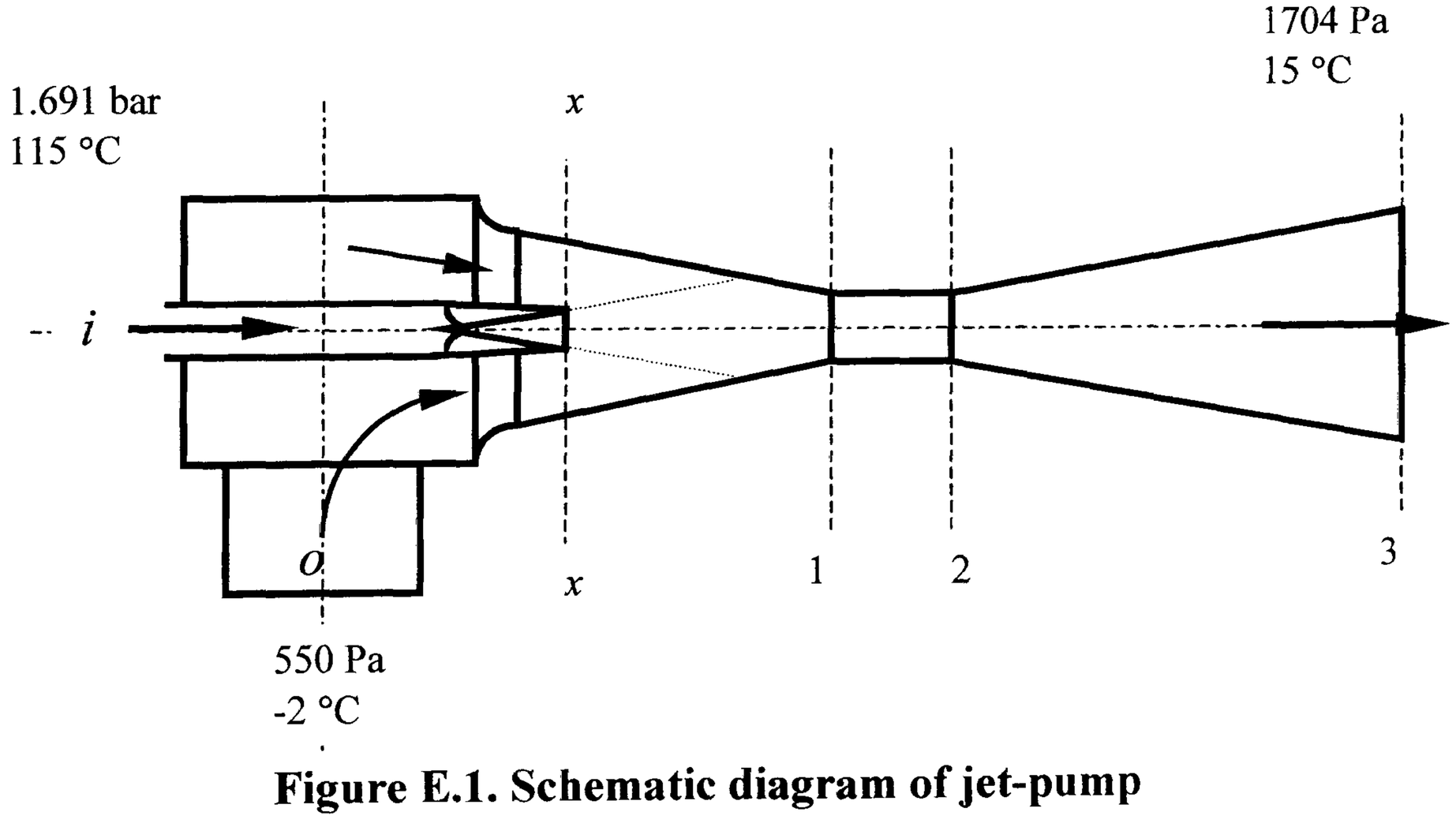

Figure E.1. Schematic diagram of jet-pump

The lowest average wet bulb temperature in July at Kew, UK was 12.3 °C, according to CIBSE [56]. A value of 15 °C was chosen as a conservative estimate for the purposes of estimating jet-pump performance. The saturation pressure at

15 °C is 1704 Pa, and given that the saturation pressure of the evaporator during testing was approximately 550 Pa, the critical pressure lift ratio is given by Equation 4.3.

$$N_s* = \frac{P_3*}{P_o} \tag{4.3}$$

$$N_s* = \frac{1704}{550} = 3.1$$

The ratio of inlet stagnation temperatures is given by Equation 4.22.

$$\tau = \frac{T_o}{T_i} \tag{4.22}$$

$$\tau = \frac{267}{393} = 0.679$$

The primary nozzle and diffuser isentropic efficiencies, and the mixing section loss coefficient used in the procedure are given below.

$\eta_p = 0.85$, $\phi_m = 0.93$, $\eta_d = 0.8$

A range of entrainment ratio values from 0.6 to 0.8 were input into the iterative procedure described in Chapter 4, and it was found that an entrainment ratio of 0.7275 gave a pressure lift ratio of 3.1 for the initial conditions described above.

The COP of the jet-pump during sublimation freezing is given by Equation 6.26.

$$COP = \omega \frac{h_{sub}}{h_{g,T_g} - h_{f,T_c}} \tag{6.26}$$

Substituting the thermodynamic values at the stated operating conditions gives

$$COP = 0.7525 \frac{2838}{(2699 - 77.97)}$$

$$COP = 0.8148$$

The test rig was designed to operate during the day-time to allow testing in the laboratory during office hours, but a jet-pump encapsulated ice TIS system designed to operate at night-time ambient conditions would boost the COP by over 3 times the value found from the results described in Chapter 6.

Appendix F1. Raw data from jet-pump at part-load

No 1 nozzle

T_g (°C)	T_e (°C)	P_3 (mbar)	H_1 (mm)	H_2 (mm)	t_1 (sec)	t_2 (sec)	m_s (g/s)	m_p (g/s)	ω
120	14	30	260	0	1325	3047	0.754936	1.0513	0.718097708
120	10	32.2	246	61.5	1200	3515	0.398488	1.0513	0.379043205
120	2.5	27.7	231	56	1382	5337	0.221239	1.0513	0.210443202
120	2.5	30.72	111	56	4150	5337	0.231676	1.0513	0.22037144
120	5	34.88	221	79	655	2932	0.311814	1.0513	0.296598297
120	7.5	30	169	47	64	4405	0.140521	1.0513	0.133663671
120	5	33.64	261	40	1293	4413	0.354167	1.0513	0.336884492
120	7.5	34.92	215	7	490	2634	0.485075	1.0513	0.461404572
120	10	33.45	227	10	0	1647	0.658774	1.0513	0.626627535
120	10	37.19	225	11	312	2159	0.579318	1.0513	0.551048999
120	10	35.94	224	1	304	2086	0.625701	1.0513	0.595169275
120	5	29.9	217	13	365	3008	0.385925	1.0513	0.367093204
120	5	31.14	168	25	780	2728	0.367043	1.0513	0.349132618
120	5	36.75	234	18	840	3720	0.375	1.0513	0.356701227
120	7.5	33.22	153	13	900	2432	0.456919	1.0513	0.434622905
120	7.5	34.17	175	28.5	840	2844	0.365519	1.0513	0.347682833
120	2.5	30.3	185	25	840	3714	0.278358	1.0513	0.264774745
120	2.5	33.75	222	65	480	3704	0.243486	1.0513	0.231605015
120	5	38.62	192	123	480	2651	0.158913	1.0513	0.151158512
130	5	30.15	215	22	300	2820	0.382937	1.38822	0.275847134
130	5	33.64	205	24	270	2756	0.364039	1.38822	0.262234096
130	5	42.11	174	26	630	2822	0.337591	1.38822	0.24318281
130	5	47.34	201	41	420	3498	0.259909	1.38822	0.18722467
130	10	35.94	213	12	913	2645	0.580254	1.38822	0.417984211

130	10	44.66	181	1	450	2072	0.554871	1.38822	0.399699277
130	10	49.65	226	92	560	3019	0.272468	1.38822	0.196271832
130	10	40.93	210	11	280	2340	0.48301	1.38822	0.347934556
130	7.5	31.68	220	27	352	2590	0.431189	1.38822	0.310605352
110	10	27.84	167	8	850	2187	0.594615	0.75745	0.785021862
110	10	29.21	194	4	364	2334	0.482234	0.75745	0.636653908
110	10	28.47	168	4	710	2208	0.547397	0.75745	0.722683383
110	10	29.71	181	11	42	4431	0.193666	0.75745	0.255681541
110	10	28.47	107	11	1385	2223	0.572792	0.75745	0.75621145
110	7.5	27.32	245	25	380	2711	0.4719	0.75745	0.623012043
110	7.5	25.45	180	25	840	2668	0.423961	0.75745	0.559720922
110	10	38.24	185	28	475	1727	0.626997	0.75745	0.827773193
110	5	25.54	215	10	660	3451	0.367252	0.75745	0.484852969
110	5	27.91	234	139	1466	3001	0.309446	0.75745	0.408536872
110	2.5	24.54	239	10	1890	6090	0.272619	0.75745	0.359916889
110	2.5	28.53	286	190	1680	5815	0.116082	0.75745	0.153253977
110	7.5	2945	183	28	1040	6257	0.148553	0.75745	0.196122263
120	2.5	2973	220	97	671	1925	0.490431	1.0513	0.466499212
125	2.5	3124	173	32	1324	4102	0.25378	1.19584	0.212218773
110	2.5	2135	238	30	861	6903	0.172128	0.75745	0.227247256
110	2.5	2723	285	124	1290	6120	0.166667	0.75745	0.220036526
100	5	2492	179	112	870	3301	0.137803	5.35E-01	0.257428678
100	7.5	2525	214	157	3285	1270	-0.141439	5.35E-01	-0.264220729
100	10	2473	227	0	42	3049	0.377453	5.35E-01	0.705114281
100	5	2367	164	43	1020	3028	0.301295	5.35E-01	0.562844911
100	2.5	2349	221	182	1620	3077	0.133837	5.35E-01	0.250018495
130	7.5	2924	176	8	600	2607	0.418535	1.38822	0.301490489
130	7.5	4518	215	8	600	3183	0.400697	1.38822	0.288640752
130	7.5	5266	173	6	660	2670	0.415423	1.38822	0.299248596

130	7.5	5640	190	34	840	3329	0.313379	1.38822	0.225741501
130	2.5	3222	212	158	71	2740	0.101161	1.38822	0.072871363
130	2.5	3471	206	53	510	5147	0.164977	1.38822	0.11884093
130	2.5	3845	197	76	530	3960	0.176385	1.38822	0.127058276
130	2.5	4966	157	102	2880	4915	0.135135	1.38822	0.097344178
130	11	4715	248	2	1080	2995	0.642298	1.38822	0.462677133
130	12.5	5401	165	16	1260	2417	0.643907	1.38822	0.463836175
130	12.5	4965	159	130	70	1652	0.091656	1.38822	0.066024212
No 2 nozzle									
120	5	3332	181	37	795	2509	0.42007	1.057	0.39741723
120	5	3239	161	11	690	2327	0.458155	1.057	0.433448592
120	5	2862	196	9	1890	4019	0.439173	1.057	0.41549037
120	5	3737	199	69	960	2456	0.434492	1.057	0.411061475
120	2.5	2349	172	10	96	3046	0.274576	1.057	0.259769415
120	2.5	3222	183	9	84	3292	0.271197	1.057	0.256572382
120	2.5	3747	205	56	1230	3593	0.315277	1.057	0.298275487
120	7.5	3360	190	3	1721	3840	0.441246	1.057	0.417451155
120	10	3968	177	10	420	1704	0.650312	1.057	0.615242693
120	10	4039	248	24	1140	4051	0.384748	1.057	0.363999536
120	10	3345	177	11	460	1648	0.698653	1.057	0.660977482
120	10	2847	213	11	840	2380	0.655844	1.057	0.620476969
120	7.5	2749	220	123	300	1238	0.517058	1.057	0.489174616
120	7.5	3772	189	3	990	2625	0.568807	1.057	0.538133718
120	7.5	3920	160	149	965	3021	0.026751	1.057	0.025308394
120	7.5	2525	168	5	360	1885	0.534426	1.057	0.50560665
120	2.5	2350	178	6	900	3240	0.367521	1.057	0.347702334
120	2.5	2723	186	11	540	2934	0.365497	1.057	0.345787205
120	2.5	3720	195	22	660	3563	0.297968	1.057	0.281899356

120	2.5	2786	190	8	660	3093	0.374024	1.057	0.353854152
120	2.5	3596	202	13	900	3563	0.354863	1.0513	0.337546786
130	10	3594	154	0	1200	2316	0.689964	1.38822	0.497013555
130	10	4965	183	6	960	2268	0.676606	1.38822	0.487390691
130	10	3968	237	8	1320	2935	0.708978	1.38822	0.510710354
130	10	5214	197	9	630	2508	0.500532	1.38822	0.360557031
130	7.5	2924	191	2	1110	2883	0.532995	1.38822	0.383941251
130	7.5	3273	208	6	1080	2938	0.543595	1.38822	0.391577173
130	5	2018	134	0	1140	2825	0.397626	1.38822	0.286428745
130	7.5	3771	171	10	1200	2756	0.517352	1.38822	0.372673053
130	5	3987	125	11	900	3391	0.228824	1.38822	0.164832495
130	5	3364	173	12	660	2614	0.411975	1.38822	0.296765235
130	5	3638	193	11	541	2802	0.402477	1.38822	0.289922909
130	2.5	3869	196	16	510	3712	0.281074	1.38822	0.202471027
110	10	2224	142	4	870	1962	0.631868	0.75745	0.834204412
110	10	2971	212	2	310	1962	0.635593	0.75745	0.839122345
110	10	3220	230	4	600	2565	0.575064	0.75745	0.759209998
110	5	2591	179	3	750	2852	0.418649	0.75745	0.552708305
110	7.5	3148	212	3	315	2482	0.482234	0.75745	0.636653908
110	5	2989	158	8	620	2481	0.403009	0.75745	0.53206038
110	7.5	3273	175	16	1070	3050	0.401515	0.75745	0.530087995
110	2.5	2349	201	19	720	3311	0.351216	0.75745	0.463681757
110	2.5	2723	215	12	240	3530	0.308511	0.75745	0.407301655
110	2.5	2599	195	7	720	3485	0.339964	0.75745	0.448826766
110	2.5	2973	192	14	900	3552	0.335596	0.75745	0.443059973
110	5	2865	236	7	540	3423	0.397156	0.75745	0.524332617
110	5	3114	195	127	600	3033	0.139745	0.75745	0.184494251
100	2.5	1976	250	81	930	4256	0.254059	5.35E-01	0.474604161
100	2.5	2225	243	92	690	8921	0.091726	5.35E-01	0.171352888

100	5	2242	255	45	1140	6700	0.188849	5.35E-01	0.352786197
100	5	1370	200	8	780	3492	0.353982	5.35E-01	0.661269703
100	5	1993	223	97	840	4294	0.182397	5.35E-01	0.34073386
100	7.5	2151	275	255	540	2853	0.043234	5.35E-01	0.080764674
100	7.5	2027	210	4	540	2855	0.444924	5.35E-01	0.831157459
100	7.5	2400	187	7	540	2637	0.429185	5.35E-01	0.801754039
100	7.5	2276	196	9	481	2457	0.473178	5.35E-01	0.883937885
100	10	2373	185	9	600	2054	0.605227	5.35E-01	1.130616562
100	10	2597	206	23	480	3954	0.263385	5.35E-01	0.492026345
100	10	2535	223	35	840	2697	0.506193	5.35E-01	0.945612114
100	10	2224	218	7	750	2445	0.622419	5.35E-01	1.162732561

T_e	Evaporator liquid-water temperature
H_1	Water level at start of steady-state measurement
H_2	Water level at end of steady-state measurement
m_s	Secondary mass flow
m_p	Primary mass flow
ω	Entrainment ratio

Appendix F2. Primary mass flow raw data						
T_g (°C)	110	115	120	125	130	135
	0.77941	0.85694	1.05734	1.1905	1.4509	1.5488
	0.75592	0.90758	1.05734	1.19217	1.3725	1.5488
	0.75699	0.88517	1.03967	1.19535	1.39084	
	0.69517	0.8925	1.05733	1.23392	1.34967	
	0.757	0.88517	1.05733	1.19049	1.40314	
	0.75591	0.88517	1.05733	1.19617	1.41599	
	0.75699	0.88517	1.0415	1.1905	1.37852	
	0.80316	0.8033	1.05733	1.18784	1.39084	
	0.757	0.88517	1.006	1.190499	1.39083	
	0.75699	0.88517	1.0818	1.191	1.339	
Mean	0.757454	0.877134	1.051297	1.1958439	1.388223	1.5488

Appendix F3. Variable geometry results raw data. (Fig 4.10)

		N_n	164	227	310	
	$A_d = 49$	P_3^*(mbar)	36.97	39.68	70.67	
		N_s^*	4.24	4.55	8.104	
	$A_d = 81$	P_3^*(mbar)	32.33	36.2	55.01	
		N_s^*	3.707	4.153	6.308	
	$A_d = 121$	P_3^*(mbar)	30.27	34.26	49.01	
		N_s^*	3.471	3.929	5.62	

Appendix F3. Variable geometry results raw data. (Fig 4.11)

A_d	m_p	m_s	m_s/m_p	P_e(mbar)	P_3^*(mbar)	Ns^*
49	1.057	0.2204	0.2085	8.72	39.68	4.55
81	1.057	0.3674	0.3476	8.72	36.2	4.15
121	1.057	0.5142	0.4865	8.72	34.26	3.929

Appendix F3. Variable geometry results raw data. (Fig 4.12)

		N_n	164	227	310	
		P_g(bar)	1.433	1.985	2.701	
	$A_d = 49$	N_s^*	4.24	4.55	8.104	
		N_p	38.76	50.03	38.22	
	$A_d = 81$	N_s^*	3.707	4.152	6.308	
		N_p	44.32	54.83	49.1	
	$A_d = 121$	N_s^*	3.471	3.929	5.62	
		N_p	47.34	57.94	55.11	

N_p	Primary pressure ratio P_g/P_3^*	
A_d	Ratio of the diffuser to primary nozzle throat areas	
N_s^*	Critical pressure lift ratio P_3^*/P_e	
N_n	Nozzle pressure ratio P_g/P_e	
P_e	Evaporator pressure = 872 mbar	
P_3^*	Critical condenser pressure	

Appendix F4. Raw data from the measured pressure distribution downstream of the jet-pump entrance. (Nozzle No 1)													
Axial distance along jet-pump (mm)				20	60	100	140	180	220	260	300	340	380	500
			P_3^*(mbar)	8.097	6.85	6.85	11046	21.93	25.17	25.91	27.41	29.4	30.89	37.37
Appendix F4. Raw data from the measured pressure distribution downstream of the jet-pump entrance. (Nozzle No 2)													
Axial distance along jet-pump (mm)				20	60	100	140	180	220	260	300	340	380	500
			P_3^*(mbar)	11.28	11.28	11.28	12.78	19	24.36	26.23	26.89	27.48	28.47	36.2
			P_3(mbar)	14.3	14.3	14.05	15.05	15.55	19.66	23.02	23.27	25.01	26.26	30.99

Appendix F5. Spray ice TIS raw data				
T_g	Hi (mm)	t (s)	m_i (g.s^{-1})	m_{ch}(g.min^{-1})
110				
	29	1840	1.114214674	9
	7.5	662	0.800925227	
	8	643	0.879564541	
	41	6377	0.454523287	10.1
	48	8112	0.418313609	
115	25	1837	0.96209853	9
	32	1824	1.240263158	
	29	1801	1.138342587	
	4	469	0.602942431	10.1
	21	2186	0.679137694	
	11	1559	0.498810135	
120	45	4554	0.698567194	10.1
	55	4416	0.880485734	
	12	1043	0.813365292	
	19	1414	0.949932815	
	41	2779	1.04299928	9
	49	3304	1.048442797	
	34	2153	1.116409661	
	51	3101	1.162671719	
	44	2571	1.209871645	
125	17	1714	0.701175613	10.1
	20	1910	0.74026178	
	18	4242	0.299978784	
	25	1509	1.171222664	9
	29	1981	1.034909137	
130	22	1845	0.84297561	9
	26	1997	0.920415623	
135	11	1453	0.535199587	9
	15	1004	1.056200199	
	6	643	0.659673406	
	31	3235	0.677448223	
	10	2176	0.32488511	10.1
	2	586	0.241279863	
T_g = generator temprature				
t = time duration of ice formation				
H_i = height difference due to ice formation				
m_i = rate of ice formation				
m_{ch} = circulation pump mass flow				

Appendix F6. Spray ice TIS cooling curve raw data. (spray nozzle flow 10.1 g.s-1)

t (min)	0	1	2.02	4.11	6.01	11.04	14.39	16.06	17.12	19.43	21.43	31.48	34.19	54.33	76.11
T_v(°C)	11.1	8.7	8	6.1	5	2	0.5	0	0	0	0	0	-0.1	-0.1	-0.1
T_L (°C)	10.1	9.1	9.2	7.9	6.5	3.1	1.4	0.9	0.5	0.2	0.1	0.1	0	0	0
P_v(mbar)	27	11.21	10.59	12.46	11.21	11.21	11.21	10.96	10.59	8.79	8.79	8.79	7.17	5.2	5

Appendix F6. Spray ice TIS cooling curve raw data. (spray nozzle flow 9 g.s^{-1})

t (min)	0	1	3.41	6.05	7.35	11.33	12.52	14.13	15.34	17.33	21.54	55			
T_v(°C)	13.6	9.4	6	4	3	1	0.5	0	-0.3	-0.3	-0.3	-0.2			
T_L (°C)	12.8	11.8	8	5.6	4.5	2.2	1.5	1	0.5	0.1	0	0			
P_v(mbar)	27	15.59	13.73	12.82	11.82	10.57	7.74	7.24	7.24	5.62	6.17	5.5			

T_L	Evaporator liquid-water temperature
T_v	Evaporator vapour temperature
P_v	Evaporator vapour pressure

Appendix F7. Encapsulated ice TIS charge cycle raw data							
t (min)	T_2 (°C)	T_3 (°C)	T_6 (°C)	T_{10} (°C)	T_{11} (°C)	P_e (mbar)	P_3 (mbar)
0	17.7	17.8	17.9	18	18.3	21.12	23.66
1	15.6	17.5	17.5	14.9	11.8	16.38	32.33
2	13.4	15.8	15.5	12.9	13.3	14.13	30.33
3	12	14.2	14	11.5	14	12.89	30.33
4	10.5	12.3	12.3	10	14.7	11.89	30.33
5	9.7	11.3	11.1	9.2	15	11.39	30.33
6	8.7	10.3	10.3	8.3	15.4	11.39	30.33
7	7.9	9.4	9.2	7.5	15.7	10.65	30.33
9	6.1	7.3	7.2	5.9	15.7	10.15	29.66
10	5.3	6.3	6.2	4.9	15.9	9.39	29.66
11	4.5	5.3	5.4	4.1	16.1	8.48	29.66
12	3.8	4.5	4.5	3.5	16.3	8.48	29.66
13	3	3.7	3.7	2.8	16.3	8	29.66
14	2.3	2.9	2.9	2.1	16.5	7.73	29.66
15	1.6	2.1	2.2	1.4	16.5	7.73	29.66
17	1	1.3	1.5	0.8	16.6	7.73	29.66
18	0.5	0.8	0.8	0.3	16.6	7.48	28.66
19	0.1	0.3	0.3	0	16.8	6.23	28.66
20	-0.3	-0.3	-0.1	-0.5	16.9	6.23	28.66
21	-0.6	-0.5	-0.5	-0.7	17.1	6.23	28.66
22	-1.1	-1.1	-0.9	-1.2	17.4	6.23	28.66
23	-1.3	-1.4	-1.1	-1.4	17.5	6.23	28.66
24	-1.5	-1.6	-1.5	-1.6	17.6	6.23	28.66
25	-1.8	-2	-1.9	-2	17.6	5.75	28.66
28	0.4	-0.2	0	0.3	17.3	5.24	28.66
30	0.3	-0.2	0	0.3	17.7	5.53	27.33
32	0.4	-0.1	0	0.3	17.8	5.53	27.33
34	0.4	-0.1	0.1	0.3	17.8	5.65	27.33
36	0.4	-0.1	0	0.3	17.9	5.53	27.33
39	0.4	-0.1	0	0.2	18	5.65	27.33
41	0.4	0	0	0.3	18.2	5.65	27.33
42	0.4	0	0	0.3	18.2	5.65	27.33
44	0.4	-0.1	0	0.3	18.2	5.65	27.33
46	0.4	0	0	0.3	18.2	5.65	27.33
48	0.4	0	0	0.3	18.3	5.62	27.42
50	0.4	0	0	0.3	18.4	5.24	27.42
52	0.4	0	0	0.3	18.4	5.24	27.42
55	0.4	0	0	0.3	18.3	5.24	27.42
58	0.4	0	0.1	0.3	17.9	5.24	27.76
60	0.4	0	0	0.3	18	5.24	27.76
62	0.4	0	0	0.2	18	5.24	27.76
64	0.4	0	0	0.2	17.8	5.62	27.76
66	0.4	0	0.1	0.3	17.9	5.24	27.76
68	0.4	0	0.1	0.2	18.3	5.33	27.76
70	0.3	0	0.1	0.2	19	5.33	27.76
72	0.3	0	0.1	0.2	19.1	5.24	26.42
74	0.3	0	0	0.2	19.2	5.24	26.42

76	0.3	0	0	0.1	19.2	5.66	26.42
78	0.2	0	0	0	19.3	5.66	27.09
80	0.2	0	0	0.1	19.3	5.66	27.09
82	0.2	0	0	0	19.2	5.29	27.09
84	0.2	0	0	0	19.4	5.29	27.09
86	0.1	-0.1	0	0	19.8	5.16	27.09
94	0	-0.1	0	0	20.3	5.29	27.09
98	0	-0.1	0	-0.1	20.1	5.16	27.09
100	0	-0.2	0	-0.2	20.3	5.16	27.09
102	-0.1	-0.2	0	-0.3	20.4	5.16	27.09
104	-0.2	-0.2	-0.1	-0.3	20.7	5.2	27.38
108	-0.2	-0.2	-0.1	-0.4	20.7	5.33	27.76
110	-0.2	-0.2	-0.2	-0.4	20.7	5.09	27.76
112	-0.2	-0.3	-0.2	-0.4	20.7	5.09	27.76
114	-0.3	-0.4	-0.3	-0.5	20.6	4.71	27.76
116	-0.4	-0.5	-0.4	-0.6	20.5	4.71	27.76
120	-0.6	-0.7	-0.6	-0.8	20.6	4.59	27.76
125	-0.9	-1.3	-0.9	-1.1	20.9	4	27.42
130	-1.2	-2	-1.3	-1.5	21.1	3.75	27.42
135	-1.1	-1.9	-1.7	-1.5	21.1	3.75	25.09
140	-1.6	-2.4	-2.2	-2	22.1	3.91	25.09
145	-2.8	-3.6	-3.6	-3.2	22	4.52	25.09
150	-3.6	-4.5	-4.3	-4	21.4	3.91	25.09
160	-5.2	-6.2	-6.1	-5.8	20.2	3.91	25.09
165	-3.1	-5.6	-3.8	-3.3	23.2	3.91	25.09
170	-3.8	-4.8	-4.6	-4.3	21.2	3.66	24.94
175	-3.6	-4.6	-4.5	-4.2	22.5	3.76	24.94
180	-4.6	-5.7	-5.6	-5.3	22.4	4.76	24.94
185	-5.3	-6.4	-6.2	-6	21.4	3.81	24.74
190	-3.6	-6	-4.5	-4.1	24.2	3.56	24.74
195	-4.2	-5.3	-5.2	-4.7	23.6	3.81	24.74
200	-5	-6.2	-6	-5.8	22.8	3.1	25
205	-5.4	-6.7	-6.5	-6.2	22.4	3.1	23.06
210	-5.9	-7.1	-7	-6.7	22.4	3.1	32.03

T_2	Temperature in the top capsule
T_3	Temperature in the bottom capsule
T_6	Temperature outside the mid-section capsule in the evaporator/ice store
T_{10}	Temperature in mid-secton capsule
T_{11}	Condenser temperature
P_e	Evaporator vapour pressure

Appendix F8. Encapsulated ice TIS discharge cycle raw data

	t	T_2	T_3	T_6	T_{10}	T_{11}	T_5	T_7	T_8	T_9	T_{12}
220	0	1.4	-0.5	-0.3	0.5	28.7	22.2	19.3	0.4	19.7	20
222	2	7.6	-0.4	-0.2	0.6	28.2	3.7	17.9	0.6	19.7	14.9
224	4	12.3	-0.4	-0.1	0.9	27.7	2.3	18.5	0.5	19.8	13.4
226	6	13.9	-0.3	-0.1	1	27.3	1.9	18.3	0.5	19.7	13.2
228	8	15.3	-0.3	-0.1	1	27	1.9	18.4	0.5	19.8	13.2
230	10	16.3	-0.4	-0.1	1	26.9	1.9	18.3	0.4	19.7	13.1
232	12	17.1	-0.4	-0.1	1.1	26.9	2	18.4	0.4	19.7	13.1
234	14	17.6	-0.3	-0.1	1.4	26.7	2.3	18.4	0.4	19.7	13.2
236	16	17.9	-0.3	-0.1	1.7	26.6	2.4	18.4	0.3	19.7	13.1
238	18	18	-0.3	-0.1	2.9	26.5	2.3	18.4	0.3	19.7	13.2
240	20	18	-0.3	-0.1	4	26.5	2.4	18.3	0.3	19.7	13.2
242	22	18.1	-0.3	0	5.4	26.5	2.5	18.3	0.3	19.7	13.2
244	24	18.2	-0.3	0	6.7	26.4	2.6	18.4	0.3	19.7	13.2
246	26	18.2	-0.3	0.1	8.2	26.4	2.7	18.4	0.3	19.7	13.2
248	28	18.2	-0.3	0.7	9.7	26.3	2.7	18.4	0.4	19.7	13.2
250	30	18.2	-0.2	2.2	11.2	26.2	2.8	18.4	0.4	19.7	13.3
252	32	18.2	-0.3	4.2	12.5	26.1	3.1	18.4	0.4	19.7	13.3
254	34	18.2	-0.2	7.2	14.1	25.8	3.1	18.4	0.4	19.7	13.4
258	38	18.2	-0.2	13.4	16.2	25.5	3.3	18.4	0.4	19.7	13.5
260	40	18.2	-0.2	14.8	16.7	25.5	3.6	18.4	0.3	19.6	13.5
264	44	18.3	-0.2	16.7	17.6	25.3	3.8	18.4	0.6	19.6	13.6
266	46	18.3	-0.2	17.1	17.9	25.2	4.1	18.4	0.9	19.7	13.7
268	48	18.3	-0.2	17.5	18	25.1	4.7	18.4	1	19.6	13.9

270	50	18.3	-0.2	17.7	18.2	25.1	4.8	18.4	0.9	19.6	14
272	52	18.3	-0.2	17.9	18.3	25	5.3	18.4	1	19.6	14.1
274	54	18.3	-0.2	18	18.3	24.9	5.8	18.4	1.7	19.4	14.3
276	56	18.3	-0.2	18.1	18.4	24.9	6.3	18.4	4.6	19.2	14.4
278	58	18.3	-0.2	18.3	17.4	25	7	18.4	7.6	19	14.6
280	60	18.2	-0.2	18.2	18.4	25.1	7.5	18.3	9.7	18.6	14.7
282	62	18	-0.2	18.2	18.4	25	8.5	18.2	12.1	18.3	14.9
284	64	17.9	-0.1	18.2	18.3	24.9	9.3	18.2	13.3	17.8	15
287	67	17.6	-0.2	18	18.3	24.7	10.7	18	14.6	17.4	15.2
290	70	17.3	-0.2	17.8	18	24.3	11.8	17.8	15.7	17.4	15.4
292	72	17.1	-0.2	17.5	17.7	24.2	12.7	17.5	16.3	17.5	15.8
294	74	17.2	0	17.4	17.6	25	13.4	17.4	16.7	17.6	16.3
296	76	17.3	1.4	17.4	17.5	23.8	14.4	17.4	17.1	17.8	16.5
300	80	17.5	10.2	17.3	17.6	23.7	15.6	17.3	17.2	17.8	17
302	82	17.6	11.5	17.4	17.6	23.6	15.6	17.4	17.2	17.8	17.2

T_5	Temperature of re-circulation flow entering heat exchanger
T_7	Temperature of re-circulation flow entering evaporator/ice store through spray nozzle
T_8	Temperture of the liquid-water surrounding the capsules in the bottom of the evaporator/ice store
T_9	Temperature of the heat load fluid entering the heat exchanger
T_{12}	Temperature of the heat load fluid leaving the heat exchanger

Appendix F9. Convergent-divergent throat jet-pump raw data

P_e (mbar)	H_c (mm)	t (min)	m_g (g.s^{-1})	m_c (g.s^{-1})	m_s (g.s^{-1})	m_s/m_p
35.71	586	31.55	1.057	1.5477458	0.4907458	0.464281741
28.03	1093	65.28	1.057	1.395215839	0.338215839	0.319977142
32.68	1181	66.083	1.057	1.489229151	0.432229151	0.408920673
31.82	1010	62	1.057	1.3583	0.300472581	0.284269234
24.01	1062	60	1.057	1.474941	0.417941	0.395403027
19.68	1032	60	1.057	1.433276	0.376276	0.355984863
46.43	1095	64.233	1.057	1.42055252	0.36355252	0.343947512
30.42	1008	54.08	1.057	1.553192308	0.496192308	0.469434539
24.43	398	22	1.057	1.507515455	0.450515455	0.426220865
23.4	1036	60	1.057	1.438831333	0.381831333	0.361240618
26.3	1117	62	1.057	1.501284032	0.444284032	0.42032548
45.7	1039	60.0833	1.057	1.440997249	0.383997249	0.363289734

H_c	Difference in level in the condensate measuring vessel
m_c	Condensate mass flow

Table 3.1. Drawing legend of Figure 3.2.			
1. Suction pipe-jet-pump section	14. Flanges, bolts and inserts	27. Condenser vessel	40. Generator temperature cut-out
2. Flange, seals, and bolts-jet-pump section	15. Suction pipe-evaporator section	28. Plates and seals	41. Thermocouple selector
3. Jet-pump insert housing	16. Differential pressure gauge-condenser/evaporator	29. Flanges, bolts and seals	42. Thermocouple indicator
4. Primary nozzle flange	17. Storage vessel	30. Cooling coil	——— Evaporator circuit
5. Flange, seals, bolts-condenser	18. Plates and seals	31. Flow meter	——— Heat load circuit
6male-male connector	19. Flanges, bolts and inserts	32. Pressure gauge	——— Storage circuit
7. Plug seal	20. Circulation pump	33. Manometer	——— EVP evaporator vapour pressure line
8. Stainless steel tube	21. Spray nozzle	34. Measuring vessel	——— JWP jet-pump wall pressure
9. Compression fitting	22. water heater	35. Plates, seals and inserts	——— CP condenser pressure
10. Copper manifold	23. Centrifugal pump	36. Flanges, bolts and inserts	——→ CWI condenser cooling water in
11. Differential pressure gauge-evaporator/wall	24. Flow meter	37. Diaphragm pump	←—— CWO condenser cooling water out
12. Evaporator vessel	25. Header tank	38. Pressure gauge	——— Condensate return and generator circuit
13. Plates, seals	26. Heat exchanger	39. Generator temperature controller	—⊟— Thermocouple location

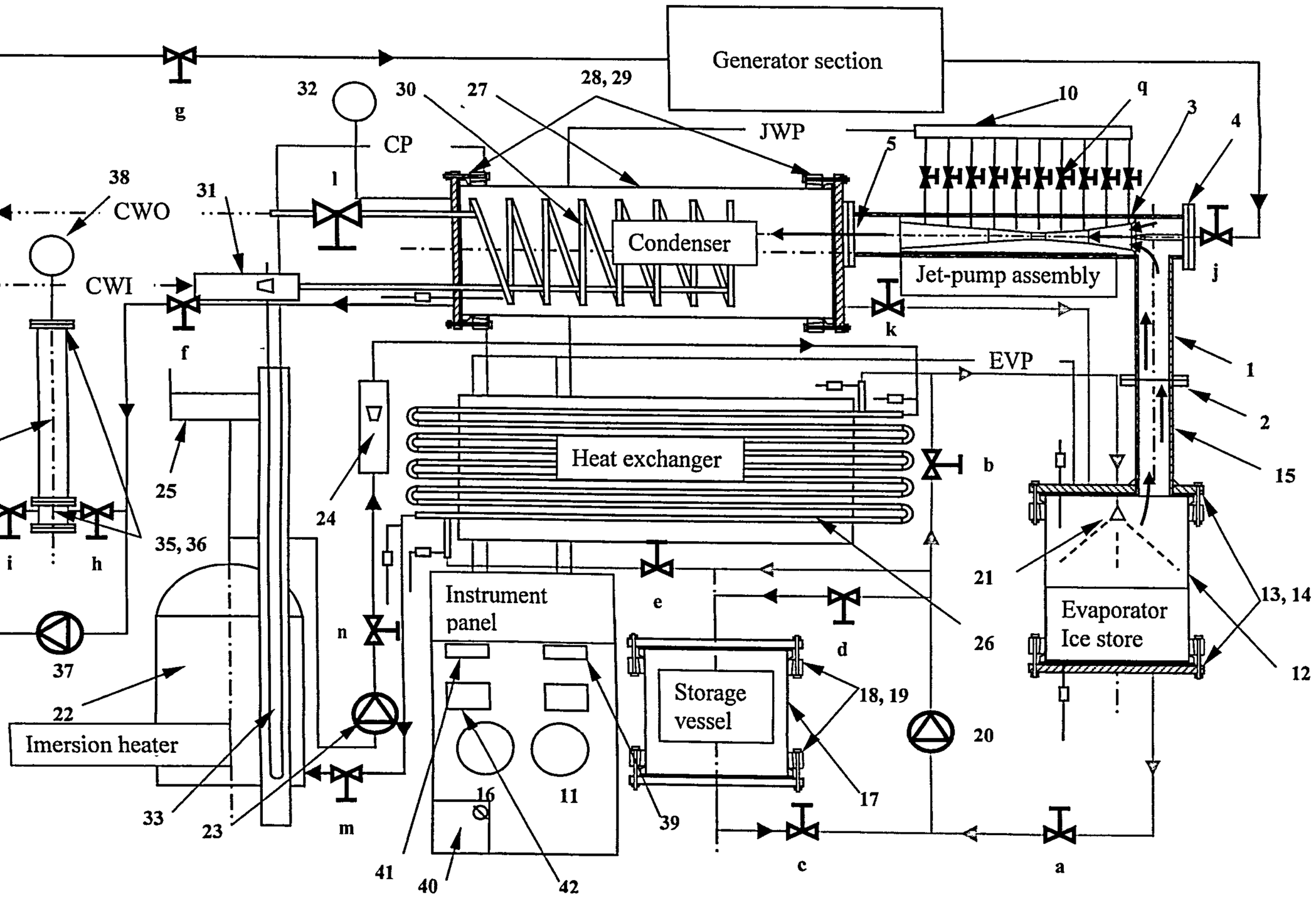

Figure 3.3. Flow diagram of the jet-pump TIS test rig.